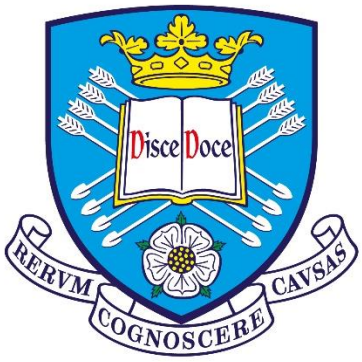

The University Of Sheffield.

Oxide Scales Behaviour During Descaling and Hot Rolling

By:

Daryoush Ahmadi

The University of Sheffield
Faculty of Engineering
Department of Materials Science and Engineering

June 2019

A thesis submitted in partial fulfilment of the requirements for the degree of Doctor of Philosophy

Acknowledgements

First, I would like to express my sincere gratitude to my supervisor Professor Mark Rainforth, for his great support throughout my studies and his unlimited patience to allow me to complete this research.

I would also like to thank my industrial supervisor Dr Didier Farrugia for granting the Industrial Case Award and for his help and support throughout the project.

I am also thankful to Professor Michal Krzyanowski for his help, supervisions, and suggestions during this research.

I would like to thank Professor Barbara Shollock and Professor Eric Palmiere for their guidance and suggestions.

I extremely obliged to Tata Steel Europe for offering me the Industrial Case Award, and I sincerely grateful to the Engineering and Physical Sciences Research Council (EPSRC) for financial support of this project.

Special thanks to Dr Krzysztof Muszka and Dr Lin Sun for all their help with engineering drawings and thermomechanical testing. I would also like to thank Dr Amit Rana, Dr Thomas Simm and Dr Jiang, Xiaoqing for all their support.

I would like to acknowledge all academic staff of the Department of Materials Science and Engineering who helped me over the years.

A big thank you to all Administrative, managerial, secretarial and technical staff in the Department of Materials Science and Engineering at the University of Sheffield and the members of staff in Sorby Centre.

I would like to thank all my friends in the Department of Material Science and Engineering for creating a pleasant environment throughout my stay in Sheffield.

I express my sincere gratitude to my parents for their limitless support and encouragement.

Finally, I would like to thank my lovely wife and my best friend Zohreh, who stands by me and constantly supports me in any difficult moments and I would love to thank my beautiful daughter Anahita for giving me hope and strength to work harder.

Abstract

The impact of the descaling process on the surface finish of steel products in hot rolling has been established over the years. However, most of the studies completed on the effect of the secondary scales and the influence of the primary scales has been unnoticed. The aim of this research was to study the behaviour of oxide scales during the descaling and hot rolling of two steel grades, particularly the influence of primary scales. In this research, the oxide scale behaviour of two key steel compositions was studied. High carbon rail steel and high silicon electrical steel (DSP) provided by Tata Steel Europe as-cast condition. The project consisted of two main sections: 1. Assessment of the oxidation kinetics and characterisation of the oxide scales microstructure developed under different conditions. 2. Evaluation of the mechanical properties of the steel grades at elevated temperatures.

Isothermal oxidation experiments were conducted to evaluate different oxidation parameters, including the atmosphere, temperature and alloy compositions. All isothermal oxidation experiments were conducted under controlled environment using dry or humid atmospheres. The characteristic zones and microstructure of the oxide layer were studied by different techniques, including X-ray diffraction (XRD) and backscattered electron (BSE) imaging and energy dispersive X-ray spectroscopy (EDX) to assist the identification of the oxide phases. It was found that the compositions of the oxide scales were influenced by the oxidation parameters, including temperature, time and oxidant atmosphere composition.

Furthermore, it was confirmed that the parent material chemistry not only significantly influenced the oxidation kinetics but also it affected the microstructure and composition of the oxide scales. In long isothermal oxidation of both grade Wüstite and was the predominant phase and the amount of Hematite was small. In addition, a considerable amount of Magnetite was developed under the same oxidation condition. The spinel phase of Fayalite was detected at the oxide-metal interface during oxidation of both alloys; however, the amount of this phase was significantly higher in DSP steel. In the oxidation of two alloys under dry condition, it was observed that the oxide outer scales completely detached from the parent materials. The amount of Wüstite phase in DSP samples was negligible when oxidised under a dry atmosphere.

A high temperature compression test was designed to evaluate the failure mode of the oxide scales under compressive stresses at elevated temperatures. All thermomechanical experiments were carried under a dry air atmosphere using the Arbitrary Strain Path (ASP) rig at The University of Sheffield. The results confirmed that FeO had higher plasticity than Fe_3O_4 and Fe_2O_3. However, it was observed that Wüstite behaved in a brittle manner at 850˚C.

A new tensile test designed based on previous works of Krzyzanowski and Beynon [31]. The test allowed direct measurement of the ultimate tensile strength of the oxide scale. The oxide scale failed in two different manners, as reported previously by the above researchers [31]. The first mode was in transverse direction due to cracks initiation and propagation perpendicular to the oxide-metal interface, and the second failure mode was due to the slide of the oxide scale along the oxide-metal interface. However, it was found the test deformation temperature is not governing the failure mode exclusively. The alloying elements of the parent metal and the temperature of the oxidation had great importance in the failure mode of the oxide under tensile load.

Oxide scale blistering was observed during the oxidation of rail steel during the reheating stage of thermomechanical tests. However, this phenomenon was not detected in the oxidation of DSP grade under the same condition.

Contents

Chapter 1

Introduction

1.1 Background

In hot rolling of steel, unravelling the technical hitches associated with the development of primary and secondary oxide scales is one of the major concerns. The oxide scale behaviour during hot rolling is complicated and has a strong effect on the final product quality. In recent years, the behaviour of the secondary oxide scales during multi-pass rolling has been studied extensively, and some models have been developed successfully to predict the behaviour of the secondary oxide scales. However, these models only cover alloys with simple chemistries, as the effects of alloying elements have been ignored. A greater challenge lies in the understanding of scaling/descaling behaviour of primary scales. This is crucial especially for steel chemistries, which exhibit major differences in the oxide compositions and morphology in comparison to plain carbon steels. The oxidation of steel at elevated temperatures is significantly influenced by different parameters including temperature, time, the partial pressure of oxygen, oxidant environment and cooling rate. These factors govern the development and growth rate of the oxide scale, oxide scale microstructure and morphology, as well as the scale composition [1-4]. Furthermore, several other aspects need to be assessed, including mechanical properties and oxide scale integrity and failure mode of the oxide scales under applied stresses. The failure of oxide scales during hot forming is governed by induced tensile, compressive and shear stresses. A key aspect of model development requires basic mechanical property data about the scale as a function of temperature, in particular, strength, ductility and failure stress. Several test methods have been developed to calculate the mechanical properties of the oxide scale at elevated temperature, including hot tensile testing, hot compression testing.

1.2 Aims of the research

This research was proposed to evaluate the development and behaviour of the primary oxide scales during reheating, descaling and hot deformation of two steel grades. Several process parameters including time, temperature and the oxidant atmosphere were studied. Also, the effects of alloying elements on oxidation kinetics and the oxide scale microstructure and compositions were assessed by isothermal oxidation studies of two different steel grades. Furthermore, the failure modes and mechanical properties of the oxide scales of the oxide scale were studied by designing new high temperature compression and tensile test systems.

- **Isothermal oxidation studies**

Initially, the isothermal oxidation of steel was studied by reheating the materials in a closed tube furnace under certain conditions. The oxidation key parameters were assessed, including temperature, reheating time, the composition of the oxidant.

- **Thermomechanical evaluation of the oxide scales**

In the next step, the thermomechanical properties and behaviour of the oxide scale including ultimate tensile strength and brittle to ductile transition, scale plasticity, the critical strain of the oxide scales at high temperatures were examined via tensile and compression tests at elevated temperature.

For the compressive test mode, the test method developed by Trull and Beynon [4] was adopted. However, the test method was modified by designing a new compressive curved tool to imitate the roll bite in a hot rolling mill. For the tension mode, the test followed the technique developed by Krzyzanowski and Beynon [15] at The University of Sheffield using an advance testing rig (ASP). Due to errors associated with the above test method, the procedure was completely modified to eliminate undesirable testing parameters including the effect of hydraulic vibrations during the reheating stage and the effect of the friction forces caused by the original design of the test piece.

1.3 Layout of the Thesis

In Chapter 2, a brief description of the literature around the subject is given, which includes the oxidation mechanisms and oxidation kinetics of iron and steel. Other factors including the effect of different process parameters including time, temperature and alloy chemistry and the composition of the oxidant atmosphere are reviewed in this section. Moreover, the previous works of other researchers for thermomechanical evaluation of the oxide scales are summarised.

The materials composition and dimensions, along with experimental methodology, are detailed in Chapter 3, which include the details of the equipment for testing and facilities used for oxide scale characterisations.

The results of the isothermal examinations of the two steel grades are listed in Chapter 4. First, the oxidation kinetics are detailed, and the oxidation parameters analysed. Then a comprehensive cross-sectional examination of the oxide scales microstructure and phase distribution are given. This includes the results obtained by different characterisation techniques including XRD, SEM, EDS and laser Raman spectroscopy.

Chapter 5 contains the details of the compression tests and tensile tests results at elevated temperatures. Furthermore, the oxide scale cross-section analyses of the deformed samples are described in this chapter.

The discussions of the results of all experiments are made in Chapter 6. The effect of the different parameters of the oxidation behaviour of the materials, including the temperature, time and the effect of the water vapour in the oxidant atmosphere are debated in this part. The thermomechanical test results also are discussed in details, and they are compared with the works of other researchers.

Finally, the list of contributions and relevant conclusions are listed in Chapter 7.

Chapter 2

Literature Review

Steel alloys are among the most important and widely used materials in today's industries, and hot rolling is the most favourable manufacturing method for production of long and flat steel products. In high temperature corrosive conditions such as the atmosphere of a reheating furnace, the oxidation of metals is inevitable. The influence of the oxide scales on the hot forming of metals can be understood and optimised only by gaining a deep knowledge of the oxidation process during reheating and forming the materials. Many parameters are involved in assessing the thermomechanical properties of the oxide scales, such as the structure and morphology of the oxide layer, the thickness, chemical compositions of the oxide and the substrates.

This chapter initially provides the backgrounds of the two steel grades used in this research, including the high carbon steel grade as long product and the high silicon steel in flat product form.

Furthermore, the alloys oxidation phenomenon is methodically reviewed. Although the oxidation kinetics and mechanisms of iron oxide formation are explained extensively in many textbooks [1, 2, 3], a brief description of iron and steel oxidation process will be presented in this section. Also, the literature around the morphology and microstructure of various oxide scales along with the development and distribution of the oxide phases are reviewed.

Finally, an overview of the behaviour of the oxide scale during hot processing, including plastic and elastic deformations, development and propagation of the defects and the failure mechanisms of the oxide scale is discussed.

2.1 Overview of manufacturing and metallurgy of high carbon steel and high silicon steel

As this research financially sponsored by Tata Steel Europe, it was suggested that the focus of the research be on the oxide scale behaviour of the following steel grades of Tata's product catalogue:

1. High carbon steel (standard grade) produced in forms of long product for railway manufacturing.
2. High silicon / low carbon steel produced in flatforms for electrical applications.

2.1.1 High carbon steel for railway production

The metallurgical properties of carbon steel are highly influenced by its chemical composition along with process and production conditions. Carbon is the most important alloying element in the production of ferrous alloys. The carbon level extremely influences the development and extent of different phases during production, including casting and heat treatment of the products. As demonstrated in Figure 2.1.1.1, often based on the temperature and the carbon content, the curves of equilibrium or phase transformation boundaries are plotted, which is known as the iron-carbon phase diagram. The amount of carbon defines the type of alloys in plain ferrous alloys. In general, the ferrous alloys containing 0.002 to 2.1% carbon are known as steel. The plain carbon steels are divided into the following categories:

- Low carbon steel: typically, these steel alloys contain up to 0.25 wt% carbon. The microstructure of these alloys is constructed of ferrite and pearlite. The low carbon steel is relatively week with a yield strength of 280 MPa.
- Medium carbon steel: the amount of carbon content of these alloys may vary between 0.25 and 0.6 wt%. The medium carbon steel alloys have higher mechanical properties than low carbon grades, with a typical yield strength of 450 MPa.
- High carbon steel: if carbon content of the steel is between 0.6 and 1.4 wt%, the alloy is categorised as high carbon steel. These alloys are considerably stronger than the

low and medium carbon grades. The yield strength of these alloys can reach 1700 MPa; however, they suffer from low ductility [113].

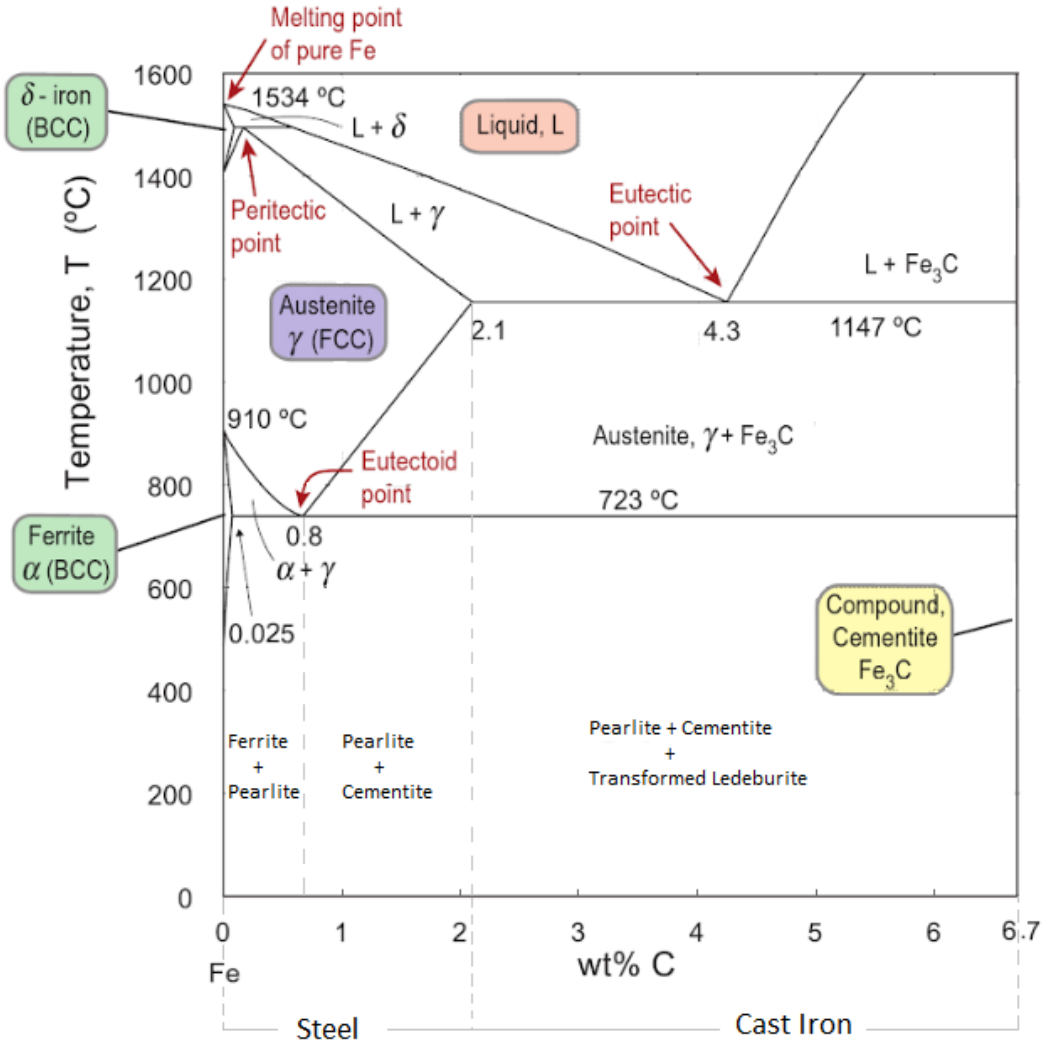

Figure 2.1.1.1 iron-carbon equilibrium phase diagram after Ashby et al. [112].

Nevertheless, the addition of other alloying elements may alter the type and the extent of each phase in ferrous alloys at any certain condition. For instance, rail steel usually contains up to 1wt% manganese, which slightly alters the critical temperatures in the iron-carbon phase diagram.

The materials used for the production of the railway must be wear resistant and resilient to induced stresses and subsequent failure during the service. The properties of a steel alloy are highly depended on its composition in conjunction with the process parameters including time, temperature, reduction ratio and final heat treatment regime. Carbon and manganese

are the two key alloying elements that play major roles in the foundation of desirable microstructure and mechanical properties. In modern manufacturing of rail steel, 0.4%-1.05% of carbon and 0.7%-1.7% of manganese are added to achieve the desired hardness and wear resistance.

The provided rail steel grade in this research contains 0.76% of carbon and 1.0% of manganese that can be categorised as standard 260-grade rail steel. The alloy is eutectoid steel with 100% perlite microstructure. This high carbon steel has a pearlitic lamellar microstructure. As demonstrated in Figure 2.1.1.2, the perlite lamellar structure is constructed of ferrite (α Fe) and cementite (Fe3C). In this composite structure, ferrite provides the ductility that makes the alloy tough while cementite makes the alloy strong and hard [115]. The combination of the above mechanical properties makes this steel grade highly wear resistant and suitable for the railway industry. The mechanical properties of perlite are highly influenced by a microstructural factor, which is known as pearlite interlamellar spacing (PIS). In eutectoid, pearlitic steels the proof stress and ultimate tensile strength have a reverse relationship with PIS. However, the effect of PIS reduction on plane-strain fracture toughness (PSFT) is more complex. The initial reduction of PIS weakens the PSFT, but further refinement of pearlite increases this factor [116].

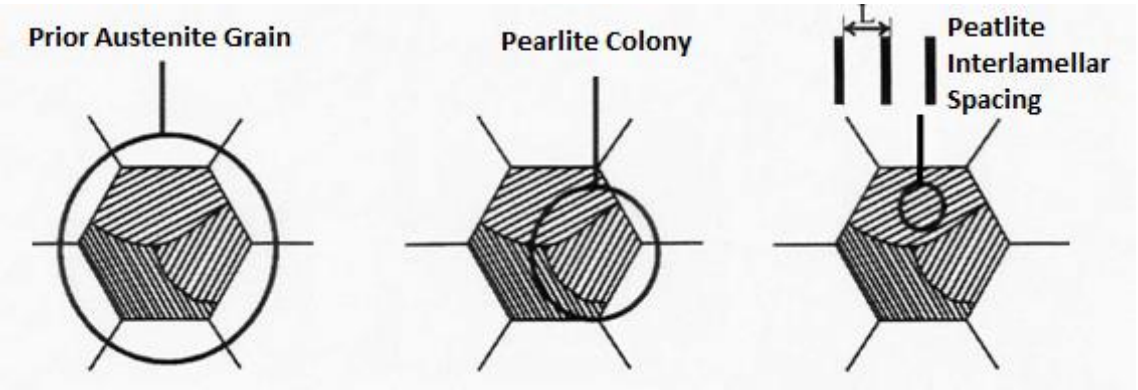

Figure 2.1.1.2 Schematic representation of a pearlitic microstructure [114].

In advance rail steel manufacturing, after primary steel making, the material is sent through a secondary melting process, which includes vacuum degassing to reduce the undesirable gas contents, especially hydrogen. The molten steel then continuously cast and cut into blooms for further processing [115]. For hot deformation, the rail steel must be reheated to a

maximum temperature of 1280°C. As a result, the surface of the workpiece is heavily oxidised, and eventually, a thick primary scale covers the entire surface of the material. The rolling of the workpiece, which contains a thick oxide scale on the surface, would result in poor surface finish and possible rejection of the product at the end of the process. Therefore, understanding the behaviour of the primary oxide scale is crucial for developing a robust descaling process before rolling stage.

2.1.2 High silicon steel for electrical applications

The importance of electrical steel alloys is indisputable in modern industries. Evermore, the demand of electrical steel grades is surging due to global mandates for reduction of carbon footprint by the production of clean energy via revolutionary methods such as new wind turbines generators, and by commissioning green types of machinery such as electric vehicles. Because the main alloying element in the manufacturing of the electrical steels is silicon, they are also known as iron-silicon alloys. The magnetic properties of the electrical steel alloys are highly depended on high permeability and low core loss, which includes Hysteresis and Eddy current losses [117]. The desirable physical properties are achieved by attaining precise chemical composition along with highly controlled manufacturing process, including tailored heat treatment.

Commercial electrical steel grades may contain up to 3.5% Si, however using modern techniques, new grades are developed which contain up to 6% Si. The addition of silicon above 3.5% significantly reduces the ductility of the material [126].

Electrical steels are mainly divided into two different categories; grain oriented (GOES) and non-oriented (NOES) [121]. The controlled grains orientation offers minimal power loss and high permeability. The Si content of GOES anisotropic products is between 2.9-3.15% (+Al), and the materials are produced via hot and cold working operations in conjunction with precise annealing practice to achieve (110) [100] crystallographic orientation [126, 117].

On the other hand, the amount of silicon in NOES is usually between 0.5 and 3.25%. In the production of NOES alloys, secondary recrystallisation is not required for achieving the

desired physical properties; therefore, the chemical composition may contain a lesser amount of silicon in comparison to the GOES grades.

In terms of chemistry, although several different alloying elements influence the magnetic properties of the electrical steel, silicon and carbon are the most important elements due to their prominent effects on the phase transformation characteristics of the alloy including the equilibrium of austenite (γ) and ferrite (α).

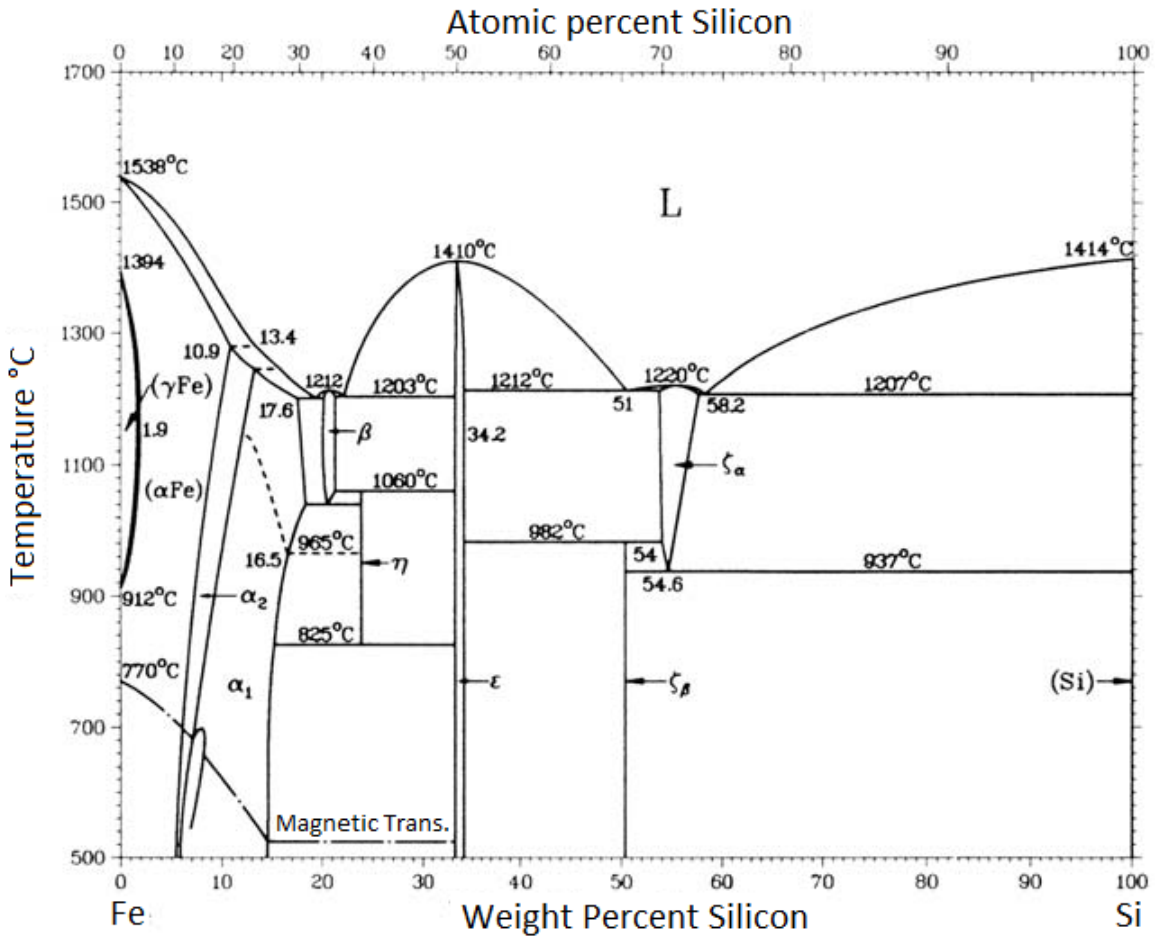

Figure 2.1.2.1 iron-silicon equilibrium phase diagram [122].

Because silicon is a strong ferrite (α) stabiliser, increasing the Si content raises the transformation temperature of α → γ and reduces the transformation temperature of γ → δ in Fe-Si binary alloys. As can be seen in Figure 2.1.2.1, when the proportion of Si reaches the 2.5% limit, the alloy crystal structure would be body centre cubic below the solidus temperature. In contrast, small carbon addition can expand the austenite (γ) region

in the iron-silicon phase diagram. As demonstrated in Figure 2.1.2.2, when the carbon content reaches the 0.1% limit, austenite can coexist with ferrite between 800°C and 1400°C even if the silicon content surpasses the 6.0% margin [117].

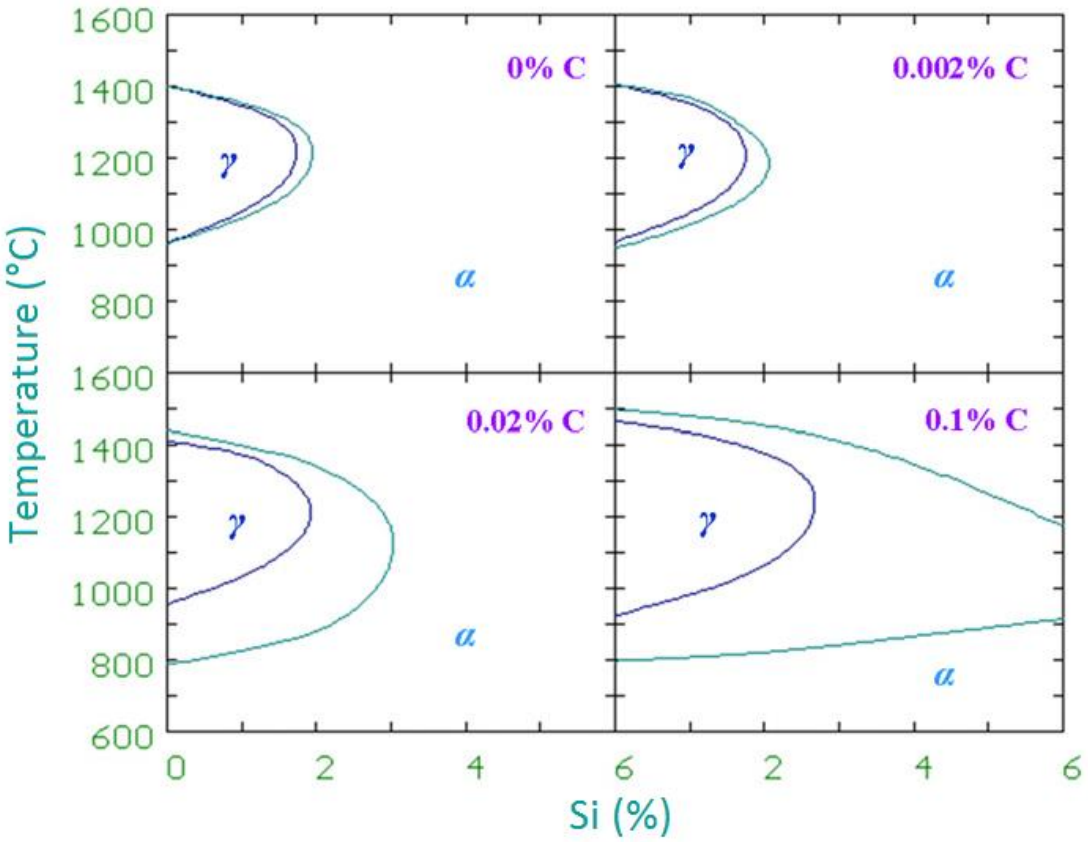

Figure 2.1.2.2 Effect of carbon on the iron-silicon phase diagram [118].

If the production process is not tightly controlled, carbon and silicon may segregate within the Fe matrix, promoting a mixed distribution of austenite and ferrite throughout the workpiece [118]. Generally, in manufacturing of electrical steel, the carbon content is kept below 0.01% [120]. For further reduction of carbon level, the cold–rolled steel sheets are decarburised under a controlled atmosphere containing water vapour and hydrogen. This procedure is vital for the texture and the magnetic properties of the final products. The slow precipitation of iron carbides that is also known as magnetic ageing significantly deteriorates the magnetic properties of the materials due to an extensive surge of the core loss. It is suggested that the magnetic ageing anisotropy is attributed to the crystallographic and morphological characteristics of Fe_3C and $Fe_{2.4}C$ precipitates [120].

Figure2.1.2.3 demonstrates a typical ferritic microstructure of a full processed NGO electrical steel sheet that contains

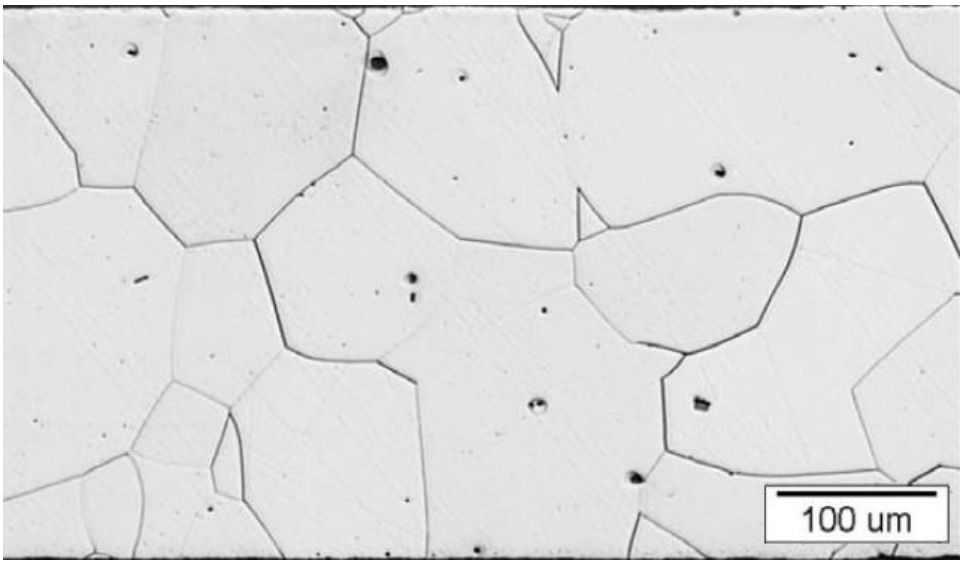

Figure 2.12.3 Ferritic microstructure of a fully processed NGO electrical steel sheet [120].

The other alloying element, which can potentially improve the magnetic properties of the product by intensifying the electrical resistivity of the high silicon steels, is manganese [123]. However, Mn is an austenite stabiliser; therefore, the addition of this element must be at an optimum level to avoid the development of austenite. It is vital to reduce the amount of sulphur and oxygen to maintain manganese in solid solution and to avoid the precipitation of deleterious phases such as sulphides and oxides within the ferrite matrix [124]. Schulte et al. [123] studied the effects of various level of Mn on the properties of the electrics steel containing 2.66% Si. As demonstrated in Figure 2.1.2.4, increasing the Mn level-up to 1.4%, reduces the average grain size of the matrix at various temperatures. The addition of Mn up to 1.4% does not result in the formation of austenite. The literature indicates that the electrical steel containing 2.7 wt% Si and up to 1.4 wt% Mn can be fully ferritic without phase transformation under a controlled process condition. Furthermore, it is known that Mn contributes to solid solution hardening of the electrical steel [123].

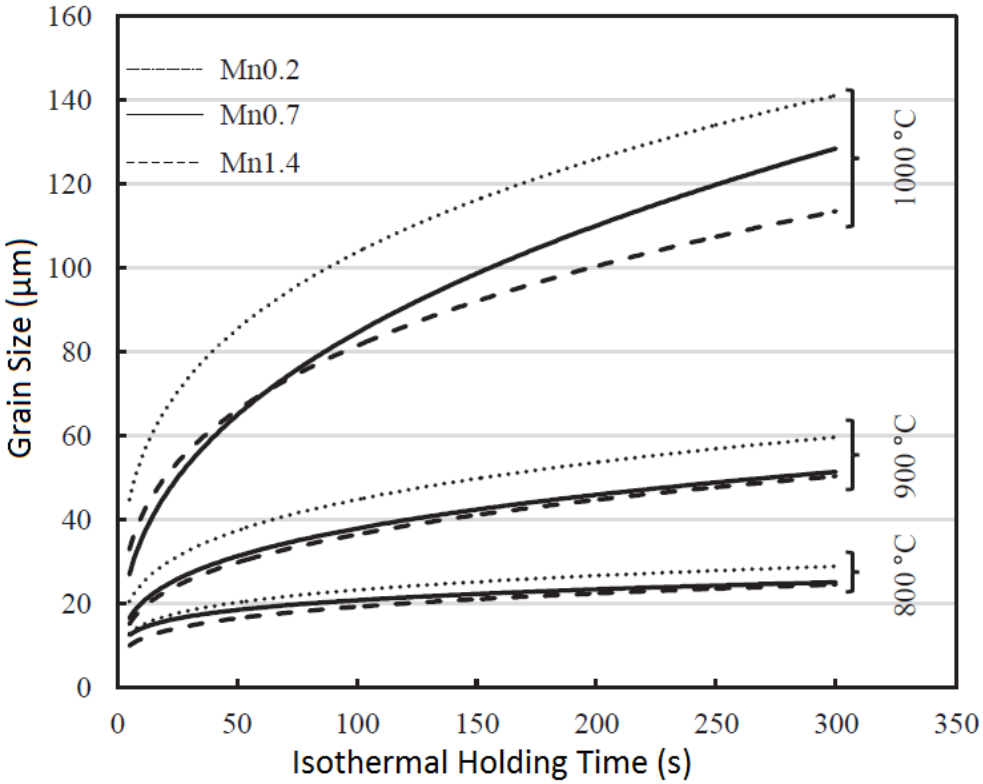

Figure 2.1.2.4 Grain growth during isothermal heat treatment of high silicon steel at 800 °C, 900 °C and 1000 °C [123].

Aluminium that is a strong ferrite stabiliser can also be used as an alloying element in the production of electrical steel to increase the electrical resistance of the product [117]. Increasing the amount of aluminium above 0.1 wt% leads to enlargements of aluminium-nitride (AlN) precipitates above 1.0 µm, which eradicates the grain boundaries pinning and subsequent undesirable core loss in the alloy [125].

There are different methods for the production of electrical steel sheets. In April 2000, Corus (currently known as Tata Steel Europe) commissioned a new facility in Ijmuiden for production of flat products by sending the materials directly under rolling process directly after the continuous casting process. This manufacturing facility, which is also known as Direct Sheet Plant (DSP), predominantly produces thin gauged material via a single casting strand combined with a compact semi-endless rolling mill [119]. The B9S23 UT23 electrical steel grade proposed for this research is one of the grades manufactured via the DSP process in Ijmuiden. This is a NOES grade that contains 2.3% Si and 0.4% Al with ultra-low carbon level with a ferritic (α) microstructure. The Corus DSP production line layout is demonstrated in Figure 2.1.2.5. One of the major changes in DSP production is the removal of the primary and

secondary oxide scales. The development of the primary scale formation initiates immediately after casting and continues during the heating process within the tunnel furnace. The material is descaled in two different stages. The primary scales are removed by sending materials through a descaling process before entering the roughing mill. If the oxide scales partially remain on the surface of the slabs due to inadequate descaling, the gradual scale build-up not only deteriorates the surface quality of the final product but it can also stop the production by blocking the rolling mill. The nature and behaviour of the electrical steel primary oxide scale will be discussed in the upcoming chapters.

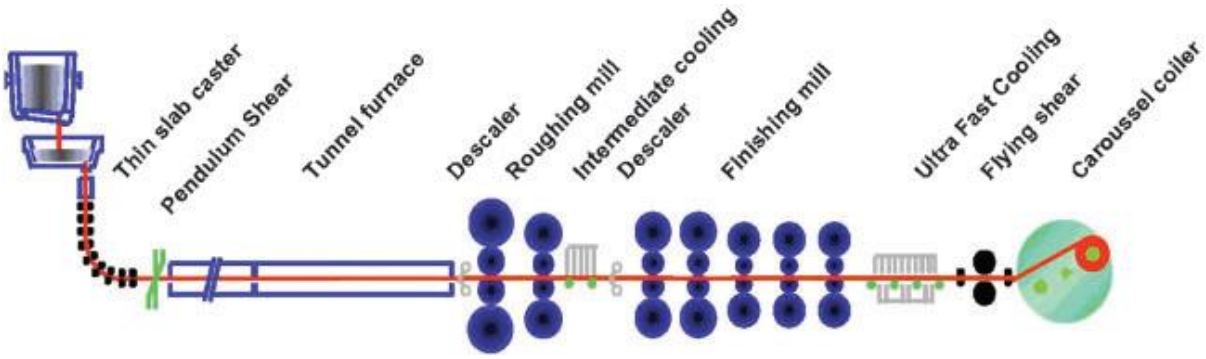

Figure 2.1.2.5 Layout of Corus IJmuiden Direct Sheet Plant [119]

2.2 Oxidation mechanisms

The oxidation process in metals can be defined as the interaction of metal atoms with oxygen with several factors involved in oxide formation and growth including time, temperature, environment, partial pressure of oxygen and chemical compositions.

The second law of thermodynamics defines the probability of a chemical reaction. In reactions with constant temperature and pressure, the second law can be written as Equation (2.1):

$$\Delta G = \Delta H - T\,\Delta S \qquad (2.1)$$

Where ΔG is free energy of the system, which is also known as Gibbs free energy, ΔH is the enthalpy of the system, T is the absolute temperature, and ΔS is the entropy of the system. ΔH is a factor that defines the actual energy released or absorbed during the reaction. If the value of the enthalpy is negative, then the system releases energy, contrarily if the ΔH value is positive, then the reaction requires energy to progress. The entropy is defined as the degree

of disorder probability of the system. Based on the second law of thermodynamics, the reaction of an isolated system is naturally spontaneous if ΔG value is negative. In contrast, if ΔG is greater than zero, then the reaction is thermodynamically impossible. Furthermore, when the ΔG value is equal to zero, then the system is at equilibrium [2].

For a reaction defined as:

$$\alpha A + bB = cC + dD \tag{2.2}$$

The Gibbs free energy can be written as:

$$\Delta G = \Delta G^\circ + RT \ln\left(\frac{a_C^c\, a_D^d}{a_A^a\, a_B^b}\right) \tag{2.3}$$

Where ΔG° is the standard free energy, T is the temperature, R is the gas constant (= 8.31 J K^{-1} mol^{-1}), and α is the thermodynamic activity of reaction species. At system equilibrium, where ΔG is equal to zero the Equation (2.3), is simplified as:

$$\Delta G^\circ = - RT \ln\left(\frac{a_C^c\, a_D^d}{a_A^a\, a_B^b}\right) \tag{2.4}$$

A simple form of a metal oxidation process is demonstrated in Equation (2.5):

$$M\,(s) + O_2\,(g) = MO_2\,(s) \tag{2.5}$$

If thermodynamically the activities of the metal and metal oxide are considered as a unity, according to Equation (2.4), the partial pressure of oxygen for the simultaneous existence of the metal and the metal oxide can be expressed as:

$$P_{O_2}^{M/MO_2} = exp\frac{\Delta G^\circ}{RT} \tag{2.6}$$

The thermodynamics is often used to predict statuses of chemical reactions, including the prediction of products along with the feasibility of reduction or oxidation (or any other analogical reactions such as sulphidation, carburisation, etc.). However, a range of thermodynamic statistics can be obtained from the plots of the standard free energy (ΔG°) as a function of temperature, which is also known as Ellingham diagram (Figure 2.2.1). Since the thermodynamic data of several systems are typically incorporated into an individual diagram,

it facilitates the comparison of the components stabilities of different systems. Moreover, generally, the Ellingham diagram enclose a nomographic scale which allows the partial pressure of oxygen of the system ($P_{O_2}^{M/MO_2}$) to be acquired directly from the diagram for any desired temperature [2].

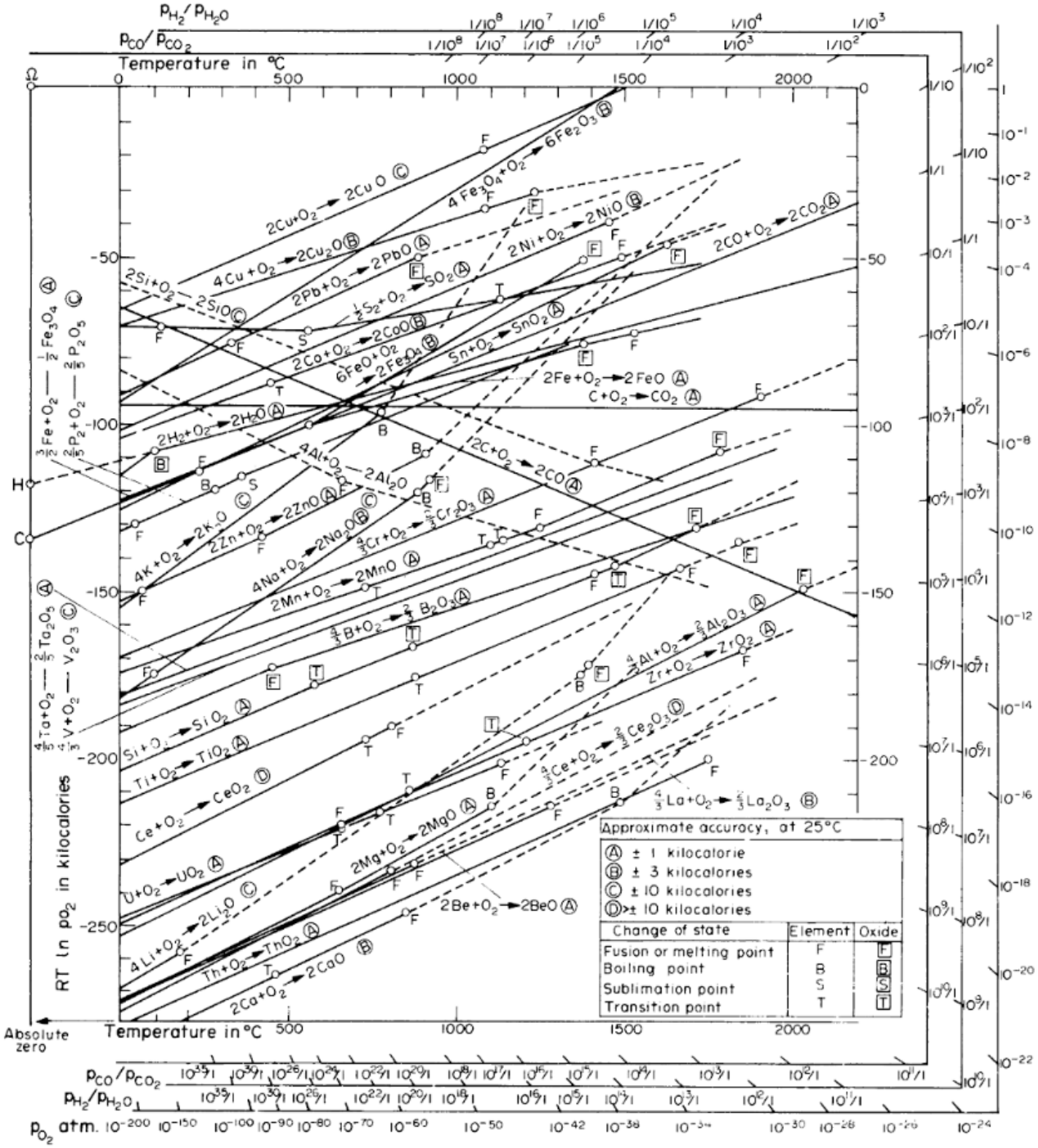

Figure 2.2.1 Standard free energies of development of selected oxides as a function of temperature [111].

Thermodynamically metal is oxidised when the partial pressure of oxygen is smaller than the potential of the oxygen on the atmosphere at equilibrium.

As the process continues and the oxide film covers the surface of the metal, the solid product of MO_2 will act as a barrier between oxygen and the substrate metal.

M (metal) / MO_2 (oxide) / O_2 (Gas)

From this point onward, the reaction continues, either by diffusion of oxygen ions through the oxide layer towards the oxide-metal interface or by the migration of metal ions towards the oxide-gas interface. It is possible that the above transport mechanisms occur simultaneously. Consequently, the diffusion mechanism of the reactants is a crucial part of the oxidation process either at high or low temperatures. The same principle applies to the formation of other types of high temperature reaction products such as sulphides [2].

In the development of thin films an electric field may be considered as the driving force behind the movement of ions, on the other hand, the potential chemical gradient can be recognised as the driving force on the thicker oxide layer [3].

Reviewing the thermodynamics of the metal-oxygen equilibrium provides a general understanding of the oxide development phenomena [1], [3]. However, there are some constraints on the system thermodynamics as they do not embrace the kinetics of the reaction. Sometimes, even there is a possibility for the reaction to occur thermodynamically, it needs a very long period to progress because the kinetics are very slow. Therefore, a combination of thermodynamics and kinetics data is required to understand the development of the oxide phases [2], [3].

2.3 Oxidation kinetics

Many parameters influence the oxidation rates of the metals such as temperature, the partial pressure of oxygen, surface condition and pre-treatment process. Oxidation rates are defined by rate equations. However, mathematical definitions alone cannot explain the oxidation mechanism, but they can be used to classify oxidation phenomena [1], [3].

In simple terms, the rate equations can be classified into three main categories: linear, logarithmic and parabolic. It is sometimes very difficult to adopt one of these categories on a complicated oxidation process as they only represent ideal situations [1]. Parabolic, linear and logarithmic oxidation mechanisms are demonstrated in Figure 2.31.

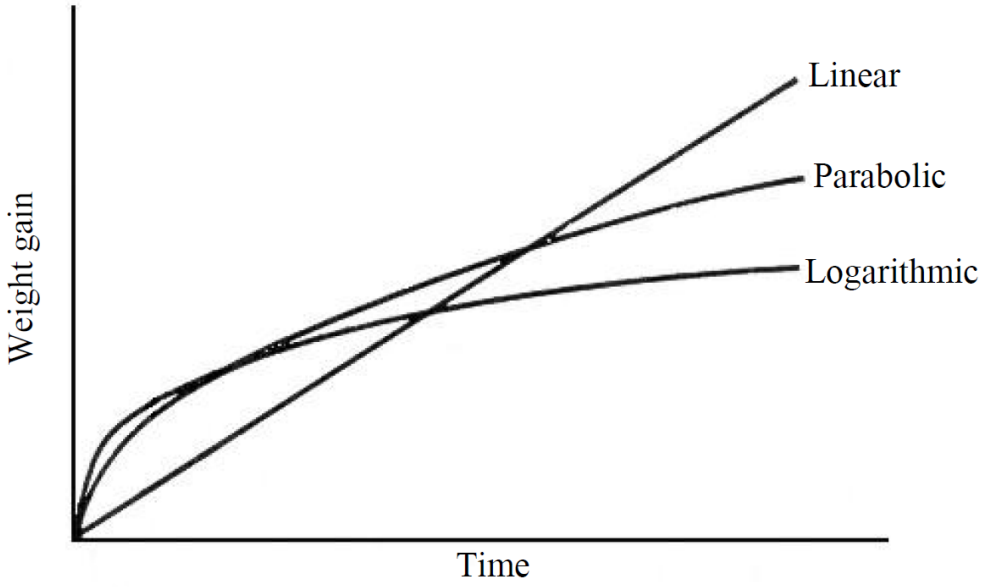

Figure 2.3.1 Schematic Parabolic, linear and logarithmic oxidation mechanisms after [6].

2.3.1 Linear rate equations

The oxidation rate of metals under specific conditions is constant, and linear rate law can define the progress of the oxidation, which can be written as:

$$dx/dt = k_l \quad (2.7)$$

$$x = k_l t + {}_i \quad (2.8)$$

Where k_l is constant of the linear rate and x is the thickness of the oxide layer, and C_i is the integration constant. For an oxidation process, which obeys the linear rate law, the oxidation reaction is constant with time, and it is independent of the amount of the reactants consumed during the process. In the early stage of the oxidation, the process when the metal surface is in direct contact with the oxygen gas, the reaction obeys the linear rate law. Even by forming a very thin uniform oxide layer on the metal surface, it is unlikely that the rate of the reaction to be limited by the diffusion and the oxidation follows the linear rate law [1], [3].

2.3.2 Logarithmic rate equations:

If the oxidation of metals occurs at low temperature (i.e. below 400°C), the first stage of the formation of the oxide film, up to 100nm, is quite rapid and this reaction speed decreases to a very slow rate quickly. Direct and inverse logarithmic equations define this type of oxidation behaviour of metals:

Direct logarithmic: $x = B - k_{log} \log (t+t_0) + A$ (2.9)

Inverse logarithmic: $\frac{1}{x} = B - k_{il} \log t$ (2.10)

Where x can be defined as oxide thickness or the volume of metal transformed to oxide or the amount of oxygen used per unit surface area. t represents the time, and A, B, t_0, k_{log} and k_{il} are constants.

In the development of the oxide film, the oxygen adsorption determines the rate of the reaction. In the initial stage of the process, oxygen either adsorb or rebounds on the clean surface of the metal. Therefore, it is anticipated that the rate of the reaction remains the same at a constant temperature and a fixed partial pressure of oxygen. However, as the oxidation process continues, the growth of an oxide monolayer significantly decreases the rate of the oxidation. This is because the oxide layer acts as a barrier and reduces the movement of oxygen atoms towards the surface of the parent material [1, 2, 3].

2.3.3 Parabolic rate equations

Oxidation reactions of many metals at high temperatures obey a parabolic time dependence law. In high temperature, the parabolic oxidation system, a thermal diffusion process determines the rate of the reaction. The parabolic rate law is defined by:

$$\frac{dx}{dt} = \frac{k'_p}{x} \quad (2.11)$$

$$x^2 = k_p t + c_p \quad (2.12)$$

Where k'_p and k_p represent rate constants, and c_p is the integration constant. The parabolic equations indicate that the reaction rate decreases as the oxides layer growth. In parabolic oxidation system, the reaction mechanism is governed by diffusion of the oxygen or the metal ions or electrons through a growing dense oxide film formed on the surface (Wagner mechanism) [1].

2.3.4 Combinations of rate equations

The oxidation process is complex, and it follows a combination of oxidation laws [1]. In such systems, two types of oxidation mechanisms can be observed simultaneously. However, one of these systems dominates the oxide growth, which highly depends on the process condition. This is due to the nature of the oxide scale, which may alter the process conditions such as the diffusion rate of metal and oxygen ions.

On the early stages of formation of the oxide film at low temperature, the process usually follows the logarithmic rate law; this can be explained by diffusion of the ions through the oxide layer due to the electric field. Eventually, by increasing the temperature, the reaction rate is dominated by thermal diffusion of ions and the process is governed by the parabolic law. Equation 2.9 defines a combination of parabolic and logarithmic mechanisms in a complex oxidation system:

$$x = k_{log} (t+t_0) + k_p t^{\frac{1}{2}} + c \qquad (2.13)$$

At high temperature complex oxidation, a combination of linear and parabolic mechanisms can be observed. High temperature oxidation can be defined by:

$$x = k_p \frac{t}{x} - k_l \qquad (2.14)$$

2.3.5 Oxygen and temperature dependences

As stated earlier, the partial pressure of oxygen is a key parameter in the oxidation of metals. In the early stage of the oxidation process, if the pressure of oxygen is very low the oxidation rate depends on the rate of impingent of the oxygen molecules and reaction speed is proportional to the oxygen pressure. On the other hand, at high temperature oxidation

especially in the linear system at the metal-gas interface, the oxidation rate is proportional to $P_{O_2}^{\frac{1}{2}}$. In the later stages of the oxidation process, the reaction rate is governed by the diffusion in the solid state.

The effect of the temperature on the oxidation rate at a constant partial pressure of oxygen can be defined as:

$$K = K_0 \exp(-Q/RT) \qquad (2.15)$$

Where R is the gas constant and Q is activation energy (cal/mole), and T is the absolute temperature. If the reaction rate only follows one rate mechanism (e.g. parabolic), the activation energy remains constant consequently from the equation above; the reaction rate is governed by the temperature variation [1].

2.4 Oxidation of iron and steel

By exposing iron to the oxygen, different types of oxide, phases are formed on the surface of the material subject to the environmental conditions. Following high temperature oxidation of pure iron, the oxide structure is multi-layered and depending on the process temperature; three different phases are produced; FeO (Wüstite), Fe_3O_4 (Magnetite) and Fe_2O_3 (Hematite) as shown in Figure 2.4.1 [2].

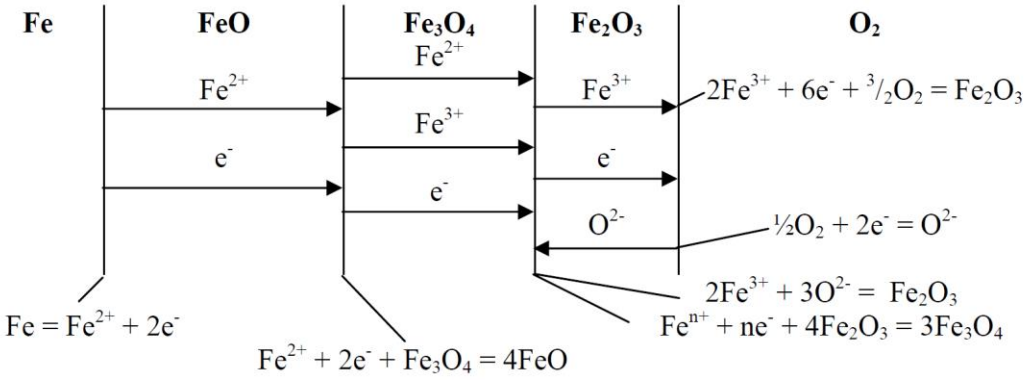

Figure 2.4.1 Oxidation mechanism of iron above 570°C and formation of multilayer oxide scale consisting: Wüstite, magnetite and hematite [2].

Ionisation of iron occurs at the Wüstite-iron interface according to:

$$Fe = Fe^{2+} + 2\ e^{-} \quad (2.16)$$

Iron ions and electrons travel through the FeO towards the Magnetite. The reduction of Magnetite and development of FeO is observed at FeO-Fe_3O_4 interface according to:

$$Fe^{2+} + 2\ e^{-} + Fe_3O_4 = 4\ FeO \quad (2.17)$$

The migration of electrons and Fe^{2+} and Fe^{3+} ions through the Magnetite towards the Magnetite-Hematite interface leads to formation of Fe_3O_4 according to:

$$Fe^{n+} + ne^{-} + 4\ Fe_2O_3 = 3\ Fe_3O_4 \quad (2.18)$$

Mobile electrons and iron ions travel across the Hematite phase and the gas-Hematite interface and new Fe_2O_3 is produced according to:

$$2\ Fe^{3+} + 6\ e^{-} + {}^{3}\!/_{2}\ O_2 = Fe_2O_3 \quad (2.19)$$

At the oxide-gas interface, another reaction is observed:

$$^{1}\!/_{2}\ O_2 + 2\ e^{-} = O2^{-} \quad (2.20)$$

The produced oxygen ions will travel through the Hematite layer and by reaction with iron ions new Hematite phase is formed according to:

$$2\ Fe^{3+} + 3\ O^{2-} = Fe_2O_3 \quad (2.21)$$

The consistent electrons travel across the Hematite layer towards the oxide-gas interface to participate of ionization of oxygen. Because of higher mobility of defects within FeO, the thickness of Wüstite layer is much greater than Magnetite and Hematite layers. The thickness ratio of three oxidation phases formed at 1000°C is reported as: 95% FeO, 4% Fe_3O_4, and 1% Fe_2O_3 [2]. This phenomenon is due to higher defects mobility in Wüstite with a NaCl crystal structure in comparison to α-Fe2O3 with a rhombohedral structure where oxygen ions occupying a close-packed hexagonal pattern along with Fe ions located in interstices [2].

As can be seen on the iron-oxygen phase diagram (Figure 2.4.2), iron oxidation below 570°C does not produce FeO, and the structure of the oxide scale is a two-layered film of Magnetite

and Hematite. Oxidation above 570°C leads to the formation of the three-layered scale of FeO, Fe_3O_4, and Fe_2O_3 in sequence, with Wüstite forming on the metal surface. Since Wüstite does not form below 570°C, the reaction rate is relatively slow. The oxidation rate of iron above 570°C is rapid; thus, a thick oxide scale grows on the surface. As the oxide layer thickens a highly porous FeO layer forms on the metal surface in spite of the high plasticity of the Wüstite phase. A rapid oxidation rate generates stresses within the oxide layer and subsequently induces physical defects in the outer layer of the oxide scales structure which leads to the diffusion of the gas particularly the CO/CO_2 and H/H_2O redox system and this influences the development of the oxide scale.

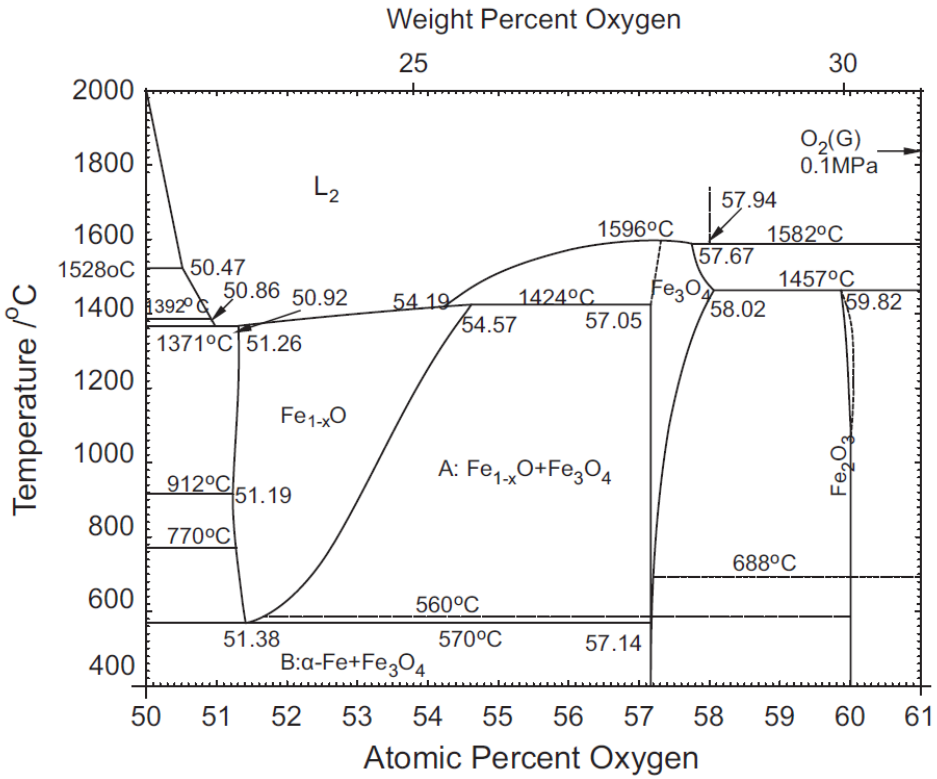

Figure 2.4.2 Fe–O equilibrium phase diagram, region A: high-temperature proeutectoid above 570˚C, region B: Wüstite decomposition below 570˚C [45].

FeO has the highest volume fraction of the reaction products during the oxidation of iron above 570°C; therefore, the overall oxidation rate is dominated by the development of Wüstite.

By reaching the equilibrium at the metal-oxide and FeO-Fe_3O_4 interfaces at a given temperature, the defect concentrations are stabilised in these regions. Consequently, the

parabolic oxidation rate constant is not influenced by the external oxygen partial pressure. In theory, by increasing the partial pressure of oxygen in the oxidation environment, the thickness of the Fe_2O_3 layer should increase. Since the amount of Hematite is only 1% of the thickness of the oxide scale, therefore identifying any changes in the rate constant related to the partial pressure of oxygen would be difficult [2].

For oxidation of iron below 570°C, a similar mechanism has been observed. In low partial pressure of oxygen in the atmosphere, at the metal-Fe_3O_4 and Fe_3O_4-Fe_2O_3 interfaces, the low defect concentrations are fixed by reaching equilibrium [2].

2.4.1 Influence of the oxidation conditions on the development of the oxide scale

In most high temperature oxidation environments such as industrial reheating furnaces, oxygen usually does not exist as a pure gas, but it is present in the form of combustion products such as CO, CO_2, SO_2, H_2O or air. The compositions and amount of the gases in the oxidant atmosphere significantly influence the rate of the oxidation and morphology of the developed oxide layer.

Garza and Rainforth [32, 39] proposed a similar model for the effect of the water vapour addition on isothermal oxidation of high-speed steel at 550°C and 610°C. They suggested that the higher oxidation rate under humid atmosphere occurred because water vapour appeared as a second source of oxygen for the oxidation reactions, in addition to the available free oxygen in the dry atmosphere. The above observations were in good agreement with the research of Tuck et al. [38].

Tuck et al. [38] studied the effect of the presence of steam on the oxidation process of iron and mild steel at 950°C. They found that adding water vapour into the oxidant environment increased the oxidation rates of both pure iron and mild steel. In the oxidation of pure iron, this effect was only detected if the specimen was heated up to the required temperature in argon. Their research also verified that the acceleration of oxidation rate was higher in round shape samples in comparison to oxidation of rectangular specimens. Furthermore, it was revealed that the oxide scale formed under dry oxygen atmosphere had poor adhesion to the

substrate, but the oxidation in the presence of water vapour led to the development of a dense adherent oxide layer.

Yu et al. [46] studied the development of different phases during oxidation of low carbon micro-alloyed steel under dry and moist (19.5% H_2O) environments at 800-900°C. They found that at high temperature oxidation of steel water addition on the atmosphere significantly influenced the precipitation process of Fe_3O_4 within the FeO phase. The study demonstrated that the water addition not only increased the oxidation rate but also influenced the morphology and structure of the oxide scale, including the development of Fe_3O_4 precipitates. A thin dense Hematite layer adjacent to the steel substrate was detected which was absent in oxidation under dry air.

Jansson and Vannerberg [40] studied the effect of the partial pressure of oxygen variation on the oxidation rate of pure iron at elevated temperature. They confirmed that below 570°C, by increasing the partial pressure of oxygen, the oxidation rate would increase, which was in agreement with findings of Caplan et al. [41]. However, they found increasing the partial pressure of oxygen at temperatures above 625°C would decrease the oxidation rate. It was explained that the reduction of oxidation rate was due to nucleation and growth of well-oriented oxide grains and Fe_2O_3 whiskers along the surface, which acted as barriers and reduced the oxidation rate. They found that this phenomenon could not be seen on the oxidation of pre-cold-rolled specimens.

Genève et al. [48] studied the descaling ability of low-alloy steel wires at 920–970°C. Their study demonstrated that the reduction of the cooling rate and increasing the oxidation temperature improved the descaling process. Reduction in steel cooling rate amplified intrinsic stresses during the growth of the oxide scales. On the other hand, increasing the oxidation temperature intensified cooling related extrinsic stresses. This phenomenon explained why between specimens with the same oxide scale thicknesses, the one oxidised at highest temperature displayed better descaleability. However, the excessive oxidation temperature intensified defect growth and stress relief, which deteriorated the descaling properties of the material. Furthermore, the oxide-metal interface roughness enhanced the adherence of the oxide scale, thus reducing the descaleability.

Wang et al. [75] reported that the oxidation of medium and low carbon steels was parabolic when the material isothermally oxidised for 60 minutes at 1100˚C and 1200˚C under a humid atmosphere. Likewise, Lee et al. [77] testified that isothermal oxidation of medium carbon steel between 700˚C to 1200˚C in a humid atmosphere led to parabolic weight gain. In an atmosphere with a high air/fuel ratio (112%), the oxidation obeyed parabolic law. However, it was found where the air/fuel ratio dropped to 99%; the kinetics followed the linear law.
Abuluwefa [74] examined the isothermal oxidation behaviour of medium and low carbon steels at high temperature under an atmosphere containing N_2-O_2-CO_2-H_2O. He witnessed that after 10 minutes of rapid linear oxidation at 1200˚C, the oxidation process changed to a parabolic mode and the process controlled by solid-state diffusion of the oxidising species. In contrast, he observed that the oxidation followed the linear law at 1000˚C under the same atmosphere. He stated that overall, the oxidation rate dominated by the amount of free oxygen in the atmosphere containing gas mixtures of O_2, CO_2, H_2O and N_2.

2.4.2 Effects of alloying elements

Steel grades are very diverse, and they are highly depended on their chemical compositions and process conditions. Even a small variation in any of the alloying elements can prominently transform the metallurgical characterises and properties of the products. The oxide scale development and behaviour are also highly influenced by the chemical composition of the parent material. The effects of the additions of key alloying elements on high temperature oxidation of steel and their influences on the oxide scale characteristics are briefed in this section.

Chang and Wei studied the effects of small additions of different alloying elements on oxidation of low alloy steel [5]. They stated that the elements, which were less noble than iron, such as aluminium, chromium and silicon would produce a protective layer at the steel-oxide interface, during the oxidation at elevated temperature. The saturation and segregation of alloying elements could be detected in this region. They found the silicon produced the most protective layer and chromium had the least effect. Furthermore, an increase in the oxidation resistance of steel could be observed if elements more noble than iron, such as

copper and nickel, were present in steel composition. They suggested this was due to the rejection of these elements at the steel-oxide interface, and consequently, it created a tight mechanical bond between the oxide and the substrate.

The study of Genève et al. [48] demonstrated that at 920–970°C increasing the amount of alloying not only retarded the defect growth within the oxide scale but also modified the descaleability. It was stated that the addition of alloying elements could reduce the oxide growth rate as well as deteriorating the oxide scale's plasticity. Furthermore, increasing the alloying elements reduced the oxidation kinetics, which increased the oxide scale adherence on metals, whereas reduction in plasticity had an adverse effect. It was claimed that among oxides produced under identical conditions, the one with fewer alloying elements had the best descaling aptitude. Conversely, they observed in the oxidation of different steel grades if the thickness of the oxide scales and the oxidation temperatures were the same, the material with the highest alloying elements additions showed the best descaling properties. They concluded that the addition of alloying elements in combination with a decreased cooling rate could promote the descaleability of steels without enhancing the metal loss by oxidation.

Carbon

The effect of carbon on oxidation kinetic of steel is complex. The oxidation parameters, including time, temperature and partial pressure of oxygen, as well as the amount of carbon within the parent material, can promote or hinder the oxidation rate. Moore et al. [89] evaluated the oxidation rate of eight different steel grades (0.028%C) at various oxidation conditions.

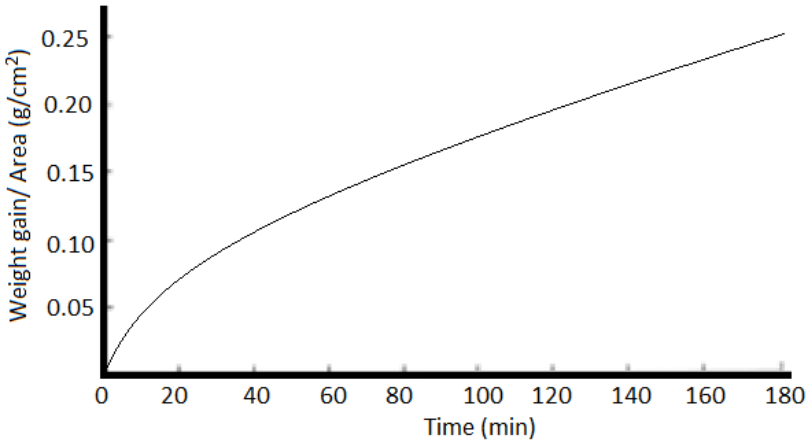

Figure 2.4.2.1 Oxidation kinetic curve for low carbon steel at 1200°C after Moore et al. [89].

Figure 2.4.2.1 demonstrates a parabolic kinetic curve of a low carbon steel (0.028%C) oxidised at 1200˚C under an atmosphere containing 8.6% CO2, 16.8% H2O, 2.1% O2 and 73.5% N2. As can be seen, the oxidation rate obeyed the parabolic law. Overall, the study confirmed the oxidation regimes of the specimens were highly depended on the chemical composition of the materials, oxidation temperature and the oxidant atmosphere.

Wie et al. [90] reported a similar scenario for the oxidation of high and low carbon steel alloys in the temperature range of 700 to 900˚C under air atmosphere. They found that the oxidation rate of steel with 0.82% C was less than that for steel grade containing 0.06% C.

The work of Caplan et al. showed that the oxidation rate of medium and high carbon steels at 700˚C is slower than pure Fe. They claimed the reduction of oxidation rate was due to residual graphite at the oxide-metal interface, which was formed by the oxidation of Cementite [87].

Likewise, Malik and Whittle [88] reported that the oxidation rates of steel alloys with 0.1 to 1.2 wt% carbon content were lower than that for pure iron at 850˚C. However, their research revealed that increasing the amount of carbon content did not necessarily reduce the oxidation rate. The oxidation rates of the alloys at 850˚C with respect to their carbon content were expressed as 0% C > 0.4% C > 1.2% C > 0.8% C > 0.1% C. The higher oxidation rate in steel with 0.4%C among the Fe-C alloys was related to the high adherence of the oxide scale to the parent metal and lack of a separation gap between substrate and the oxide scale. Sheasby et al. [18] found that the carbon content as low as 50 ppm can affect the oxidation kinetic by developing porous oxide scale. Chang and Wie [5] suggested this phenomenon were due to the diffusion of carbon from parent material into the oxide-metal interface and its subsequent reaction with iron oxide. As a result, the voids and porosity formed within the oxide scale.

They claimed if the pressure arose by further development of CO within the cavities, led to the development of large cracks across the oxide structure. Consequently, the oxidant gasses available in the atmosphere to penetrate the oxide-metal interface and to react with parent material, which increased the overall oxidation rate. On the other hand, if within the oxide scale CO developed insufficiently, the oxygen flux was hindered due to the presence of the cavities.

Chen and Yuen [33] reported that high temperature oxidation rate of low-carbon steel was mostly lower than pure iron. They specified that in short time oxidation of low-carbon steel alloys, where the oxide layer adhered to the substrate, the scale morphology was similar to oxide scale developed on pure iron, and the oxidation process obeyed the parabolic law. The adherence of the oxide/metal in early stages of the oxidation process was due to the absence of defects such as porosities and cavities which could be formed by mobility and concentration of the micro defects and inward or outward diffusion of gases through the oxide scale. The influence of carbon on the oxidation kinetics of steel alloys with carbon content higher than 0.1% varied at different temperatures. Due to higher carbon content oxidation below 570°C led to greater oxidation rate, this was because the oxidation of pearlite created a more adherent oxide scale with finer microstructure, which allowed a rapid diffusion of iron ions through the oxide structure. At 700°C, these alloys produced a less adherent oxide layer with irregular oxide structure. They also reported the oxidation of carbon steel alloys at temperatures above 700°C led to decarburisation of the near surface region. This feature was more evident in high-carbon steel alloys, where carbon enrichment in the near-surface area might occur at a temperature below 700°C [33].

Manganese

Manganese may act as a substitute for iron atoms in FeO and Fe_3O_4 lattices; hence, its effect on high-temperature oxidation of steel is very limited.

Jackson and Wallwork [127] testified that during oxidation of Fe-Mn binary alloys the solid solution phases of (Fe, Mn)O, $(Fe, Mn)_3O_4$, and $(Fe, Mn)_2O_3$ might form and the arrangement the multilayer scale would be the same as iron-oxide. Furthermore, the phases of Mn_3O_4 and Mn_2O_3 were developed within the main body of the oxide scale. MnO that is also known as Manganosite, has the same crystal structure of Wüstite, this phenomenon facilitates the formation of the solid solution of $(Mn_{1-x}Fe_x)O$ which is known as Manganowüstite [128].

The proportion of the iron ions within the external oxide scale has a direct relation with the partial pressure of oxygen within the reheating atmosphere. Respectively, the compositional concentration of the (Mn1 −xFex)O within the internal oxidation zone is influenced by the local activity of oxygen [128, 129].

Moreover, Mn may react with Si and Fe to form iron-manganese-silicate within the oxide scale. It is suggested that this reaction might slightly increase the oxidation rate and would enhance the adherence of the oxide scale to substrate metal [5].

Silicon

As stated in Section 2.1.2, silicon is added to low carbon steel alloys to improve the electrical resistivity, which is one of the essential factors that dictate the desirable electromagnetic properties of the material. Like any other types of steel, the surface of the material is oxidised during the production of high silicon electrical steel sheets and Si reacts with other species during the oxidation process and forms other types of oxide phases including Silica and Fayalite.

Yang et al. [47] studied the effects of Si content on the scale formation on hot-rolled steel strips. They reported that the Si concentration of the parent material significantly influenced the oxidation rate and composition of the oxide scale. They found that in the oxidation of a steel alloy containing 0.51wt% silicon, the oxide scale consisted of FeO, Fe_3O_4 and Fe_2O_3 phases. It was observed that if the silicon content of the steel exceeded 1.14wt%, Hematite was the dominant phase in the oxide scale. It was suggested that Fayalite was developed within the oxide-metal interface leading to a reduction in outward diffusion of iron ions and as a result, the oxidation rate decreased. In steel with lower Si content, signs of internal oxidisation were detected in the near surface region, in addition to parallel silicon oxide seams were precipitated within the oxide iron constituents. It was reported that in a steel grade containing 1.91wt% Si, oxide nodules were developed above the internal oxidation zone. Increasing the volume fraction of silicon in the parent material not only extended the thickness of the Fayalite layer but also a complex structure was developed by the distribution of Si oxides across the oxide scale. For improving the steel descaleability, the amount of

reactive alloying elements with Si and Cr that developed soluble compounds within the iron oxide should be increased.

Taniguchi et al. [72] studied the scale-substrate interface characteristics of low-carbon steels containing Si of up to 1.5wt%, which were oxidised at 1143˚C and 1203˚C in air. The study revealed that by increasing the alloy Si content, the critical stress for oxide scale spallation intensified during cooling from 1143˚C, whereas virtually no differentiate was detected for cooling the material from 1203˚C. The microstructure of the oxide scale was mainly constructed of two layers of Wüstite when the specimen with higher Si content oxidised at 1143˚C. For specimen containing 0.01% of Si, a porous inner structure containing a mixture of FeO and Fe_2SiO_4 grains and a dense outer layer of FeO was developed. It was observed that the size of the porosity increased by increasing the Si quantity. During oxidation at 1203˚C, a eutectic liquid phase was developed at the metal-oxide interface, which then penetrated the metal substrate as well as the FeO grain boundaries. The scale thickness dependence to the Si content is demonstrated in Figure 2.4.2.2 a and b [72].

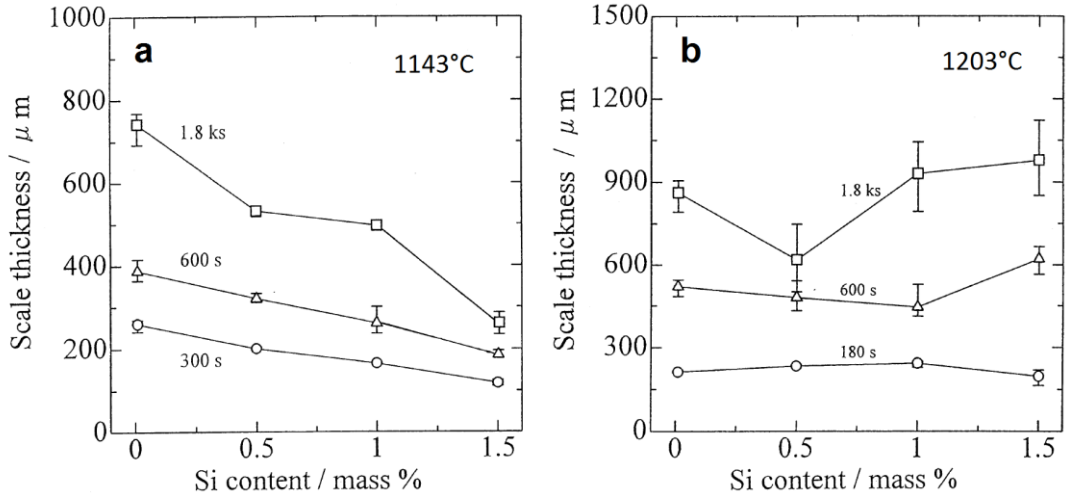

Figure 2.4.2.2 Variation in the scale thickness with the Si content with oxidation time as a parameter: a) 1143˚C b) 1203˚C [72].

Takeda and Onishi [81] studied the effect of Si content on the oxidation rate of low carbon steel. They studied the oxidation of two steel grades with different Si contents at 1100˚C and 1200˚C for 60 minutes under an atmosphere containing 74%N_2-17%H_2O-8%CO_2-1%O_2. The results revealed that above 1100˚C, the increase of silicon content stimulated the transformation of SiO_2 to Fayalite within oxide sublayer. This reaction suppressed the

development of Wüstite and promoted the formation of Magnetite. At 1100˚C, the lowest oxidation rate belonged to steel with 3% Si content. On the contrary, they reported the same steel grade had the highest oxidation rate at 1200˚C.

Mouayd et al. [76] studied the relationship between the oxidation periods and the oxidation kinetics of a steel grade containing 1.55% Si under 15% moist atmosphere at 900˚C, 1000˚C, 1100˚C and 1200˚C. Their research showed that below 1100˚C for initial 10 seconds, the oxidation mode was linear. Furthermore, between 30 and 120 seconds, the mass gain stagnated depending on the oxidation temperature, and after this passivation period, the process obeyed the parabolic law conversely, no passivation period was apparent when material oxidised at 1200˚C. They noticed after very short oxidation period, the mass gain followed the parabolic law at all temperatures.

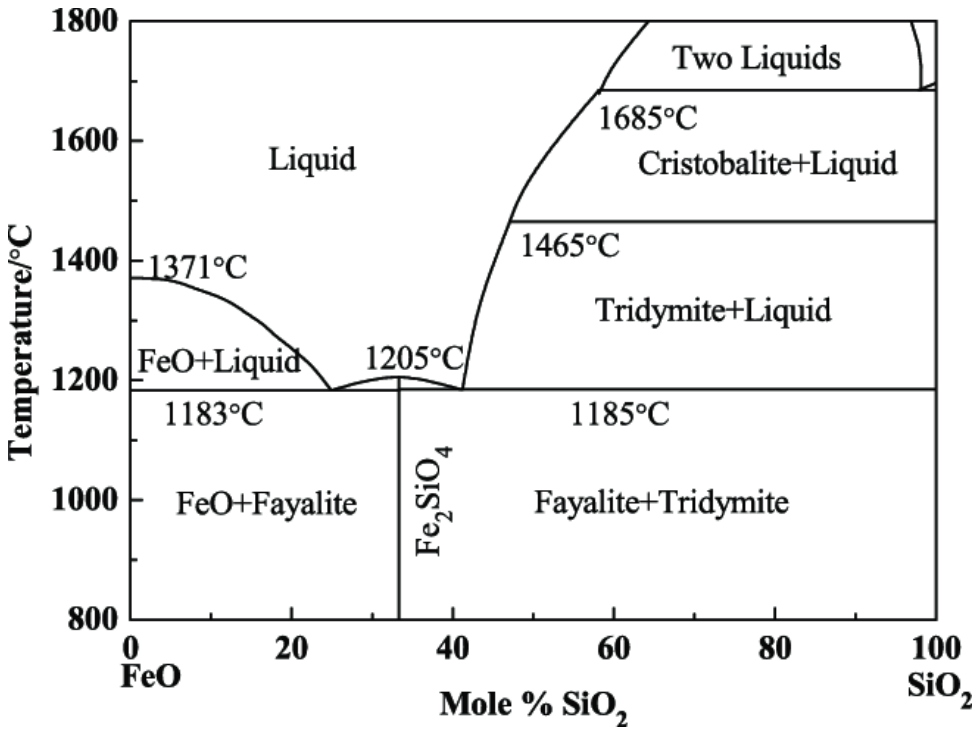

Figure 2.4.2.3 FeO-SiO2 binary system [103].

Suarez et al. [80] studied the isothermal oxidation of low alloy steel and ultra-low carbon silicon steel in a temperature range of 750-1200˚C under a dry air atmosphere. It was reported that below 1177˚C, the oxidation rate of the silicon steel was slower than that for the low alloy steel. In contrast, the oxidation kinetics of the Si steel was much higher above 1177˚C

because as per Figure 2.4.2.3, Fayalite along with Wüstite formed a eutectic phase with which promoted the rapid growth of the oxide by liquid oxide attack.

Martinez et al. [79] investigated the oxidation behaviour of silicon-containing steel under dry atmosphere between 950 ˚C and 1180˚C. They witnessed that up to 20 minutes; the oxidation kinetics followed the parabolic law in all experiments performed at the above temperature range.

Aluminium

Like any other element less noble than iron, aluminium develops, an enriched film at the oxide-metal interface that retards the outward mobility of Fe ions and as a result, it reduces the oxidation rate. However, the effect of Al on oxidation of steel alloys vastly depends on the concentration of this element in the parent material and the temperature of the reaction [5]. Saegusa and Lee [91] suggested if iron alloy containing 1% Al oxidised at 500-700˚C under 1atm O_2 atmosphere, the Al-enriched layer at the oxide-metal interface was Al_2O_3. Conversely, $FeAl_2O_4$ spinel layer developed when the same alloy oxidised at 700-900˚C under the same atmosphere.

Additionally, aluminium may escalate the development temperature of FeO and subsequently reduces the oxidation rate. Huang and Zhu [92] found that the development temperature of Wüstite from 570˚C in Fe-O phase diagram rose to 798˚C for a steel alloy containing 1.8% Al. Atlas and Sumida [130] studied the determination of phase relations in the Fe-Al-O isothermal system. It was demonstrated that in Fe-Al-O system, the phases of $FeAl_2O_4$, FeO, Fe_3O_4, Fe_2O_3 and Al_2O_3 were all stable below 1250°C. Furthermore, a total solid solution of spinel existed between the composition spots of $FeAl_2O_4$, Fe_3O_4. As a solid solution, Hematite could dissolve Alumina to a maximum limit of 24% and Al_2O_3 could contain up to 12% of Fe_2O_3 just below the dissociation temperature. According to Atlas and Sumida, the FeO-Al_2O_3 system could not be considered as binary due to cation deficiencies in Wüstite solid solution. As can be seen in Figure 2.4.2.4 by increasing the temperature, the Alumina content in the spinel vertex of the spinel-Wüstite-iron region would increase by moving toward $FeAl_2O_4$ [130].

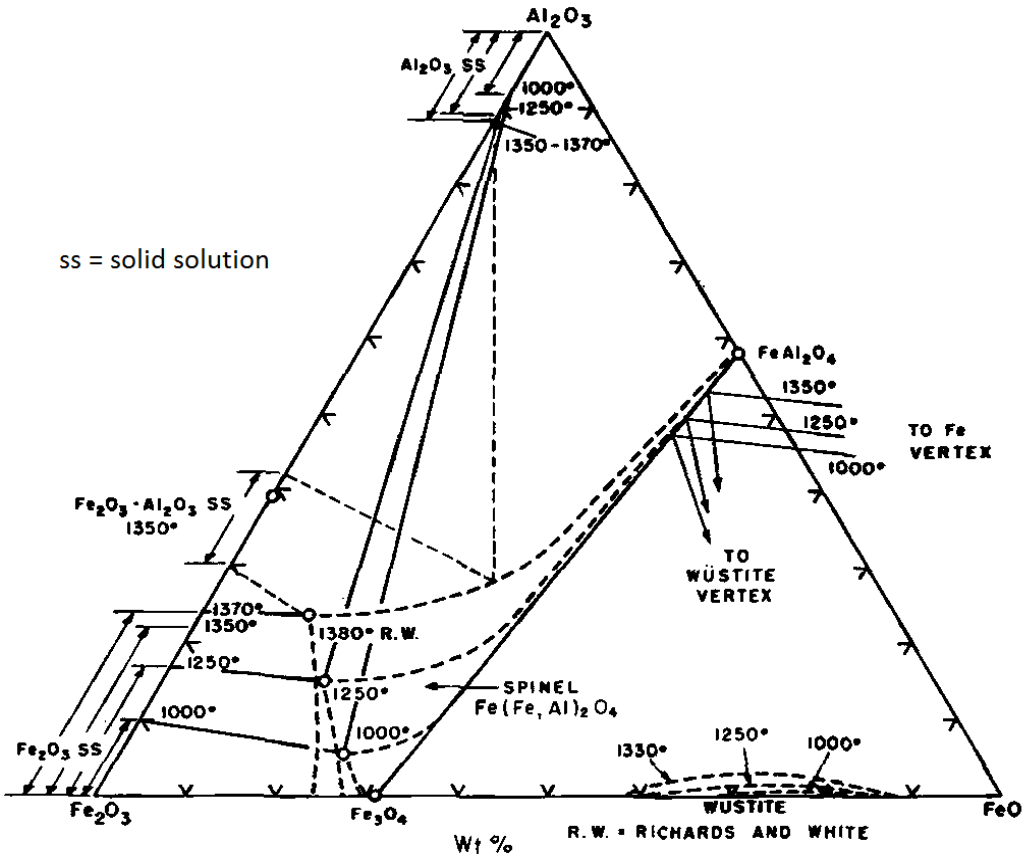

Figure 2.4.2.4 Changes in solid-solution equilibria with temperature. [130]

Iron Oxide-Al_2O_3-SiO_2 system

The oxidation of steel that contains aluminium and silicon is more complex than the scenarios described earlier. Guan [131] confirmed that in the ternary alloy of Fe-Si-Al, a complex oxide scales could form on the metal surface at 800°C and alumina (α) would be the predominant phase. It was established that in a ferrous alloy containing 0.6% Si and 0.6%% Al, the concentration of Al required to form a uniform layer of Al_2O_3 was considerably lower in comparison to a Fe-Al binary alloy. The observations revealed that the combined addition of silicon and aluminium provided an interactive improvement on the high temperature oxidation of the material. This was because silicon confined the oxidation of iron and amplified the outward diffusion of Al flux towards the oxide-metal interface during the parabolic oxidation stage.

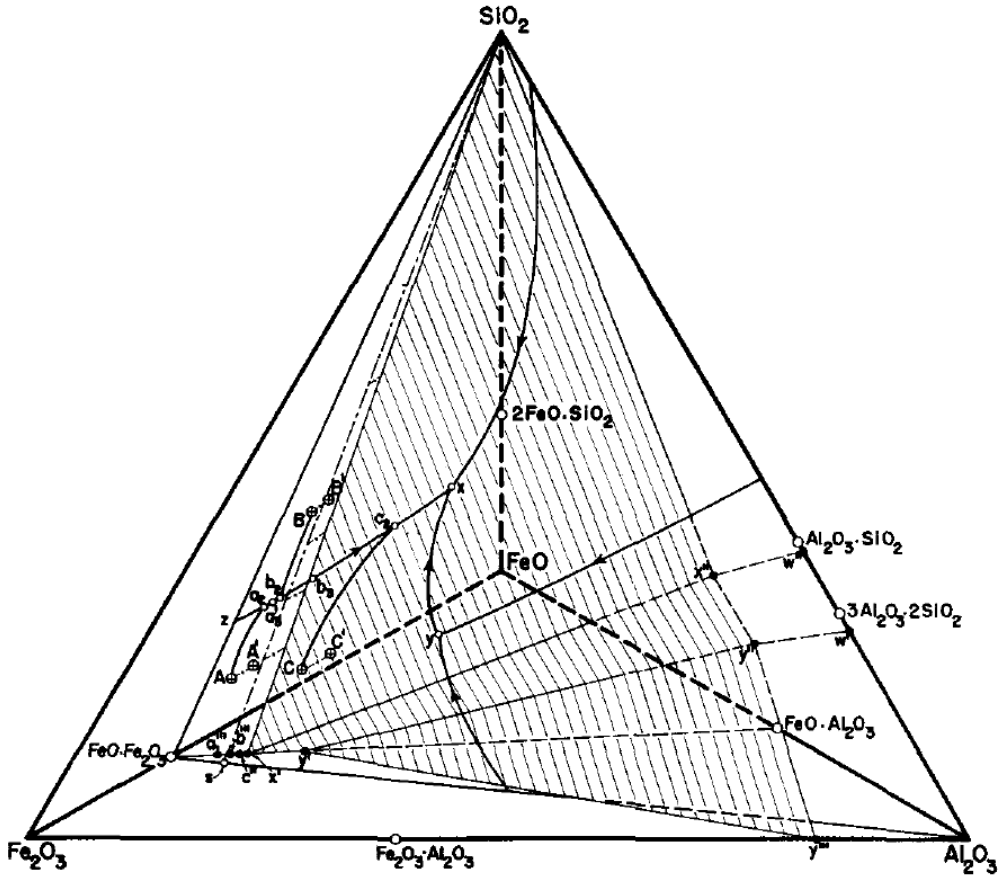

Figure 2.4.2.5 Diagram representing the system FeO-Fe_2O_3-Al_2O_3-SiO_2 [131].

Muan [131] proposed a phase diagram (Figure 2.4.2.5) for FeO-Fe_2O_3-Al_2O_3-SiO_2 system. The diagram illustrated the approximate curves in a tetrahedron format which one component at located on each apex for oxidation in air. The shaded regions represented the compositions of the phases in crystalline form at equilibrium with the liquid phase. The composition of liquids was pointed out with opened circles, whereas crystalline phases marked as solid spots.

2.5 Microstructure of Oxide Scales

Oxidation of steel at elevated temperatures is significantly influenced by the parameters temperature, time, partial pressure of oxygen, oxidant environment and cooling rate. These factors govern the development and growth rate of the oxide scale, oxide structure and morphology as well as the oxide compositions. According to the literature, a multi-phase oxide scale is developed during the oxidation of steel alloys [4]. The structure of the primary oxide scale can be divided into two major sections: inner and outer layers. Researchers

reported different structure and morphology of oxide scale steel over the years [60-64] for various oxidation environments.

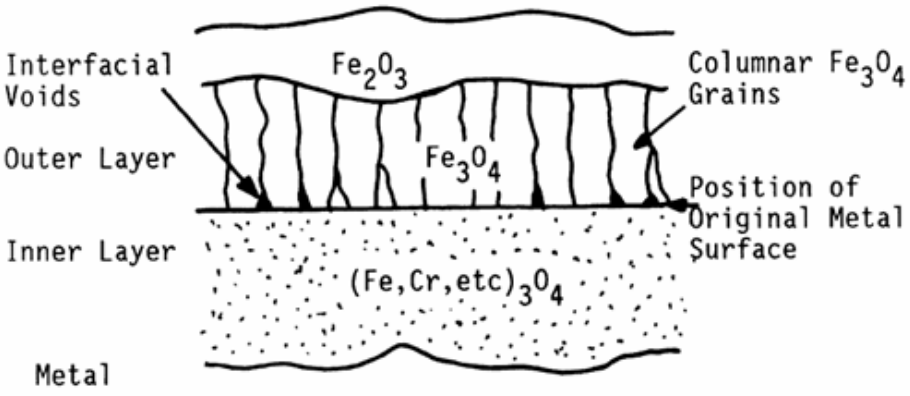

Figure 2.5.1 Schematic diagram of a duplex oxide scale formed on steel [65].

Metcalfe [65] suggested that the interface between the outer and inner layer of the oxide state was the original steel surface, as demonstrated in Figure 2.5. He stated that below 570°C, a thin Hematite (Fe_2O_3) layer was formed in the oxide top outer layer.

Gittins [60] proposed a multi-layer oxide structure for the scales developed during the reheating process of steel, as shown in Figure 2.5.2. However, in high temperature oxidation of steel under different conditions, various oxide structures and compositions were reported by other researchers [61-63].

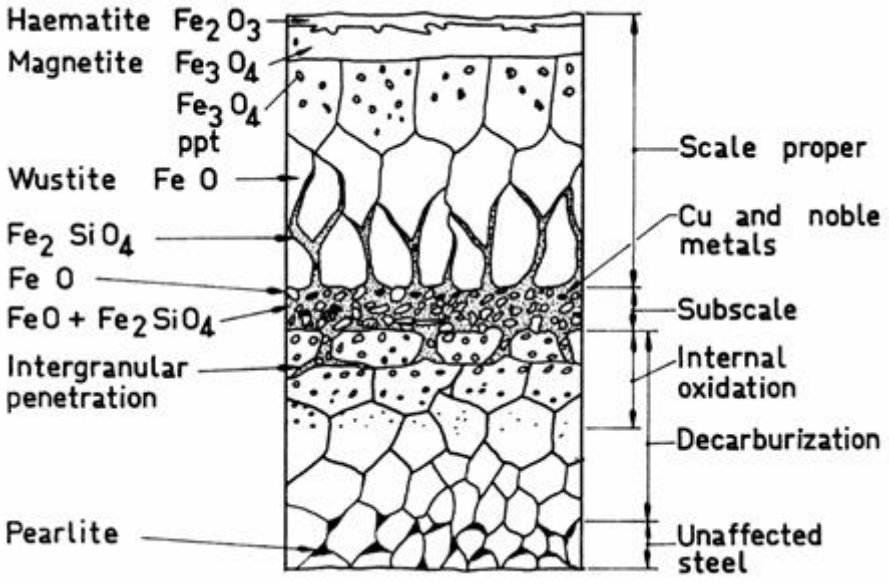

Figure 2.5.2 Structure of the surface layer of steel after reheating [60].

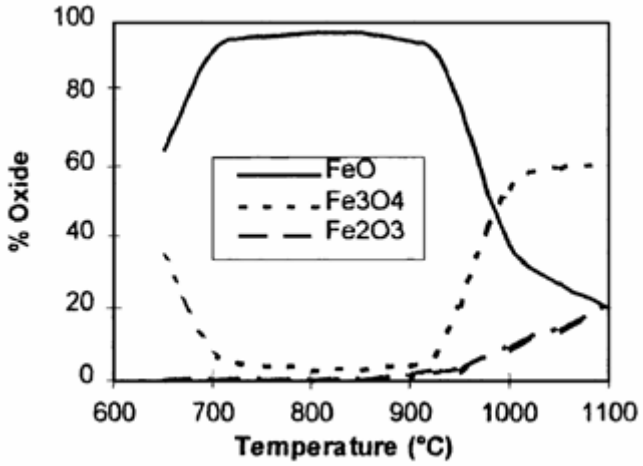

Figure 2.5.3 Relation between oxide composition and temperature [64].

Figure 2.5.3 demonstrates the volume fraction of each oxide phase during oxidation of steel at different temperatures. It was clear that FeO did not form below 570°C and development of Hematite were insignificant. Conversely in oxidation at a temperature range of 570˚C to 950˚C Wüstite was the predominant phase. Above 950˚C, the development of Wüstite reduced drastically, and the scale mostly contained Magnetite and Hematite [64].

Since in hot rolling of steel, the temperature of industrial reheating furnaces is well above 1000°C, the oxide scale predominant phase is Fe_3O_4. As can be seen in Figure 2.5.1, the spinel phase of Magnetite develops and grows in the form of long columnar grains in the outer region of the scale. On the other hand, the spinel phase of M_3O_4 forms within the inner layer of oxide scale where M encompassed Fe and other alloying elements, including silicon and manganese [4].

Liu et al. [93] studied the relation of the temperature on the development rate of FeO, Fe_3O_4 and Fe_2O_3, for the oxidation of low carbon steel under an atmosphere containing 80%N_2–15%CO_2–5%O_2. Their research showed that Wüstite had the highest thickness fraction in all conditions.

Time is another key factor in the oxidation of steel, which significantly influences the microstructure and morphology of the oxide scales [4], [66-69], etc.

Chen and Yuen [33] confirmed that in short oxidation period of steel, the scale morphology and structure were comparable to those developed on oxidation of pure iron. Furthermore, when the oxidation period was extended, the structure of the oxide scale became far more complex.

The research of Basabe and Szpunar [9] revealed that in early stage (up to 30s) of mild steel oxidation in a temperature range of 800°C to 1200°C, the predominant phase was FeO. The higher volume fraction of Wüstite was due to the higher diffusion coefficient of iron in Wüstite in comparison to Magnetite. Conversely, the diffusion coefficient of oxygen and iron ions were extremely small in Hematite. They established that the volume fraction of Fe_3O_4 and Fe_2O_3 increased in longer oxidation time.

In another research, Chen and Yuen [70] found that the composition of the oxide scale near to substrate contained a higher content of iron (FeO), while the outer oxide layer, which was in direct contact with the oxidant atmosphere, had highest oxygen level in its composition (Fe_2O_3).

Abuluwefa et al. [71] reported that the reheating atmosphere significantly influenced the development of porosity and large voids within the oxide structure. They reported that during oxidation of low carbon steel under CO_2-N_2 and H_2O-N_2 atmospheres at 1100˚C, only Wüstite was developed and microstructure of the oxide scale was free from pores. Furthermore, they found that when the atmosphere contained free oxygen gas, a porous oxide scale containing FeO, Fe_3O_4, and Fe_2O_3 was developed.

Chen and Yuen [33], [70] stated that oxide blistering could be observed in the oxidation of carbon steel in the air. They observed that the thick inner layer adhered to the substrate while the very thin outer layer was detached from the inner layer. Their research showed in a thin outer scale, Hematite was the main phase, but a small amount of Magnetite was also detectable. This was due to the separation of two layers and discontinuing the migration of iron ions. The process was followed by the transformation of Wüstite to Magnetite and Hematite by absorbing oxygen from the atmosphere. In contrast, they witnessed a typical three layers structure in the thick inner region.

2.6 Oxide scales behaviour during oxide development

Oxide scale behaviour during hot deformation can be predicted by studying its mechanical properties, including adhesion and cohesion of the scales and elastic and plastic properties. The mechanical properties and the failure mechanism of the oxide scale at elevated temperatures are influenced by several factors including morphology and the structure of the oxide layers, the size and shape of the defects, plasticity of the oxide layer, the parent material composition and pre-treatment of the material before oxidation. Oxide growth at the metal surface develops stresses particularly at the oxide-metal interface, due to an increased volume of oxide products in comparison to the original metal source. This phenomenon can be defined by the Pilling-Bedworth ratio, which can be written as:

$$\mathrm{P.B_{ratio}} = \frac{\mathrm{A_0}\rho_\mathrm{M}}{\mathrm{A_M}\rho_0} \tag{2.22}$$

Where $\mathrm{A_M}$ is atomic mass of metal, $\mathrm{A_0}$ is the molecular mass of the reaction products and ρ_M and ρ_0 represent metal and oxide densities, respectively. It is clear if the Pilling-Bedworth ratio is smaller than 1, oxidation will cause tensile stresses, or if the ratio is greater than 1, it will produce compressive stresses [6], [8], [9]. Oxide scale failure and spallation occurs if the $P.B_{ratio}$ is larger than 2-3 due to high compressive stresses. The $P.B_{ratio}$ for FeO-iron is reported to be 1.78, thus oxidation of iron above 700°C generates compression stresses [6], [10], [11], [12], [13].

In a different study, Sherwood and Shatynski [37] examined the effects of prior surface roughness of the parent metal on adherence of the oxide scale. It was confirmed that improving the primary surface finish of the test piece would increase the adherence of the oxide scales.

The differential between thermal expansion coefficients of metal and oxide scales and even between different phases within the oxide was found to be the other stress source during the oxidation process [6].

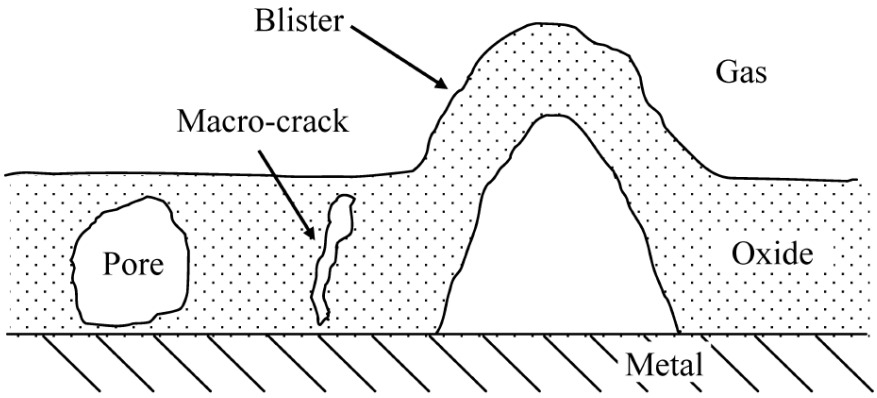

Figure 2.6.1 Schematic illustration of oxide scale macro-defects formed during isothermal oxidation process above 850˚C [9].

Increase in stress concentration leads to deformation of the oxide layer, which may form either cracks or pore within the oxide layer. Investigation of the oxide morphology by Basabe and Szpunar [9] revealed that the morphology of the oxide scale was uniform with a low percentage of porosity and micro-cracks during isothermal oxidation of steel at the temperature below 850°C.

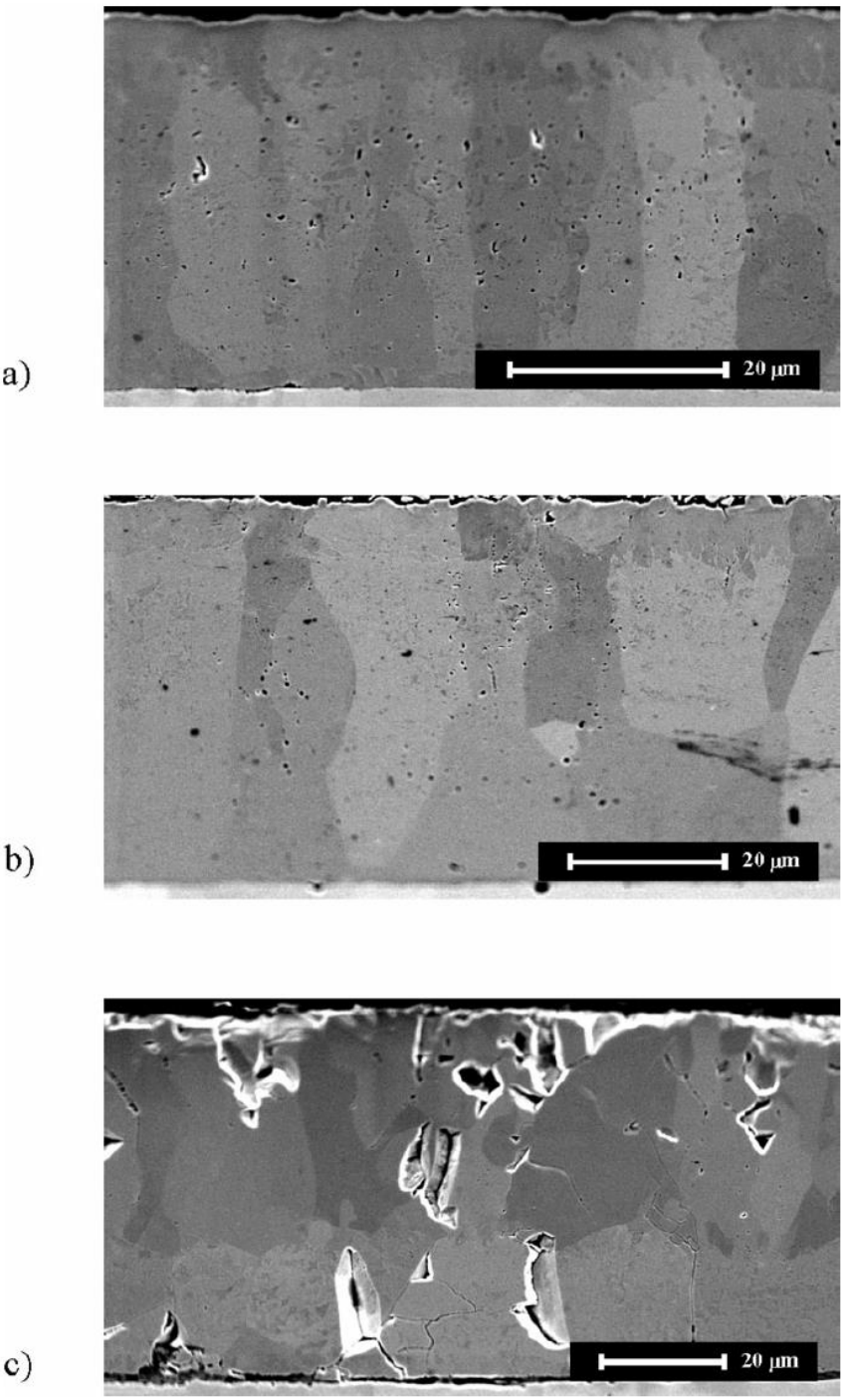

Figure 2.6.2 Microstructure of oxide scale developed at: a) 800˚C b) 850˚C c) 900˚C [9].

They reported oxidation above 850°C lead to the development of a non-uniform oxide structure containing medium to a high volume of porosity, blisters and macro-defects as shown in Figure2.6.1. The study confirmed that in the hot deformation of steel above 850°C the tensile stresses rose within the scales due to the high volume of defects and blisters and as a result crack growth and oxide failure occurred during the hot deformation. They

recognised that 850°C was the transition temperature for homogeneous to a non-homogeneous oxide scale formation (Figure 2.6.2). Their research facilitated the proposal of a hypothesis for the pore development mechanism above 850°C. The theory divided the pore formation into three different stages:

i. Initially, the growth of columnar Wüstite grains, perpendicular to the metal substrate, prompted the development of pores at the grain boundaries.
ii. Further oxidation progress and the oxide growth induced compressive stresses within the oxide scale and stimulated the porosity formation.
iii. In a longer oxidation process, the pores merged within a denser oxide layer [9].

Matsuno [35] investigated the blister development mechanism during isothermal oxidation and air-cooling. His research showed that the oxide stress concentration would form blisters on the oxide structure during isothermal oxidation above 850°C, it was concluded that the development of the oxide scale with a non-uniform morphology above 850°C was due to stress growth during oxidation. By increasing the process temperature, the oxidation rate increased. The stress concentrations were increased by this phenomenon and accordingly volumes, and dimensions of the defects increased within the oxide scale.

Chen and Yuen [33] reported the development of blisters during isothermal oxidation of steel at temperatures above 800°C. However, they identified that the most susceptible temperatures for blister formation under isothermal oxidation conditions were between 950°C and 1000°C. Furthermore, they found if the oxidation occurred under continuous cooling conditions, the critical temperatures were between 1050°C and 1100°C. They found at the most susceptible temperature; blisters were developed after just 30 seconds oxidation.

2.7 Oxide scale behaviour during hot deformation

During the hot forming of steel, particularly hot rolling, the surface finish of the products is significantly influenced by the oxide scale behaviour. These effects are directly related to the properties of the oxide layer and the oxide-metal interface. If the oxide layer behaves like a

brittle solid, the oxide can damage the surface [14], [15]. Many researchers tried to evaluate the oxide mechanical behaviour during hot rolling by employing different testing method such as hot tensile test [14], [16], [17] hot compression test [14], [18], [19] and hot rolling test [14], [15], [20-24]. They were interested to understand the conditions of the process and mechanical properties including adhesion, fracture toughness and plasticity of the oxide scales as well as their influence on the deformation and failure of the oxide scales [7], [14], [26].

Utsunomiya et al. [43] studied the development mechanism of surface defects during hot rolling of low carbon steel using a glass coating technique. They reported that the behaviour of oxide scale during hot deformation was strongly affected by the rolling temperature and the oxide scale thickness before deformation stage. They classified the morphology of the hot rolled oxide scale into three different categories:

a. Ductile: The deformed scale exhibited adequate plasticity to deform uniformly with no signs of cracks and fractures with a smooth interface between metal and oxide.
b. Mixed: Cracks were developed along the rolling direction in the near outermost surface, and the defects were not propagated throughout the scale cross-section.
c. Brittle: The scale was fragmented to small particles, which were then implanted into the steel substrate during rolling, and consequently a rough oxide-metal interface was developed.

They reported that by reducing the rolling temperature and by increasing the scale thickness, the oxide morphology reconstructed from category a to type b and c. They proposed a critical scale thickness limit ($d_{critical}$) where the oxide scale behaved ductile over the thickness. They clarified if the thickness of the oxide scale exceeded $d_{critical}$ thickness, the scale might crack or fracture during hot deformation. Figure 2.7.1 shows the estimated critical scale thickness as a function of rolling temperature. Their experimental work was in good agreement with the estimated critical values.

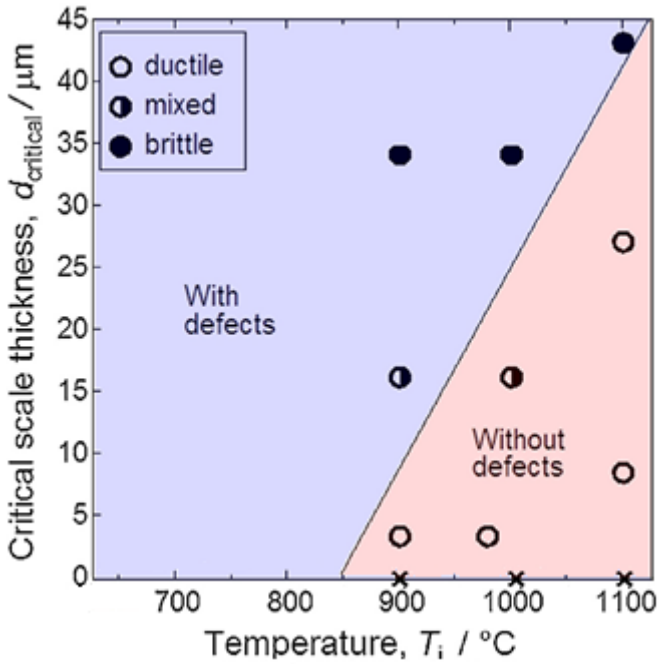

Figure 2.7.1 Estimated critical scale thickness $d_{critical}$ as a function of rolling temperature T_i with experimental scale morphologies [43].

They claimed for preventing the oxide growth exceeding the critical thickness limit ($d_{critical}$), the maximum oxidation duration ($t_{critical}$) could be predicted using equation (2.23):

$$d_{critical} = 1.1x10^{6}\exp\left(-\frac{128{,}000}{RT_i}\right) t_{critical}^{0.5} \qquad (2.23)$$

Where T_i is the rolling temperature and R is the gas constant ($8.314 JK^{-1}mol^{-1}$).

As demonstrated in Figure 2.7.1, above 847˚C the critical scale thickness limit linearly amplified with increasing the rolling temperature. The study predicted that even 45µm thick oxide scale could be deformed homogeneously above 1127˚C. On the other hand, defects development was inevitable during rolling below 847˚C as critical thickness had a direct relation with rolling temperature. They clarified that a sudden drop of temperature of the oxide scale caused by touching the cold roll tools was the major reason for the development of defects within the oxide scales. Cracking defects and oxide fragmentation were observed when the surface temperature decreased below the brittle/ductile transition temperature of

Wüstite. It was concluded that the thinner oxide scale was more ductile; therefore, uniform deformation was observed during rolling.

As shown in Figure 2.7.2, the longest critical duration was predicted to be around 947°C. Utsunomiya estimated the longest oxidation time at 927˚C for reaching the oxide scale critical thickness to be approximately 20s [43].

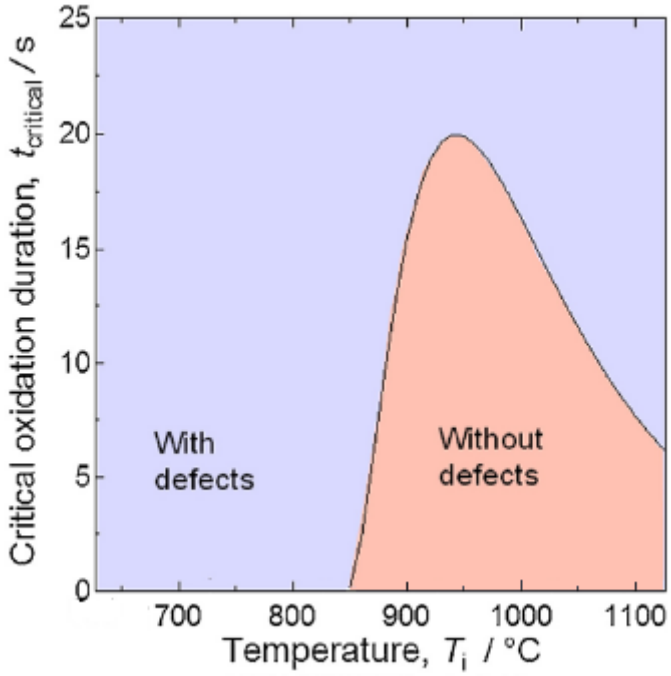

Figure 2.7.2 Estimated critical oxidation duration $t_{critical}$ as a function of rolling temperature T_i [43].

2.7.1 High temperature tensile test

The surface of the material is under tension as the workpiece enters the roll gap during hot rolling. The tensile stress leads to crack initiation within the oxide scale as well documented in the previous work of Krzyzanowski et al. at Sheffield [14], [16], [22], [31], [34]. Mechanical properties of oxide scales under hot working conditions can be evaluated by hot tensile testing at elevated temperatures. Different methods of tensile testing were developed previously in various institutes including the University of Sheffield (e.g. see [4], [6], [14], [16], [22], [31], [34]).

The uniaxial tensile test is the most favourable testing method for determining the mechanical properties of materials at elevated temperature. The hot tensile test allows scientists to assess different mechanical properties of the materials, including ultimate tensile strength and Young's modulus as well as evaluating the failure modes.

Krzyzanowski and Beynon developed an interesting method to assess the tensile strength of the oxide scale and evaluated the ductile to the brittle transition temperature of the oxide scale [14], [16]. In their design, 20mm round specimens were made from mild steel, with a gauge length of 6.5mm. Before testing all samples were sectioned from the centre of the gage segment for eliminating the parent material involvement on the tensile load during the test. A hole was created on the centre of each part of the specimens to insert a ceramic pin. This was done to prevent the transverse movement at the joint section during the test. The drawing and schematic representation of the tensile specimen is demonstrated in Figure 2.7.1.1. A cylindrical quartz tube along with an induction coil was used to create a heating source with a controlled oxidising atmosphere.

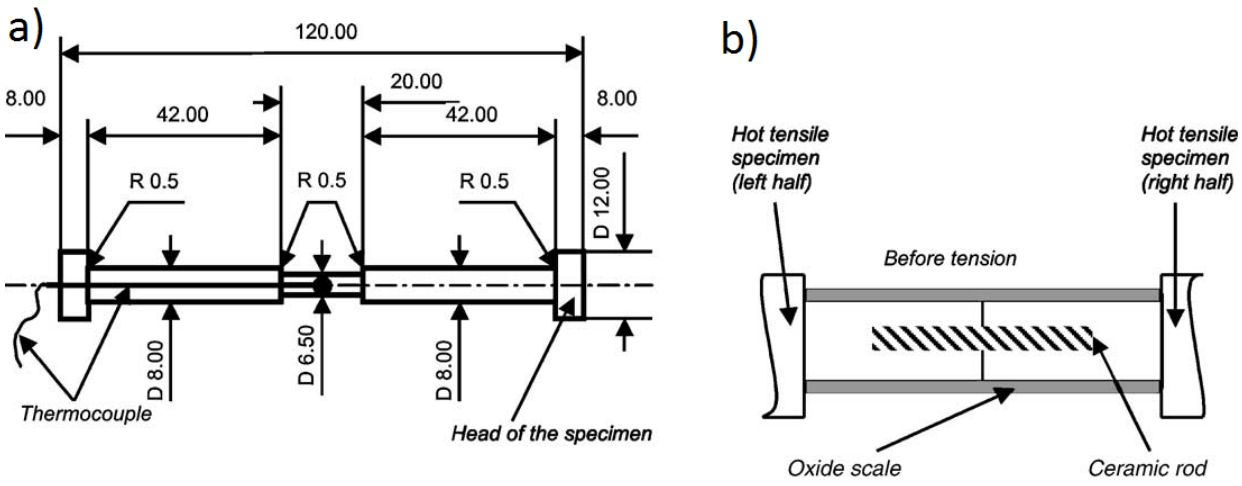

Figure 2.7.1.1 (a) Drawing of the tensile specimen (dimensions in mm); (b) schematic representation of the tensile specimen Krzyzanowski et al. for evaluation of the oxide scale adhesion and fracture loads [34].

The tests were performed in different stages: heating up for 120s followed up by stabilisation at a certain temperature for 300s under a protective gas atmosphere (nitrogen). The oxidation stage was performed in the range of 100-3000s using dry air. Then for about 120s, the inert gas was introduced to the chamber to prevent further oxidation. The tensile testing stage

lasted up to 40s. The specimens then were cooled to room temperature for about 900s. The test provided detailed data on the failure of the oxide scales under tensile load. The knowledge obtained from this method was used to simulate the oxide scale failure under hot forming conditions. As demonstrated in Figure 2.7.1.2, the oxide scale failed in two different modes under tension. At lower temperatures, the oxide fractured, and cracks propagated in the transverse direction, which clarified the brittle nature of the oxide at lower temperatures. Conversely, at higher temperatures, the failure was due to sliding and separation of the oxide layer from the bulk material exhibiting ductile behaviour.

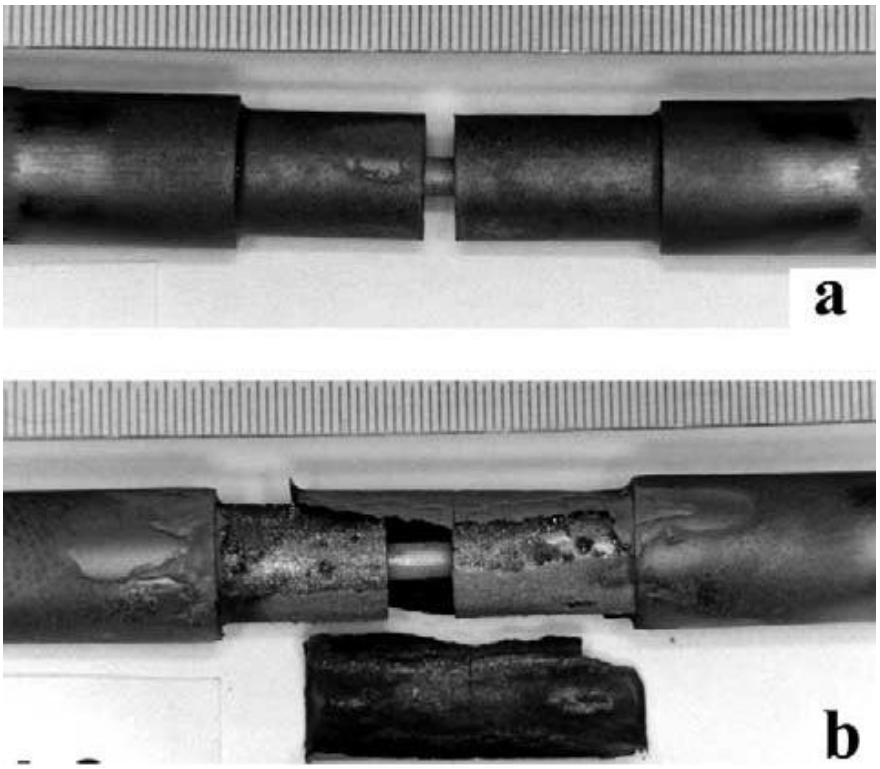

Figure 2.7.1.2 Two different modes of oxide failure in tension during measurement of separation loads: a) through-thickness crack formation; b) sliding along the oxide/metal interface.

They found that the changes in transition temperature from one failure mode to the other one was quite sharp and depended strongly on the material composition. The load versus displacement curves plotted for two modes of failure are shown in Figure 2.7.1.3 [14].

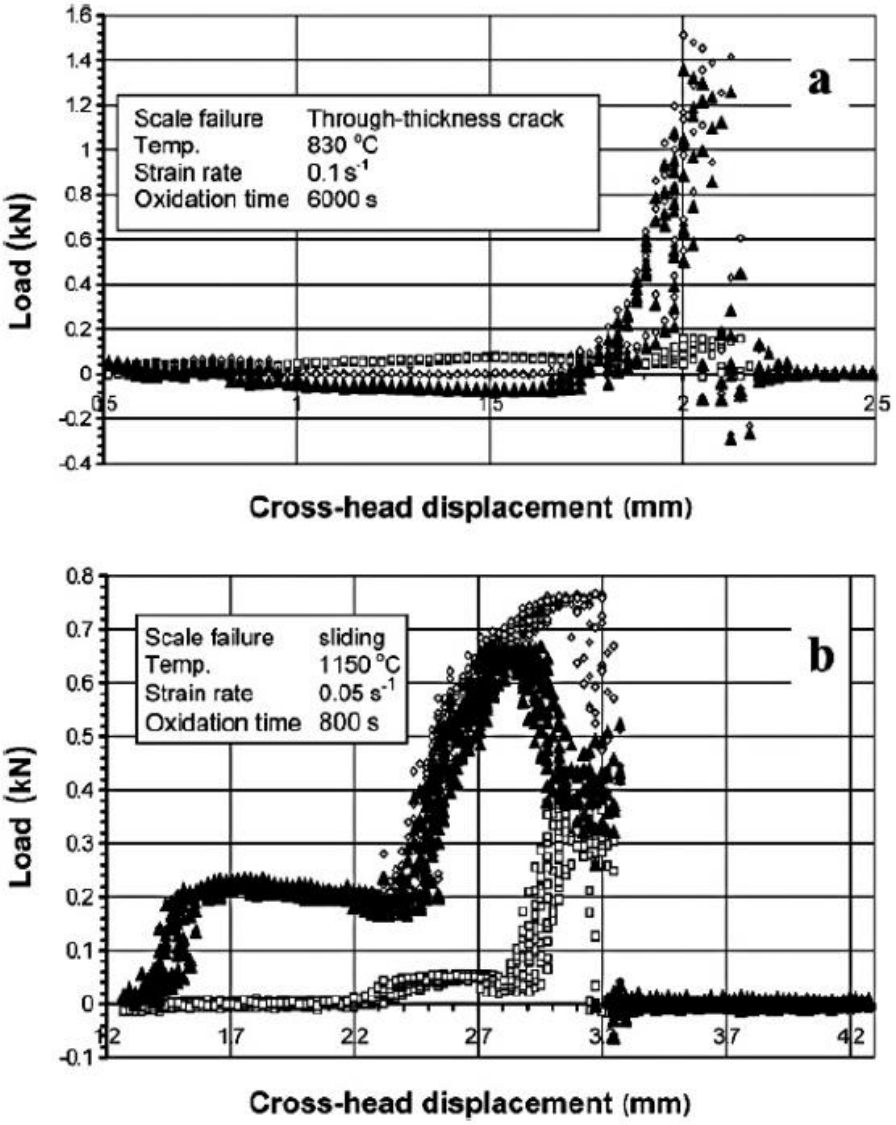

Figure 2.7.1.3 Load versus displacement curve plotted for two modes of failure of oxide scales under tension: a. Through thickness crack and b. Sliding along the interface; ◊, testing with oxidation; □ testing without oxidation; ▲ subtraction of □ from ◊ [14].

Hidaka et al. studied the tensile properties and failure modes of virtually pure FeO, Fe_3O_4 and Fe_2O_3 at 600–1250°C under controlled gas atmospheres by employing strain rates of $2x10^{-3}$–$6.7x10^{-5}$ s^{-1} [17]. For Fe_2O_3 they reported that at a strain rate of $2x10^{-4}s^{-1}$ no ductile behaviour was noticed at 1150–1250°C and the failure mode was cleavage with a fracture strain less than 4%. They explained the plastic deformation of Fe_3O_4 specimen at 800°C was due to dislocation glide. At 1200°C, they witnessed steady-state deformation of Magnetite with an elongation of about 100%. Plastic deformation of FeO was observed in testing the material

above 700°C and the material deformed in a steady state above 1000°C. 160% elongation was achieved by testing the Wüstite above 1200°C. The research showed that the strain rates of FeO at 1000 and 1200°C were proportional to the fourth power of the saturated stress, indicating that the plastic deformation was under the influence of dislocation climb. The stress-strain curves of FeO, Fe_3O_4 and Fe_2O_3 specimens at various temperatures are shown in Figure 2.7.1.4a, 4b and 4c.

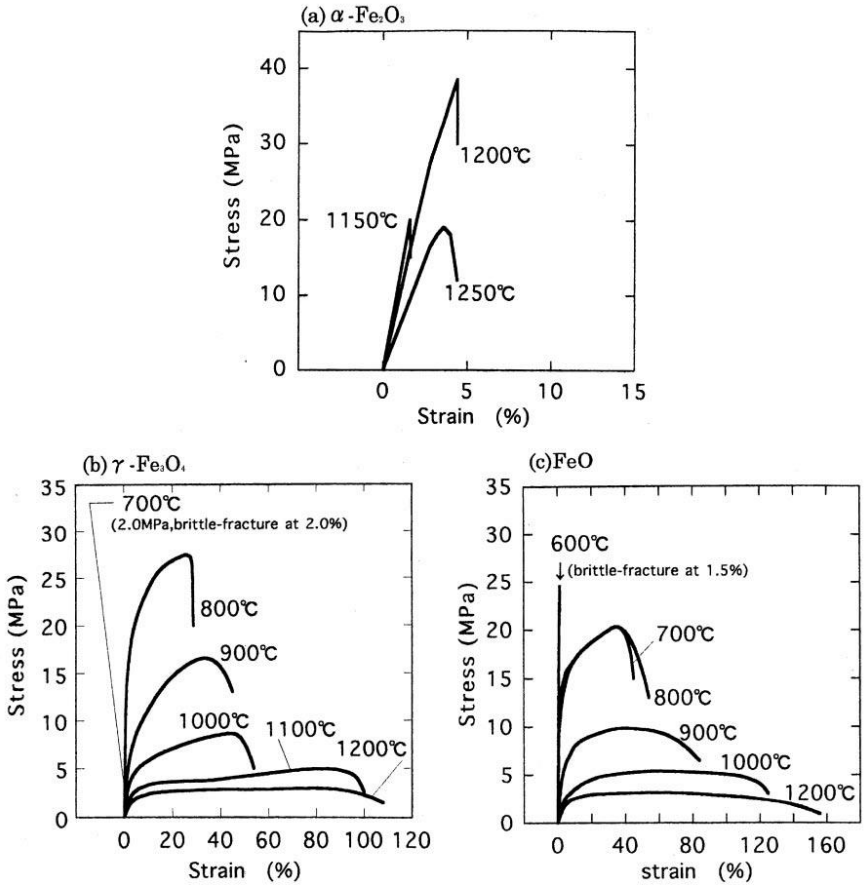

Fig 2.7.1.4 Stress-Strain curves of the tensile test specimens (a)–(c) at various temperatures for the strain rate of 2.0B10−4 s−1 under controlled gas atmospheres [17].

Evans [50] proposed a mechanism for failure of the oxide scales under tensile stress. In his model, through thickness cracks were initiated perpendicular to the stress direction and in high-stress concentrated region, the oxide fragmented to a finite number of segments as demonstrated in Figure 2.7.1.5. As a result, the stress concentrations were reduced near the cracked area and within the segmented scale. At elevated temperature, the plastic stress relaxation could be observed due to sliding at the oxide-metal interface. High shear stress at

the interface might encourage the fracture of the scale at the oxide-metal interface, and consequently, delamination and spallation might occur [4], [50].

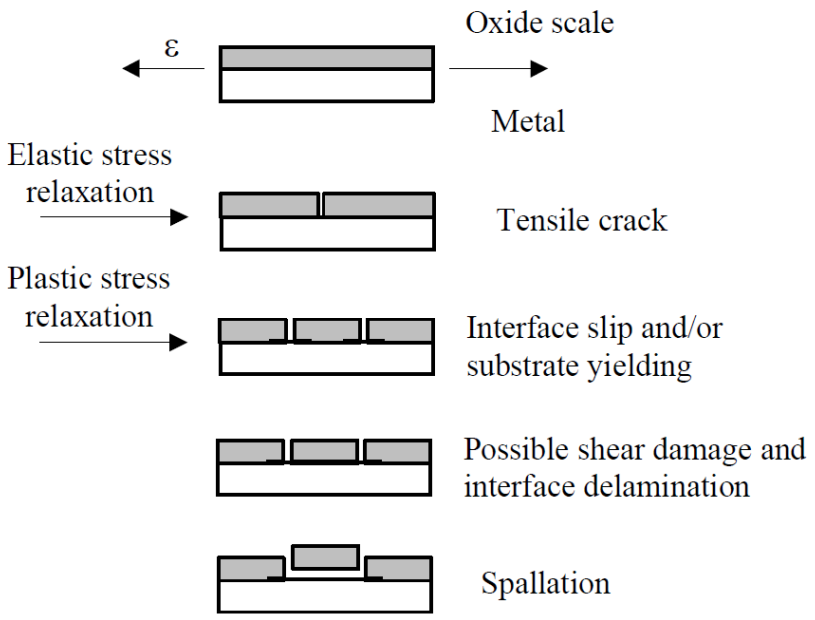

Figure 2.7.1.5 Schematic diagram of oxide failure caused by tensile stress suggested by Evans [50], after Trull [4].

Robertson and Manning [51] suggested a different type of plastic stress relaxation in oxide scale under tensile load. Substrate yielding might occur at the base of the through-thickness cracks, but in such condition, the delamination and spallation of the oxide scale were unlikely to ensue. The works of Krzyzanowski and Beynon [16] confirmed the above theory.

2.7.2 High temperature compression test

Compression stresses are also present during the hot rolling of metals on the transverse direction of rolling. The oxide scale behaviour under compression can be studied by using the hot plane strain test. The hot plane strain compression test determines the behaviour of materials under a compressive load at elevated temperatures. This test method is a practical alternative to high temperature tensile testing for evaluating mechanical properties of the materials, including plasticity. However, it should be noted that based on the direction of the force, materials exhibit differently. For instance, ceramics have excellent strength under

compressive load, but they have very poor tensile strength. Nevertheless, any mechanical testing provides valuable information about the nature of the materials.

Many researchers have tried to evaluate the mechanical properties of the oxide scale using hot plane strain compression test [28], [29], [30]. In most hot compression test instruments, a chamber is installed to control the oxidation atmosphere.

Grenier et al. [29] developed a method for evaluation of plane strain compression behaviour of oxide layer under a hot-formation state by applying a load to a strip, sandwiched between two flat dies. A protective glass vessel was used to let the control of the heating atmosphere. At a constant temperature of 900°C, they produced oxide scales with a different thickness between 10-100µm by controlling the oxidation time. The failure occurred very quickly after the application of compression. An inert atmosphere was used for cooling down the test sample to room temperature for further evaluation. The test allowed the observation of the oxide deformation and cracked propagation under a plane strain compression load [14], [29].

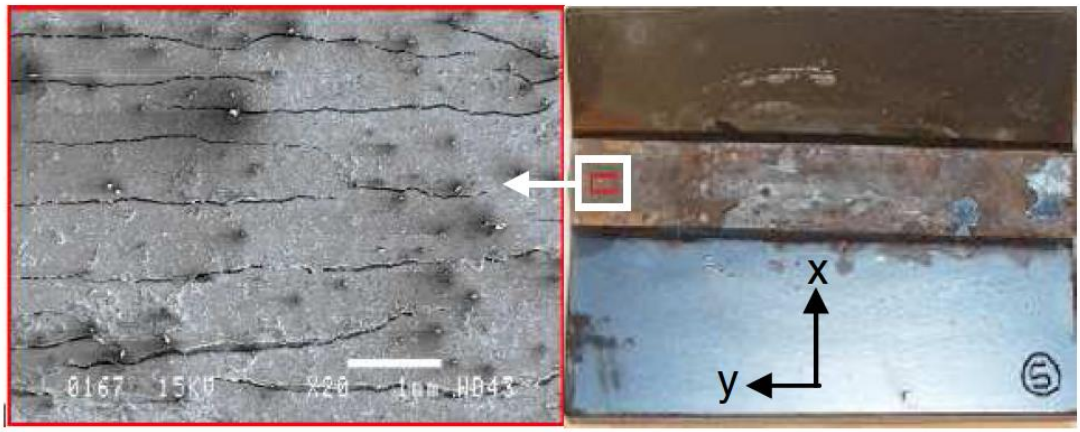

Figure 2.7.2.1 Fractured oxide scale at the side of the specimen under plane strain compression, oxidised at 900˚C, strain rate $1s^{-1}$, oxide layer thickness 50µm [29].

As can be seen in Figure 2.7.2.1, cracks appeared perpendicular to the major flow direction (direction x on Figure 2-17.b) comparable to cracks initiation before roll bite. Grenier et al. [29] testified that the origin of the defects was the movement of underlying metal conducting tensile stress to the oxide layer and it did not occur by oxide scale bending before the bite. The works of Picqué et al. [42] and Krzyzanowski et al. [14] showed punching the oxide surface

by the peaks of the tool surface roughness could also develop localised defects on the top surface of the oxide scale.

Trull [4] divided the failure of the oxide scale under compressive stress into two different categories:

- Normal compressive mode
- Tangential compressive mode

In the normal compression mode, the compressive load is applied perpendicular to the surface of the oxide scale, but if the compressive load is applied in a direction parallel to the oxide layer, it was termed the tangential compression mode. The most common compression mode observed in the hot formation of metals is the normal category, and the failure of scales under this type of stress is not entirely understood yet. Other researchers [4], [52-54], suggested that the oxide scale rupture failure might appear under normal compression stress similar to the failure of concrete under uniaxial compression load. In the tangential compression mode oxide scale could fail in different ways including shear damage, buckling, delamination and failure due to the substrate yielding [4], [7], [12], [25], [50]. The failure of the oxide scale is more complicated than metals under uniaxial compression due to irregular and defective structure. For understanding the complex failure mode, the damage mechanism must be extensively investigated by going through the fracture mechanics including rupture criterion [55] and damage caused by void growth within the structure [56-57] or possibly via concrete failure modelling [58-59]. Overall at elevated temperature and under normal compressive load, the oxide scales might fail in different manners including damage initiation and growth around the structural defects such as voids and porosity, transverse cracking and crushing of the crack edge and sliding of the scale on the oxide-metal interface [4].

The oxide might fail in a different manner under tangential compressive mode. Complete or partial spallation might occur depending on the test condition. A schematic model of the oxide scale behaviour in tangential mode is given in Figure 2.7.2.2. Various types of oxide failure under tangential compressive mode have been proposed by other researchers [7], [12]. Trull concluded that in the first type (Figure 2.7.2.2 case A and C) in which the oxide-metal bonding was strong, the scale failure was initiated by shear cracking and it was followed

by cracks development and propagation along the oxide-metal interface. In the second failure mode, the interface of the oxide-metal was weak, and the oxide structure was strong. The failure was due to sliding of the oxide layer along the interface and consequently buckling and formation of through-thickness crack (Figure 2.7.2.2 case B).

The other type of oxide failure under tangential compressive mode is shown in Figure 2.7.2.2D. The oxide failed in this manner because of the substrate grain-boundaries sliding movement near the interface. The weak bonding between the oxide layers might lead to delamination one of the layers; this is demonstrated in Figure 2.7.2.2E.

Designation	Critical initiation condition	Schematic diagram of the failure mechanism
Case A: Route I (shear failure by wedging)	Critical shear strength	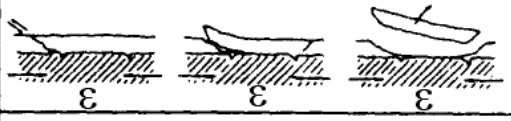
Case B: Route II (buckling)	Critical buckling stability	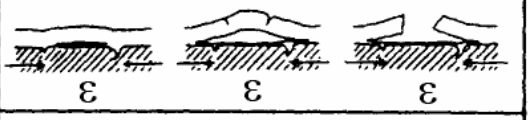
Case C: (shear failure)	Critical shear strength	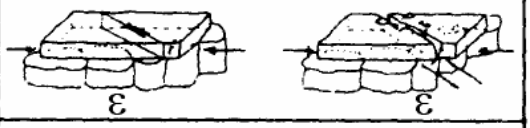
Case D:	Substrate yielding	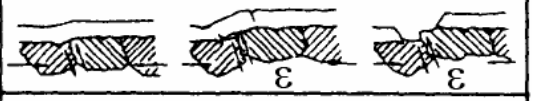
Case E:	Critical buckling stability	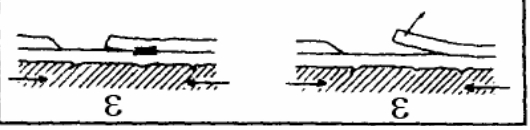

Figure 2.7.2.2 Schematic diagram of different oxide failure mechanisms observed under compressive stresses [12].

Chapter 3

Experimental Procedure

This project was initiated to study the oxide scale behaviour at elevated temperature during descaling and hot deformation. The research was initiated by evaluating the oxidation kinetics of steel alloys. In the next step, the research focused on the characterisation of the oxide scales developed under different conditions. Furthermore, the thermomechanical properties of the oxide scales were evaluated through high temperature tensile tests and high temperature compression tests.

3.1 Materials selection

For this research, Tata Steel UK provided two key steel grades of its product catalogue with the following chemical compositions:

Steel Grade	Wt%	C	Si	Mn	P	S	Al
Rail B9S34		0.75	0.3	1.0	0.01	0.02	-
DSP B9S23 UT23		0.002	2.3	0.2	-	-	0.4

Table 3.1. Chemical compositions of rail steel B9S34 and DSP B9S23 Electrical UT23

Tata proposed the above grades to extend their knowledge on the behaviour of the oxide scales of these alloys. This allows Tata to increase the surface quality of its product by optimising the descaling process. For high temperature isothermal oxidation and oxide characterisation studies, specimens were cut from the provided materials in the as commercially cast condition. For high temperature oxidation studies, specimens were prepared in four different shapes with the following dimensions:

- 15x5x5 mm for isothermal oxidation and microstructural examinations
- 15x15x5mm for XRD examinations

These dimensions were selected with respect to the experimental equipment requirements. Before the oxidation stage, all side surfaces of each sample were ground to a 1200 grit surface

finish with silicon carbide (SiC) grinding papers to eliminate the effect of the surface roughness variations on the oxidation rate.

3.2 High Temperature Oxidation Investigations

The aim of the study was to assess the effect of process conditions on the oxidation of steel, including oxidation rate, the oxide scales morphology, microstructure and crystal structure.

Due to the limitation of the equipment used for TGA analysis, i.e. lack of water vapour addition and usage of dry air as the only gas for oxidation, the environment was a long way from the atmosphere of an industrial reheating furnace. Therefore, an isothermal oxidation experiment was designed to simulate the industrial reheating conditions using a tube resistance furnace (Figure 3.2.1).

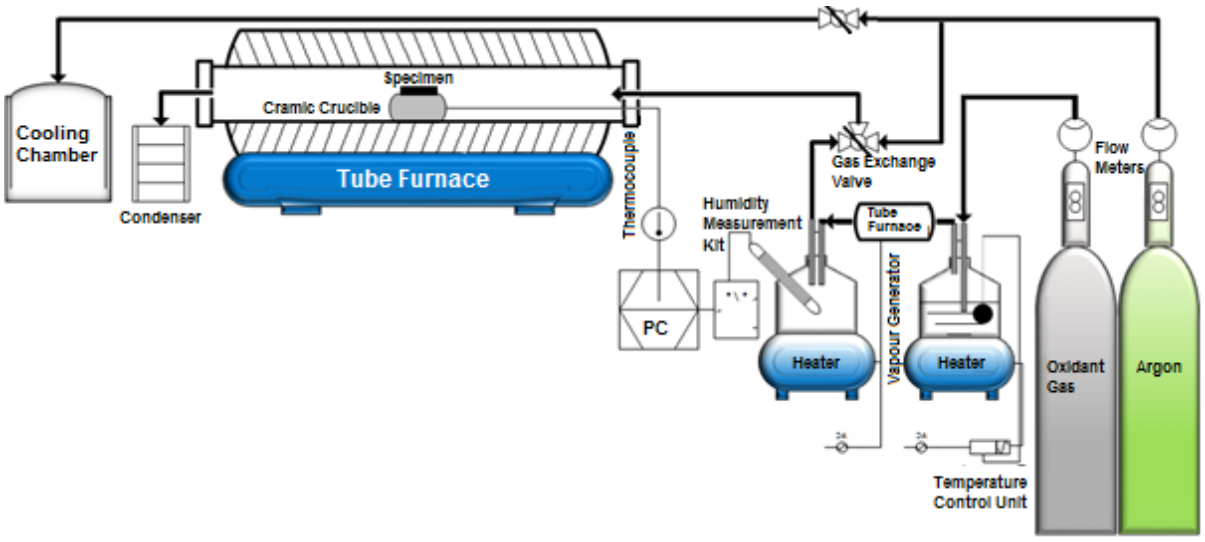

Figure 3.2.1 Schematic representation of isothermal oxidation furnace assembly

The atmosphere of the furnace was controlled by introducing different gas type with respect to the condition required at each stage of the experiment. Argon gas flow of 4 l/min was used as a protective atmosphere to prevent the oxide formation during ramping to the required temperature. Before the oxidation stage injection of argon was sustained for 5 minutes to stabilise the temperature within the furnace and the specimen. For the oxidation stage, a gas mixture (produced by BOC Ltd.) was used with the following composition: "2.1% O_2, 12.2% CO_2 and the balance N_2". This composition was based on Tata Steel information of the

reheating furnace atmosphere of rail steel production plant at Scunthorpe. Based on the given data, the atmosphere of a combustion-reheating furnace contained 17% of water vapour. The oxidant gas was passed through a glass flask containing distilled water to simulate the above condition. The temperature of the water governed the amount of added moisture by regulating the dew point of the liquid. For adding 17% moisture into the oxidant gas, the temperature of the water was kept at 57°C (based on the data provided by Tata Steel Europe). For this purpose, a temperature regulator was installed to control the temperature of the water inside the flask. The amount of the moisture was monitored at 120-130°C by installing HX15-D high temperature humidity measurement kit made by Omega. Prior to humidity measurement, the oxidant gas was passed through a small tubular furnace at 400°C to avoid the condensation of the water. Figure 3.2.2 demonstrates relative humidity of the oxidant gas during oxidation of a rail specimen at 1280°C for 10800s.

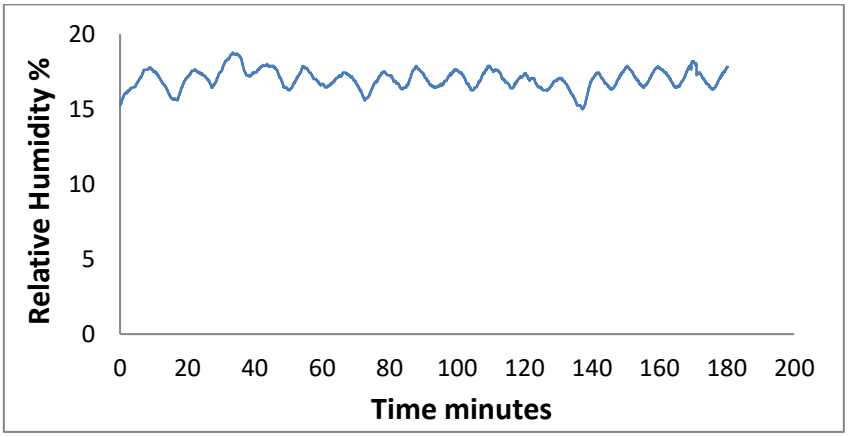

Figure 3.2.2 Average humidity curve of oxidant gas plotted during oxidation of a rail specimen for 180 minutes.

For the dry oxidation condition, the dry oxidant gas was directly introduced into the furnace containing 0% moisture. The temperature of the furnace was calibrated by regulating the temperature in the central area of the tube. For this task, a dummy sample was placed on a Mullite ($3Al_2O_3.2SiO_2$) crucible, and a K type thermocouple was inserted into an axisymmetrical hole created in the centre of the sample. Then the specimen was placed in the hottest spot of the furnace, and the temperature of the oxidant atmosphere was measured by insertion of another K type thermocouple into the oxidation chamber in parallel to the specimen. The

furnace was heated up to 1300°C, and the temperature reading was compared with the temperature displayed on the furnace's digital display. Argon gas flow was used during the temperature calibration process to eliminate the oxidation of the thermocouple and the dummy specimen.

The isothermal oxidation experiments were performed at a temperature range of 850°C to 1280°C for 600 to 10800 seconds. For the cooling stage, an external cooling hub was installed alongside the furnace, as demonstrated in Figure 3.1. After the oxidation stage, the sample was immediately removed from the furnace, and it was placed inside the cooling chamber under 4 lit/min Argon gas flow. This action was taken to eliminate further oxidation of the specimen in addition to achieve a faster cooling rate and consequently to attain significant reduction in phase transformation of the oxide during cooling. Heating profiles of the isothermal oxidation process were generated by connecting K-type thermocouples to a dummy specimen and recording the real-time temperature using a data acquisition unit (Pico Technology TC-08). Figure 3.2.3 shows the heating profile of the rail specimens oxidised for 600-10800s at 1280˚C.

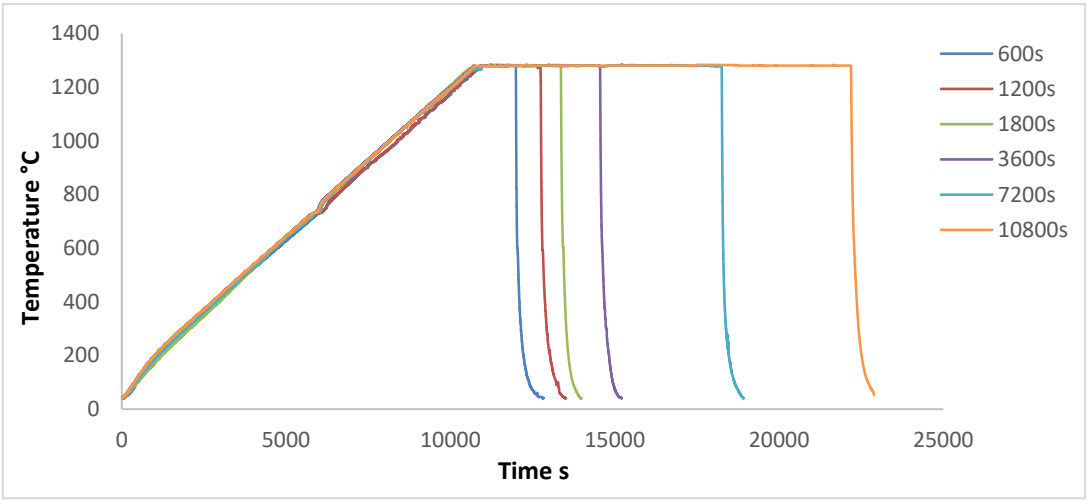

Figure 3.2.3 Heating profile of rail steel specimens oxidised at 1280°C under an atmosphere containing 17% of water vapour.

Prior to the oxidation experiments, the surface area of each sample was calculated by measuring the specimen dimensions using a precision Vernier with an accuracy of $\pm 1 \times 10^{-2}$

mm. The mass gain of each specimen was calculated by measuring the weight prior and after the oxidation using a high precision scale MS104S made by Mettler Toledo with an accuracy of $\pm 1x10^{-4}$g. The oxidation kinetic parameters for both steel grades were calculated for each oxidation condition. For the isothermal oxidation experiments that followed the parabolic law, the oxidation rate constants were calculated using the following Equation (3.1):

$$(\Delta m/A)^2 = k_p t \quad (3.1)$$

Where $\Delta m/A$ is the mass change per unit area (mg/cm^2), k_p is parabolic growth rate constant, and t is the absolute temperature (°K). For certain condition that the oxidation rate followed the logarithmic regime, the rate constant was calculated as follow:

$$\Delta m/A = k_{log} t \quad (3.2)$$

Where k_{log} is the logarithmic growth rate constant. The parabolic and logarithmic rate constants (k) are governed by activation energy. (K) is defined by the Arrhenius equation, as demonstrated in Equation (3.3):

$$k = k^0 \exp(-Q/RT) \quad (3.3)$$

Where k^0 is a pre-exponential factor, Q is the activation energy, R is the universal gas constant, and T represents the absolute temperature. Curves of mass gain per unit area (g/cm^2) as a function of time (s) were plotted, and the parabolic and logarithmic rates constants were obtained by the slope of curves.

All oxidised specimens were cold mounted using epoxy resin to prevent undesirable damage caused during sample preparation. The mounted specimens were sectioned by Isomet 5000 precision saw made by Buehler. The samples were ground to a 1200 grit surface finish using SiC grinding papers. The preparation followed by refining with 9, 6 and 1µm diamond abrasive suspension and finally the surface was highly polished using 0.25 and 0.05 µm polycrystalline diamond abrasive compounds.

In addition to assessing the oxidation rates by mass gain analysis, the oxidation kinetics was assessed using the oxide scale thickness. The average thickness of the oxide scale was measured by scanning the cross section of the sample using a Nikon Eclipse LV100N high-resolution optical microscope, as shown in Figure 3.2.4.

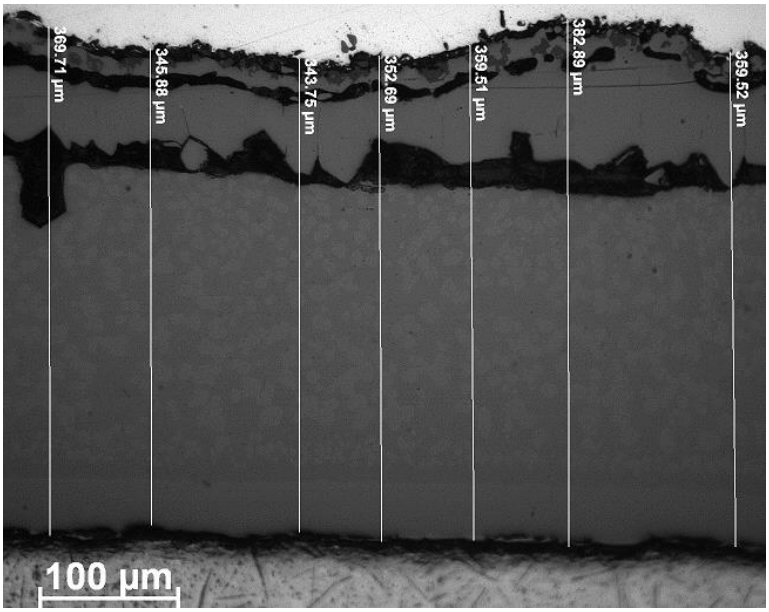

Figure 3.2.4 Measurement of the oxide scale average thickness of a rail steel specimen, oxidised under oxidant atmosphere containing 17% water vapour at 1280°C for 20minutes.

3.3 Characterization techniques

Secondary and backscattered electrons imaging was used to study the structure of oxide scales and oxide-metal interface as well as type and morphology of defects within the oxide layer. For phase analysis and identification of elemental compositions, X-ray diffraction and EDX analysis were carried out.

3.3.1 X-Ray diffraction

The X-ray diffraction analysis was used for phase identification within oxide scales and the oxide-metal interface. Since the thicknesses of the primary oxide scales were considerably higher than the maximum penetration depth of X-rays for the first diffraction line, hence the specimens were descaled, and the obtained oxide scales were crushed to produce a fine powder for XRD analysis. Furthermore, the oxide-metal interface and the residual oxide particles at the interface were examined by inspecting the surface of the substrates

individually. In this study, Siemens D5000 diffractometers with Co Kα and Cu Kα sources were used. The specimens were examined with a fixed scan rate of 1°/min and a step size of 0.05 by setting the angle of the incidence (2θ) from 20 to 90°. The X-ray diffraction peaks obtained from the experiments were compared to JPDS diffraction data cards created by International Centre for Diffraction Data (ICDD) using STOE WinXpow software (version 2.10).

3.3.2 Scanning electron microscopic investigations

In a scanning electron microscope (SEM), a region of a solid object is scanned by a focused electron beam to produce a high-resolution image. Incident of the focused electron beam with the surface of the specimen leads to emission of secondary electrons, backscattered electrons (BSE) and characteristic X-rays. The secondary electrons are low energy electrons discharged from near-surface regions of the specimen because of an inelastic incident of the electron beam and the material. The population of the emitted secondary electrons are subjective to the surface profile of the specimen. This effect generates image contrast deviations, which signify the surface profile. Backscattered electrons are high energy electrons which can be emitted from the atoms located beneath the surface of the material. BEI provides channelling contrast because of crystallographic structure and orientation. The emission of the backscattered electron is directly related to the mean material's atomic number. In backscattered imaging materials with lower atomic numbers are seen darker in comparison to materials with higher atomic numbers, which makes the BSE imaging a powerful tool for phase analysis.

Further information on electron microscopic principles can be found elsewhere [73]. In this research a high-resolution field emission gun scanning electron microscope (Inspect F) made by FEI used for secondary electron imaging, backscattered electrons imaging and EDX analysis. The accelerating voltage on the SEM was set to 10, and 20 KV and the spot size was fixed 3.0nm. The working distance of 6-10mm was used to scan the specimen's surface. All specimens were carbon coated before electron microscopic examinations.

The oxide scale compositions were analysed using an EDX (Energy Dispersive X-ray Spectroscopy) installed on the Inspect F FEGSEM with a resolution of ~1.0 μm^3. Quantitative EDX point analysis and line scan over the oxide scale and oxide-metal interface exploited the

atomic concentration of Fe, O, Si, Al and Mn using a standard less ZAF correction method. The results were presented as weight and atomic percentage. In this technique, the elemental fractions were obtained by applying several corrections into the calculations from the measured X-ray intensities. Count time was set to 30 seconds to produce the EDAX spectra.

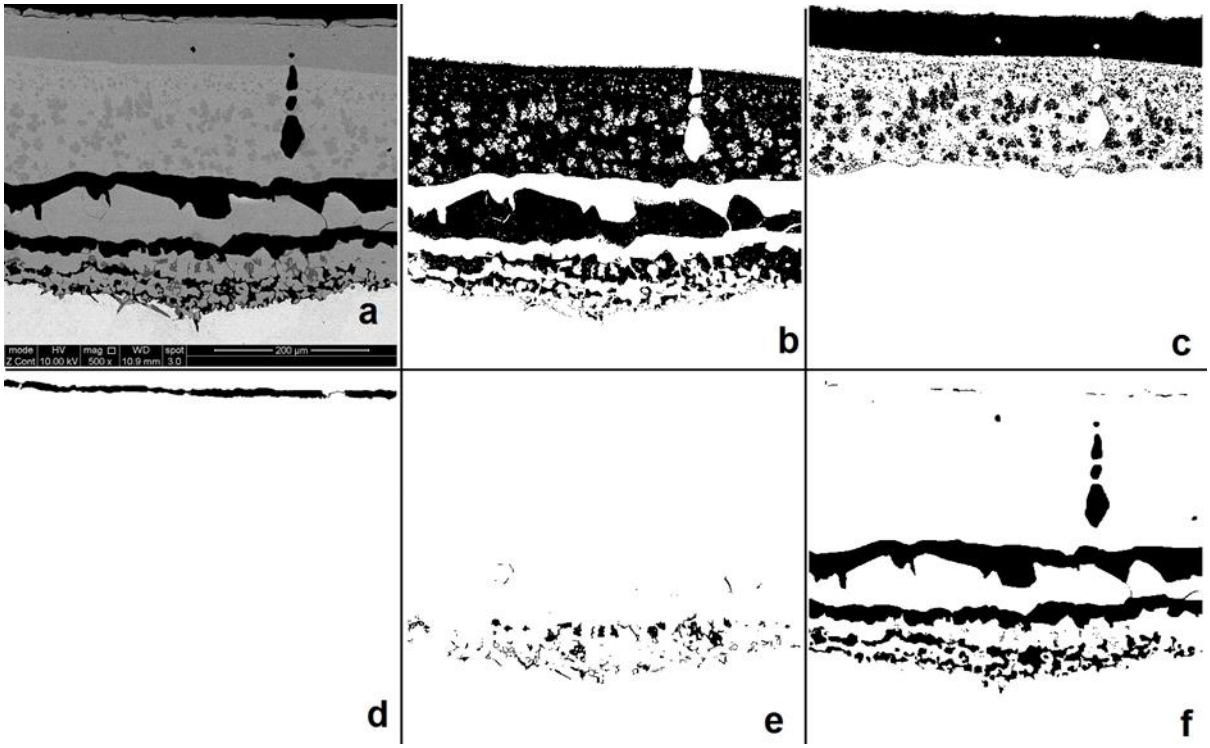

Figure 3.3.2.1 BSE image of a rail specimen oxidised for 60min at 1150°C and area fraction for each phase and defects area by image analysis using ImageJ:
a. BSE image b. FeO phase c. Fe_3O_4 phase d. Fe_2O_3 phase e. Fe_2SiO_4 phase f. defects regions.

The high contrast of backscattered electrons imaging was used to distinguish the phase variations of the oxide scale. Quantitative image analysis was carried out by converting the BEI images to black and white format for further image processing using ImageJ software version 1.37c with added WCIF plugins package. The volume fraction of each phase and also the defects density, including porosity, cracks and cavities were evaluated as shown in Figure 3.3.2.1.

3.3.3 Laser Raman Spectroscopy

Local crystallographic structure of the oxide layers was characterised by Laser Raman Spectroscopy (LRS). Although in recent years, LRS has been used as a micro-analytical tool for oxide scale characterisation [42, 43] surprisingly, it has not been extensively used for cross-sectional characterisation of primary scale. The LRS is based on the elemental bonds, arrangements of atoms and crystals similar to X-ray diffraction analysis. In this method, the incident of high-frequency emission of light or laser with electron clouds in materials (created because of chemical bonds between elements) generates a vibrational response as a form of Raman spectrum. In the past Raman spectroscopy was confined to particular applications due to the immensely low intensity of Raman shift; however, the development of advance double monochromatic systems for stray light distinction in addition to the adoption of continuous lasers as monochromatic sources has made this method to be a powerful tool for structural characterisation of materials. Since LRS is based on spectral analysis of a laser beam scattered from a region as small as few square microns, the structure of the material can be identified locally. A comprehensive description of the theory behind this method can be found elsewhere [98].

In this research, the LRS spectra were obtained using a Renishaw Raman System RM 1000B coupled with a Leica DMLM microscope. A laser beam with a wavelength of 514.5nm was used to excite the samples, and the power was set at 0.2mW. The equipment had a spectral resolution of 1 cm^{-1} and spatial resolution of 2µm.

3.3.4 Oxide-metal interface roughness evaluation

Condition of the interface between the parent metal and oxide scale plays a major role during the descaling process. The roughness of the oxide-metal interface is highly influenced by oxidation parameters including time, temperature, oxidation atmosphere and the parent metal composition. Random deviation from a mean surface develops a three-dimensional topography is known as a surface profile. The surface profile or surface roughness of an object can be expressed by single numerical values such as arithmetic average (R_a) or peak to valley high (R_t). Although this information is useful, but they only represent the deviation of the

surface profile in the vertical direction, and they do not define other surface characteristics such as shapes, sizes and slopes of the surface texture. One of the extensive representations of surface topography is known as a surface bearing area which very well defines the surface roughness profile of the materials including the heights, sizes and slopes of the asperities. A model for bearing area was proposed by Abbot and Firestone (1933) which is known as Abbot-Firestone Curve or simply Abbot Curve. It defines space to material ratio at any certain height; in other terms, it can be described real contact surface area of the material as a function of level [72], [73]. For calculation the bearing area curve of a surface, a parallel line is plotted at a certain height (d). The proportion of the sum of all material intercepts along the drawn line to the total length ($\frac{a_1+a_2+a_3+a_4}{L}$) is the bearing ratio as shown in Figure 3.3.4.1.

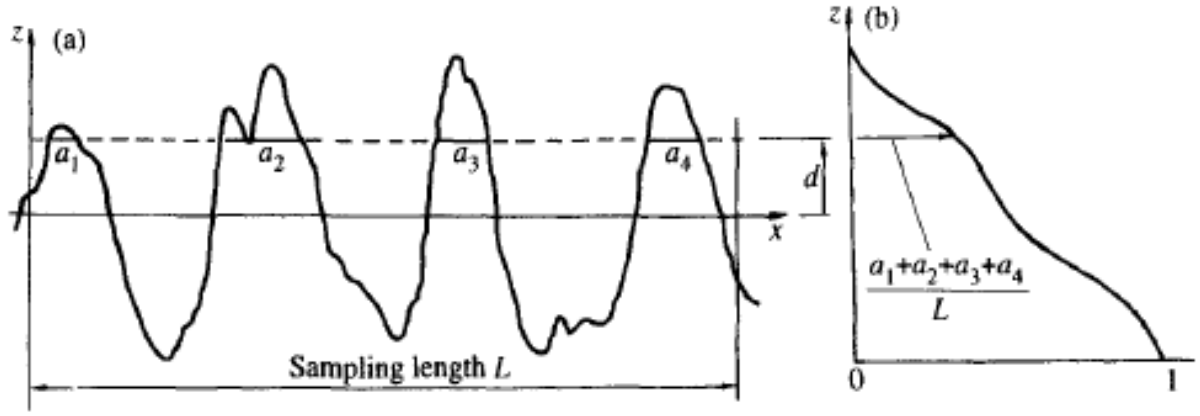

Figure 3.3.4.1 Construction of Abbot bearing area curve from the topography of a surface: a. The surface profile b. Associated bearing area curve [73].

A Nikon Eclipse LV100N optical microscope was used to plot the Abbot bearing area curve of oxide-metal interface for each specimen using the same method described earlier.

3.4 High Temperature Tensile Tests

The uniaxial tensile test is one of the most desirable testing methods for determining the mechanical properties of materials. The great advantage of the tensile test is that mechanical properties of the oxide scale including ultimate tensile strength and Young's modulus can be calculated from the experimental raw data. However, evaluation of mechanical properties of the oxide scale by a uniaxial tensile test is a challenging practice, particularly at higher temperatures. In this research, the test method developed by Krzyzanowski et al. [34] was adopted to evaluate the tensile strength and failure modes of the oxide scales. The purpose of the hot tensile testing was to evaluate the ultimate failure load of the oxide scale under tension and to determine the influence of the temperature on the failure mode. In this study, all thermomechanical tests were performed using Servotest Arbitrary Strain Path machine (ASP), which was a computer-controlled servo-hydraulic thermomechanical testing rig. The specimen's geometry and the tensile test assemblies were modified based on the specimen's properties and the capability of equipment. Figure 3.4.1 displays the arbitrary strain path machine (ASP) used for the tensile tests.

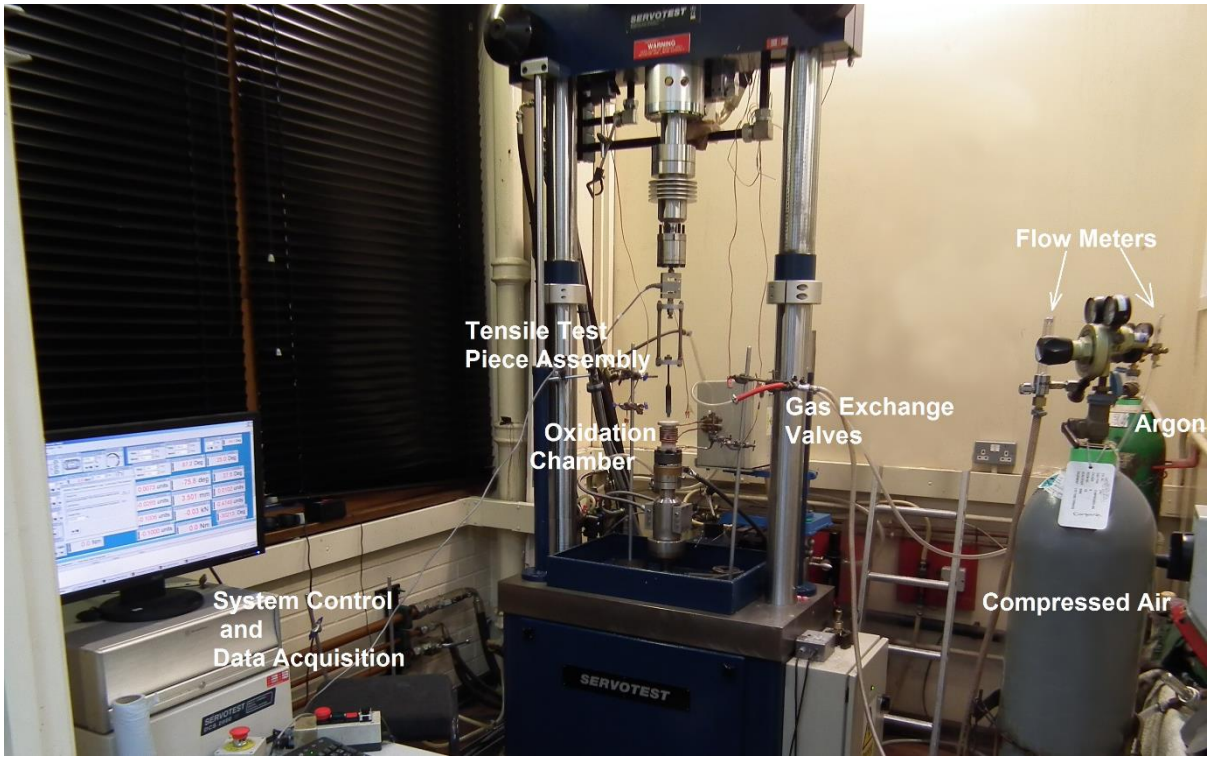

Figure 3.4.1 Hot tensile test machine and the tensile test specimen assembly.

For this test, 200mm long round specimens with a gauge length of 20mm and 10mm diameter were made of each steel grade. The samples were sectioned in halves. On the sectioned surface, a hole with 8mm diameter and 5mm depth was created to minimise the thermomechanical bonding during the oxidation. A cylindrical quartz tube with specially designed ceramic caps was used to create a chamber for controlling the oxidation atmosphere. A vertical induction coil was installed around the glass tube as a heating source. Figure 3.4.2 gives a schematic representation of the specimen assembly within the oxidation chamber. The bottom piece of the sample was mounted on the base of the machine to be static during the test. A steel frame was connected to the hydraulic arm of the machine to eliminate the error associated with the sample linear expansion. As it can be seen, a 200mm pooling shaft was connected to the top part of the specimen through an axisymmetrical hole on the base of the steel frame. The top section was accurately positioned on the bottom part; this allowed the specimen to move freely during the reheating stage.

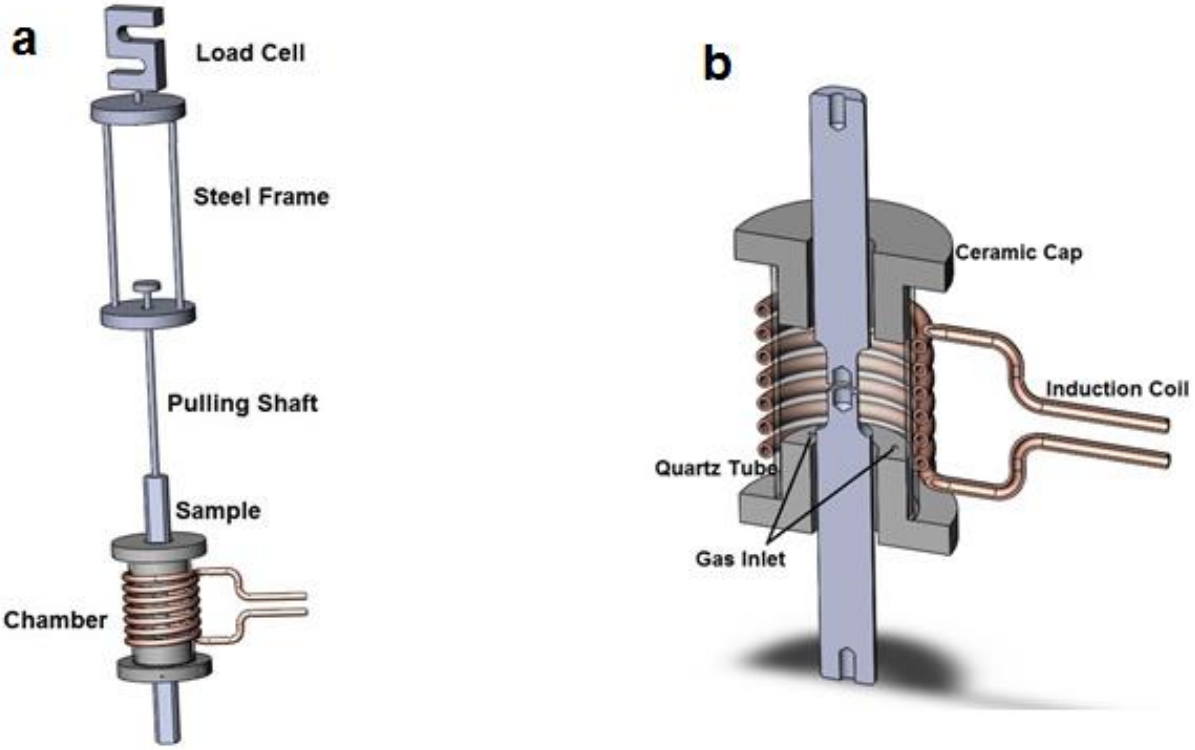

Figure 3.4.2 Schematic demonstration of:

a. Hot tensile test assembly b. Cross section of the test piece and the oxidation chamber.

The test included the following steps: heating up for 120s to the required temperature and stabilising stage for 300s. These two steps were completed under a protective Argon gas atmosphere. The specimens were oxidised at 1150°C or 1280°C for 3600s by injecting dry air into the chamber (4 lit/min). The oxidation step followed by flushing the chamber with argon for 120s to prevent further oxidation. Subsequently, the temperature was set to the test temperature and the system stabilised for 300s. The tensile stage was carried out at a temperature range of 850°C to 1200°C, and the specimen was deformed with instantaneous deformation velocity of 0.1mms^{-1}. After deformation, the sample was cooled down to room temperature under 8 litres per minute argon gas flow for up to 900s. Schedule of the tensile test is demonstrated in Figure 3.4.3

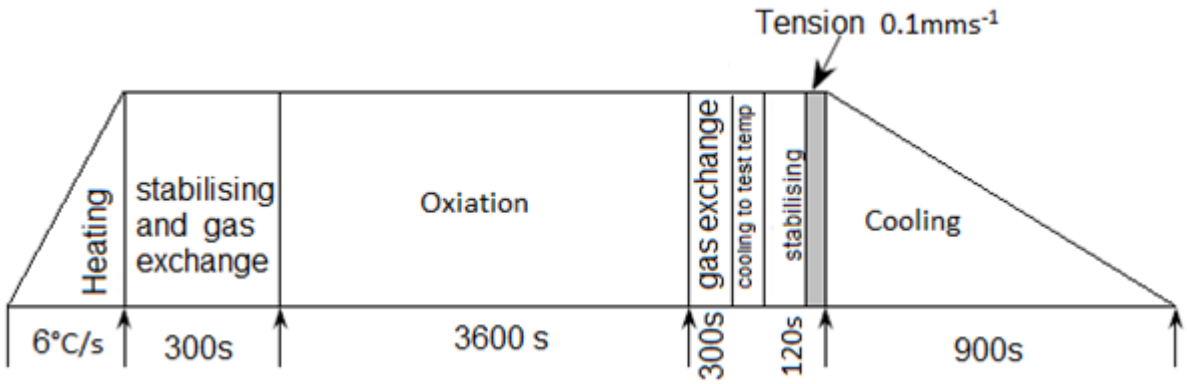

Figure 3.4.3 Process steps schedule of the high temperature tensile tests

All tests were repeated under two different conditions to eradicate the undesirable parameters on the final measurements, including thermomechanical bonding force of the substrate. First, the separation load was measured under an inert atmosphere by injecting argon into the chamber with a flow rate of 4 L/min. Testing under protective atmosphere prevented the oxide development on the gauge section, and therefore, the measured load only showed the thermomechanical and diffusion bonding forces in the joint section. Subsequently, a sample was oxidised at the same temperature and duration by introducing dry air into the chamber, followed by repeating the tensile practice. The values measured in the test performed under inert gas were subtracted from the values obtained using the oxidised specimen.

Strain rate and the percentage of engineering strain were evaluated using the following equations:

$$\dot{\varepsilon} = {}^{v}/_{l} \qquad 3\text{-}7$$

$$\varepsilon_e = \frac{l - l_0}{l_0} \times 100 \qquad 3\text{-}8$$

Where v was the instantaneous deformation speed, l_0 was the initial gauge length and l was the instantaneous gauge length. All deformed samples were prepared for cross sectional assessments in the same manner described in section 3.2. Structural features and characteristics zones were examined by back scattered electron imaging and EDX using SEM.

3.5 High Temperature Compression Test

The hot compression test was performed to evaluate the oxide scale behaviour and the failure mode under a compressive load at elevated temperature. The results helped to understand the scale failure at the point of role bite and during the rolling stage in an industrial roll-mill when the oxide and substrate metal were under the compressive and shear loads. Like the tensile tests, the Arbitrary Strain Path rig was used to perform the hot compression experiments. Rectangular cubic samples with dimensions of 20x15x10 mm were cut from the two different steel grades used for isothermal experiments. The materials supplied by Tata Steel in the as-cast condition. A distinctive compression tool was manufactured from Alloy 600 nickel-base superalloy. The tip of the top part was curved with a radius of 2.75 mm to simulate the role bite in a rolling-mill. The schematic view of the compression tool, sample and oxidation chamber assembly are displayed in Figure 3.5.1. The specimens were placed on the head of the bottom section of the compression tool inside the quartz chamber precisely at the centre of the induction coil. Prior to the test, the temperature was calibrated by comparing the temperatures of the specimen top surface and the temperature obtained from the thermocouple inserted into a hole which was drilled on the side surface 5mm above the bottom of the sample.

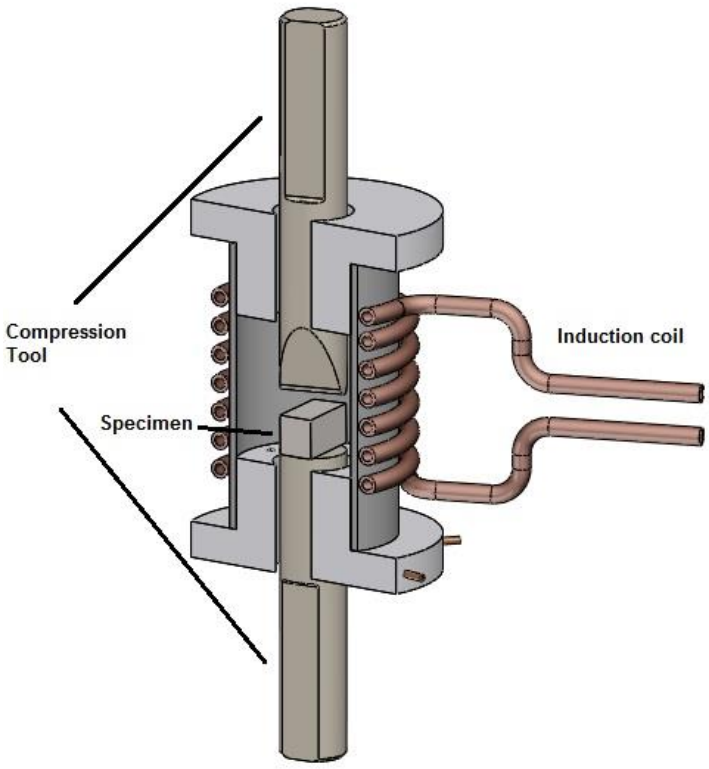

Figure 3.5.1 Schematic view of the compression test assembly

The samples were heated up to the oxidation temperature at the ramp of 20°C/s under 4 lit/min argon gas flow. After reaching the required temperature, the sample was kept under argon atmosphere for an additional 5 minutes to stabilise the temperature. At the oxidation stage, compressed air with a flow rate of 4 lit/min was injected into the chamber. Samples were oxidised for 20 and/or 60 minutes at 1150°C and 1280°C. The top part of the tool was kept 25mm above the sample to maintain the stiffness of the tool as well as minimising the oxidation of that. After the oxidation stage, the air flow inside the tube was replaced by injecting argon. The compression tool was lowered to near the surface of the oxidised sample prior to deformation stage. The specimens were deformed at a temperature range of 850°C-1280°C using $0.8s^{-1}$ strain rate. The different stages of the compression process are demonstrated in Figure 3.5.2.

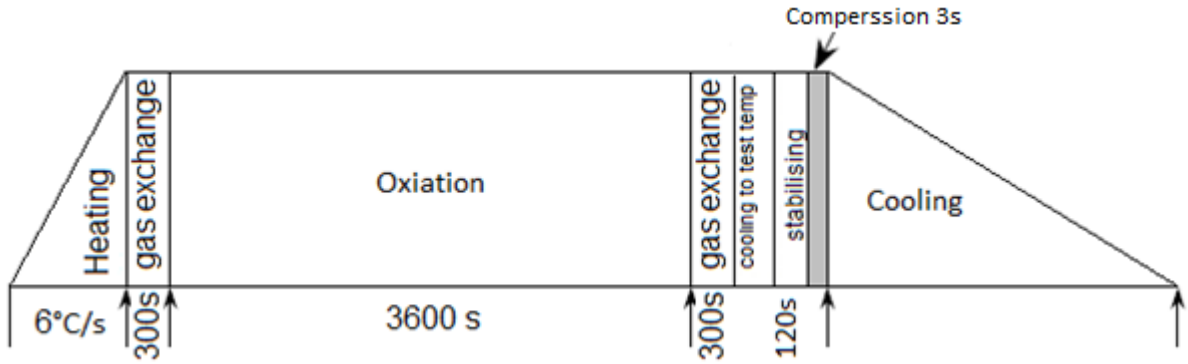

Figure 3.5.2 Time Schedule for high temperature compression test.

All deformed samples were prepared for cross-sectional assessments in the same manner described in Section 3.2. Structural features and characteristics zones were examined using backscattered electron imaging.

Chapter 4

Results I: Oxide scale development and oxidation kinetics

4.1 Introduction

For understanding the oxide scale behaviour during the hot deformation of steel, it is essential to gain a broad knowledge of oxide scale development and oxidation kinetics. This study helped to build a foundation on the oxide scale behaviour at different stages of the oxidation and hot deformation process in an industrial steel plant.

In this chapter, the outcome of isothermal oxidation experiments was explained, which included studying the oxidation kinetics and the effects of the oxidation conditions, including time, temperature and environment. Furthermore, details of the oxide scale microstructure, morphology, phase distribution and oxide-metal interface characteristics for undeformed samples at different conditions were elucidated.

4.2 Oxidation Kinetics

A series of isothermal oxidation experiments were carried out under various conditions to evaluate the oxidation kinetics of the supplied steel grades. As this research aimed to study the developments and behaviour of primary oxide scales, the materials were oxidised isothermally from 600 to 10800 seconds at a temperature range of 850°C to 1280°C. Table 4.1 demonstrates the experimental conditions for isothermal oxidation tests.

The curves of mass gain per unit area($\mathrm{g/cm^2}$) versus time of the oxidation were plotted, and the oxidation kinetics were calculated using the methods proposed by Kofstad [1]. To verify the parabolic mode, the curve of Δx^2 vs (t) and for the logarithmic behaviour, the curve of Δx vs log (t) was plotted.

Table 4.1 Experimental conditions for isothermal oxidation tests.

Test Condition	Oxidation Temp. ˚C	Relative Humidity %
1	1280	17
2	1150	17
3	1050	17
4	950	17
5	850	17
6	1280	0
7	1150	0

As explained in the literature, the initial stage of the oxidation was rapid, and the process was expected to obey the linear law. The oxidation rate then decreased by the development and the growth of continuous thick scales over the substrate. Figure 4.1 shows the mass gain per unit area of rail steel during isothermal oxidations under conditions 1, 2 and 6. The parabolic behaviour was observed in all three oxidation conditions.

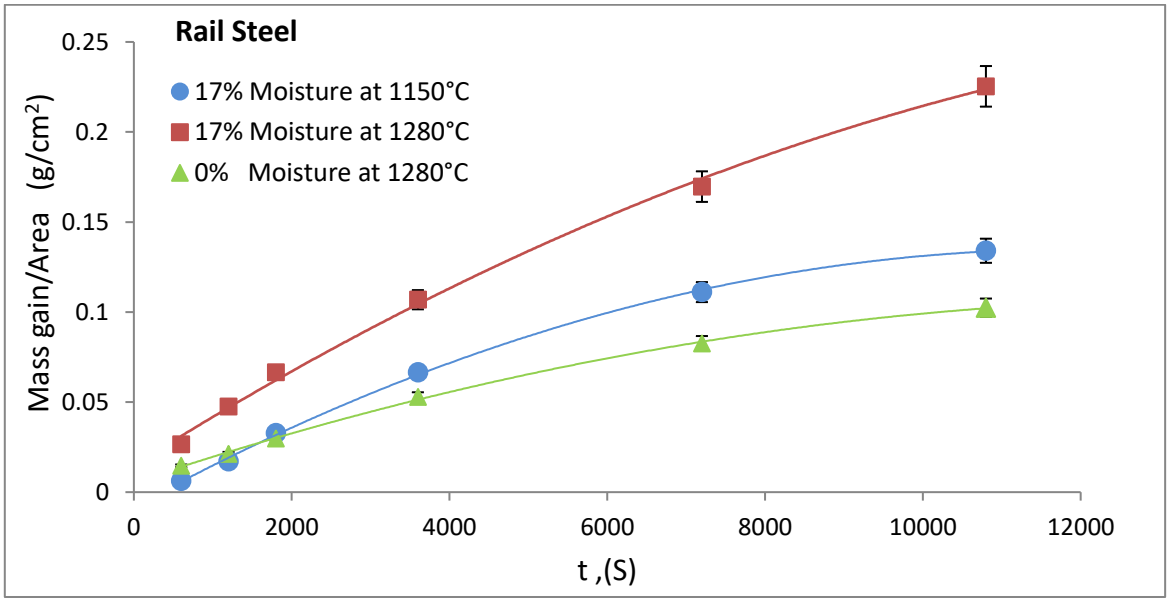

Figure 4.2.1 Isothermal oxidation kinetic curves for rail steel specimens oxidised at 1150°C and 1280°C, under atmospheres containing 17% moisture and dry atmosphere.

Under moist atmosphere, the rate of the process was considerably higher at 1280°C, in comparison to oxidation of the material at 1150°C. The oxidation rate significantly reduced

when the material oxidised under the dry atmosphere. The oxidation mode verifications and determination of the oxidation rate constants are shown in Figure 4.2.2.

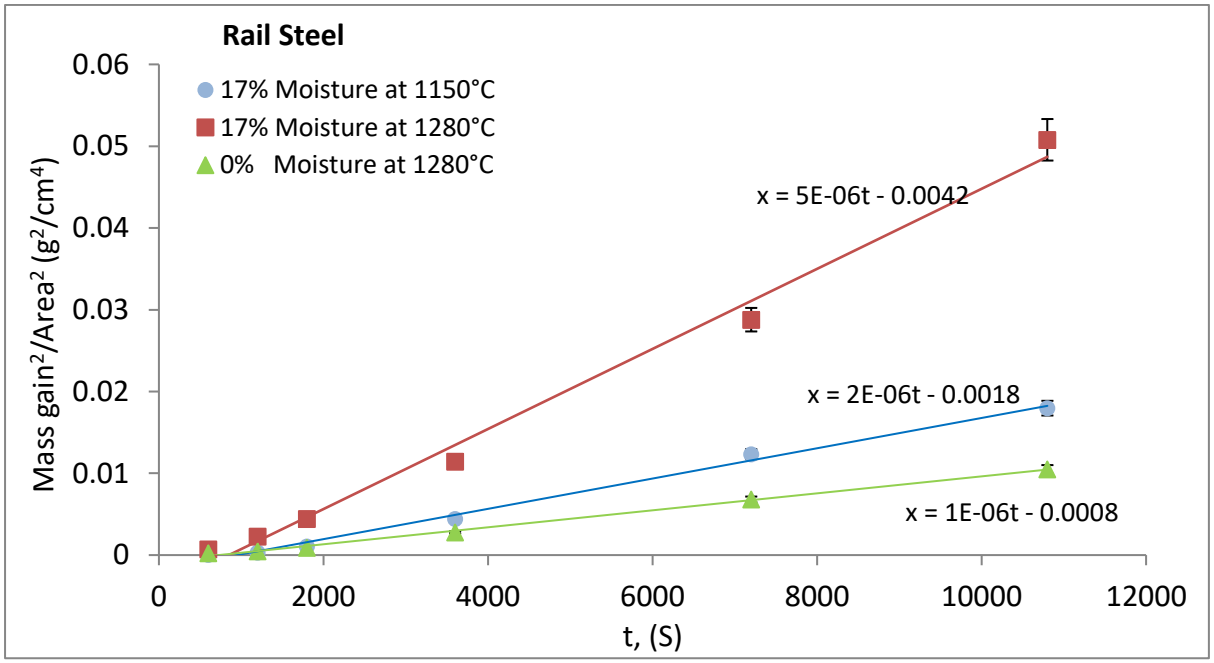

Figure 4.2.2 Oxidation modes verifications and calculations of the rate constants for the oxidation of rail steel under condition 1, 2 and 6.

After plotting the trend lines, good linear fits with confidence intervals of 99% were apparent in all three conditions. The oxidation constants (k_p) were obtained from the slope of the curves, and the results were tabulated in Table 4.2.

Figure 4.2.3 a, b and c give the mass gain per unit area of DSP steel during isothermal oxidations under conditions 1, 2 and 7. The tests at 1280˚C and 1150˚C clearly showed that after 600s oxidation under humid condition, the process obeyed the parabolic law. In contrast, after 600s the oxidation of the material at 1150˚C under a dry atmosphere followed the logarithmic law. As shown in Figure 4.2.4.a and b the curves of $(\text{mass gain/area})^2$ vs time were plotted for oxidation under conditions 1 and 2. For the dry condition, the curve of the mass gain per unit area was plotted against the log(t) as presented in Figure 4.2.4.c. Subsequently, the parabolic and logarithmic rate constants were obtained from the slope of the curves, as explained earlier. The results were followed the linear trend lines, and confidence intervals of 99% and 97% were achieved for humid and dry conditions, respectively.

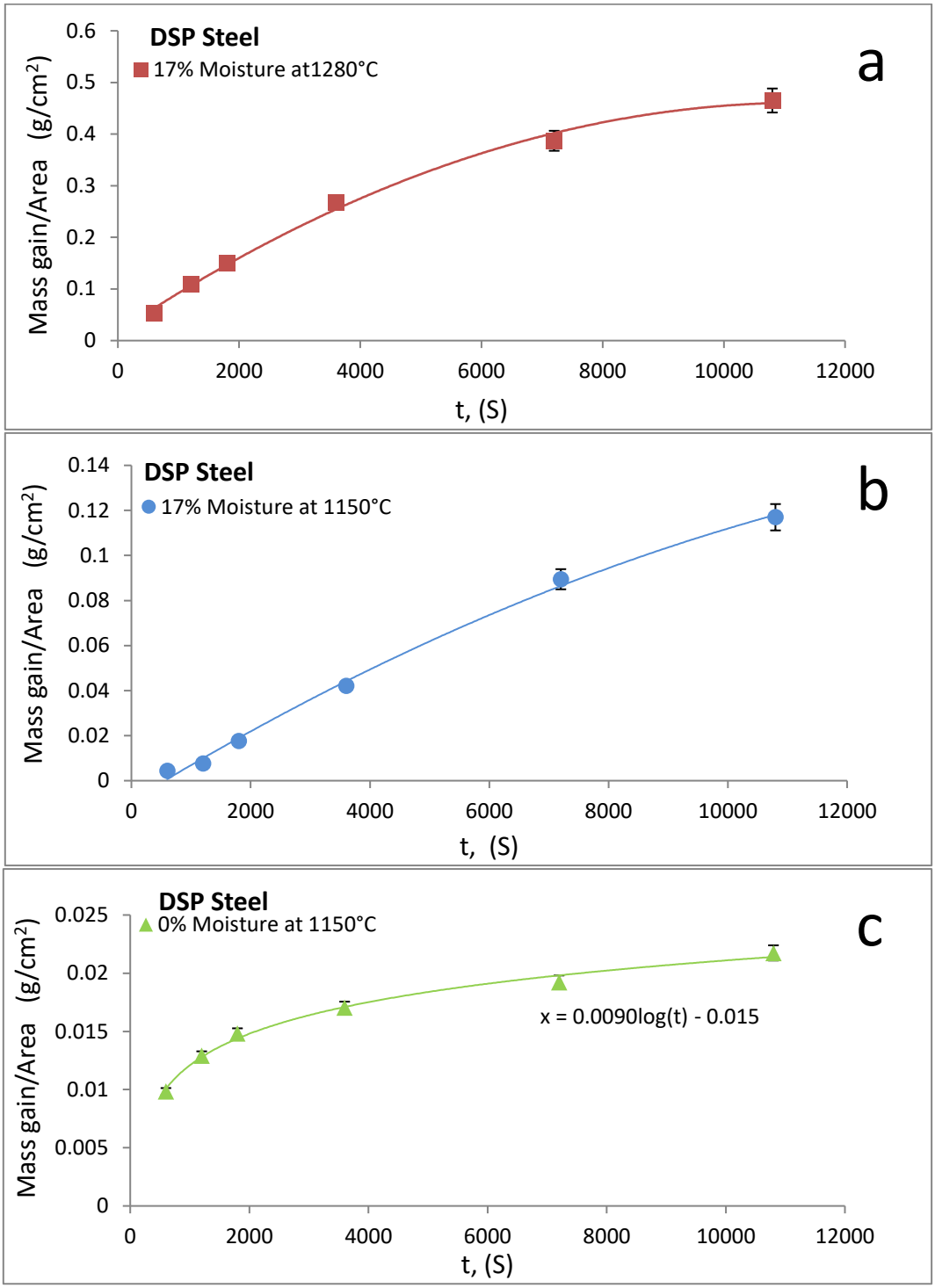

Figure 4.2.3 Isothermal oxidation kinetic curves for DSP steel specimens oxidised at 1150°C and 1280°C, under atmospheres containing 17% moisture and dry atmosphere.

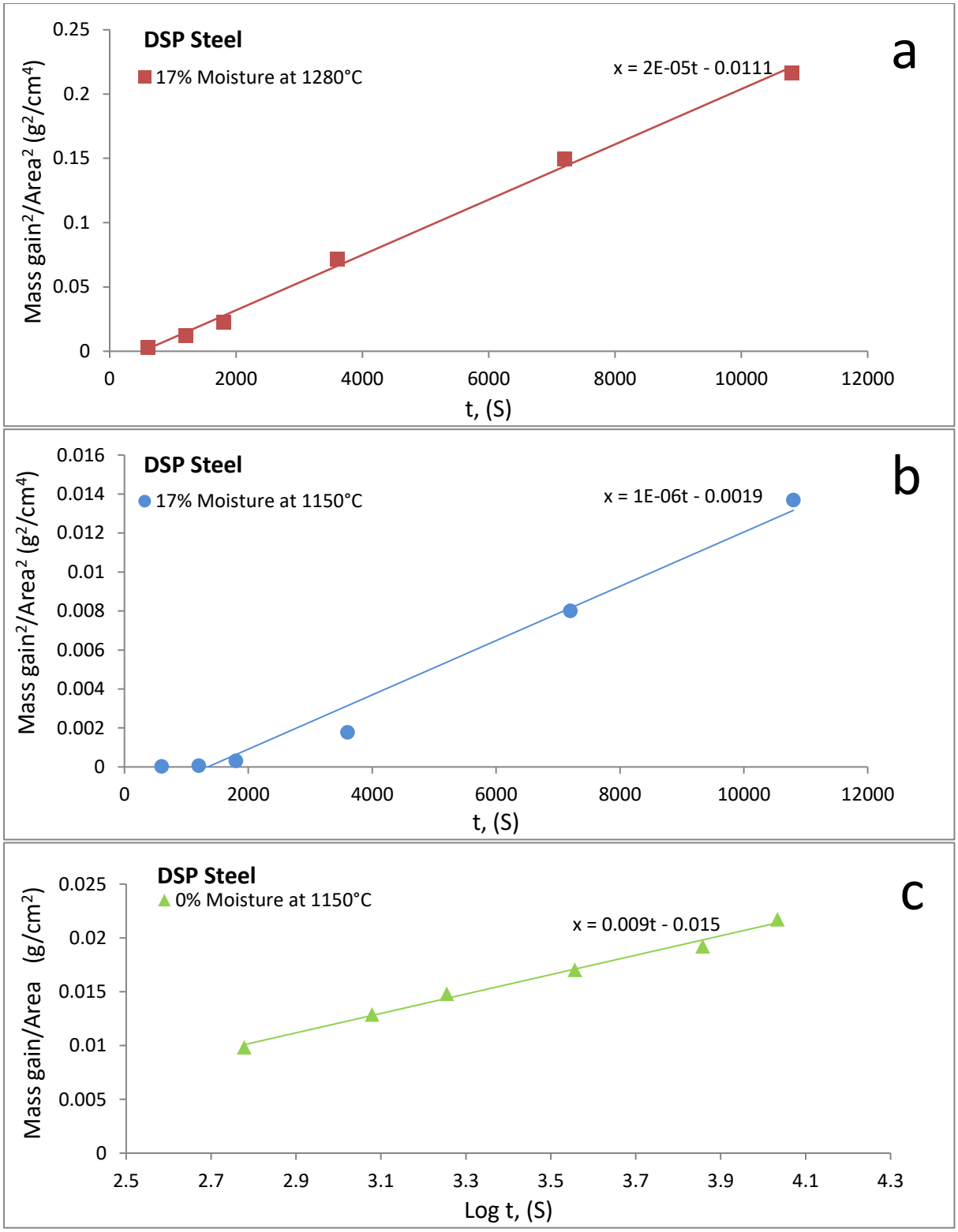

Figure 4.2.4 Oxidation modes verifications and calculations of the rate constants for oxidation of DSP steel: a) condition 1, b) condition 2 and c) condition 7.

The summary of the oxidation modes and oxidation rates constants in various conditions for each steel grade are given in Table 4.2.

Table 4.2 Oxidation characteristic modes and oxidation rate constants in various conditions for each steel grade.

Steel Grade	Temp (˚C)	Relative Humidity	Oxidation Characteristic Mode	Rate Constant k
Rail	1280	17%	Parabolic	$K_p = 5 \times 10^{-6}$ $(\frac{g}{cm^2.\ s^{1/2}})$
Rail	1150	17%	Parabolic	$K_p = 2 \times 10^{-6}$ $(\frac{g}{cm^2.\ s^{1/2}})$
Rail	1280	0%	Parabolic	$K_p = 1 \times 10^{-6}$ $(\frac{g}{cm^2.\ s^{1/2}})$
DSP	1280	17%	Parabolic	$K_p = 2 \times 10^{-5}$ $(\frac{g}{cm^2.\ s^{1/2}})$
DSP	1150	17%	Parabolic	$K_p = 1 \times 10^{-6}$ $(\frac{g}{cm^2.\ s^{1/2}})$
DSP	1150	0%	Logaritmic	$K_L = 9 \times 10^{-3}$ $(\frac{g}{cm^2.\ s})$

The relationship of the oxidation rate constants and the inverse of the absolute temperatures were plotted in Figure 4.2.5. Subsequently, the activation energy was obtained for each steel grade (Table 4.3); however, great uncertainty associated with the projected values as each curve based on two data points only.

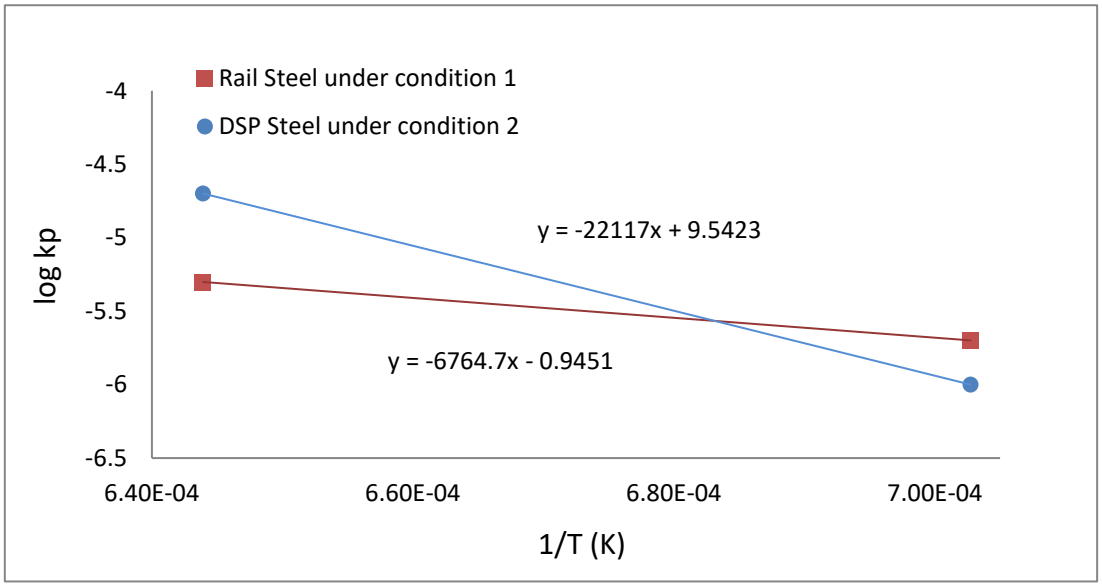

Figure 4.2.5 Arrhenius plots of relations between the oxidation rate constants and the oxidation temperature for each steel grade.

Table 4.3 Values of the activation energy for each steel grade oxidised under atmosphere contained 17% of moisture.

Steel Grade	Q Activation Energy (KJ/mol)
DSP	183.89
Rail	56.24

A further effect of temperature on the oxidation rate of each steel grade is shown in Figure 4.2.6. The experimental data obtained by oxidising the specimens under an atmosphere containing 17% moisture for 60 minutes at various temperatures. As can be seen, the oxidation rates of both steel grades were intensified, where the temperature of the process increased. Up to 1150˚C, the oxidation rate of DSP steel was lower than the rail grade but at 1280˚C, the oxide development rate of this grade rapidly increased.

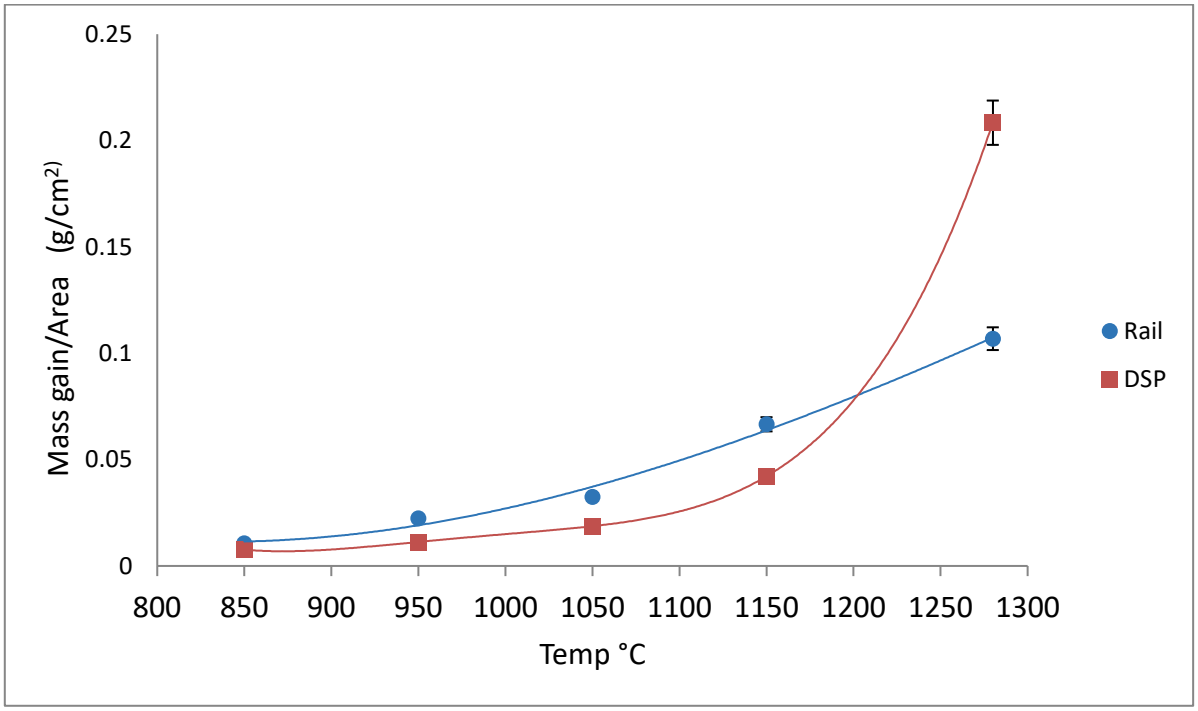

Figure 4.2.6 Effect of temperature on mass gain per unit area for rail and DSP steel oxidised for 60 minutes under an atmosphere containing 17% moisture.

4.3 Phase analysis by x-ray diffraction

X-ray diffraction investigations were carried out on two different segments of the oxide scales, as described in section 3.3.2. First, the outer scale was examined by crushing the oxide scale to a fine powder. Subsequently, the composition of the interface was studied by scanning the interface after descaling. Figure 4.3.1 displays the X-ray diffraction profile for outer scales of the rail specimens oxidised at 1280°C from 10 to 180 minutes under an atmosphere containing 17% of water vapour.

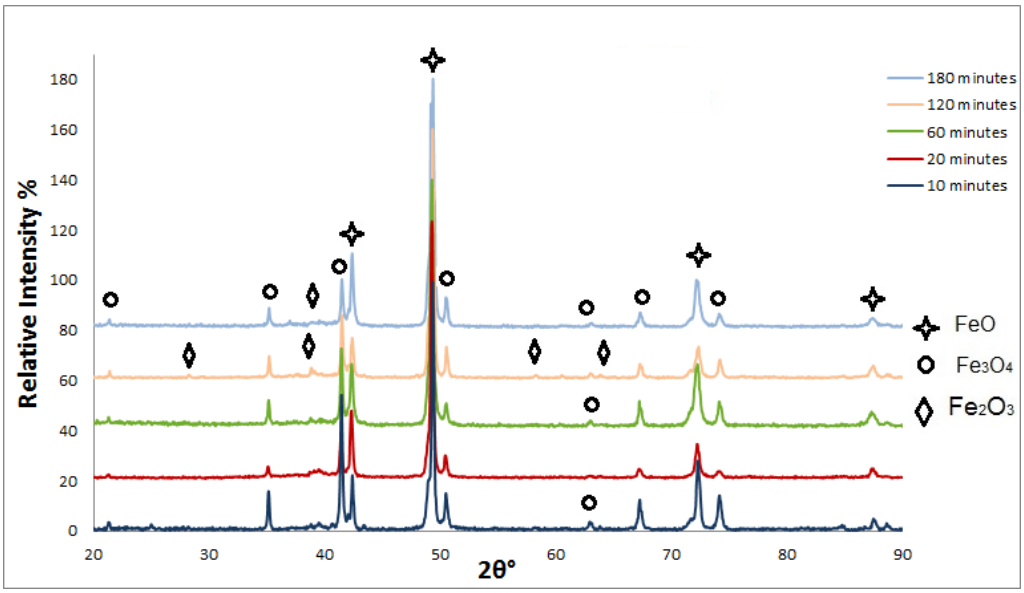

Figure 4.3.1 X-Ray diffraction patterns of the outer scale of rail specimens oxidised at 1280°C under an atmosphere containing 17% moisture.

The XRD analysis confirmed the presence of Wüstite and Magnetite in all specimens. As can be seen, the highest peak represented FeO, indicating that Wüstite was the predominant phase. In contrast, no indication of Fayalite was noticed, and minor peaks of Hematite were only visible in the specimen oxidised for 120 minutes. Difficulties in the detection of Fe_2O_3 and Fe_2SiO_4 were attributable to very small proportions of these phases within the oxide structure.

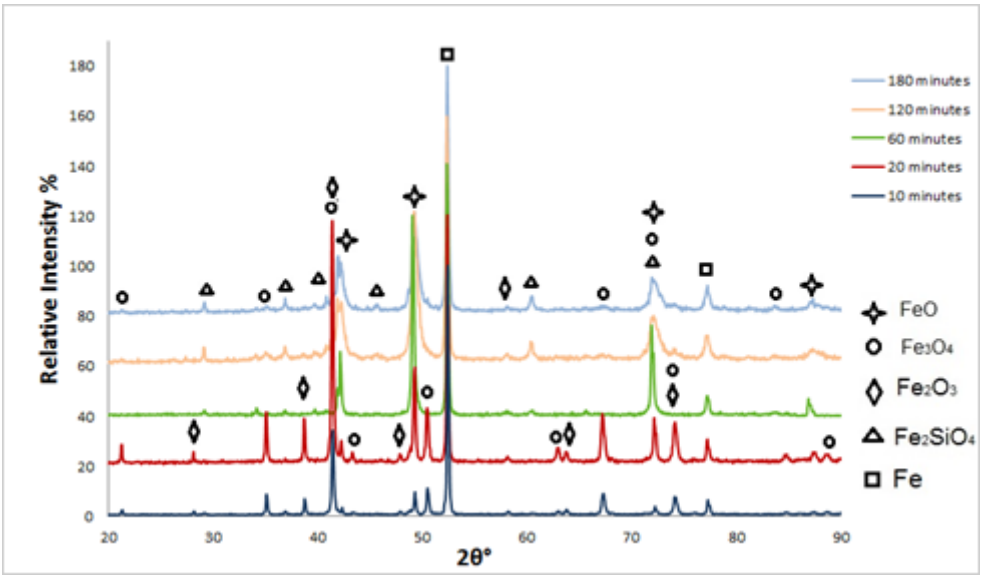

Figure 4.3.2 X-Ray diffraction patterns at the oxide-metal interface of the rail specimens oxidised at 1280°C under an atmosphere containing 17% moisture.

Figure 4.3.2 demonstrates the diffraction patterns of the oxide-metal interface of the rail samples oxidised for 10 to 180 minutes at 1280˚C under an atmosphere containing %17 of moisture. All three types of iron oxide constituents, along with Fayalite and iron were detected in those regions. The variation of XRD patterns between samples was related to the effect of oxidation time as well as the effect of the descaling process and contamination of the interface by the outer layer residual oxide particles.

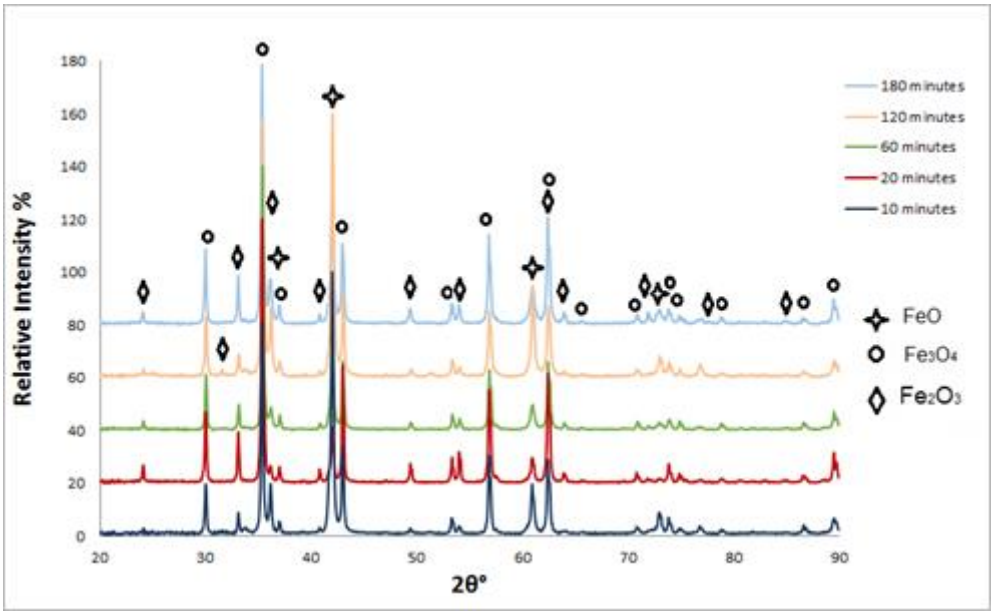

Figure 4.3.3 X-Ray diffraction patterns of the rail outer scale specimens oxidised at 1280°C under a dry atmosphere.

In all specimens oxidised at 1280°C under a dry atmosphere, all three constituents of iron oxide were detected. As can be noticed in Figure 4.3.3, peaks of Hematite were detected in all samples. This signified that volume fraction of Fe_2O_3 under dry atmosphere was higher than the moist condition. The analysis revealed that Wüstite and Magnetite were the most abundant phases for oxidation up to 120 minutes. The amount of Wüstite in the sample oxidised for 180 minutes was significantly reduced, which could be related to the transformation of FeO during the cooling stage.

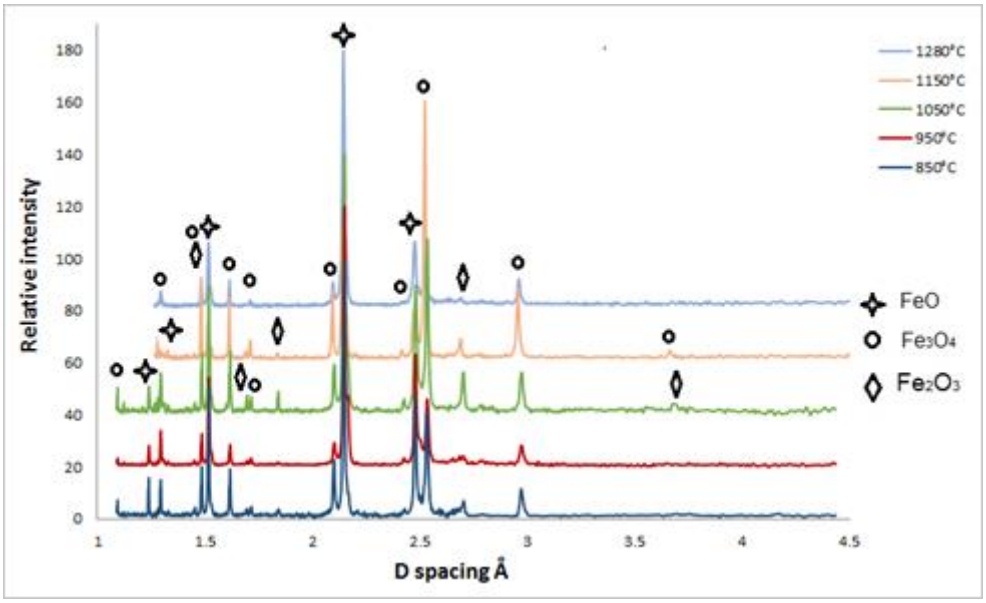

Figure 4.3.4 X-Ray diffraction patterns of outer oxide scale of the rail specimens oxidised for 60 minutes at various temperatures under an atmosphere containing 17% moisture.

To evaluate the effect of temperature on the oxide scale compositions, the oxide scale developed between 850°C to 1280°C under a moist atmosphere were examined using by XRD. However, midway through the experiments, Co Kα source of the XRD equipment was replaced by Cu Kα by the department; therefore, all diffraction patterns were plotted using d spacing by converting the scattering angle (θ) using Equation 4.1:

$$2d.\sin\theta = n\lambda \qquad \text{Equation 4.1}$$

Where n is a positive integer and λ is the wavelength of the incident [74]. As can be seen in Figure 4.3.4 Wüstite was the predominant phase in all oxidation temperatures except the sample oxidised at 1150°C, which Magnetite was the utmost oxide constituent. Small quantities of Hematite were detected in all specimens.

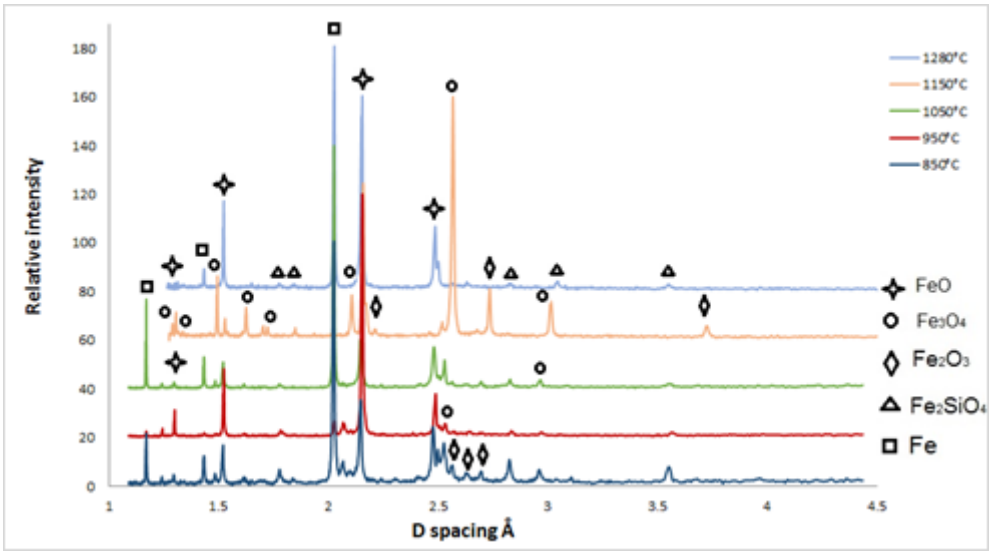

Figure 4.3.5 X-Ray diffraction patterns at the oxide-metal interface of rail specimens oxidised under an atmosphere containing 17% moisture for 60 minutes at various temperatures.

Figure 4.3.6 gives the XRD patterns of the DSP specimen's outer scales oxidised for 10 to 180 minutes at 1280°C under an atmosphere containing 17% of water vapour. X-ray diffraction patterns confirmed the presence of Wüstite, Magnetite and Hematite in all specimens. Fayalite peaks were only visible in the specimen oxidised for 180 minutes. The diffraction pattern changed by increasing the oxidation time, which was represented in the diffraction patterns as additional peaks developments along with deviations in peaks intensities.

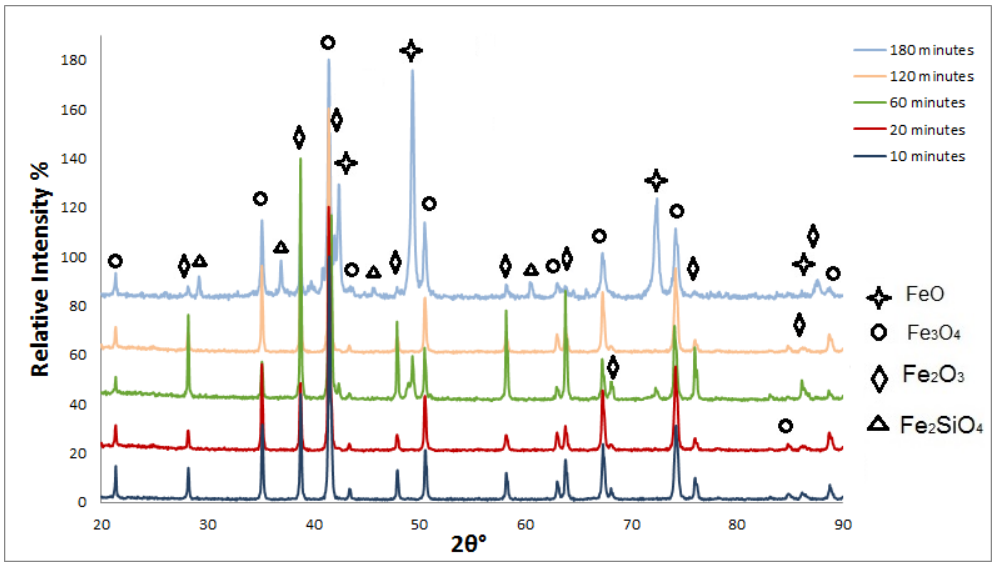

Figure 4.3.6 X-Ray diffraction patterns of the DSP outer scale specimens oxidised at 1150°C under an atmosphere containing 17% moisture.

The intensity variation of each specific peak at different oxidation condition was related to the amount of respective constituent within the oxide scale. The phase development variations during oxidation along with the effect of oxide thickness on heat transfer during the cooling stage governed the volume fraction of each phase.

Figure 4.3.7 shows the XRD patterns of the oxide-metal interface of the DSP samples oxidised between 10 to 180 minutes at 1150°C under an atmosphere containing 17% water. All three types of iron oxide, along with Fayalite and iron, were detected in all specimens. The presence of Magnetite and Hematite at the oxide-metal interface was related to the descaling practice. Increasing the thickness of Fayalite at the oxide-metal interface significantly influenced the descaling process. Fayalite layer was not entirely removed by manual descaling at room temperature as it strongly adhered to the substrate metal. Furthermore, the thickness of the Fayalite layer increased by extending the oxidation time. As a result, the amounts of the oxide residual increased at the oxide-metal interface in samples oxidised for longer.

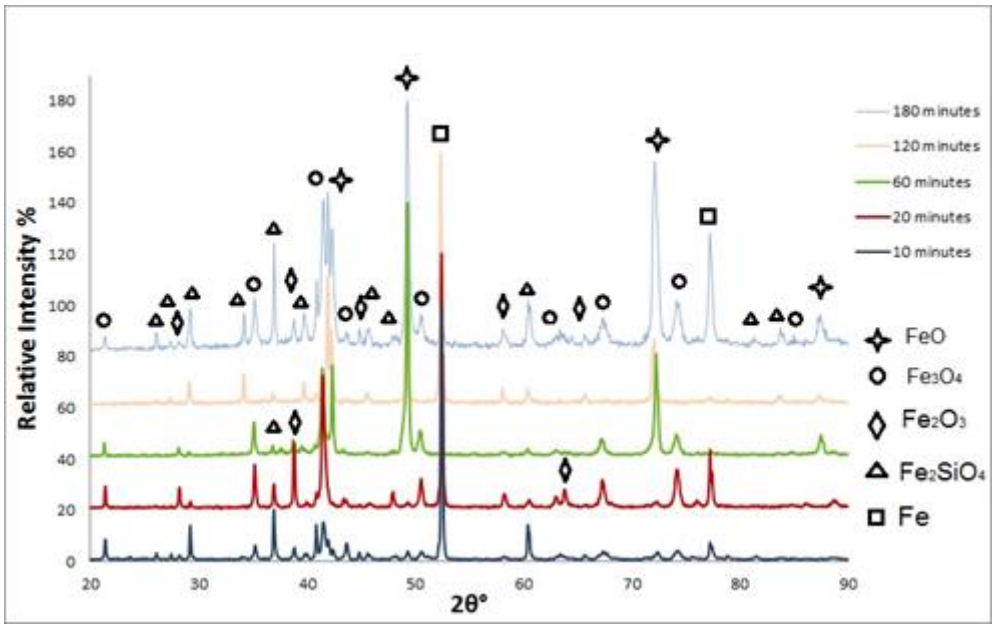

Figure 4.3.7 X-Ray diffraction patterns of the oxide-metal interface of DSP specimens oxidised at 1150°C under an atmosphere containing 17% moisture.

The X-ray diffraction patterns of DSP grade oxidised at 1150°C under dry atmosphere is given in Figure 4.3.8. Like the moist atmosphere, all three types of iron oxide were produced under the dry condition; however, the proportions of the constituents were different. Wüstite and

Fayalite were only detected in specimens oxidised for longer than 60 minutes, while a considerable amount of Hematite were detected in all samples. The highest peak in all specimens belonged to Magnetite.

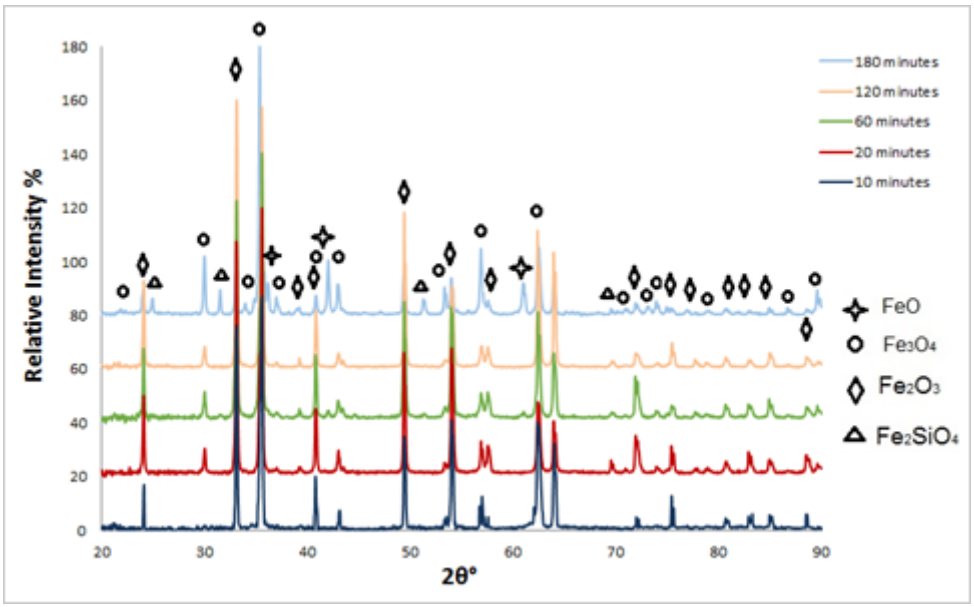

Figure 4.3.8 X-Ray diffraction patterns of the DSP outer scale specimens oxidised at 1150°C under dry gas.

The effect of oxidation temperature on oxide scale development of DSP steel under an atmosphere containing 17% of water vapour is shown in Figures 4.3.9 and 4.3.10. The scale diffraction patterns revealed that Hematite was the predominant phase in samples oxidised at 850°C and 1150°C conversely in oxidised samples at 950°C and 1050°C the largest oxide phase was Magnetite. A very small amount of Wüstite were detected in specimens oxidised for 850°C and 950°C. Fayalite was only detected in the oxide-metal interface regions of the samples oxidised for 1050°C and 1150°C.

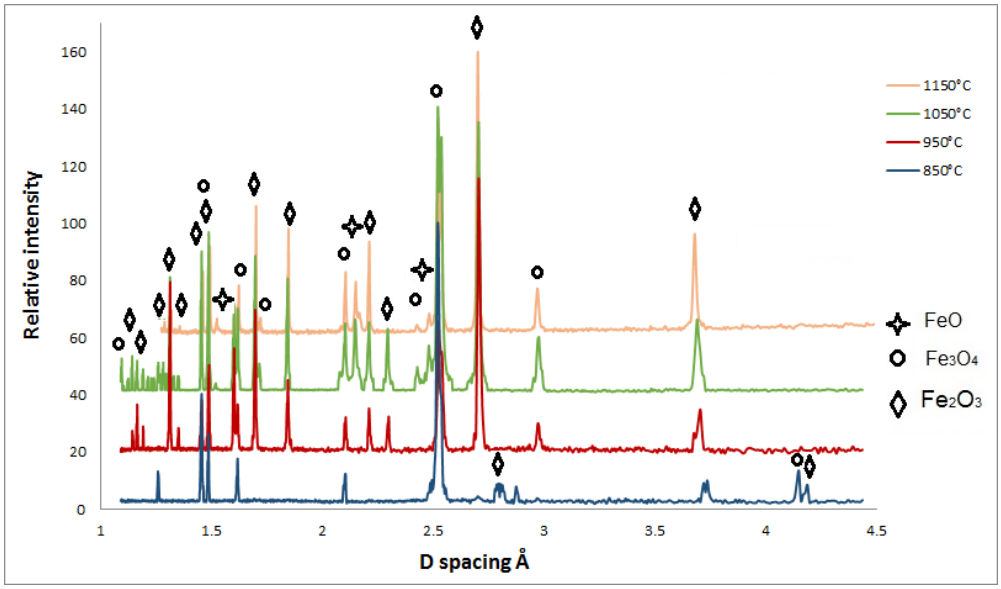

Figure 4.3.9 X-Ray diffraction patterns of the outer scale of the DSP specimens oxidised for 60 minutes at various temperatures.

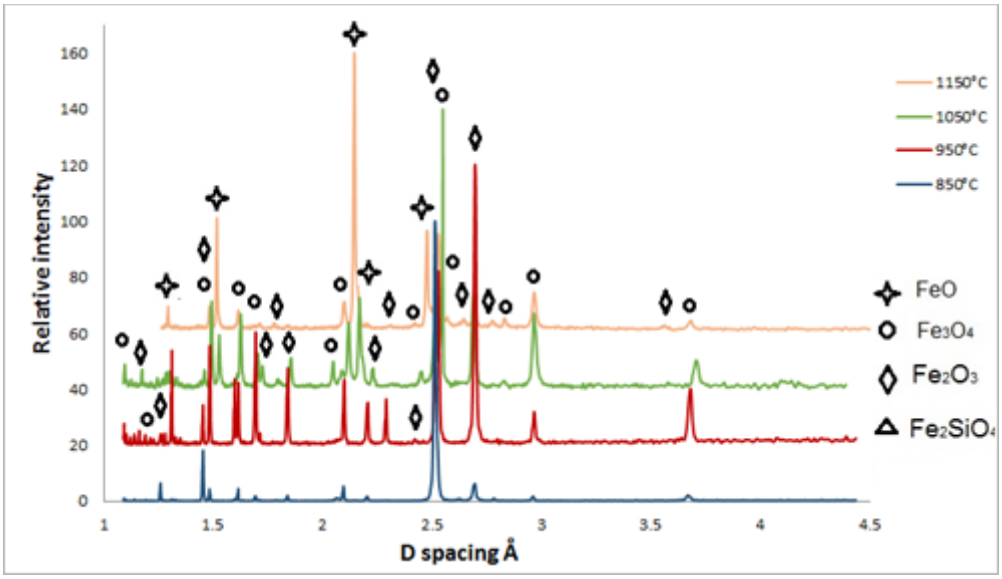

Figure 4.3.10 X-Ray diffraction patterns at the oxide-metal interface of the DSP specimens oxidised for 60 minutes at various temperatures.

4.4 Cross-sectional analysis

The microstructure and cross-sectional analysis of the oxide scales formed isothermally under different conditions are explained in this section. Optical, laser and electron microscopy techniques were used to study the characteristic zones of the oxide scale cross-section and oxide-metal interface. The examinations included chemical compositions analysis, volume fractions and distributions of all phases and assessing the oxide-metal interface roughness.

4.4.1 Cross-sectional analysis of rail steel samples

4.4.1.1 Oxidation under a humid atmosphere

Figure 4.4.1.1.1 shows the development of oxide scale in rail steel specimens for 10, 20, 30, 60, 120, and 180 minutes at 1280°C under an atmosphere containing 17% moisture. FeO, Fe_3O_4 were detected in all samples; however, the volume fractions of oxide phases varied under different oxidation conditions. Furthermore, Fayalite was detected in all oxidised specimens. The highest concentration of Fe_2SiO_4 phase was found next to the oxide-metal interface. Additionally, a small quantity of this phase elongated across the scale perpendicular to the substrate material that appeared as dark narrow lines in all images in Figure 4.4.1.1.1. As can be seen, dense thin oxide scales formed after 10 minutes of the oxidation. The scale thickness was homogeneous alongside the cross-section, and the deviations from the average did not exceed 8% at any point. The scale weakly bonded to the substrate by the development of a big separation gap alongside the oxide-metal interface. The specimen oxidised for 20 minutes showed a similar structure with additional oxide fragments along the oxide-metal interface. After 30 minutes of oxidation, a transition layer developed above the substrate metal. As oxidation extensively progressed, thick multilayer oxide scales with large pores and cavities developed. After 120 minutes within the healing layer, the number and size of pores and voids noticeably increased.

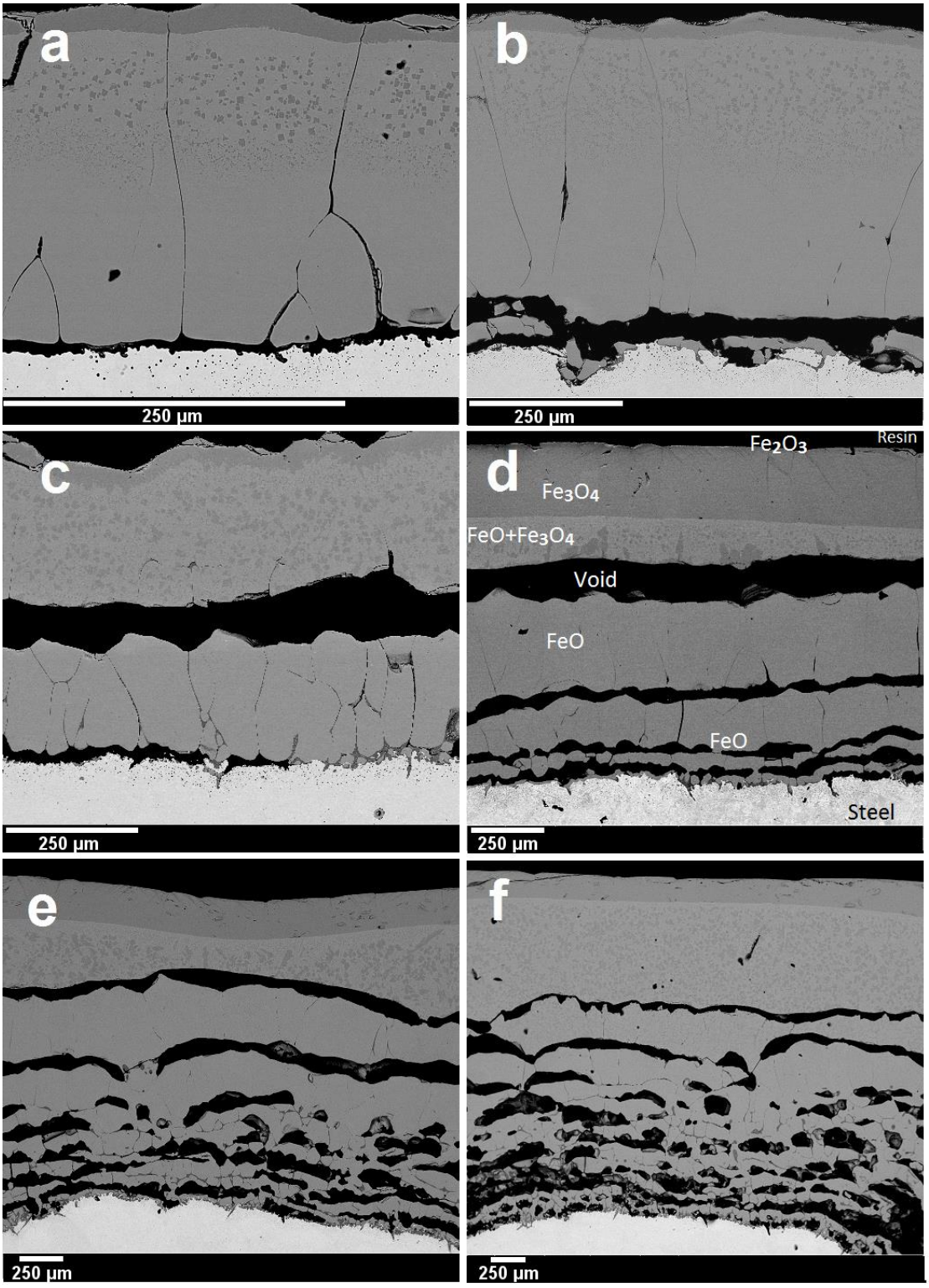

Figure 4.4.1.1.1 BSE images of rail specimens oxidised at 1280°C for:
a. 10min b. 20min c. 30min d. 60min e. 120min f. 180min

As shown in Figure 4.4.1.1.2, Wüstite was the predominant phase in all samples, however, as oxidation progressed the development of FeO gradually reduced and after 60 minutes, the slope of the curve almost flattened. Conversely, the development of Magnetite slowly

increased, and after 60 minutes, a flat trend line of Fe_3O_4 was apparent on the graph. As can be seen in Figure 4.4.1.1.3 up to 30 minutes of the development and growth rate of the defects were rapid. This was due to the fragmentation of the oxide scale from substrate metal. The rate of defect development gradually reduced. Increasing the oxidation duration enhanced the adherence of the oxide scale to the substrate metal. At the oxide-metal interface regions, external and internal oxidation simultaneously occurred. The thick multilayer oxide scales developed by external oxidation; in contrast, globular oxides developed within the substrate metal by diffusion of oxygen ions into the steel. Accordingly, nodular oxides penetrated the substrate metal, as shown in Figure 4.4.1.1.4.b.

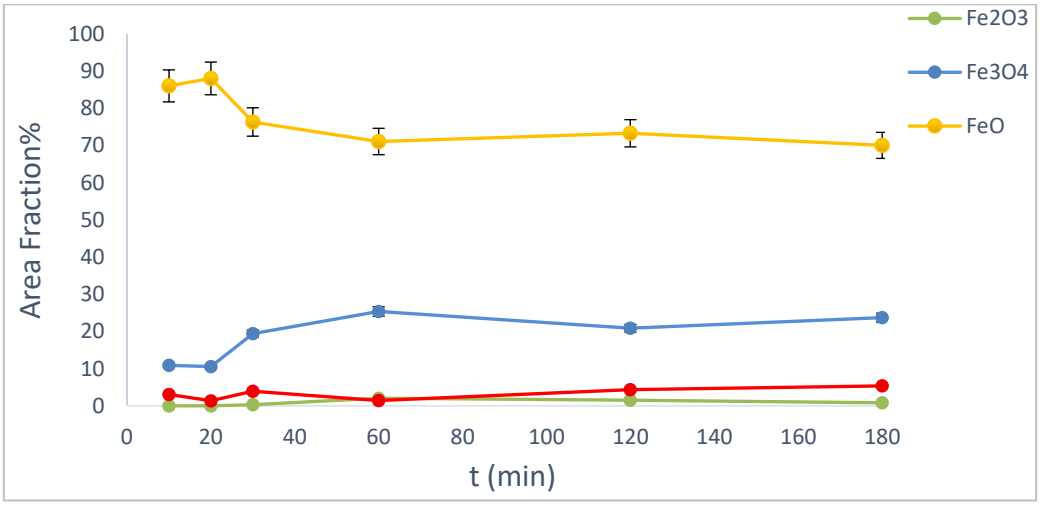

Figure 4.4.1.1.2 Relation between oxide compositions and time of rail steel oxidised at 1280°C under atmosphere contained 17% moisture.

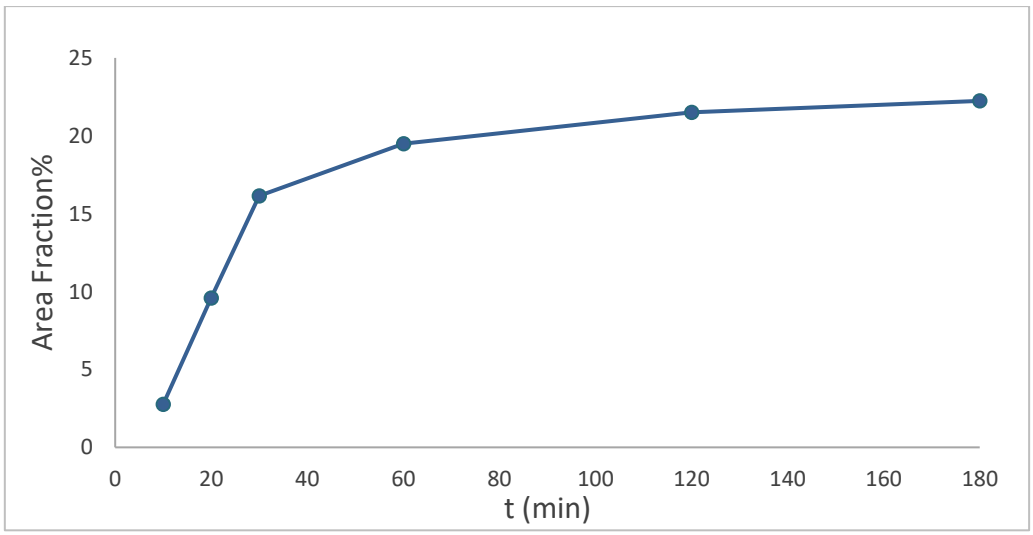

Figure 4.4.1.1.3 Relation between the amount of oxide scale defects and time of rail steel oxidised at 1280°C under atmosphere contained 17% moisture.

The EDX compositional point analysis of a rail specimen oxidised for 10 minutes at 1280°C under the moist condition as demonstrated in Figure 4.4.1.1.4. The structure of the scale was smooth free of any crack, porosity or blister. The examinations confirmed oxygen enrichment towards the surface of the oxide scale. The outer and inner segments were identified as Fe_3O_4 and FeO, respectively. Moreover, within the top region of the FeO segment, various precipitates of Fe_3O_4 formed. Among all oxidation products, Wüstite had the highest volume fraction. Although Fayalite mainly formed next to the oxide-metal interface, this phase also penetrated the oxide scale towards the surface in forms of narrow lines.

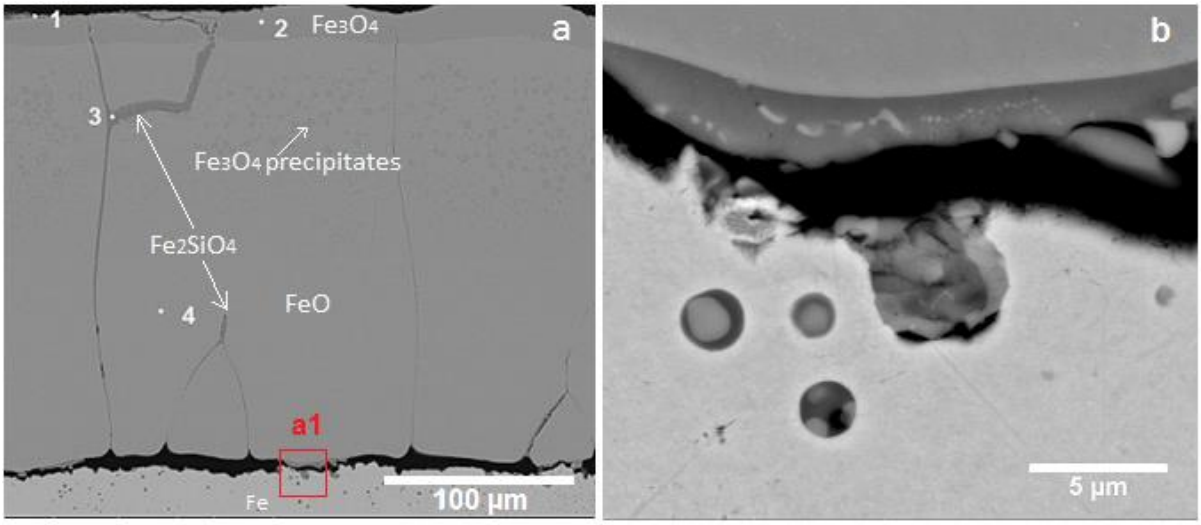

Point	At% Fe	O	Si
1	43.86	56.14	-
2	46.99	53.01	-
3	31.77	52.54	12.76
4	51.72	48.28	-

Figure 4.4.1.1.4 a. Chemical composition EDX point analysis of a rail specimen oxidised for 10 minutes at 1280°C and b. High magnification of zone a1 in image a.

Laser Raman Spectroscopy (LRS) used to examine the chemical compositions point analysis across the oxide layers. The characteristic peaks obtained in this research were compared with data reported in reference documents as summarised in Table 4.4. This method was complimentary to other characterisation techniques including SEM and XRD.

Table 4.4 Raman shifts (cm-1) for different types of oxide constituents

References	Fe_2O_3	FeO	Fe_3O_4	Fe_2SiO_4
75	290, 410, 505, 621, 670, 1320-1330	515, 650	540, 665	
76	220, 290, 410, 500, 610	660	310, 540, 670	810-40
77	220, 293, 410, 612		298, 533, 662	820

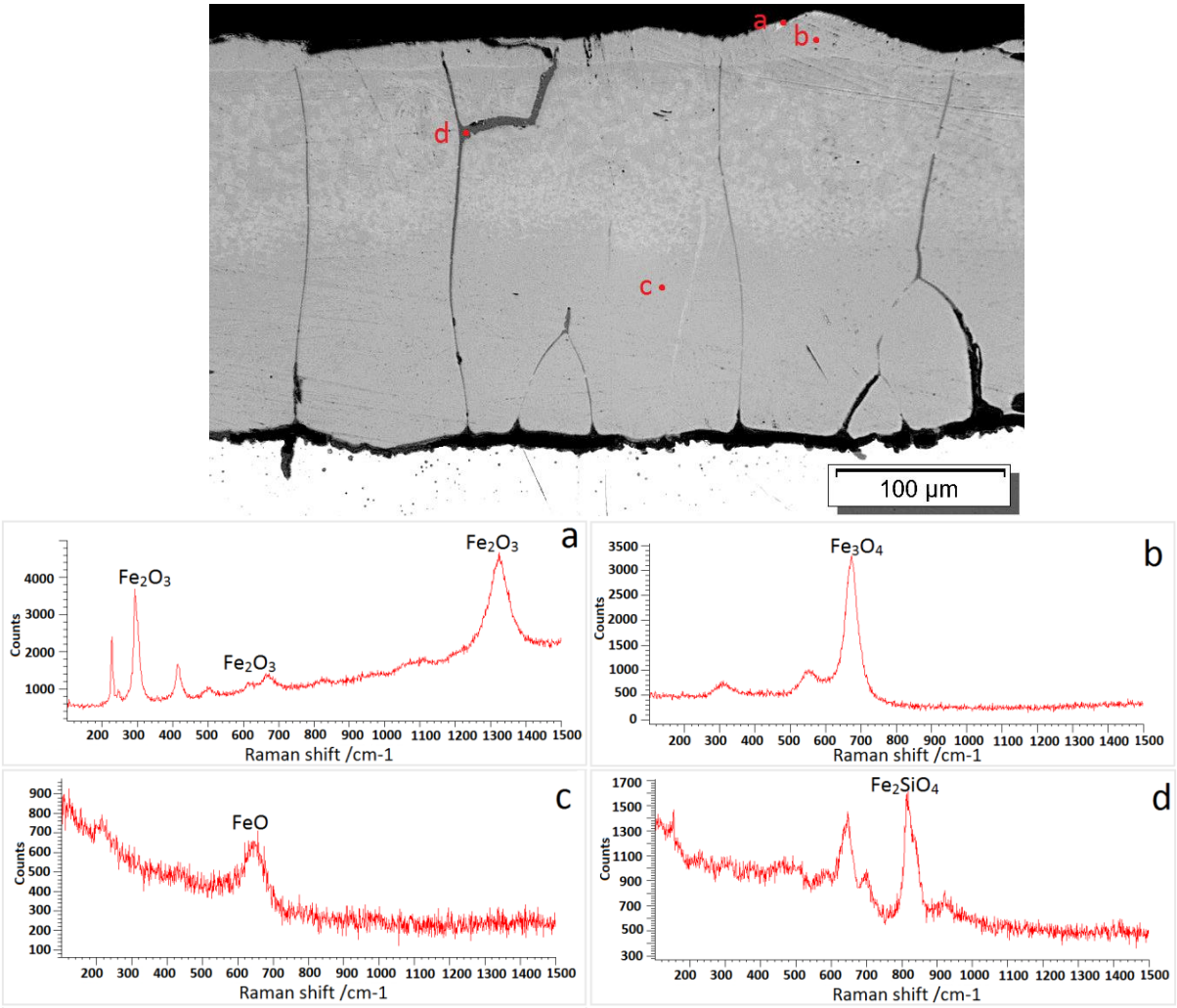

Figure 4.4.1.1.5 Optical image and Raman spectra of a rail specimen oxidised for 10 minutes at 1280°C under an atmosphere containing 17% moisture.

As demonstrated in Figure 4.4.1.1.5, the distinctive regions of the oxide scale of the rail steel sample oxidised for 10 minutes at 1280˚C under humid atmosphere were examined by LRS. The Raman spectrum of the spot (a) comprised peaks at 290, 410 and 1340 (cm^{-1}), which confirmed that the thin outermost layer to be Fe_2O_3. The detection of Raman peaks at 567 and 675 (cm^{-1}) during scanning of the spot (b) confirmed the phase identity as Magnetite. At point (c), a relatively short Raman peak at 656 (cm^{-1}) established the phase identity as FeO.

The distinctive Raman shift at 820 (cm^{-1}) confirmed the identity of Fayalite within the dark narrow transverse strands. Short peaks 656 and 675 (cm^{-1}) revealed that the dark transverse strands also contained small quantities of Wüstite and Magnetite.

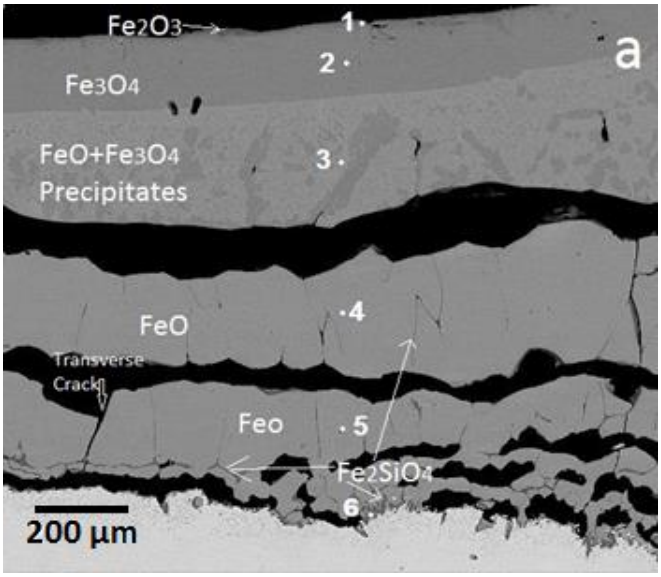

Point	At% Fe	O	Si
1	40.83	59.17	0
2	44.13	55.87	0
3	48.66	51.34	0
4	49.21	50.79	0
5	49.63	50.37	0
6	33.09	52.92	13.99

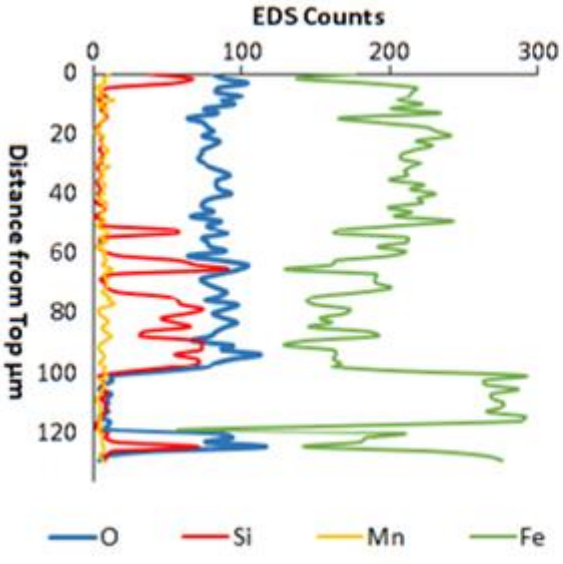

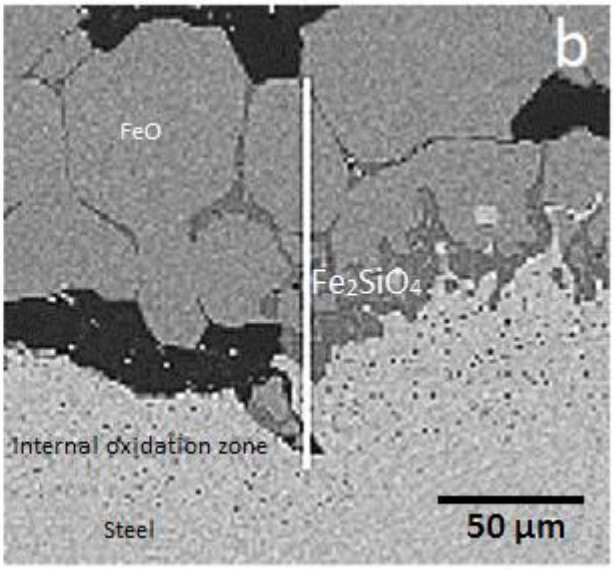

Figure 4.4.1.1.6 a. BSE image of rail specimen oxidised for 60 minutes at 1280°C including EDX point chemical composition analysis and b. Magnified oxide scale and oxide-metal interface around point 6, including the EDX line scan.

EDX point analysis of oxide scale of the rail steel specimen oxidised for 10 minutes at 1280°C under an atmosphere containing 17% moisture is demonstrated in Figure 4.4.1.1.6. Like the specimen oxidised for 10 minutes, the main oxidation product was Wüstite; however, FeO developed in forms of individual layers. The heterogeneous Magnetite precipitates were only visible in the top segment.

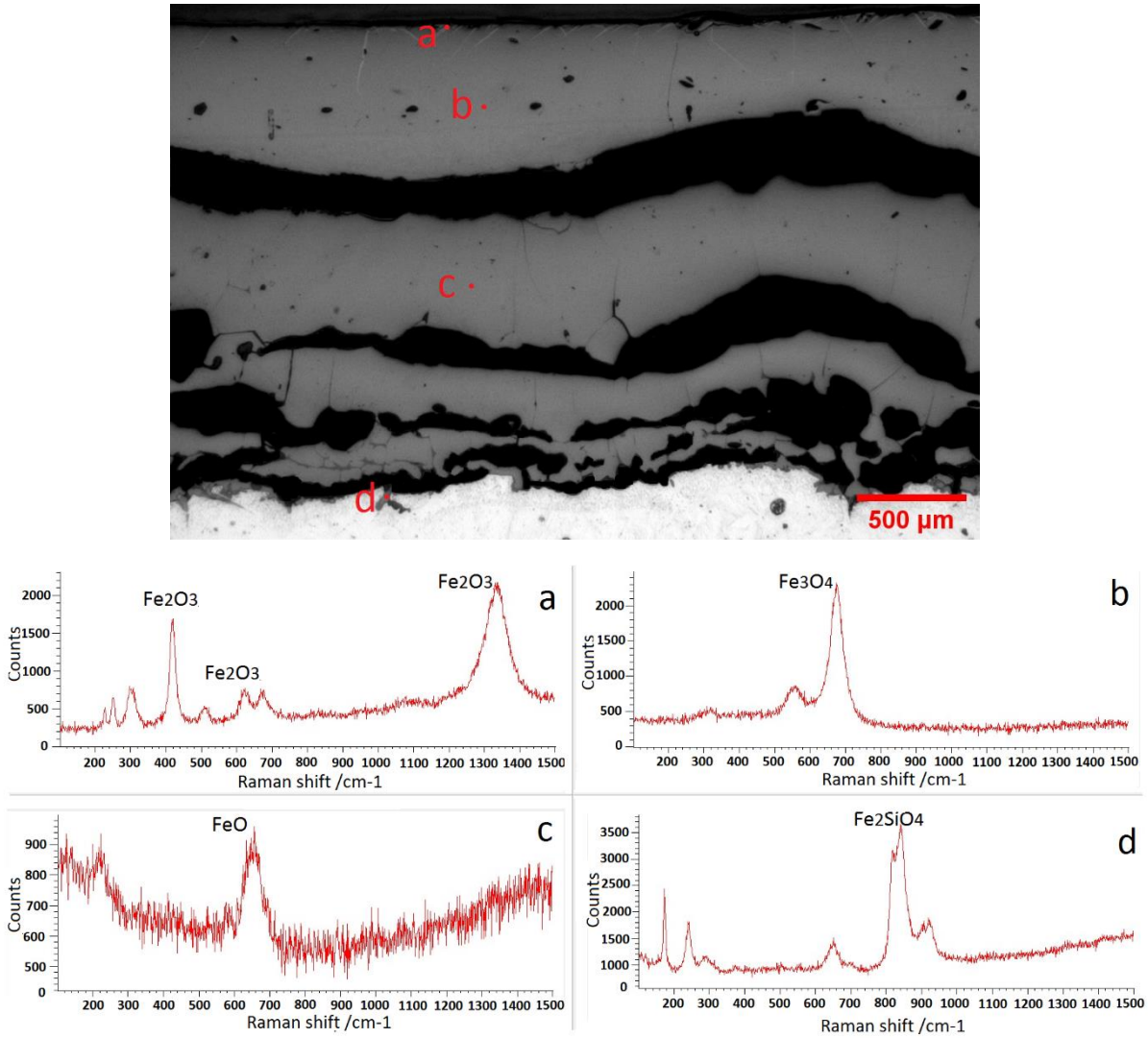

Figure 4.4.1.1.7 Optical image and Raman spectra from rail specimen oxidised for 60 minutes at 1280°C under an atmosphere containing 17% moisture.

The LRS analyses in four different locations of a rail steel specimen oxidised at 1280˚C for 60 minutes under humid condition are demonstrated in Figure 4.4.1.1.7. The peaks at and 1340 (cm^{-1}) confirmed the presence of Hematite at the edge of the oxide outermost layer (point a in the optical image). Magnetite was identified as the oxide constituent at point (b) by observing the Raman peaks at 567 and 675 (cm^{-1}). Furthermore, the mid layer (point c) was identified as Wüstite by the presence of a small peak at 656 (cm^{-1}). In the near-interface region (point d), the main peak at 842 (cm^{-1}) represented Fayalite. Besides, a small quantity of Wüstite was also visible.

The microstructure of the oxide scale in the near-interface region at higher magnification is shown in Figure 4.4.1.1.8. Considerable amounts of Fayalite developed at the oxide-metal

interface and inner oxidation zone simultaneously by inward diffusion of oxygen ions into substrate steel and outward diffusion of Si and Fe ions. As can be seen, fine Wüstite islands precipitated within the Fayalite matrix.

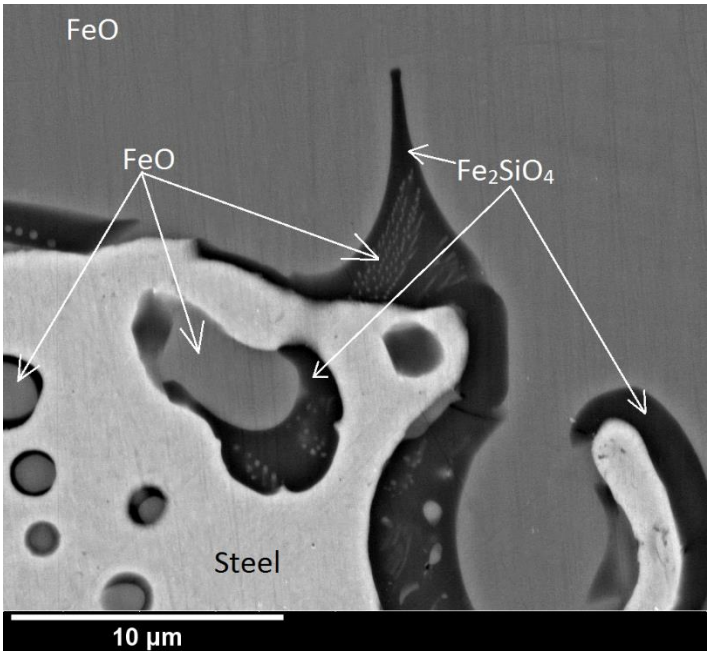

Figure 4.4.1.1.8 BSE image of the oxide-metal interface of a rail specimen oxidised for 60miutes at 1280°C.

Figure 4.4.1.1.9 demonstrates rail steel specimens oxidised for 10, 20, 30, 60, 120, and 180 minutes at 1150°C under an atmosphere containing 17% moisture. Multilayer oxides scales were observed in all rail specimens oxidised under condition 2. After 10 minutes of oxidation, the Magnetite precipitate zone detached from the Wüstite inner layer by the development of large cavities, however, as the oxidation period extended the size of the separation space reduced. All iron oxide constituents including Wüstite, Hematite and Magnetite along with Fayalite were detected in all specimens; however, the amount of each phase was governed by the oxidation time.

The image analysis confirmed that Wüstite was the predominant phase, and Magnetite was the second largest oxidation oxide constituent in all specimens, as shown in Figure 4.4.1.1.10. After 20 minutes of oxidation, the Magnetite precipitated zone and total the amount of FeO significantly expanded. Up to 30 minutes, the amount of Fe_3O_4 increased, but after that, the extent of this phase gradually decreased. The amount of developed Hematite was

insignificant in all specimens; nevertheless, the specimen oxidised for 30 minutes contained the highest percentage of this phase.

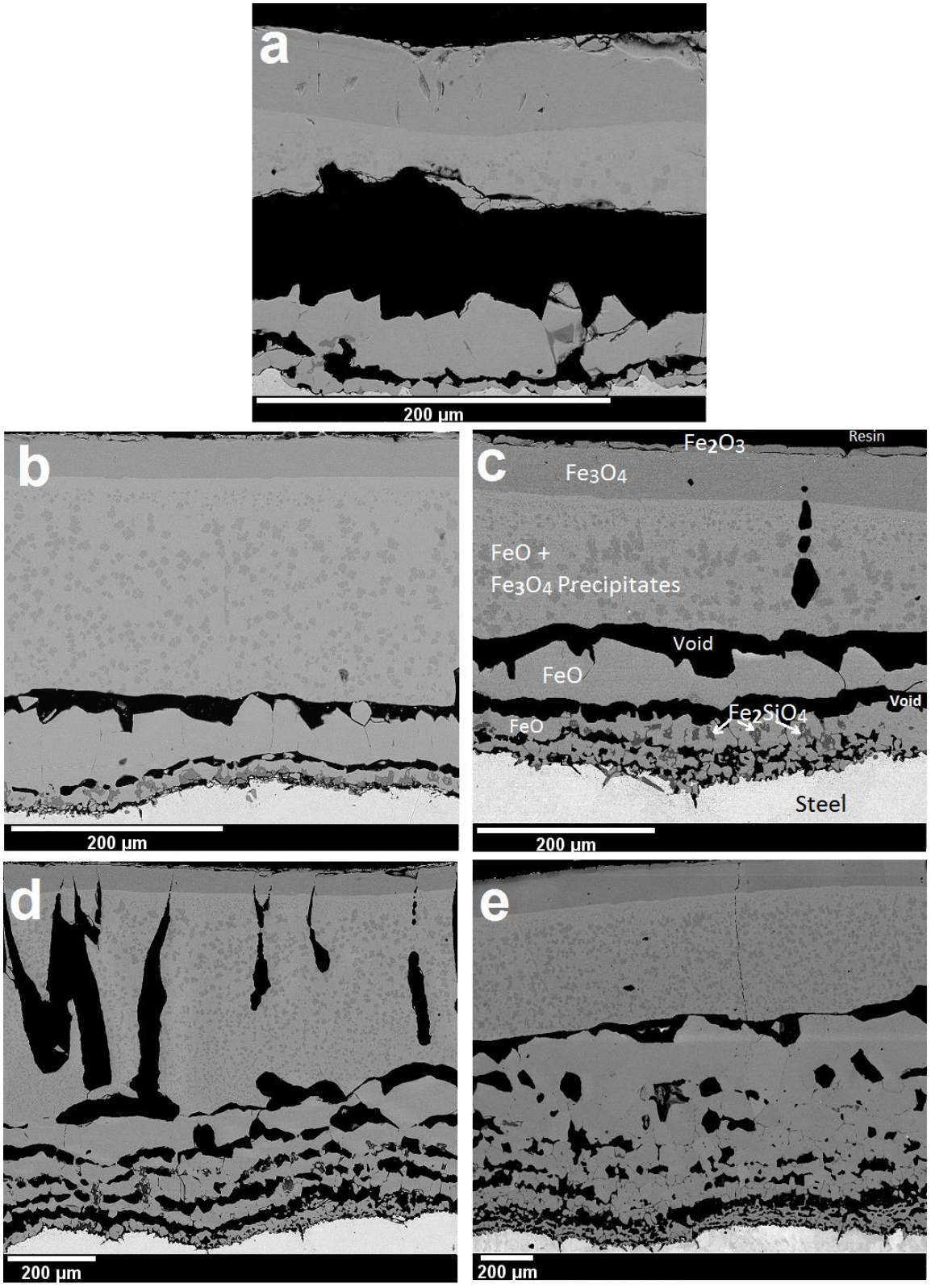

Figure 4.4.1.1.9 BSE images of rail specimens oxidised at 1150°C for
a. 10 min b. 20 min c. 30 min d. 60 min e. 180 min

Fe_2SiO_4 developed at the oxide-metal interface but unlike oxidation at 1280°C, across the oxide scale, no dispersion of this phase was apparent in any of the specimens. The proportion of Fayalite was almost similar among all samples. The presence of large elongated voids perpendicular to the oxide-metal interface were the distinguishing features of the specimen oxidised for 60 minutes.

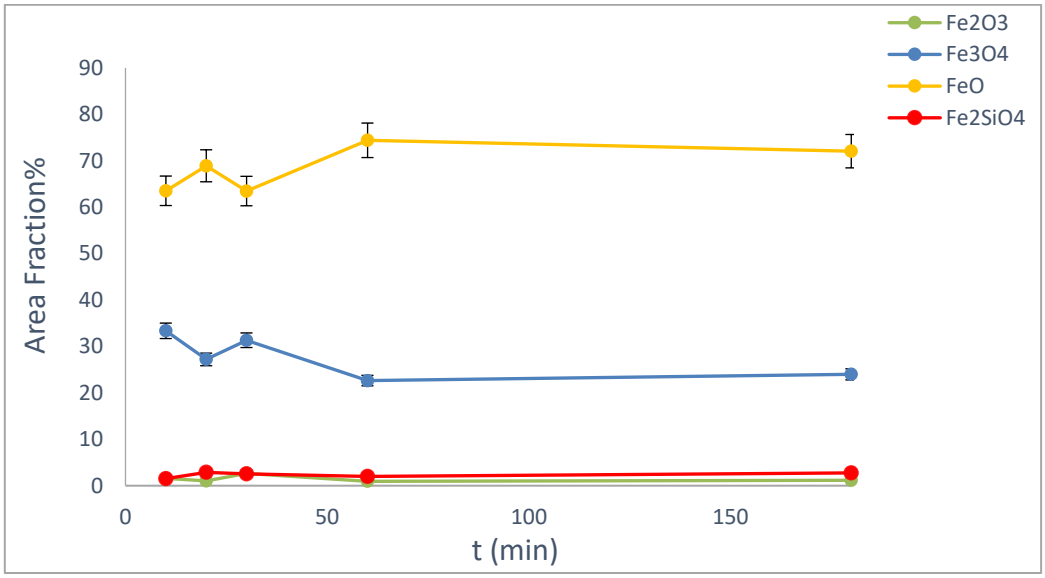

Figure 4.4.1.1.10 Relation between oxide compositions and time of rail steel oxidised at 1150°C under atmosphere contained 17% moisture.

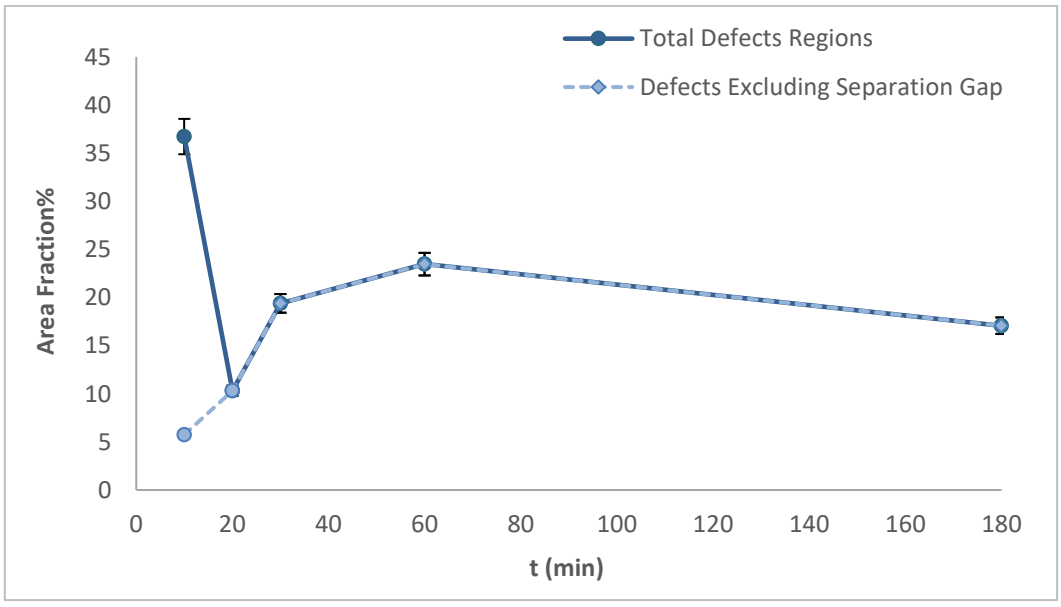

Figure 4.4.1.1.11 Relation between the amount of oxide scale defects and time of rail steel oxidised at 1150°C under atmosphere contained 17% moisture. Defects excluding large separation gap

As can be seen in Figure 4.4.1.1.11, the proportion of the cavities and porosities were plotted in forms two curves. The first plot generated based on the total area of cavities, including the large separation gap between external oxide scale and the oxide-metal interface (solid line). The relatively large separation gap was only apparent in the sample oxidised for 10 minutes. So, if the separation gap excluded from the calculation, the porosity and defects proportionally increased up to 60 minutes oxidation. However, the voids fraction reduced after 180 minutes of oxidation. In Figure 4.4.1.1.9.e a partial transverse crack was apparent at the outermost layer, which was possibly related to thermal shock during the cooling stage of the sample to the ambient temperature.

Figure 4.4.1.1.12 demonstrates the EDX chemical composition point measurements of the sample 4.4.1.1.9.b. The analysis confirmed that the scale enriched in Fe by moving towards the oxide-metal interface. Si enrichment was observed within the innermost layer adjacent to the substrate and no penetration of Fayalite into the outer oxide layers was apparent. Besides, the EDX point analyses revealed that the oxide scale next to the oxide-metal interface contained a small amount of manganese. Mn acts as a substitution for Fe atom in the development of iron oxide as explained earlier. After 20 minutes oxidation, the magnitude of the eutectoid layer, containing evenly dispersed Magnetite precipitates, vastly extended and accordingly the separation gap between the oxide's layers reduced.

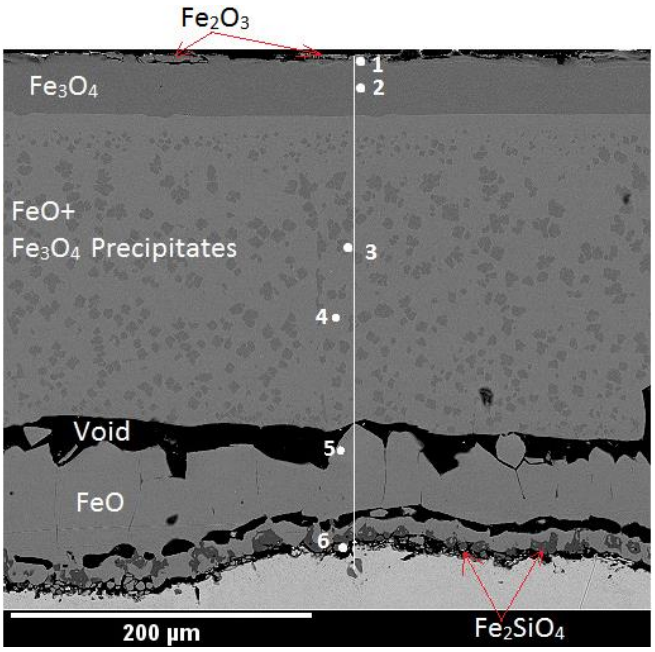

	At%			
Point	**Fe**	**O**	**Si**	**Mn**
1	39.28	60.72	-	-
2	43.71	56.29	-	-
3	43.96	56.04	-	-
4	48.47	51.53	-	-
5	49.46	50.54	-	-
6	27.31	55.88	15.35	1.46

Figure 4.4.1.1.12 Chemical composition point analysis of the rail specimen oxidised for 20 minutes at 1150°C.

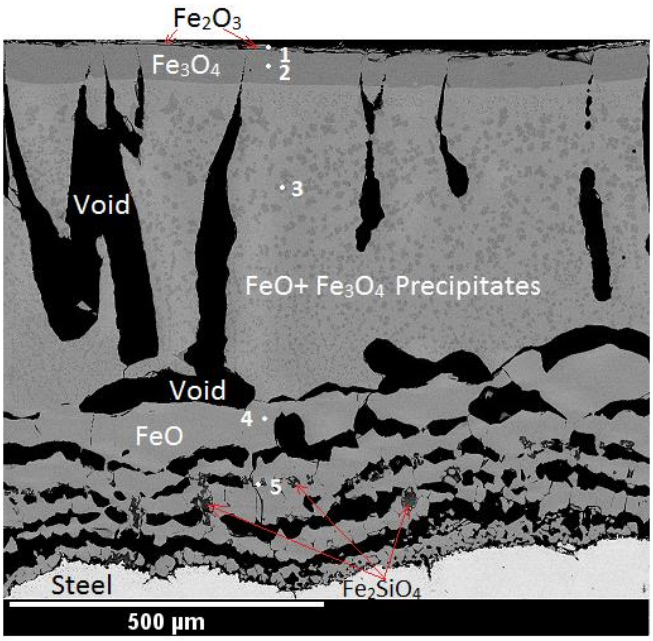

Point	At% Fe	O	Si	Mn
1	45.99	54.01	-	-
2	44.09	55.91	-	-
3	44.82	55.18	-	-
4	47.9	52.1	-	-
5	31.57	53.8	13.18	1.44

Figure 4.4.1.1.13 Chemical composition point analysis of the rail specimen oxidised for 60 minutes at 1150°C.

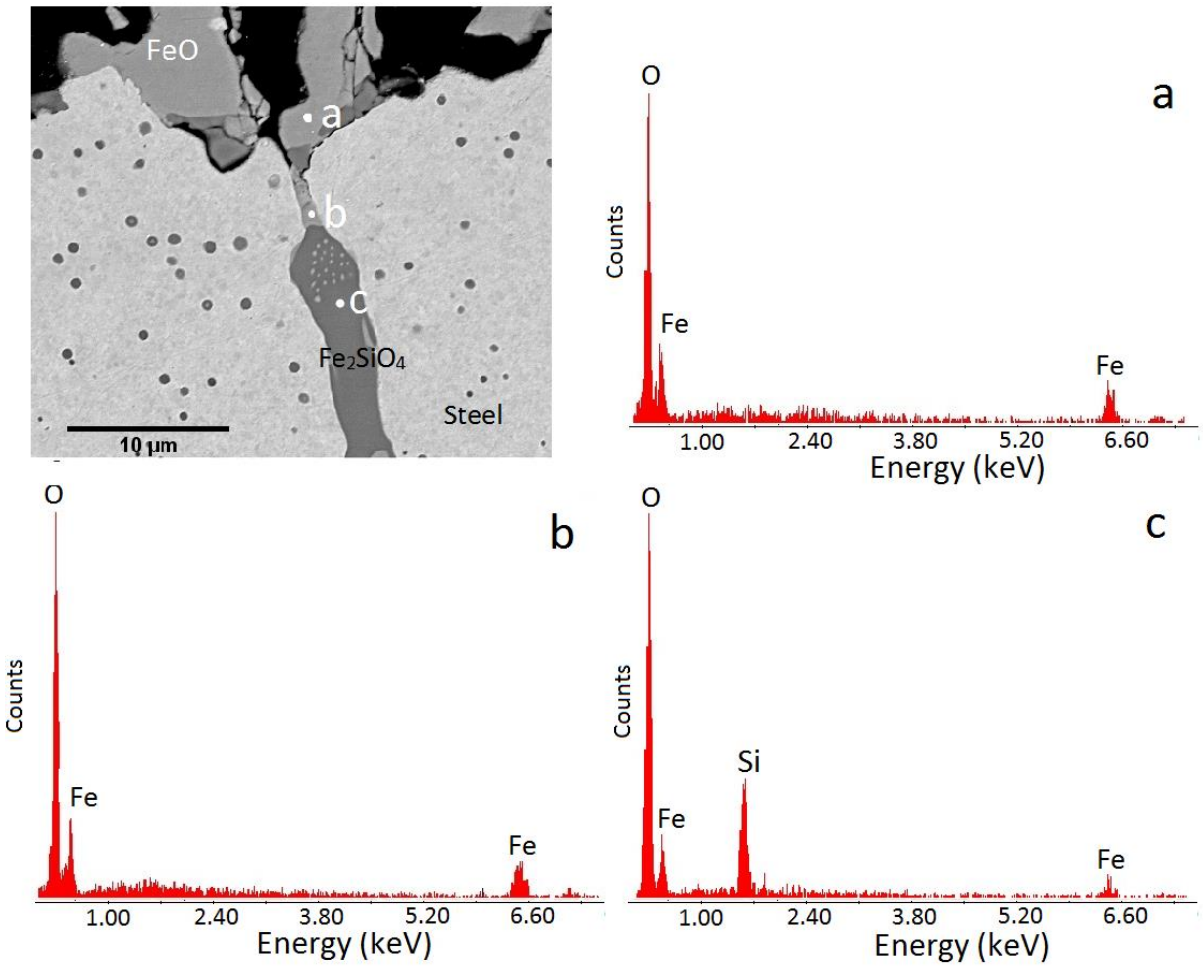

Figure 4.4.1.1.14 BSE image oxide-metal interface of rail specimen oxidised for 60 minutes at 1150°C.

The microstructure of the oxide scale distinctively transformed after 60 minutes of oxidation. The main oxide scale characteristic was the appearance of large elongated cavities within the precipitation zone perpendicular to the substrate metal and development of multilayer transitional zone, as shown in Figure 4.4.1.1.13. The EDX point analysis confirmed the high concentration of iron and silicon in near oxide-metal interface and oxygen enrichment at the scale outer region.

Internal oxidation simultaneously evolved in the near surface regions of the substrate steel alongside external oxidation by the dissolution of oxygen ions into the substrate metal. Globular and nodular oxide particles grew into the substrate metal in all specimens. The EDX point analysis confirmed that the nodular oxide features mainly contained Fayalite along with small quantities of Wüstite, as demonstrated in Figure 4.4.1.1.14.

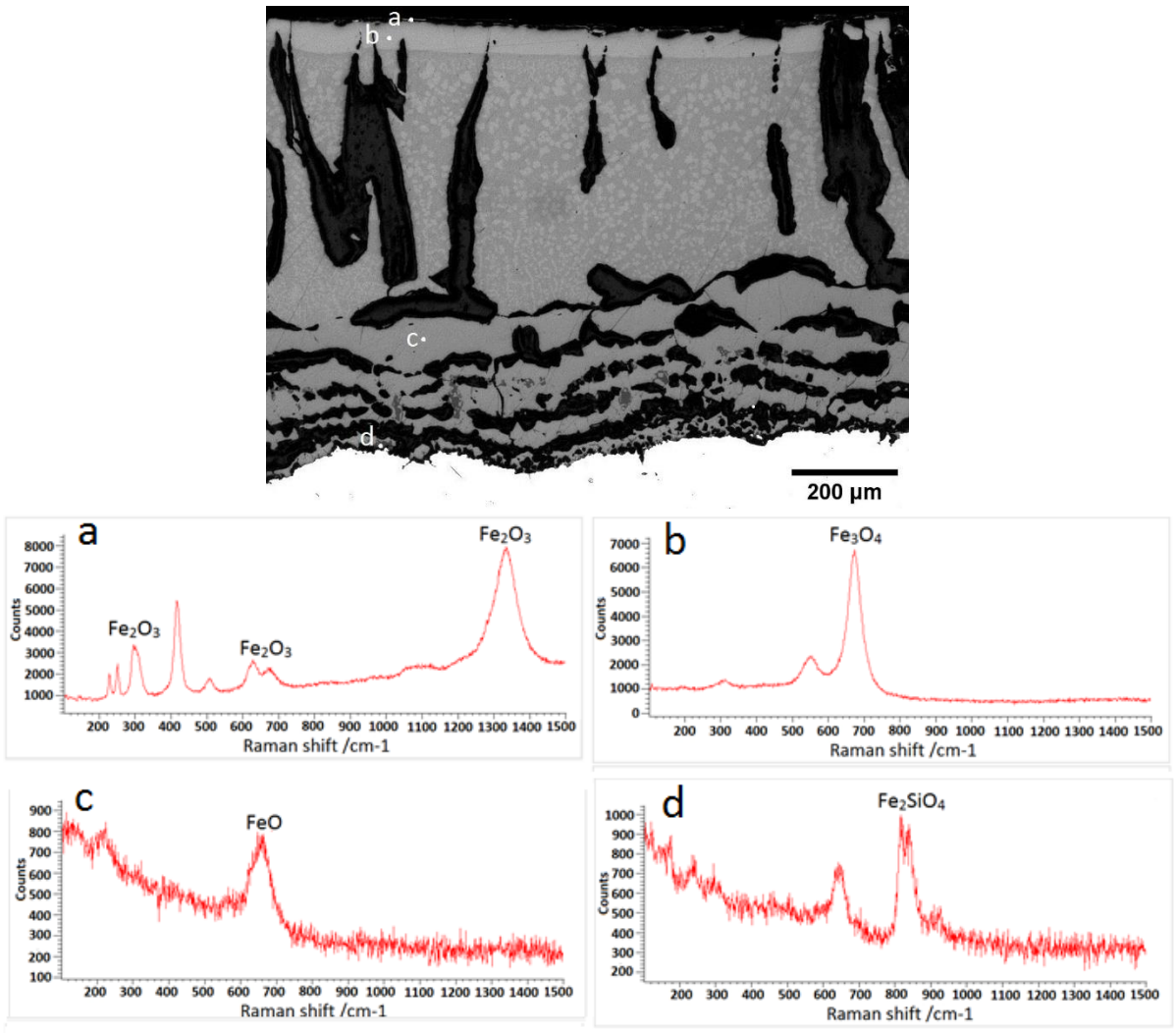

Figure 4.4.1.1.15 Optical image and Raman spectra from rail specimen oxidised for 60 minutes at 1150°C under an atmosphere containing 17% moisture.

As demonstrated in Figure 4.4.1.1.15, the LRS analysis identified the phase of the region around to be. The wide-ranging Raman shifts detected at 358, 410, 499, 621, 670 and 1340 (cm^{-1}) indicated small quantities of Hematite at point (a). The Raman peaks at 567 and 675 (cm^{-1}) confirmed that the band around point (b) to be Magnetite. The BSE, optical microscopy in association with LRS also revealed that the most predominant phase was FeO. Furthermore, at the oxide-metal interface, Fayalite and Wüstite were apparent (point d).

As demonstrated in Figure 4.4.1.1.16, the oxidation of rail steel at 1050°C for 60 minutes, led to the development of multilayer oxide scales. Like oxidation of the material at higher temperatures, Wüstite was the predominant phase; however, the amount of Hematite moderately increased. The Magnetite precipitated zone separated from the inner Wüstite layer by the development of a large longitudinal cavity. Most defects and voids developed within the inner oxide layers containing Fayalite and Wüstite. EDX chemical analysis revealed that the trends of oxygen and iron throughout the oxide scale were similar to the variations of these elements across the oxide scales formed at higher temperatures. Small quantities of Mn were also detected within the Fayalite phase.

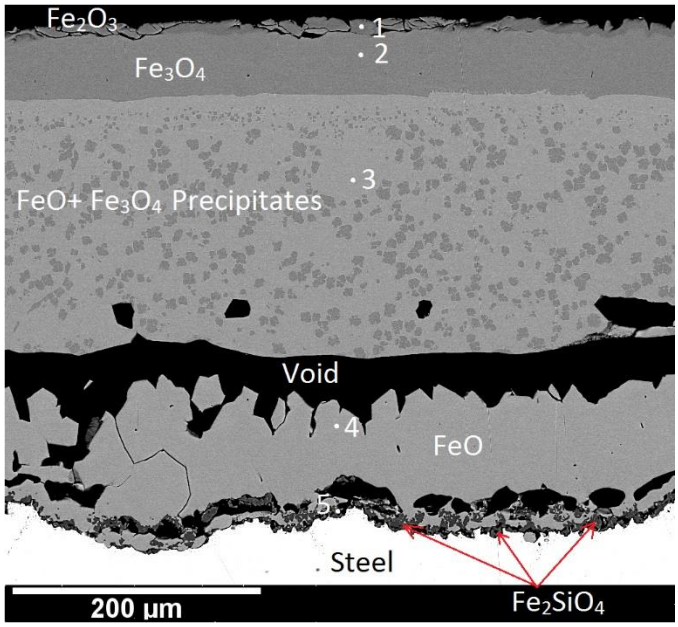

	At%			
Point	**Fe**	**O**	**Si**	**Mn**
1	39.44	60.56	-	-
2	43.8	56.2	-	-
3	49.13	50.87	-	-
4	49.32	50.68	-	-
5	31.23	50.8	16.5	1.45

Figure 4.4.1.1.16 BSE image of rail grade oxidised for 60 minutes at 1050°C and EDX point analysis.

In the oxidation of the rail steel at 950°C, the microstructural characteristics were comparable to the sample oxidised at 1050°C. The multilayer oxide scale contained all three types of iron oxide, and Fayalite, including a large Wüstite zone, containing frequent Magnetite precipitates. As can be seen in Figure 4.4.1.1.17 and 4.4.1.1.18 continuous layer of Fayalite developed at the oxide-metal interface. Like the previous condition, a large longitudinal gap separated the outer layers from the adhered inner layers. Conversely, the size and the number of scattered voids and defects reduced across the oxide scale.

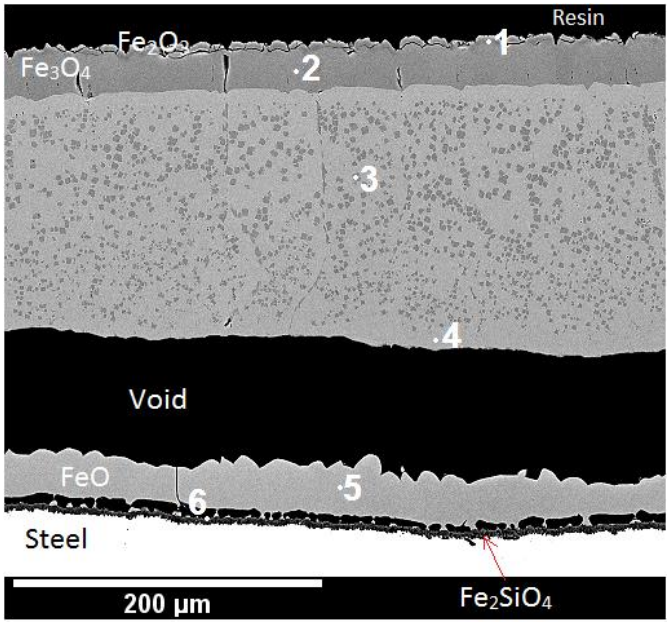

	At%			
Point	**Fe**	**O**	**Si**	**Mn**
1	39.69	60.31	-	-
2	43.75	56.25	-	-
3	45.65	54.35	-	-
4	50.44	49.56	-	-
5	49.59	50.41	-	-
6	27.55	54.88	16.18	1.4

Figure 4.4.1.1.17 BSE image of rail grade sample oxidised for 60 minutes at 950°C and EDX point analysis.

The EDX line scan (Figure 4.4.1.1.18) indicated that the oxygen concentration slightly reduced by moving towards the oxide-metal interface. In addition, a slight rise in Mn EDX trend line confirmed the presence of this element within the Fayalite layer.

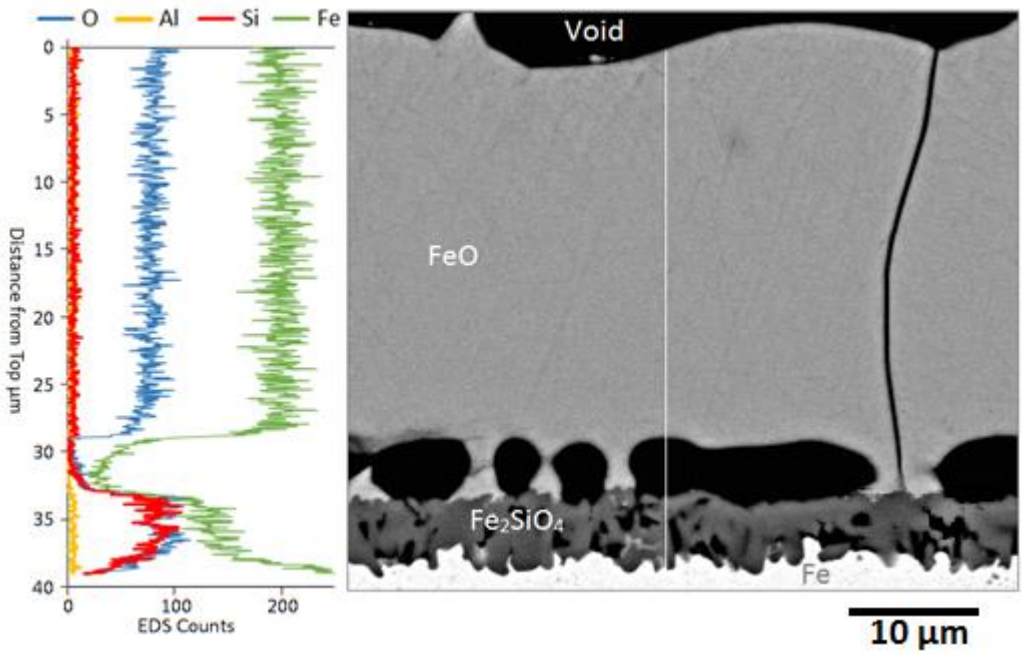

Figure 4.4.1.1.18 BSE image of the oxide-metal interface of rail specimen oxidised for 60 minutes at 950°C including EDX line scan.

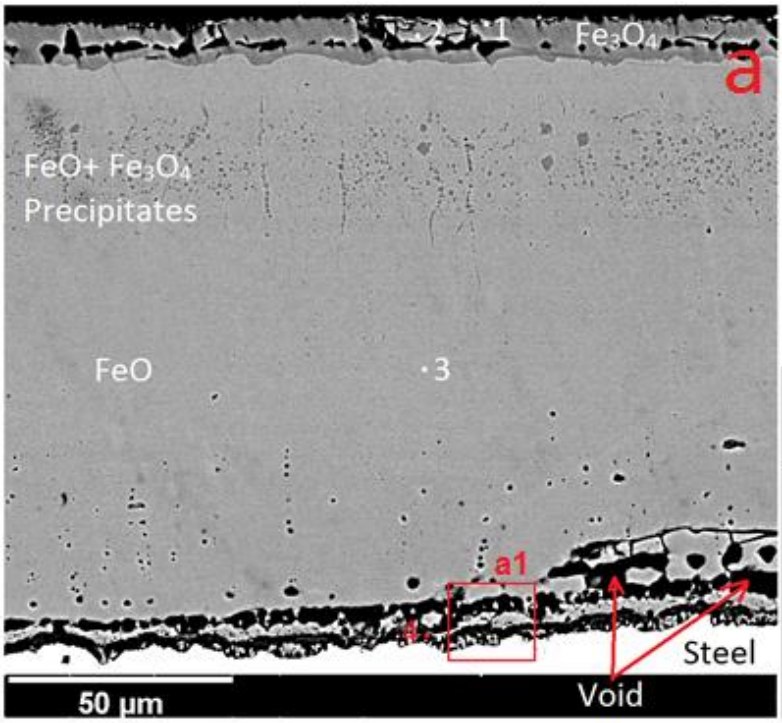

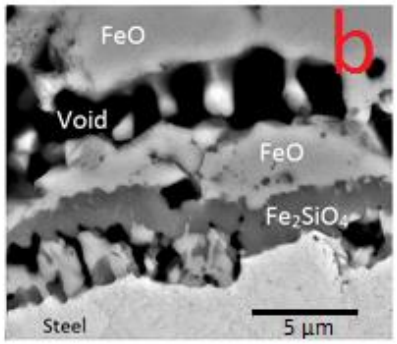

	At%			
Point	Fe	O	Si	Mn
1	41.67	58.33	-	-
2	44.41	55.59	-	-
3	51.23	48.77	-	-
4	30.51	52.29	16.15	1.06

Figure 4.4.1.1.19 a. BSE image of a rail sample oxidised for 60 minutes at 850°C including EDX chemical composition point measurements and b. Magnified oxide scale and oxide-metal interface at zone a1 in the image a.

In the rail steel sample oxidised at 850°C (Figure4.4.1.1.19), the microstructure of the oxide scale was noticeably different in comparison to oxidation at higher temperatures. The oxide developed in the form of a single continuous scale without the growth of any big voids. Most

defects were concentrated at the top scale within the Magnetite phase and around the bottom of the Wüstite segment near the oxide-metal interface. All constituents of iron oxides were detected; however, the extent of Wüstite vastly increased. Contrary the development of Hematite was insignificant. Furthermore, the extent of Magnetite precipitates within the Wüstite matrix considerably reduced. Like the oxidation at higher temperatures, a small amount of Mn detected within the Fayalite phase in the near oxide-metal interface.

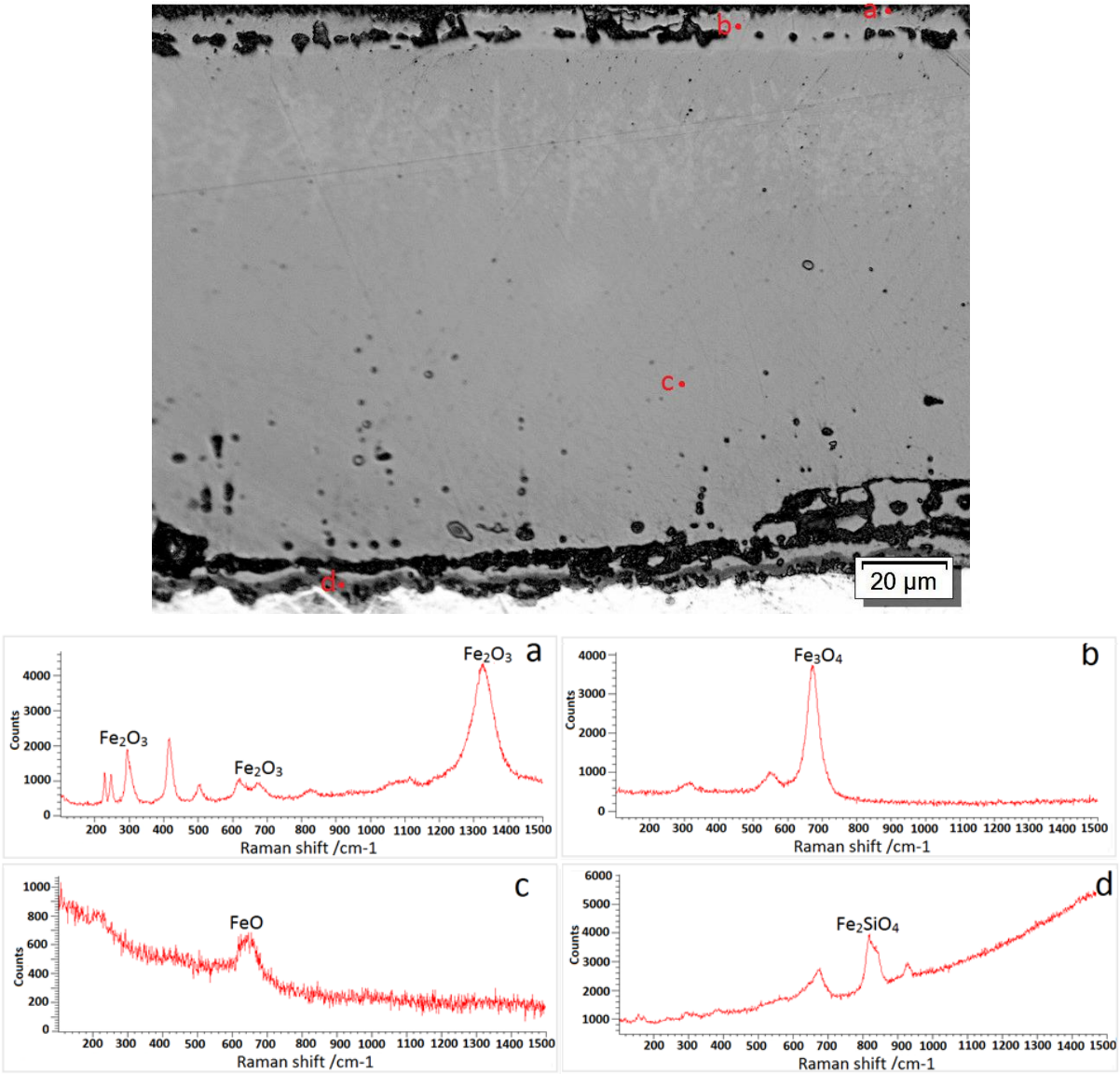

Figure 4.4.1.1.20 Optical image and Raman spectra of a rail specimen oxidised for 60 minutes at 850°C under an atmosphere containing 17% moisture.

The LRS analysis of the rail sample oxidised at 850°C confirmed the presence of all iron oxide phases within the external oxide layer along with Fayalite at the oxide-metal interface. The scan of regions near the external surface of the oxide scale (point a) confirmed that like previous oxidation conditions, the small quantity of Hematite was evident. As demon stared in BSE and optical images, a narrow layer of Magnetite was detected next to the external beneath the Hematite phase. As can be seen, the LRS peak of point (c) confirmed that the Wüstite was the predominant phase. Like oxidation at higher temperatures, a thin layer of Fayalite was detected at the oxide-metal interface.

Figure 4.4.1.1.21 summarised the variation of the area fraction of each oxide phase against the process temperatures for rail specimens oxidised for 60 minutes under a humid atmosphere. It was clear that Wüstite was the predominant phase in all temperatures; however, the highest percentage of this phase was measured at 850°C. As can be seen, the proportions of all the phases were almost constant for oxidation above 950°C. Furthermore, Magnetite was the second largest oxide constituent, and the amounts of Hematite and Fayalite were inconsequential in comparison to FeO and Fe_3O_4.

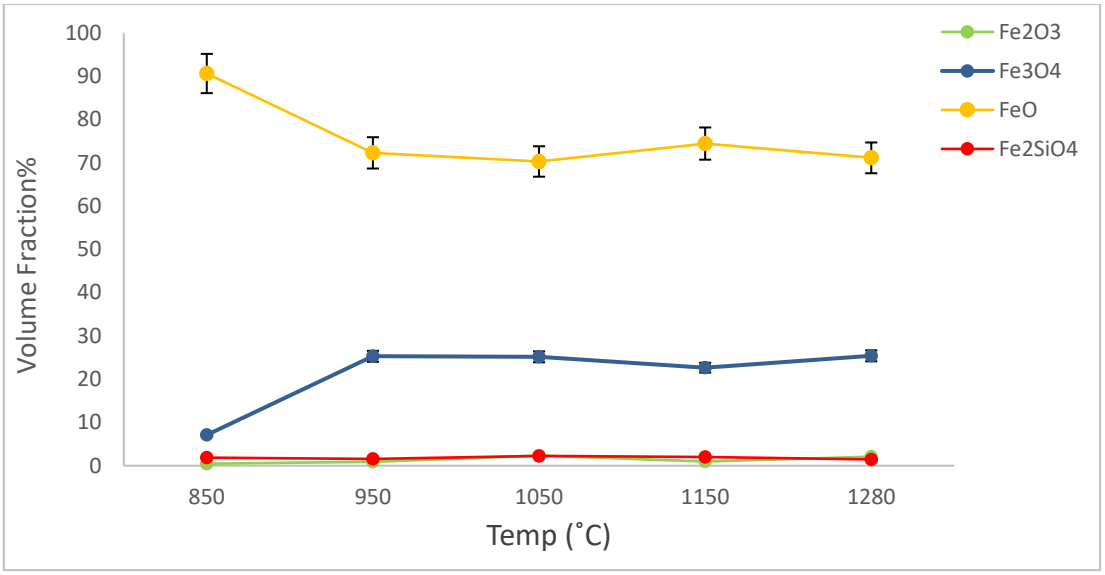

Figure 4.4.1.1.21 Relation between oxide scales compositions and oxidation temperatures of rail steel specimens oxidised for 60 minutes under atmosphere contained 17% moisture.

The relation between oxide defects regions and oxidation temperature of rail steel are demonstrated in Figure 4.4.1.1.22. The proportions were plotted in two different manners. Initially, the overall percentage of the region of the defect was measured, which was plotted as a solid line. This curve revealed that the highest number of defects was generated at 950°C

when the separation gap was included in the calculations. The large gap formed between the external oxide layer and the residual scale on the oxide-metal interface. In contrast, the lowest fraction of the defects was apparent in the oxidation of the material at 850°C.

On the other hand, when the separation gap was excluded from the calculation of the defective regions, the characteristics of the curve entirely transformed (dashed line). It was clear that the highest amount of defective region belonged to the sample oxidised at 1150°C and the lowest level of cavities were observed on the sample oxidised for 950°C.

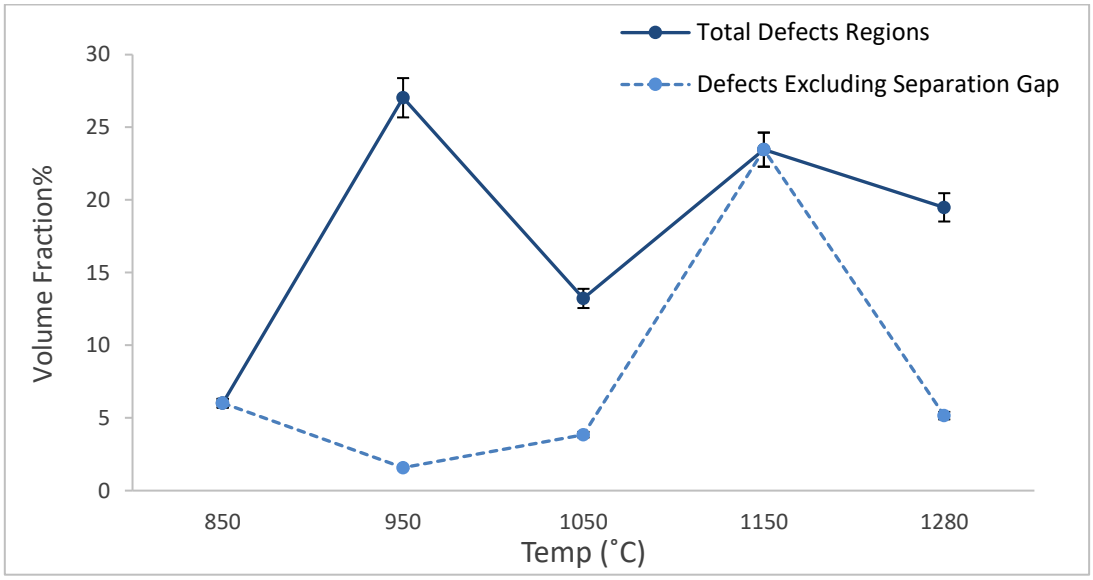

Figure 4.4.1.1.22 Relation between oxide scales defects percentage and oxidation temperatures of rail steel specimens oxidised for 60 minutes under atmosphere contained 17% moisture.

4.4.1.2 Oxidation under a dry atmosphere

The rail grade oxidised under a dry condition at 1280°C to evaluate the effect of the dry atmosphere on the oxide development, as explained in section 3.1. In comparison to oxidation under the moist condition, the oxidation rate drastically reduced, and the microstructure of the oxide scale vastly differed. In the sample oxidised for 10 minutes continues oxide scales detached from substrate metal and only small isolated oxide particles adhered to the parent material. Wüstite had the highest volume fraction amongst all oxidation products. On the top region of the scale, a thin layer of Hematite was detected, and beneath this phase, a distinctive Magnetite phased was observed. Also, relatively large Magnetite precipitates were scattered across the FeO matrix. At variance with oxidation in humid condition, Fayalite did not penetrate the outer scale at any point. However, a small

amount of this phase developed at the surface of the metal substrate and within the internal oxidation zone. As can be noticed in Figure 4.4.1.2.1.a the highest number of defects and cracks were apparent within the upper segment of the oxide scale. Also, a through thickness crack was evident across the scale.

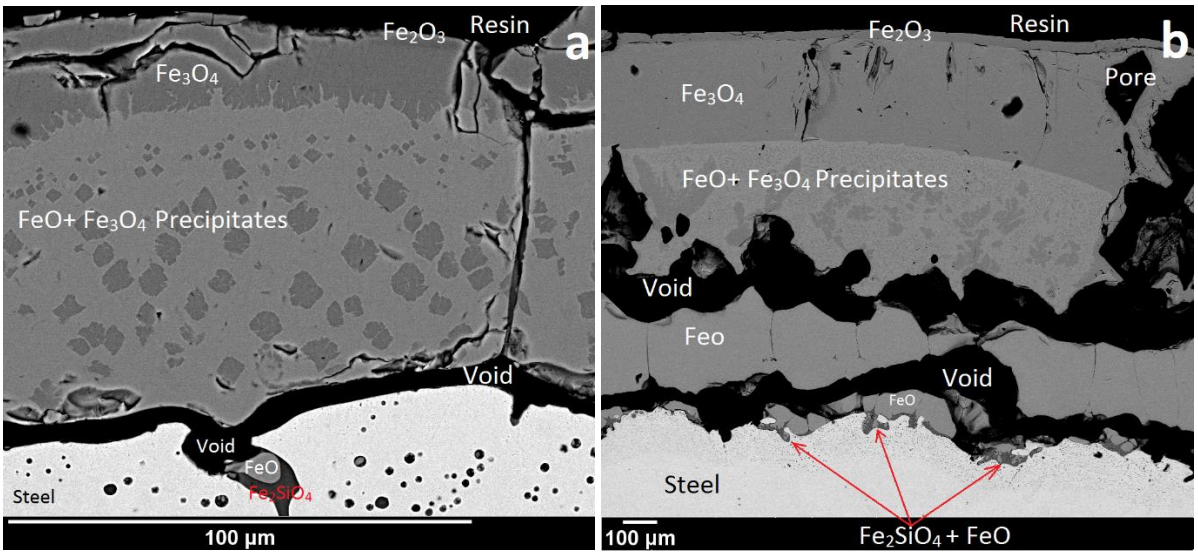

Figure 4.4.1.2.1 BSE image of rail specimens oxidised under dry atmosphere at 1280°C for:
a. 10 minutes b. 180 minutes

After 180 minutes of oxidation under dry condition, multilayer oxide scales formed. The oxide scales divided into two individual segments by the development of a big gap. The lower segment also detached from substrate metal. As shown in Figure 4.4.1.2.1.b, the extent of Magnetite phase drastically increased, whereas the scope of the precipitation zone and Wüstite reduced. Furthermore, the quantity of Hematite augmented on the top segment of the oxide scale and big voids and cavities shaped across the outer oxide layer. The other characteristic feature was partial penetration of Fayalite into the inner oxide layer.

The LRS was used to confirm the phase identity of the oxide scale produced under dry condition. As can be seen in Figure 4.4.1.2.2, the Raman spectra of the point (a) indicated that the thin Hematite layer was present at the top of the rail steel sample oxidised for 60 minutes. The scan of the point (b) confirmed the wide layer beneath the Fe_2O_3 to be Magnetite. The assessments of points (c) and (d) confirmed the layer adjacent to substrate metal consisted of Wüstite and Fayalite.

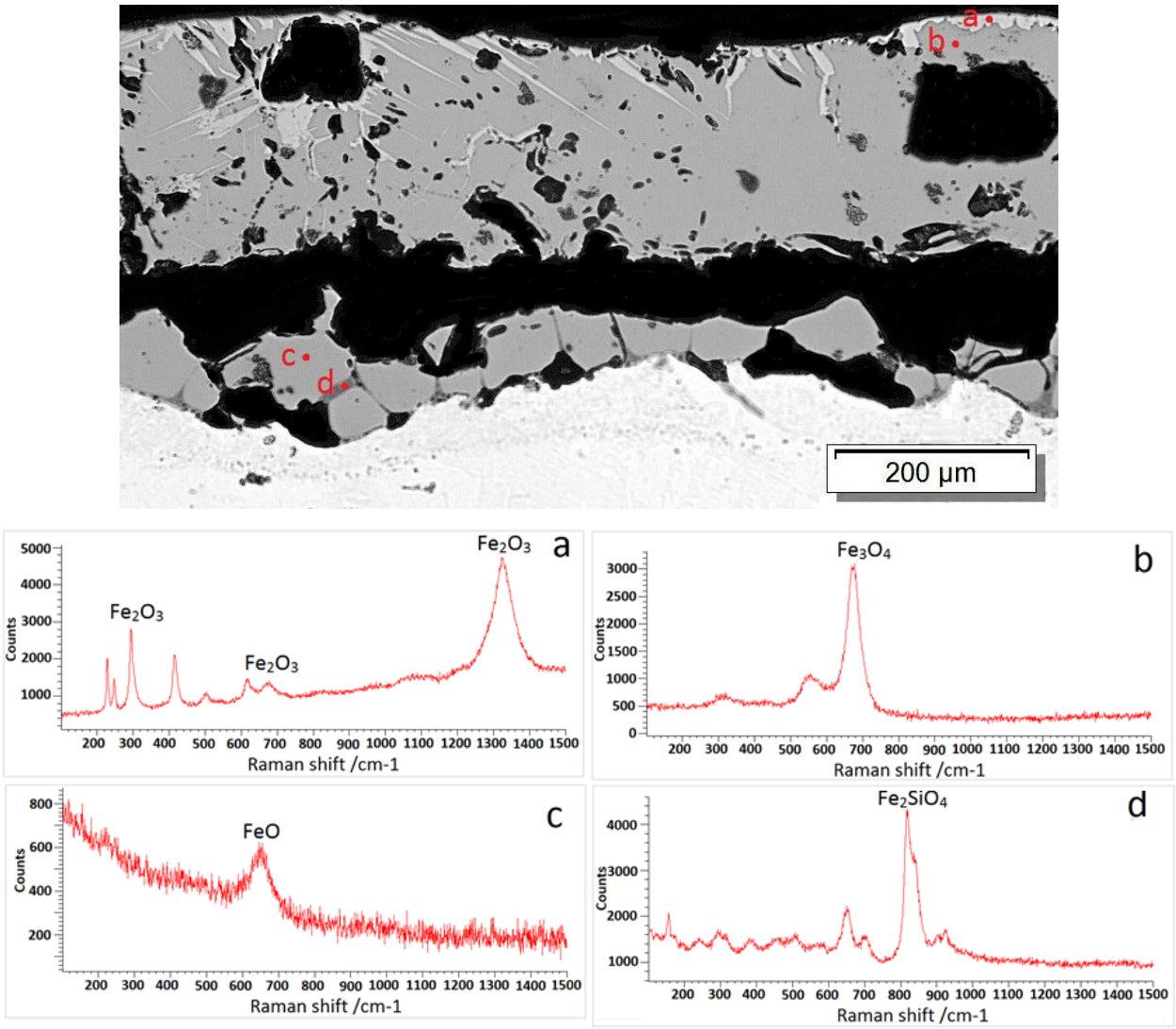

Figure 4.4.1.2.2 Optical image and Raman spectra from rail specimen oxidised for 60 minutes at 1280°C under a dry atmosphere.

4.4.2 Cross-sectional analysis of DSP steel samples

4.4.2.1 Oxidation under a humid atmosphere

The BSE cross-sectional images of DSP steel specimens oxidised for 10, 20, 30 and 60 minutes at 1280°C under an atmosphere containing 17% moisture are demonstrated in Figure 4.4.2.1.1. As can be seen, uniform dense oxide scales developed throughout the oxidation. In all specimens, the scale mainly contained FeO along with a narrow layer of Fe_3O_4 at the top. The precipitation of Magnetite was limited to the small area within the upper region of Wüstite. Moreover, a considerable amount of Fe_2SiO_4 developed at the oxide-metal interface. The Fayalite phase penetrated the Wüstite in forms of dendrites, continuous transverse lines and isolated globular particles. Eutectic liquid metal drips dispersed at the bottom of the oxide scale next to the oxide-metal interface.

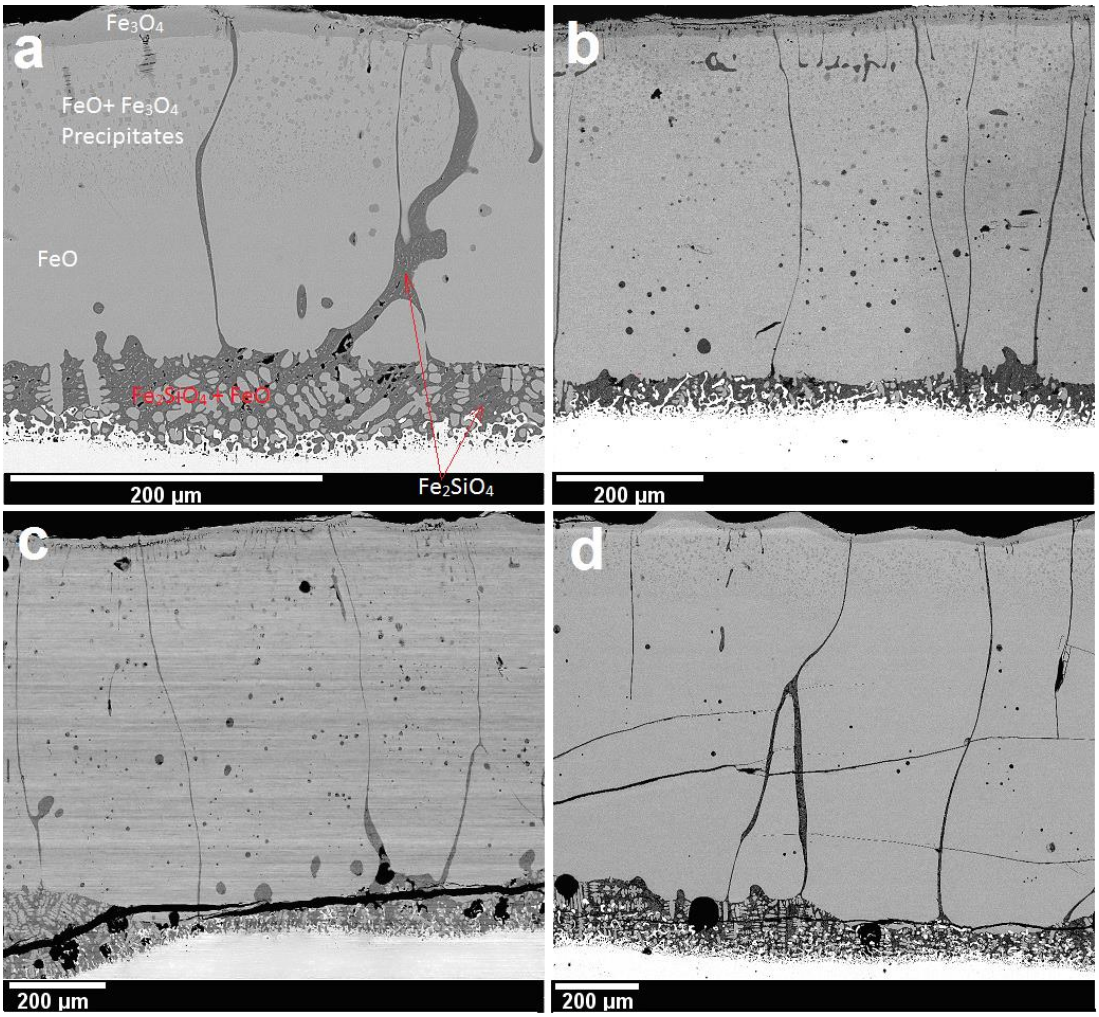

Figure 4.4.2.1.1 BSE image of DSP grade specimens oxidised at 1280°C for:
a.10min b. 20min c. 30min d. 60min

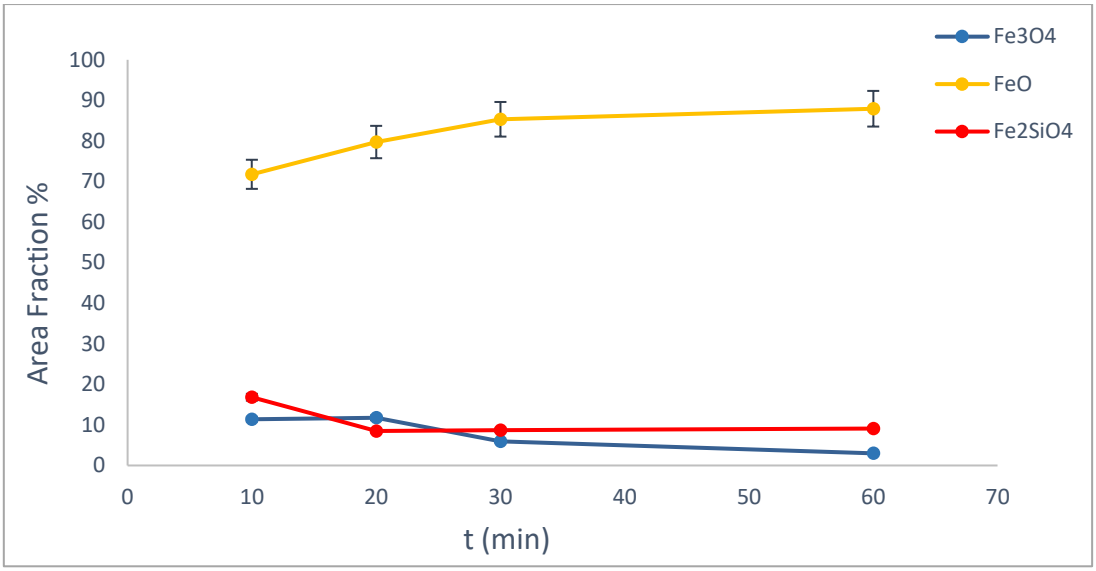

Figure 4.4.2.1.2 Relation between oxide compositions and time of DSP steel oxidised at 1280°C under atmosphere contained 17% moisture.

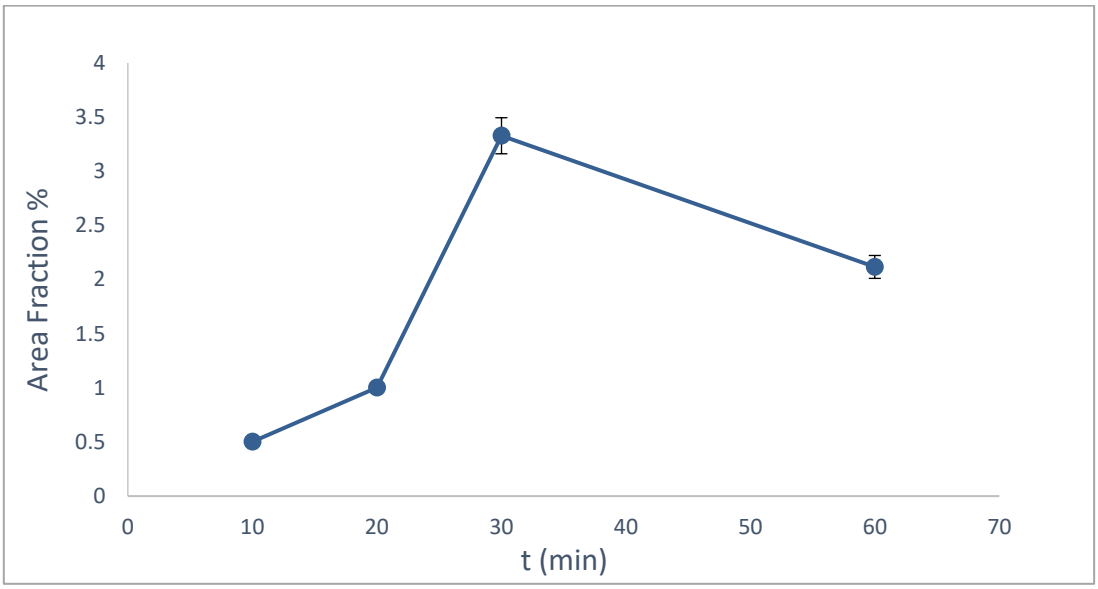

Figure 4.4.2.1.3 Relation between the amount of oxide scale defects and time of DSP steel oxidised at 1280°C under atmosphere contained 17% moisture.

As can be seen in Figure 4.4.2.1.2 as the oxidation period extended, the proportion of Wüstite slightly increased. The development of Magnetite between 10 to 20 minutes of the process was almost constant, but after that, the growth rate of this phase decreased. The highest proportion of Fayalite was observed in sample oxidised for 10 minutes, but the amount of this phase was consistent for longer oxidation periods. In all specimens, dense oxide scales developed which adhered to substrate metal, however in samples oxidised for 30 and 60 minutes, thermal shock cracks developed within the oxide scale perpendicular to the

substrate metal during the cooling stage. As can be observed in Figure 4.4.2.1.3, the highest volume fraction of defects was apparent in the sample oxidised for 30 minutes.

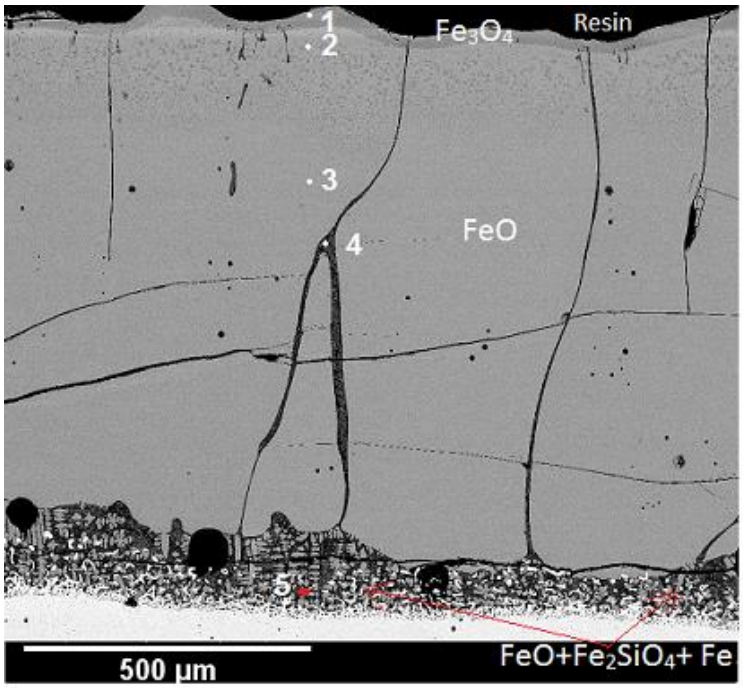

	AT%			
Point	Fe	O	Si	Al
1	43.42	56.58	-	-
2	47.8	52.2	-	-
3	47.69	52.31	-	-
4	31.62	54.92	13.46	-
5	27.29	54.32	13.79	4.59

Figure 4.4.2.1.4 EDX point analysis of DSP sample oxidised for 60 minutes at 1280°C.

EDX point analysis of DSP sample oxidised for 60 minutes at 1280°C is displayed in Figure 4.4.2.1.4 Oxide phases of Fe_3O_4, FeO and Fe_2SiO_4 was identified across the oxide scales. The EDX point analysis revealed the enrichment of aluminium within the dark Fayalite regions next to the oxide-metal interface, possibly in the form of $FeAl_2O_4/Fe_2SiO_4$.

Figure 4.4.2.1.5 demonstrates the oxide scale development in DSP steel specimens oxidised for 10 to 180 minutes at 1150°C under the atmosphere containing 17% of moisture. The microstructures of the oxide scales of this steel grade entirely differed from those samples oxidised at higher temperatures. In the first three samples, the structure of the oxide scale divided into two different segments; a thick outer layer containing Hematite and Magnetite and an inner segment (healing layer) containing Fayalite and Wüstite, which strongly adhered to the substrate metal. As demonstrated in Figure 4.4.2.1.5.d, after 60 minutes of oxidation, Hematite extensively transformed to Magnetite within the outermost layer, while Magnetite partially transformed to Wüstite simultaneously.

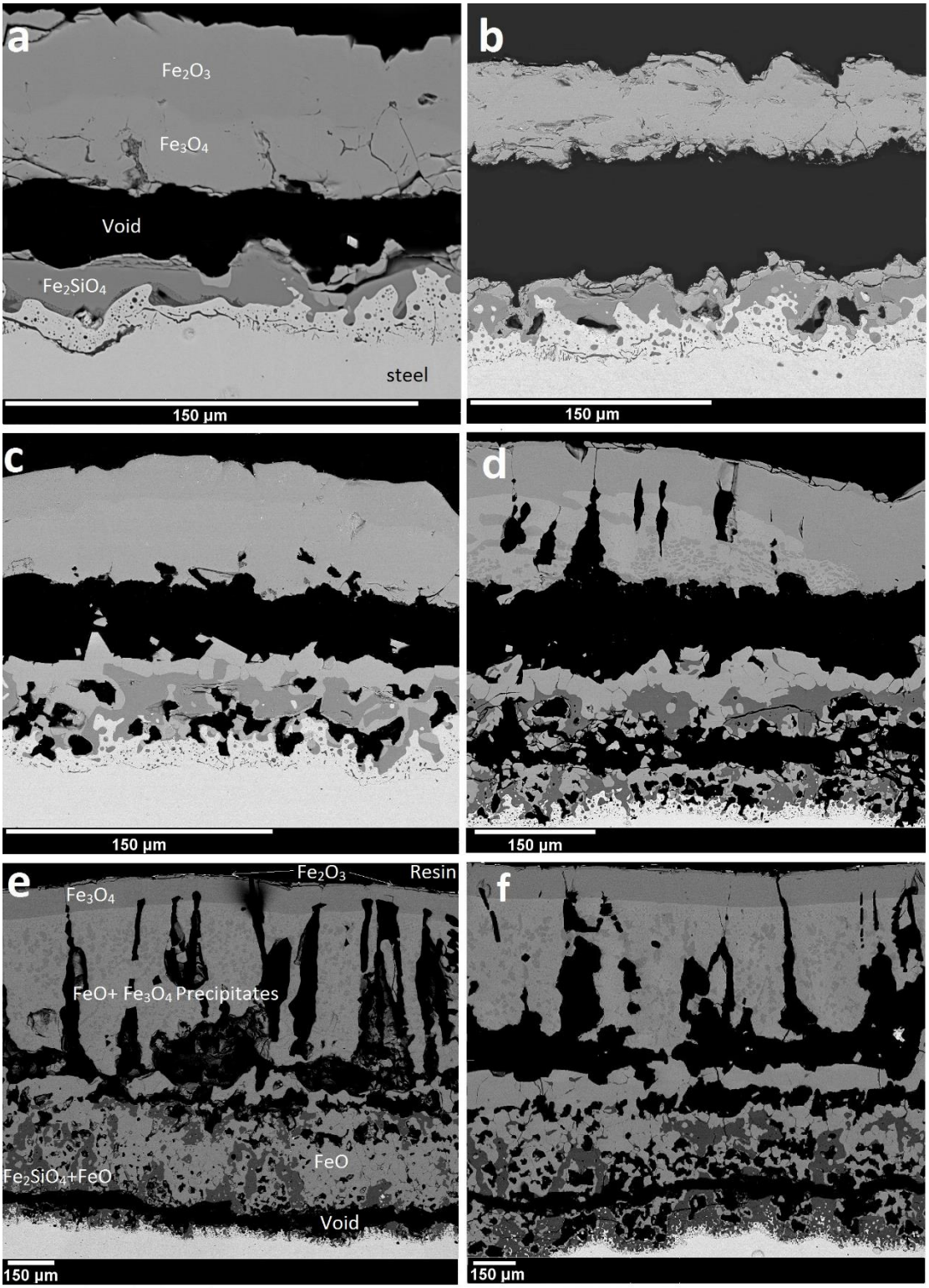

Figure 4.4.2.1.5 BSE images of DSP specimens oxidised at 1150°C under atmosphere containing 17% moisture for:

a. 10min b. 20min c. 30min d. 60min e. 120min f. 180min

The image analysis confirmed that the proportions of Hematite and Wüstite had a direct relation with time. As can be seen in Figure 4.4.2.1.6 in specimen oxidised for 10 minutes,

Fe_2O_3 was the predominant phase, however, as oxidation extended the proportion of this phase rapidly reduced and after 60 minutes, it was the least produced phase. Conversely, Wüstite volume fraction increased as the oxidation prolonged, and after 60 minutes, it was the predominant phase. The amount of Magnetite reduced for oxidation periods longer than 60 minutes.

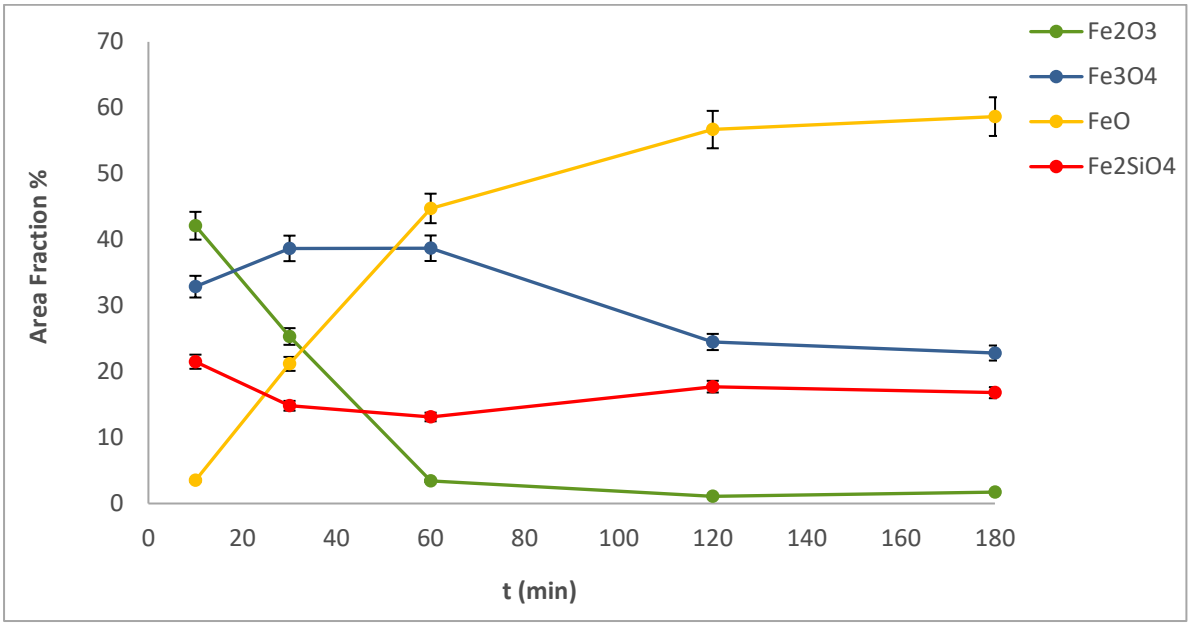

Figure 4.4.2.1.6 Relation between oxide compositions and time of DSP steel oxidised at 1150°C under atmosphere contained 17% moisture.

The microstructural transformation from one condition to the other clearly showed that extending the oxidation time not only widened the healing layer but also increased the number and size of the defects. Up to 60 minutes of the oxidation, the volume of defects increased and afterwards, it gradually reduced. The joint of voids and cavities developed a separate transitional oxide segment and within the outermost layer, additional voids and cavities introduced. After 120 minutes of oxidation, the separation gaps between the oxide layers reduced, but within the Magnetite precipitation zone, large columnar cavities considerably expanded. The microstructure of the DSP steel sample oxidised in this condition was comparable to the rail steel specimen oxidised in a similar environment. Although in the sample oxidised for 180 minutes, the volume of Fayalite considerably increased around the oxide-metal interface but similar microstructural characteristics observed across the oxide scale. The relations between the extent of defects and oxidation time of DSP steel at 1150°C under humid atmosphere were presented in Figure 4.4.2.1.7. Because a separation gap

existed in most of the specimens, the total value of the defective regions was calculated in two different ways. The solid line represented the proportion of the entire defects' regions, including the large separation gaps. The dashed curve demonstrated the sum of defects area, excluding the separation cavities. Where the large separation cavities included in the calculations, the highest volume fraction of defects were apparent in the sample oxidised for 60 minutes. On the other hand, when the separation gaps excluded from the calculations, the small number of defects were present in the sample oxidised for 60 minutes. Comparison of the defects curves pattern indicated that up to 60 minutes of oxidation, the major part of defects associated with separation gaps between oxide inner and outer layers.

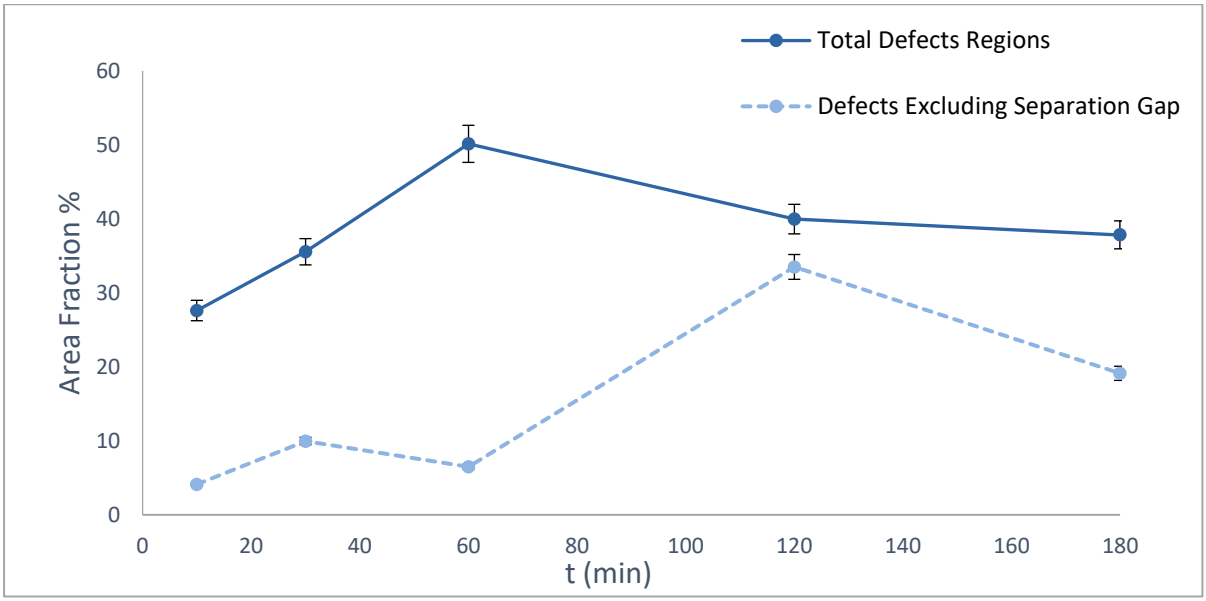

Figure 4.4.2.1.7 Relation between the amount of oxide scale defects and time of DSP steel oxidised at 1150°C under atmosphere contained 17% moisture.

The EDX chemical compositions point analysis of a DSP specimen oxidised for 10 minutes at 1150°C under an atmosphere containing 17% water vapour is shown in Figure 4.4.2.1.8. As can be seen after 10 minutes of oxidation the outer oxide layer contained two large segments of Hematite and Magnetite and an only small amount of FeO developed right above the Fayalite next to substrate metal; these observations were in good agreement with XRD analysis.

BSE image of the internal oxidation zone of a specimen oxidised for 60 minutes is given in

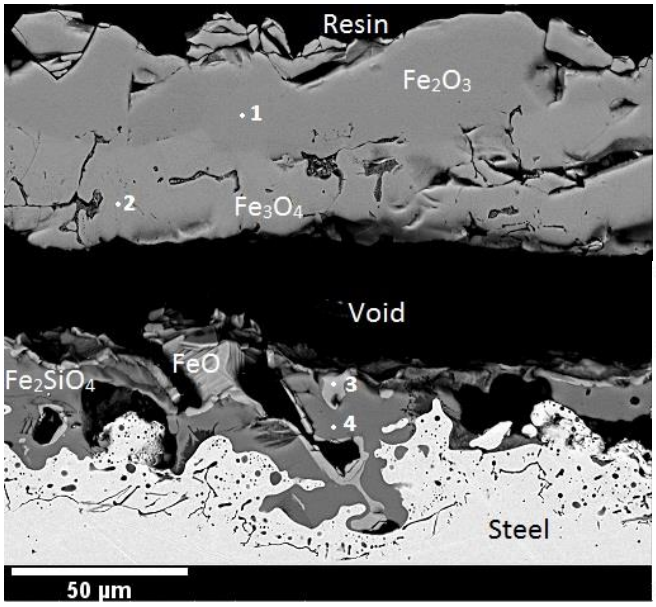

Point	At% Fe	O	Si
1	40.66	59.34	-
2	43.21	56.79	-
3	48.66	51.34	-
4	27.72	56.77	16.51

Figure 4.4.2.1.8 EDX chemical composition analysis of a DSP sample oxidised at 1150°C for 10 minutes under an atmosphere containing 17% moisture.

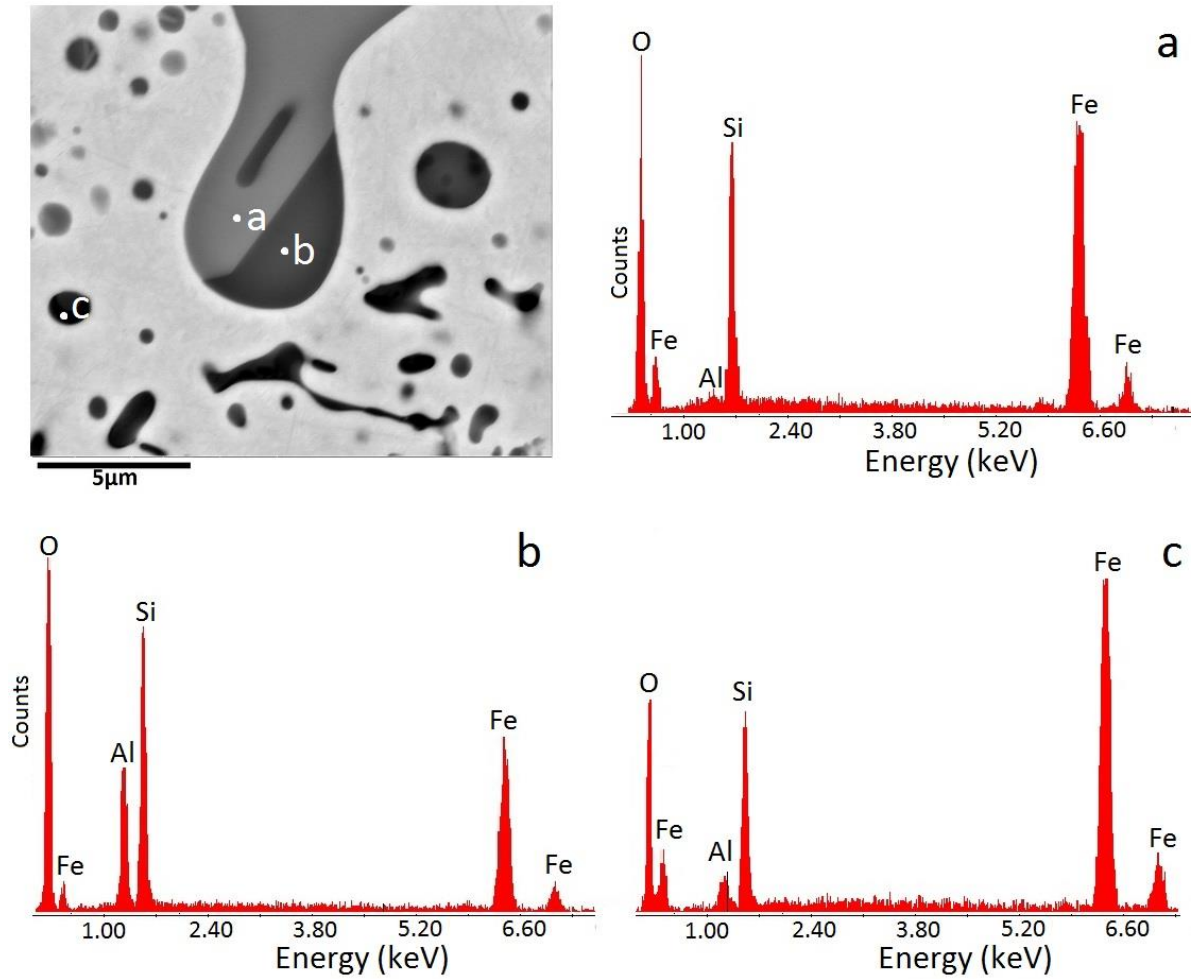

Figure 4.4.2.1.9 BSE image and EDX chemical composition analysis of the oxide-metal interface of a DSP specimen oxidised for 10 minutes at 1150°C.

Figure 4.4.2.1.9. The internal globular and nodular of Fayalite were formed at the top region and irregular oxide features created at lower regions. As can be seen, Fayalite appeared in three different shades of grey. EDX elemental patterns disclosed that the darker oxide constituents contained a noticeable amount of Al.

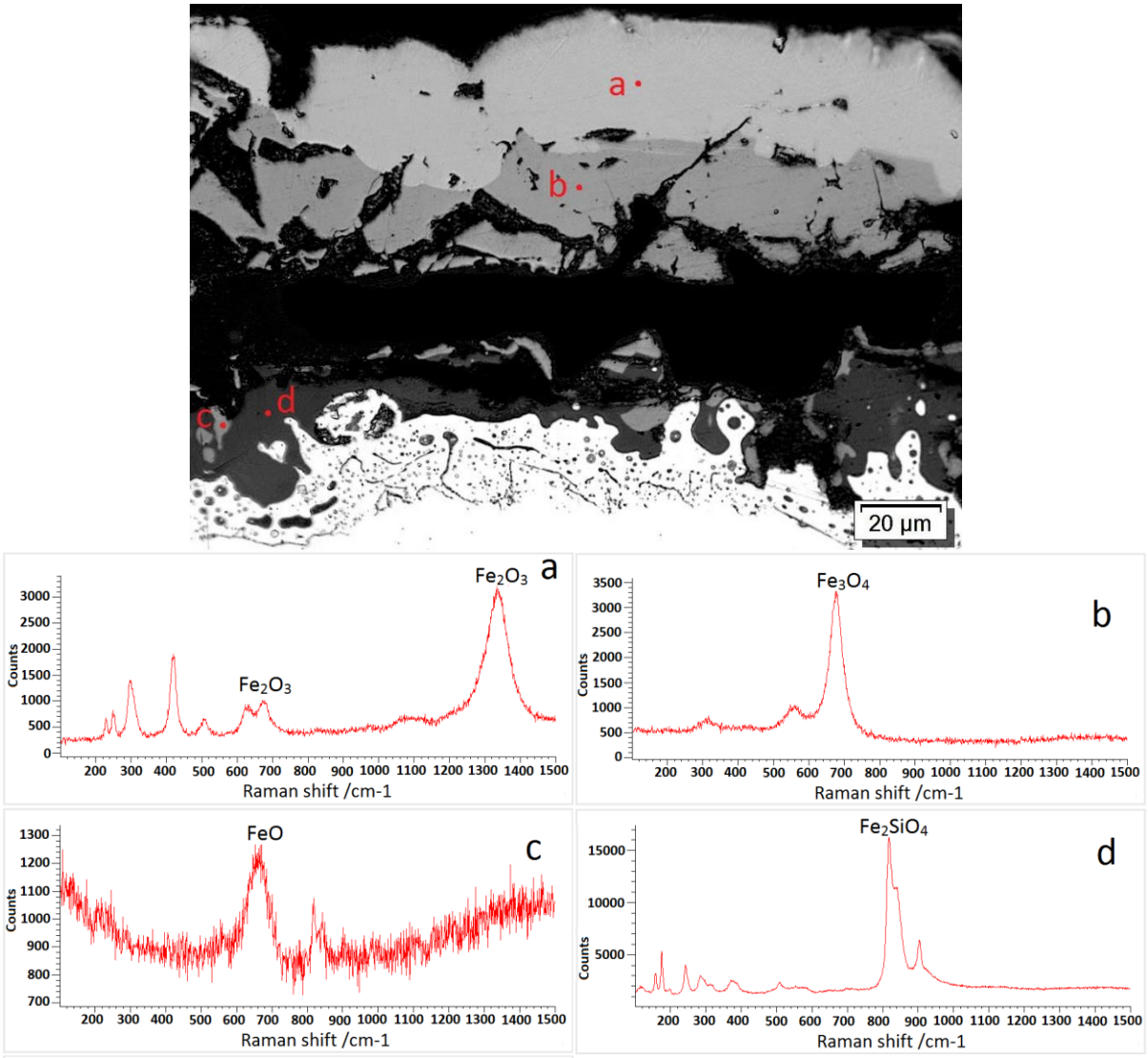

Figure 4.4.2.1.10 Optical image and Raman spectra of a DSP specimen oxidised for 10 minutes at 1150°C under atmosphere contained 17% moisture.

Typical Raman spectra of the DSP sample oxidised for 10 minutes at 1150°C under humid atmosphere were demonstrated in Figure 4.4.2.1.10. The Raman shifts at 299, 418, 637, 683 and 1340 (cm^{-1}) confirmed that the outermost layer (point a) was Hematite. Scanning the point (b) and revealed Magnetite peaks at 569 and 675 (cm^{-1}). The Raman shift at 663 (cm^{-1})

confirmed the presence of small quantities of Wüstite at the oxide-metal interface (point c). Fayalite and were apparent (point d). Moreover, the shifts of Raman spectra at 820 and 840 (cm^{-1}) confirmed Fayalite within the oxide-metal interface (point d).

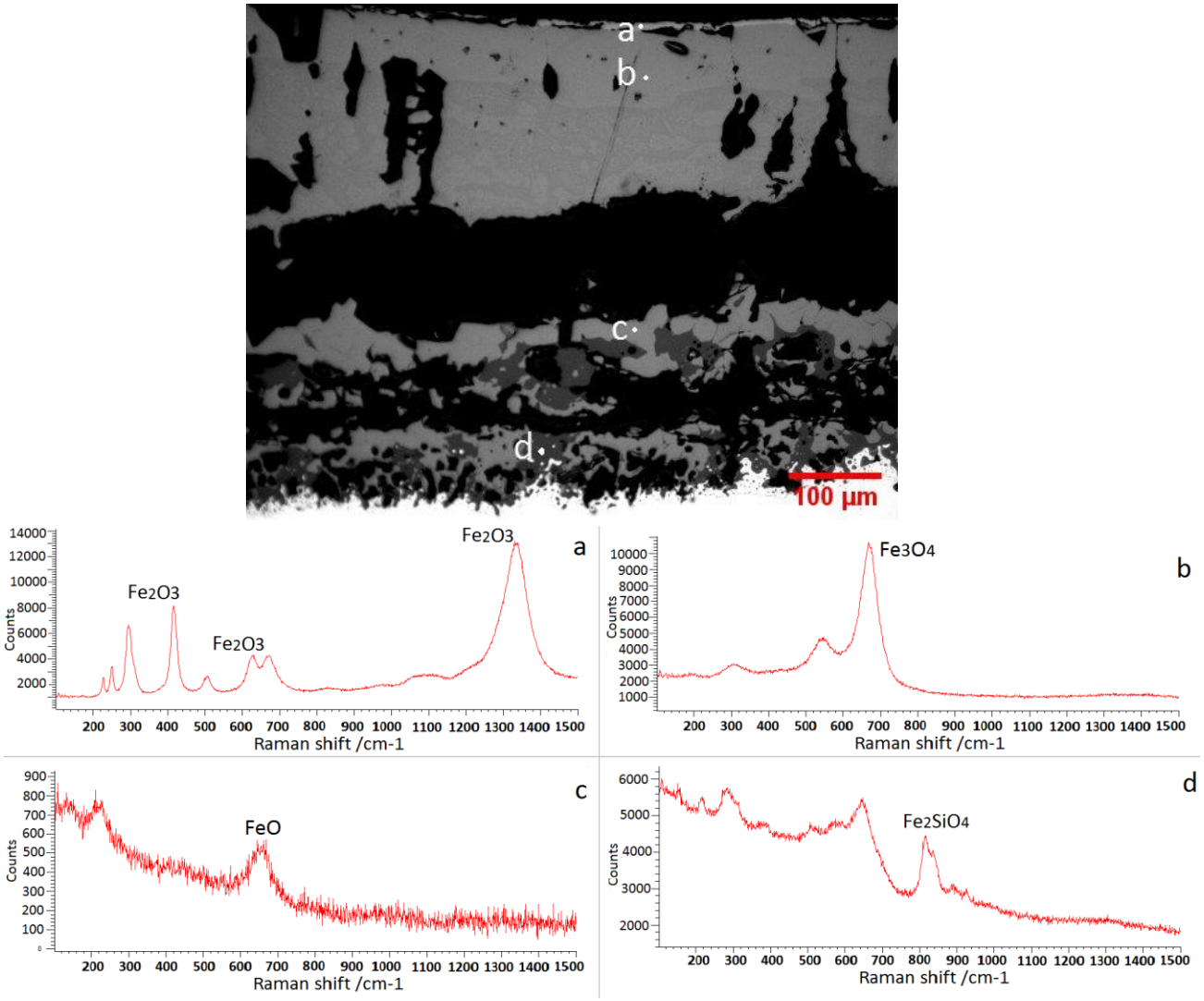

Figure 4.4.2.1.11 Raman spectra from DSP specimen oxidised for 60 minutes at 1150°C under an atmosphere containing 17% moisture.

As demonstrated in Figure4.4.2.1.11, the oxide scales chemical composition of a DSP steel specimen oxidised for 60 minutes at 1150°C under the moist condition, was analysed via LRS. The Raman peaks confirmed that thin layer at the top section of the oxide scales (point a) to be Hematite. The composition of the oxide scale at point "b" was identified as Magnetite by the Raman peak at 670 (cm^{-1}). Wüstite presence in mid-region of the oxide scale (point c), was confirmed by the Raman shift at 657 (cm^{-1}). Analysis next to the oxide-metal interface

(point d) indicated that the dark grey phase was Fayalite, and the associated Raman peak was apparent at 819 (cm^{-1}).

EDX chemical composition point analysis and line scan of a DSP sample oxidised for 180 minutes under an atmosphere containing 17% moisture are shown in Figure 4.4.2.1.12. The phase distributions of all iron oxides explained earlier were confirmed by EDX point analysis. The outer layer included a thin Hematite film at the surface of the oxide, which was adjacent to an individual Magnetite segment and a large Wüstite zone containing Magnetite precipitates. The presence of Wüstite and Fayalite were confirmed within the middle and the bottom segments. Although no Al content was detected during assessments of the marked points, the EDX line scan confirmed the presence of small amounts of Al within the Fayalite phase in a few different locations.

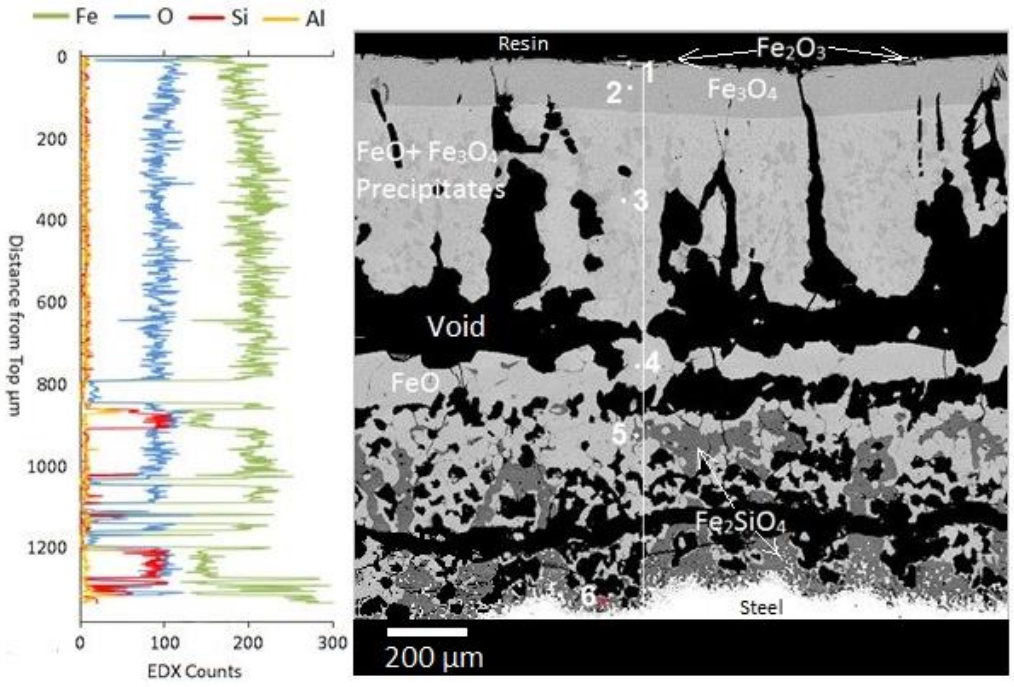

Point	At% Fe	O	Si	Al
1	40.82	59.18	-	-
2	43.78	56.22	-	-
3	48.41	51.59	-	-
4	48.31	51.69	-	-
5	27.63	55.87	16.5	-
6	27.55	57.16	15.29	-

Figure 4.4.2.1.12 EDX chemical compositional point analysis and line scan of a DSP sample oxidised at 1150°C for 180 minutes under an atmosphere containing 17% moisture.

The microstructure of the DSP steel oxide scales distinctively transformed when the specimens oxidised at lower temperatures. Figure 4.4.2.1.13 displays the BSE cross-sectional image and EDX point analysis of a DSP specimen oxidised at 1050°C for 60 minutes under an atmosphere containing 17% of water vapour. The EDX compositional analysis showed the developed oxide scale contained FeO, Fe_3O_4, Fe_2O_3 and Fe_2SiO_4. The development of a wide, porous healing layer containing fine layers of Fayalite above the internal oxidation zone was a distinctive characteristic of the oxide scales. In the midsection, large amounts of Magnetite and Wüstite along with a small quantity of Hematite were apparent. Most defects, including small and large voids formed within FeO and Fe_3O_4 segments. At the top section of the oxide scales, a large segment of Hematite detached from the rest of the scale.

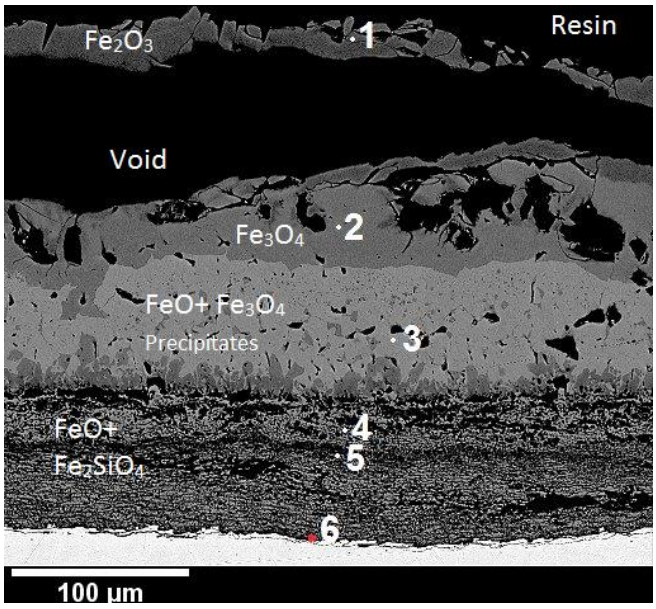

	AT%			
Point	Fe	O	Si	Al
1	40.6	59.4	-	-
2	44.25	55.75	-	-
3	48.96	51.04	-	-
4	39.52	52.73	7.75	-
5	37.27	51.65	11.08	-
6	48.02	43.89	8.09	-

Figure 4.4.2.1.13 BSE image and EDX chemical compositional point analysis of a DSP sample oxidised at 1050°C for 60 minutes under an atmosphere containing 17% moisture.

Figure 4.4.2.1.14 demonstrates a high magnification BSE image of the oxide-metal interface of the above specimen and EDX point analysis. Like sample oxidised at 1150˚C within the healing layer, Fayalite appeared in different shades, which were related to the amount of Al content.

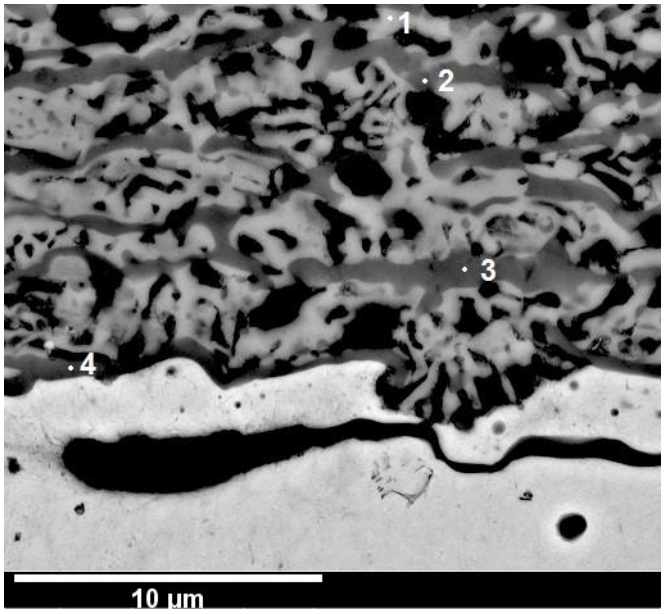

	AT%			
Point	Fe	O	Si	Al
1	40.7	54.02	5.28	-
2	32.48	54.3	11.12	2.1
3	31.7	53.71	11.91	2.68
4	35.13	52.15	11.41	1.31

Figure 4.4.2.1.14 BSE image and EDX chemical compositional point analysis of the oxide-metal interface of a DSP specimen oxidised for 60 minutes at 1050°C.

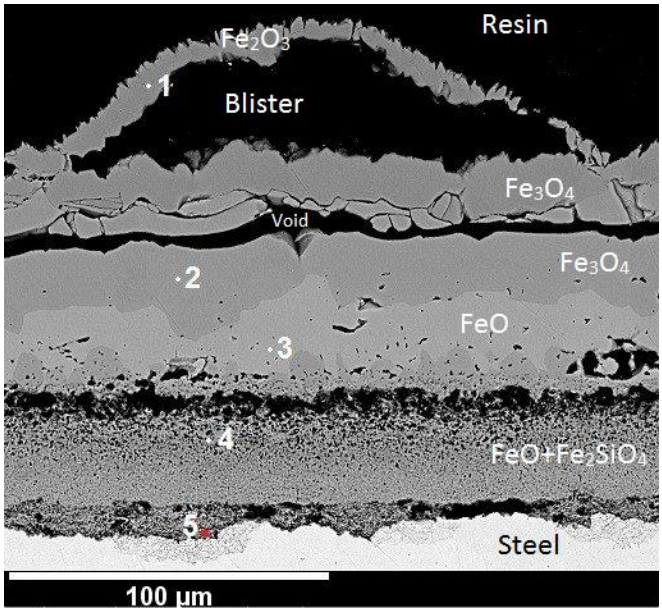

	AT%			
Point	Fe	O	Si	Al
1	37.15	62.85	-	-
2	45.44	54.56	-	-
3	48.61	51.39	-	-
4	38.13	50.87	9.82	1.18
5	37.18	49.56	12	1.26

Figure 4.4.2.1.15 BSE image and EDX chemical compositional point analysis of a DSP sample oxidised at 950°C for 60 minutes under an atmosphere containing 17% moisture.

DSP oxide scales formed at 950°C in the moist atmosphere after 60 minutes showed comparable microstructural characteristics to the sample oxidised at 1050°C. As demonstrated in Figure 4.4.2.1.15 and Figure 4.4.2.1.16, the porous healing layer containing Fayalite and Wüstite formed above the oxide-metal interface. However, the microstructure of this region was considerably finer than the previous condition. Within the Fayalite, the variation of Al content was visible as the previous condition.

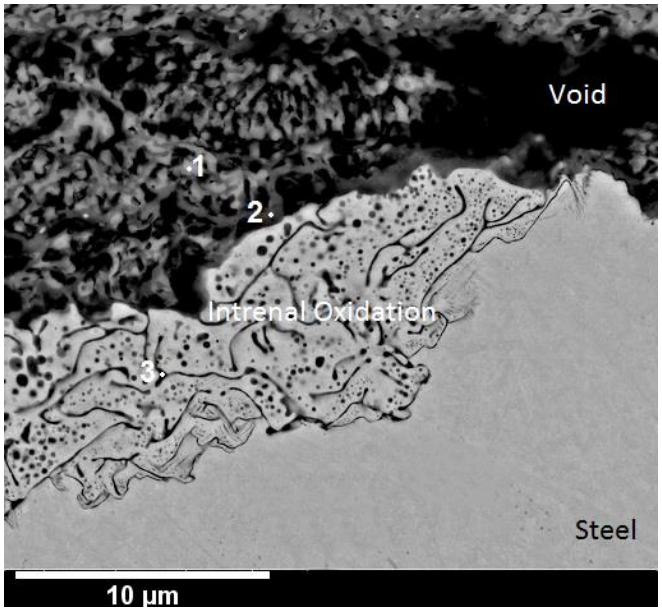

	AT%			
Point	Fe	O	Si	Al
1	40.7	54.02	5.28	-
2	32.48	54.3	11.12	2.1
3	31.7	53.71	11.91	2.68

Figure 4.4.2.1.16 BSE image and EDX chemical compositional point analysis of the oxide-metal interface of a DSP specimen oxidised for 60 minutes at 950°C.

In mid-region, Wüstite formed within the Magnetite matrix. The top layer that contained Magnetite and Hematite detached from the inner layer of the oxide scales. Like oxidation scenario at 1050°C, within the outermost layer signs of the partial breakaway of Hematite were apparent. By reducing the oxidation temperature to 950°C, the size and number of voids and porosities reduced throughout the oxide scale.

The optical image and its corresponding Raman spectra of a DSP specimen oxidised for 60 minutes at 950°C displayed in Figure 4.4.2.1.17. The Raman spectrum of point (a) exposed several peaks at 225, 243, 292, 410, 508, 616, 677 and 1320 (cm^{-1}), which indicated the oxide phase as Hematite. The LRS pattern of the point (b) was a typical Raman spectrum of Magnetite at 547 and 669 (cm^{-1}). The detection of a short peak at 660 (cm^{-1}) during the assessment of the point (c) confirmed that FeO was present within the middle of the oxide layer. This peak was also observed at the transition zone (point d), in addition to the other distinguished peak at 819 (cm^{-1}) which verified Wüstite and Fayalite as phase constituents of the transition zone.

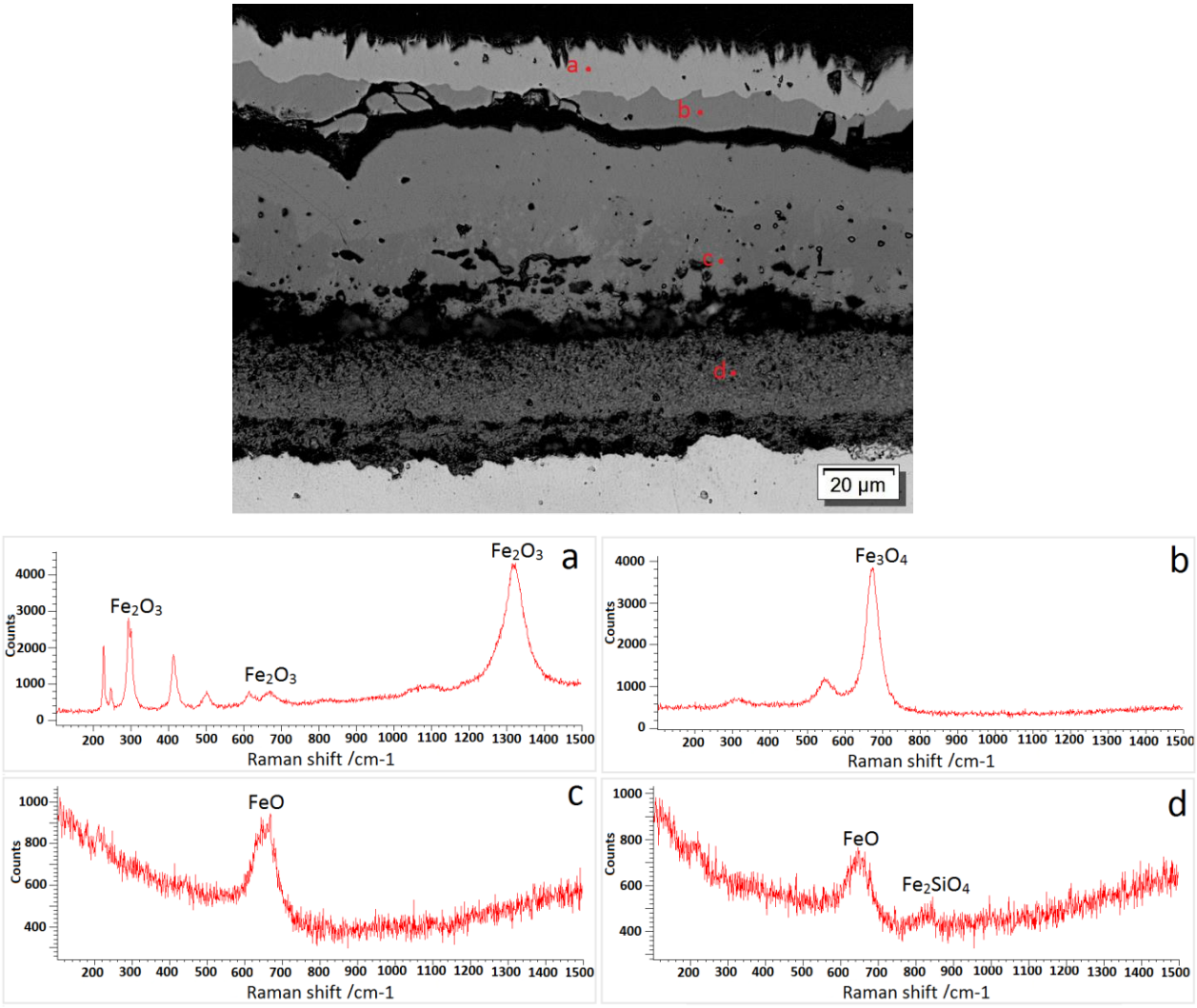

Figure 4.4.2.1.17 Raman spectra from DSP specimen oxidised for 60 minutes at 950°C under an atmosphere containing 17% moisture.

As demonstrated in Figure 4.4.2.1.18, the reduction of oxidation temperature to 850˚C significantly affected the microstructure and morphology of the DSP steel oxide scales. Oxide developed above the substrate steel in the form of adhered continuous scales. As can be seen, fine oxide whiskers of Fe_2O_3 grew above the outermost layer of the oxide scale, which was constructed from the same phase. A small layer of Magnetite was visible below the Hematite phase. The Fe_3O_4 precipitates were also scattered across the predominant phase of Wüstite. Similar to oxidation at 950˚C and 1050˚C a large healing layer that contained Fayalite formed below the FeO zone. In near-surface regions of substrate steel, a wide and relatively uniform internal oxidation zone developed. The EDX line scan also defined the chemical composition variations across the oxide scales. Si was detected throughout the healing layer and internal oxidation zone. The appearance of Al also confirmed the presence of this element in different

locations across the healing layer and inner oxidation zone. The oxygen and iron trends followed the pattern and arrangement of the iron oxide phase.

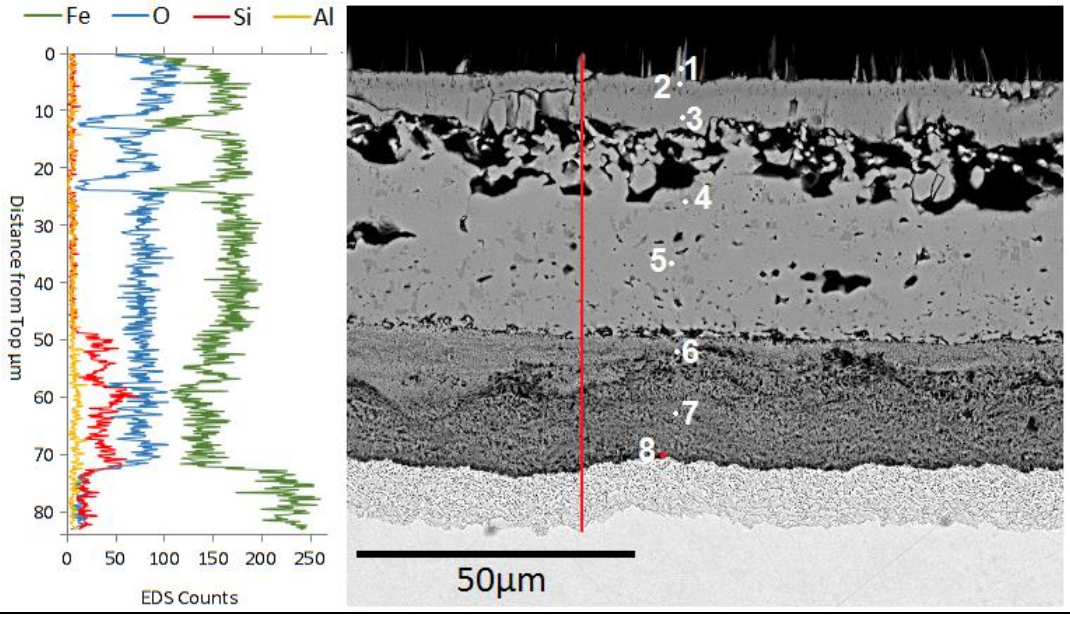

		At%		
Point	**Fe**	**O**	**Si**	**Al**
1	34.33	65.67	-	-
2	37.59	62.41	-	-
3	41.75	58.25	-	-
4	44.93	55.07	-	-
5	48.62	51.38	-	-
6	33.42	53.51	11.24	1.83
7	38.33	53.14	7.23	1.3
8	35.9	48.81	12	3.29

Figure 4.4.2.1.18 EDX chemical compositional point analysis and line scan of a DSP sample oxidised at 850°C for 60 minutes under an atmosphere containing 17% moisture.

Figure 4.4.2.1.19 displays the complex microstructures of Fayalite within the healing layer and internal oxidation zone. As mentioned earlier, the colour variation of the Fayalite was associated with deviation of Al dissolution within this phase.

The effect of oxidation temperatures on the DSP oxide scales compositions is given in Figure 4.4.2.1.20. As can be seen for all temperatures FeO was the predominant phase; however, the volume fraction of this phase was significantly higher in the oxidation of DSP steel at 1280˚C.

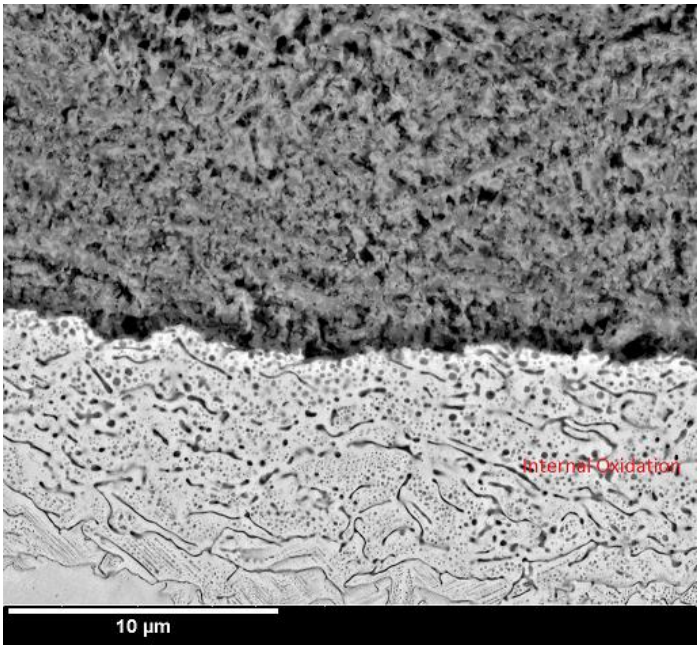

Figure 4.4.2.1.19 BSE image of the oxide-metal interface of a DSP specimen oxidised for 60 minutes at 850°C under an atmosphere containing 17% moisture.

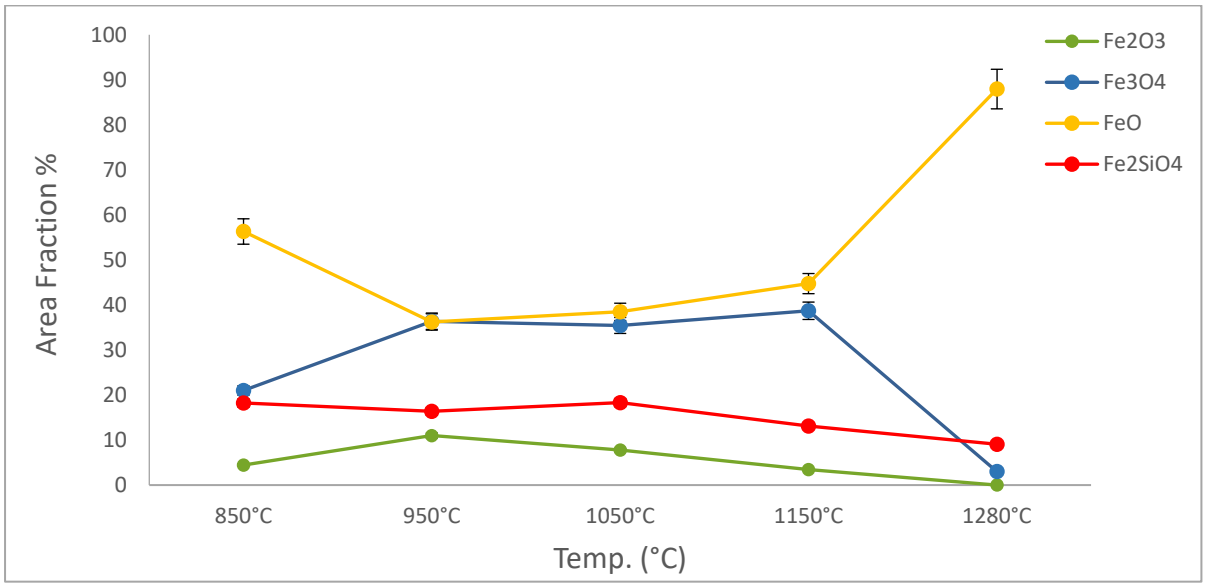

Figure 4.4.2.1.20 Relation between oxide scales compositions and oxidation temperatures of DSP steel after 60 minutes oxidation under an atmosphere containing 17% of moisture.

The amount of this phase also increased when the specimen oxidised at 850˚C. Variations in the development of Magnetite were insignificant for oxidation between 850˚C and 1150˚C, but it considerably reduced when the material oxidised at 1280˚C. The curve of Fayalite on the graph was almost linear; this showed the oxidation temperature had the lowest impact on the development of this phase in comparison to the other oxide constituents. The highest

percentage of Hematite produced when the material oxidised at 950˚C and then the amount of this phase gradually reduced at higher temperatures.

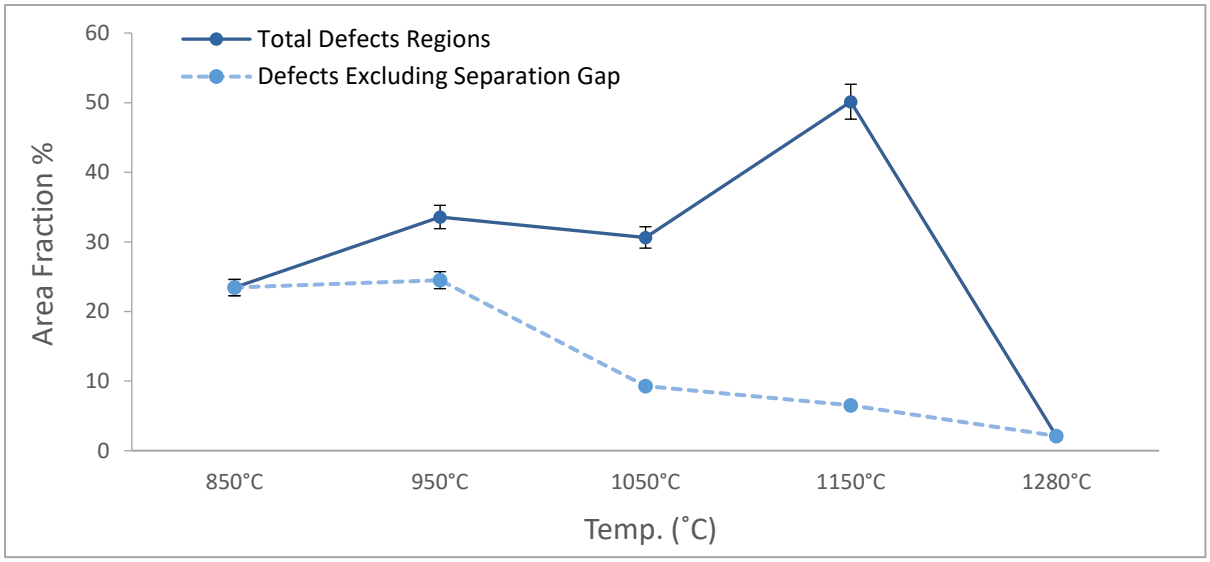

Figure 4.4.2.1.21 Relation between oxide scales defects percentage and oxidation temperatures of DSP steel specimens oxidised for 60 minutes under an atmosphere containing 17% moisture.

Figure 4.4.2.1.21 demonstrates the defects development rate against the oxidation temperatures. The defects included voids, porosities, cavities and cracks. As can be seen, two individual curves were plotted. First, the large separation cavities were included in the calculation of the defects area fraction (solid line). At 850˚C, the total defects regions were about 23% of the oxide scale cross-section. As the temperature of the process elevated to 950˚C, the proportion of defects increased by 10%. At 1050˚C, the extent of defects slightly reduced, whereas specimen oxidised at 1150˚C showed the highest number of defects. Conversely, in sample oxidised at 1280˚C, the lowest amounts of imperfections were observed.

Furthermore, the separation gaps excluded from the measurements (dashed line). In this scenario, the defects development rate reduced as oxidation time extended.

4.4.2.2 Oxidation under a dry atmosphere

The influence of the dry atmosphere on oxidation of the DSP steel was studied by oxidising the specimens at 1150°C under a dry gas flow. As demonstrated in Figure 4.4.2.2.1, in

comparison to oxidation of the material under moist conditions, the development of Fayalite significantly reduced in all specimens and the development of Wüstite entirely abolished.

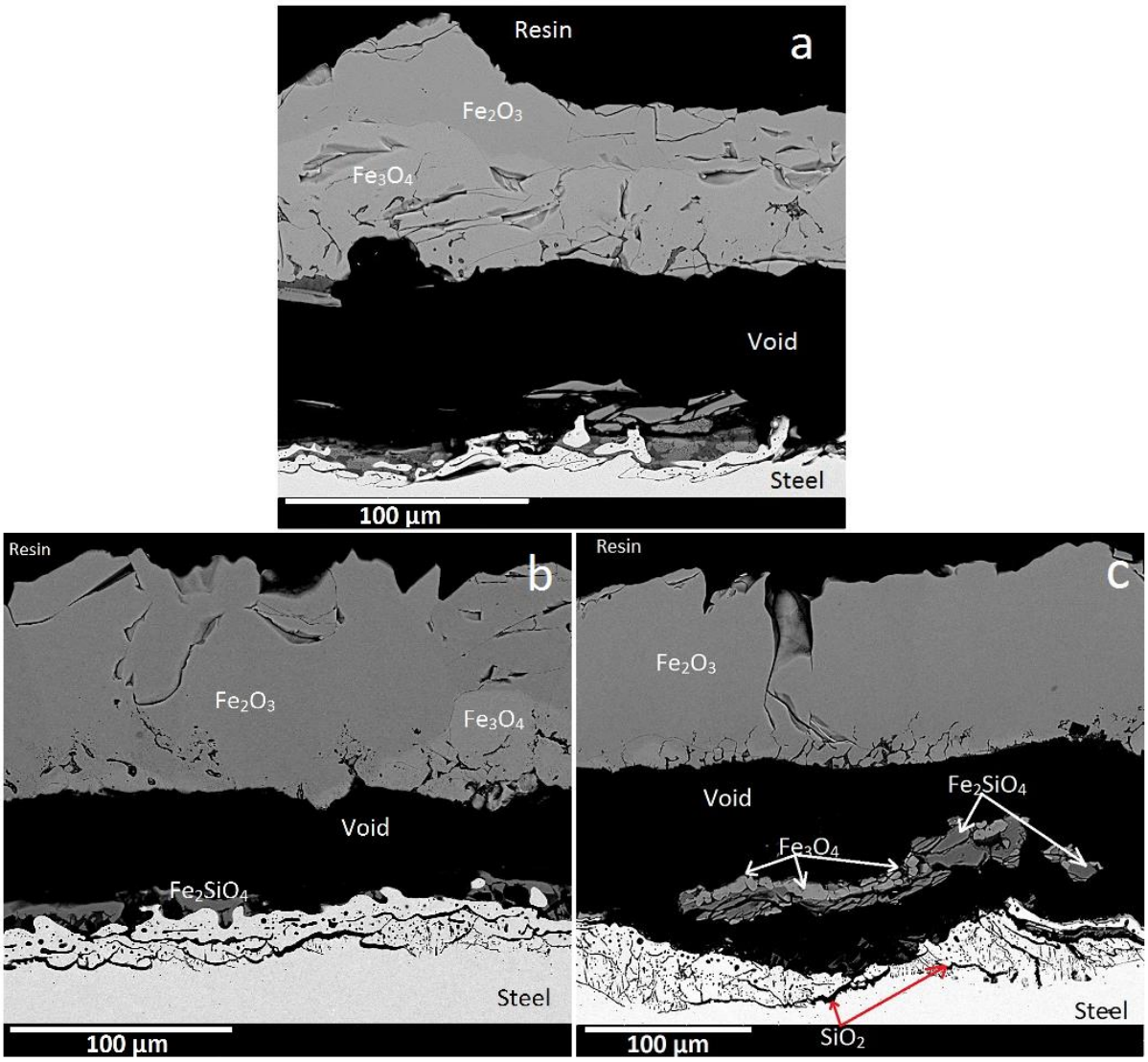

Figure 4.4.2.2.1 BSE images of DSP grade specimens oxidised at 1150°C under dry atmosphere for: a.10 minutes b. 60 minutes c. 180 minutes

In the specimen oxidised for 10 minutes the considerable amount of Hematite developed but Magnetite was the predominant phase. The Hematite region expanded due to the growth of the oxide scale along with the transformation of the Fe_3O_4 to Fe_2O_3, and after 180 minutes oxidation, almost the entire outer scale region contained Hematite and only very small fractions of Magnetite and Fayalite were present at the bottom of this layer. Moreover, Fe_3O_4 and Fe_2SiO_4 were visible as oxide fragments within the separation cavity. As can be seen, the dark Al-enriched compound (possibly $FeAl_2O_4/Fe_2SiO_4 + SiO_2$) was evident in the lowermost region of the inner oxidation zone.

4.5 Oxide-Metal Interface Roughness Evaluation

The surface roughness of the oxide-metal interface of each steel grade under different oxidation conditions was evaluated by plotting the Bearing Area Curve (BAC) as defined in Section 3.3.5. The graphical demonstrations clearly showed the effects of oxidation time and temperature on the roughness of the oxide-metal interface.

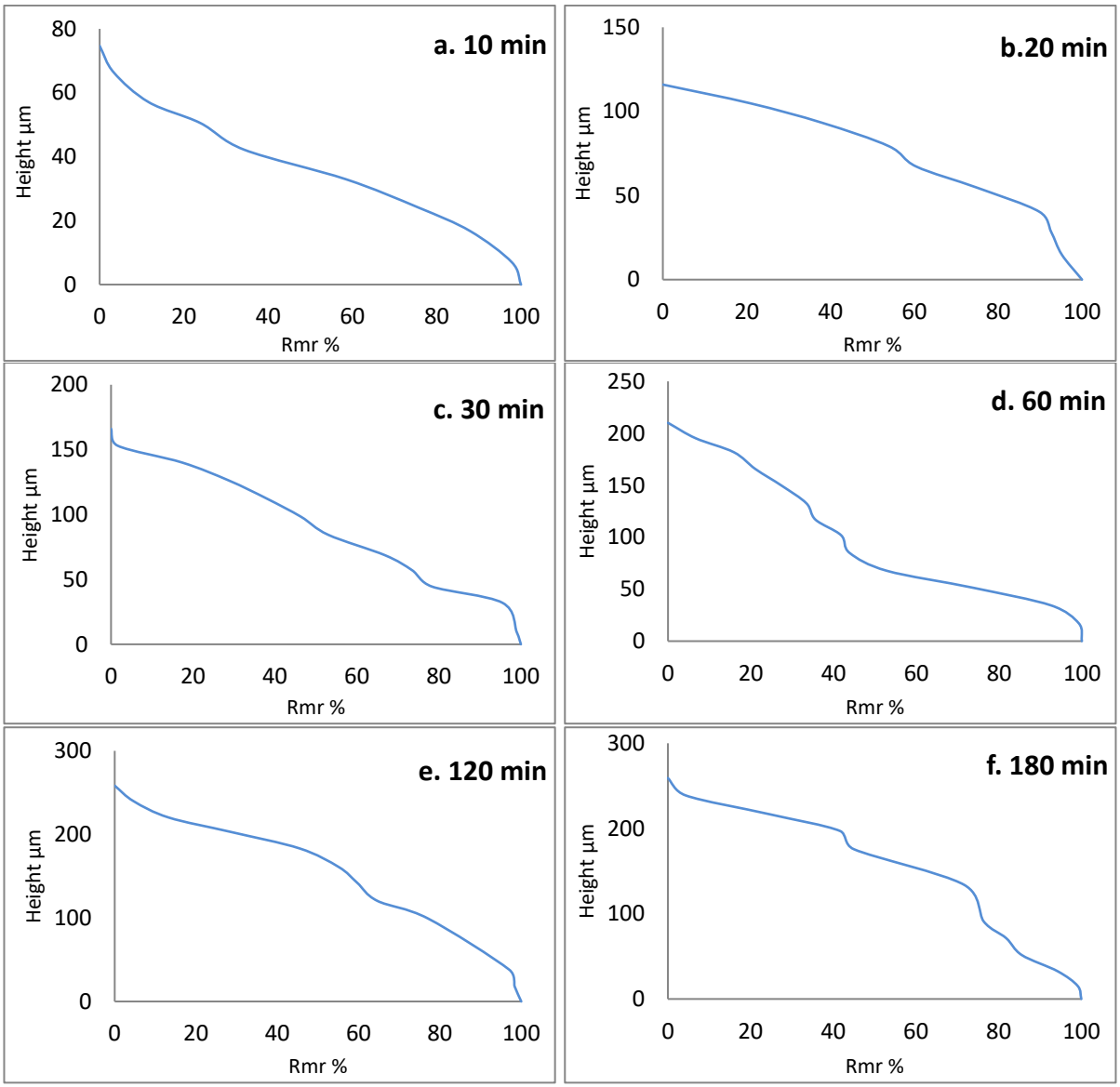

Figure 4.5.1 Bearing Area Curves of the Oxide-Metal interface of rail steel oxidised at 1280°C under atmosphere containing 17% water for:

a) 10 min b) 20 min c) 30 min d) 60 min e) 120 min f) 180 min.

As demonstrated in Figure 4.5.1, the roughness of the oxide-metal interface amplified as the oxidation extended. The BAC of early oxidation stage showed shorter picks and shallower valleys. In longer oxidation periods, due to higher consumption of substrate steel at the interface and higher sharp oxide penetrations into substrate metal, more complex interface profile developed.

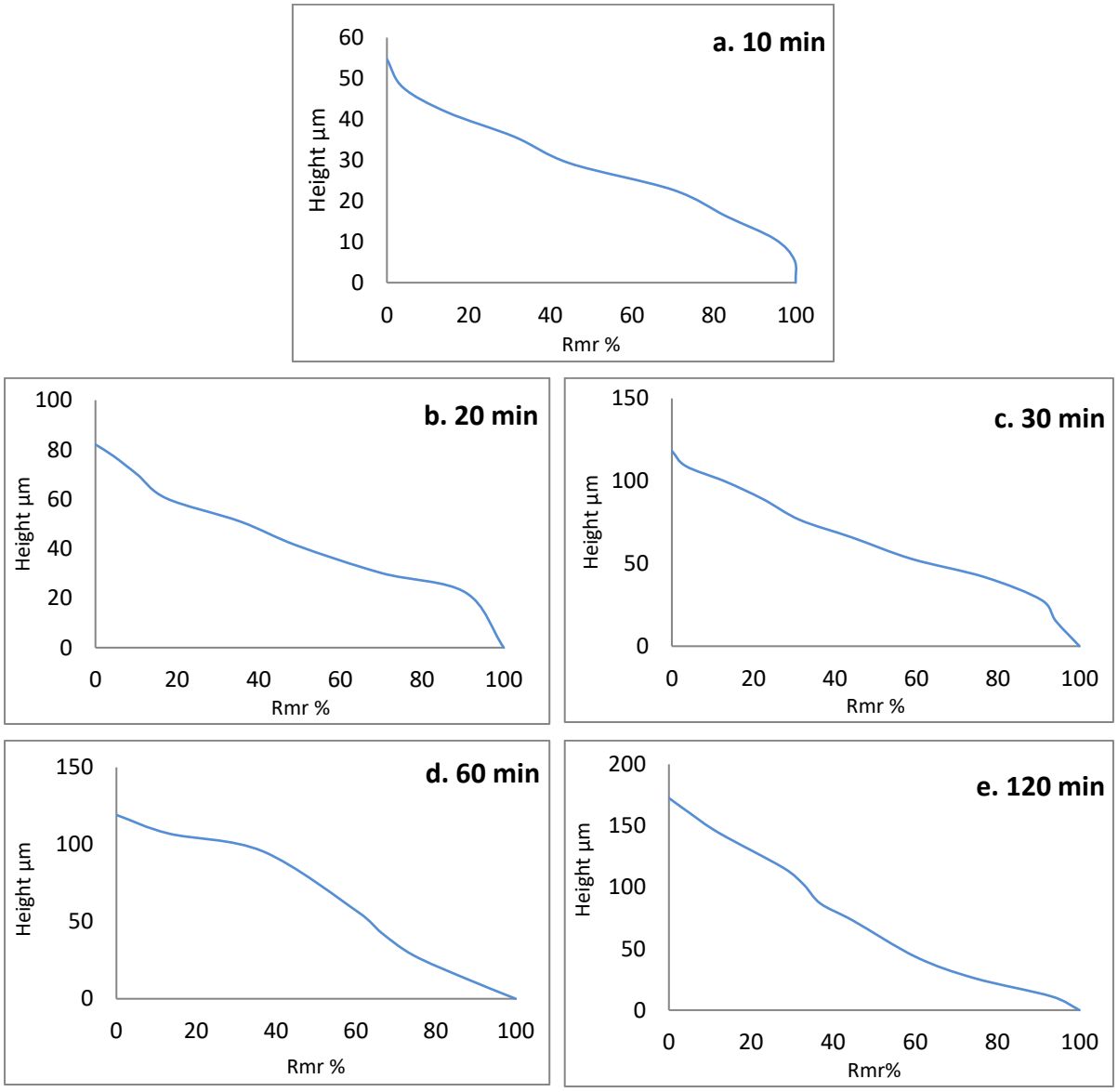

Figure 4.5.2 Bearing Area Curves of the Oxide-Metal interface of rail steel oxidised at 1150°C under atmosphere containing 17% water for:
a) 10 min b) 20 min c) 30 min d) 60 min e) 120 min.

The BAC of the oxide-metal interface of rail steel oxidised at 1150°C under an atmosphere containing 17% moisture confirmed that as the oxidation progressed the roughness of the

oxide-metal interfaced increased. However, in comparison to the oxidation of this grade at a higher temperature, the amplitude of the roughness reduced (Figure 4.5.2).

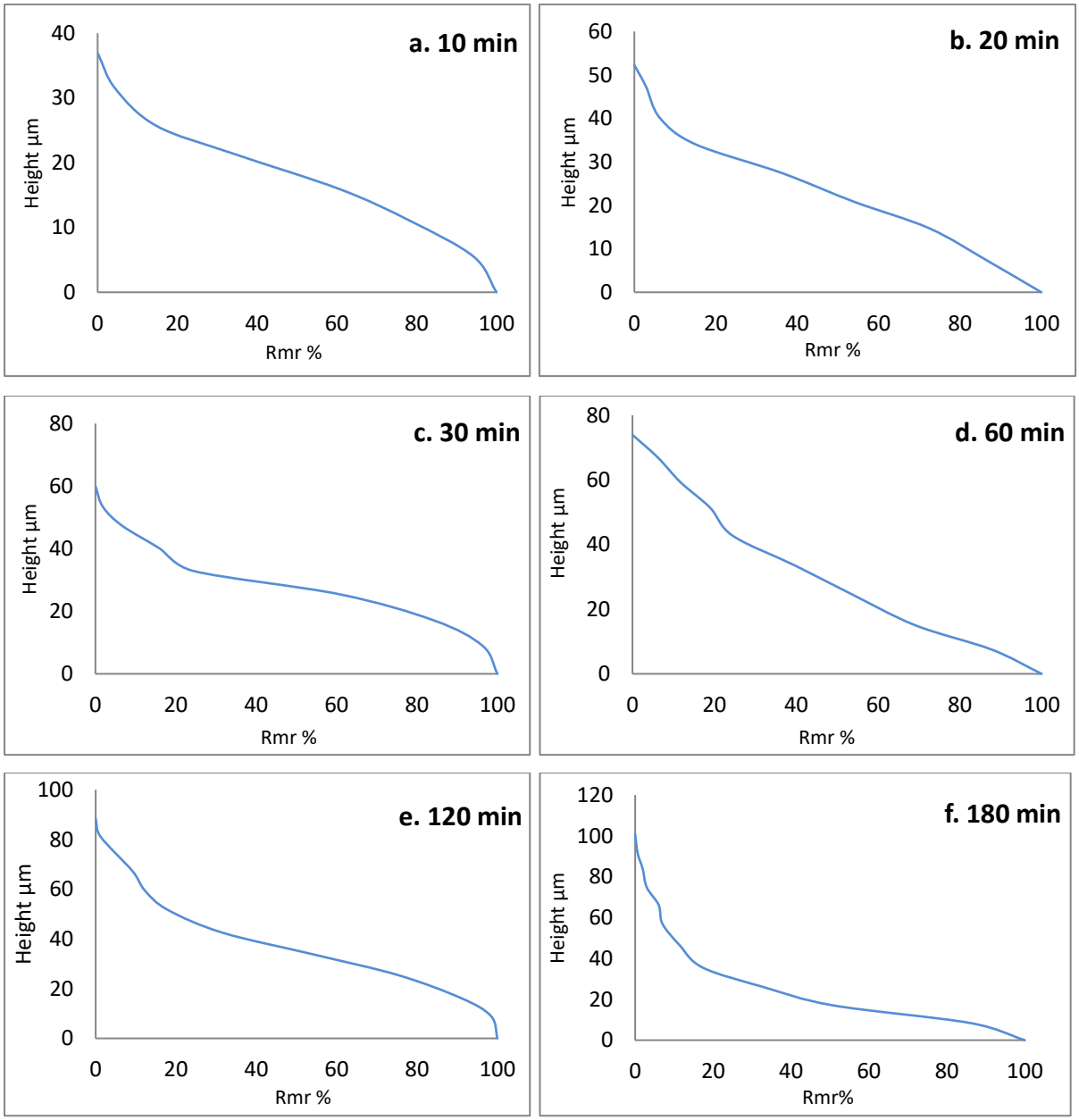

Figure 4.5.3 Bearing Area Curves of the Oxide-Metal interface of DSP steel oxidised at 1280°C under atmosphere containing 17% water for:
a) 10 min b) 20 min c) 30 min d) 60 min e) 120 min f) 180 min.

As can be seen in Figure 4.5.3, the Bearing Area curves of the oxide-metal interface of DSP specimens confirmed that the interface roughness of the material augmented as the time of

the oxidation extended. However, the oxide-metal interface profile of this grade was not as rough as the rail steel under the same oxidation condition.

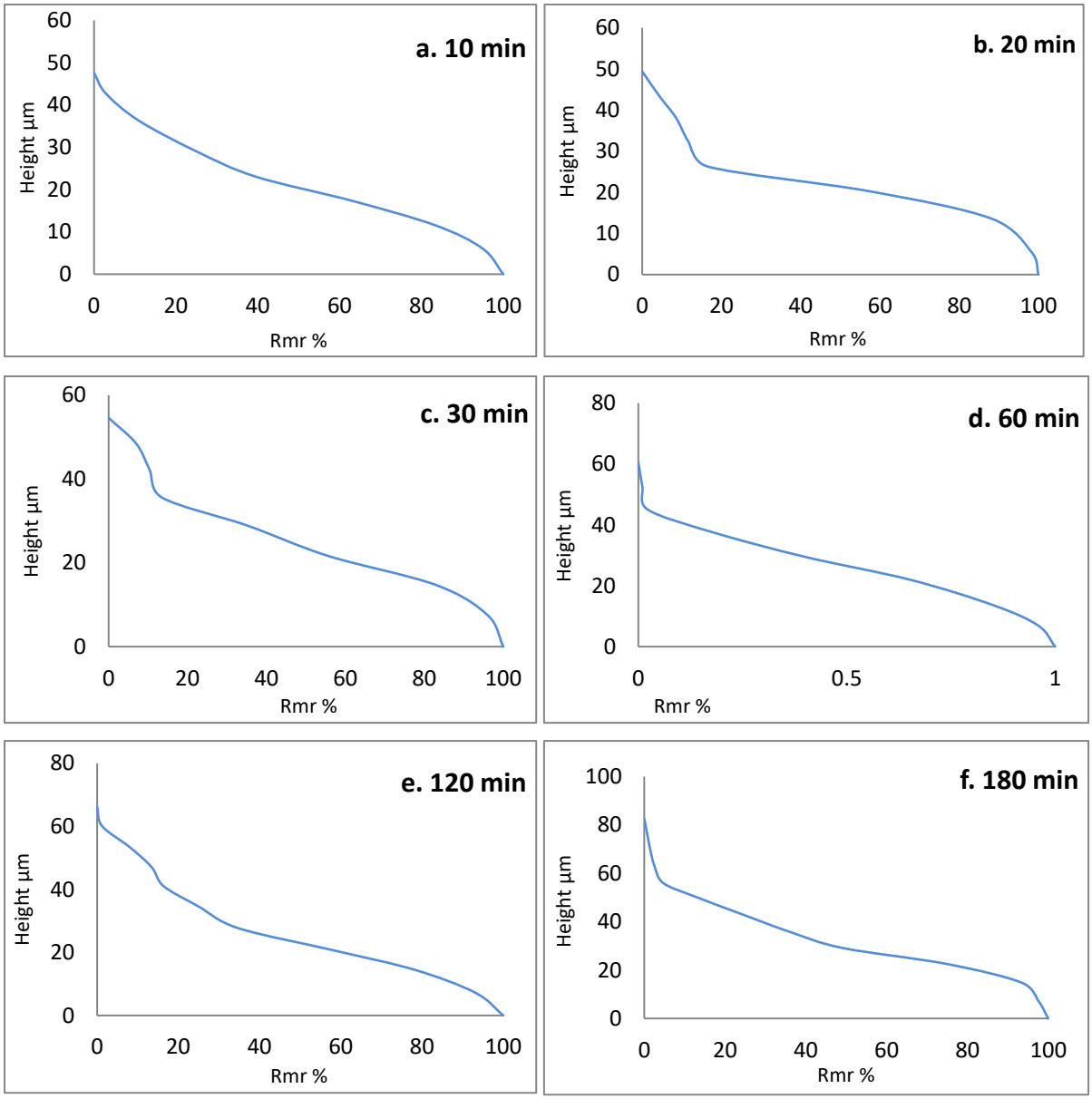

Figure 4.5.4 Bearing Area Curves of the Oxide-Metal interface of DSP steel oxidised at 1150°C under atmosphere containing 17% water for:
a) 10 min b) 20 min c) 30 min d) 60 min e) 120 min f) 180 min.

The bearing area curves of the oxide-metal interface of DSP samples for oxidation temperature of 1150˚C are displayed in Figure 4.5.4. Like the previous scenario, the roughness of the interface increased by extending the oxidation time; however, the amplitude of the roughness under this condition was smaller than oxidation at 1280˚C.

Chapter 5

Results II: Thermomechanical evaluations of the oxide scales

5.1 Introduction

The outcomes of thermomechanical experiments for evaluation of the behaviour of oxide scales at elevated temperature are reviewed in the present chapter. The deformation and behaviour of the oxide scales and substrate metal in an industrial rolling mill are very complex, and it is almost impossible to be replicated as a single comprehensive test in the lab. Two individual types of high temperature tests were designed to evaluate the behaviour of the oxide scales under mechanical load at high temperature. Initially, a uniaxial compression test was designed to investigate the deformation behaviour of the oxide scale under a load at elevated temperature, as explained in Section 3.5. Subsequently, a new technique was developed to evaluate the thermomechanical properties of oxide scale under tensile stresses, which was based on previous studies (see Section 3.4). Furthermore, visual inspection, optical microscopy and SEM, including BSE imaging and EDX, were used to study the deformation patterns, failure modes, microstructural evolutions, and chemical compositions of the oxide scales.

5.2 Hot Compression Test

The details of high temperature compression tests procedure were described in Section 3.5. All specimens were oxidised for 60 minutes under dry air with a flow rate of 4 lit/min. The oxidation temperatures were set to 1280˚C for rail steel and 1150˚C for DSP steel. The oxidation resulted in the development of homogeneous oxide scales with an average thickness of 723 µm and 211 µm in rail and DSP steel specimens respectively. Before deformation, argon was injected into the chamber to eliminate further oxidation of the material during deformation and cooling stage.

To avoid the sticking of the oxide scales residual on the tool, the surface of the curved area (tip of the tool) was coated with a thin layer of Boron Nitride suspension, using a thin brush. It was noted that the coating powder remained on the surface of the deformed samples and except the tests performed at 1150˚C and 1280˚C, there was no sign of oxide residual on the surface of the tool. The oxidised specimens were deformed in the temperature range 850°C-1280°C. The equipment was under displacement control throughout the test. For all tests, the depth of penetration was set to 2.75 mm (from the oxide scale surface), and the deformation velocity was set to 0.8 mms^{-1}. The displacement, temperature and load were recorded during the deformation stage. After the test, the specimens were cooled down to the room temperature under argon with a flow rate of 4 L/min. The details of the compression test conditions for both steel grades are shown in Table 5.1.

Table 5.1 Test conditions of high temperatures compression experiments.

Test No	Steel Grade	Oxidation Time (min)	Oxidation Temp. (°C)	Deformation Temp. (°C)	Depth of penetration (mm)	Maximum Deformation Load (KN)	Tools Temp (°C)
1	rail	60	1280	850	2.75	13.36	617.00
2	rail	60	1280	950	2.75	10.32	678.00
3	rail	60	1280	1050	2.75	6.16	759.00
4	rail	60	1280	1150	2.75	4.63	800.00
5	rail	60	1280	1280	2.75	2.71	895.00
6	DSP	60	1150	850	2.75	6.86	617.00
7	DSP	60	1150	950	2.75	3.87	678.00
8	DSP	60	1150	1050	2.75	2.58	759.00
9	DSP	60	1150	1150	2.75	1.82	800.00

5.2.1 Macro observation of deformed specimens

After cooling down to the room temperature, the deformed oxidised specimens were visually inspected and photographed using a Fuji FinePix HS10 HS11 digital camera (resolution: 3648x2736 pixels).

5.2.1.1 Compression tests of rail steel

Figures 5.2.1.1.1 demonstrates the rail steel samples deformed at various temperatures. As can be seen, the oxide scale on the sidewall of all specimens was fractured and entirely or

partially flaked off. On the top surface of the specimens, the oxide scales cracked and failed within the area around the arc of contact. The amount of damage was subject to the deformation temperature. At 850˚C, the oxide scales failed in a brittle manner, and the scales fractured at the edge of the arc zone.

Furthermore, the scales on the sidewalls almost entirely peeled off. As shown in Figure 5.2.1.1.1.b, the highest number of cracks and defects were apparent in the sample deformed at 950˚C. This was due to the chemical compositions and phase distribution of the oxide scales, which would be explained in cross-sectional analysis later. Deformation of the specimens at higher temperatures showed that the oxide layers behaved more ductile, and the extent of failure reduced.

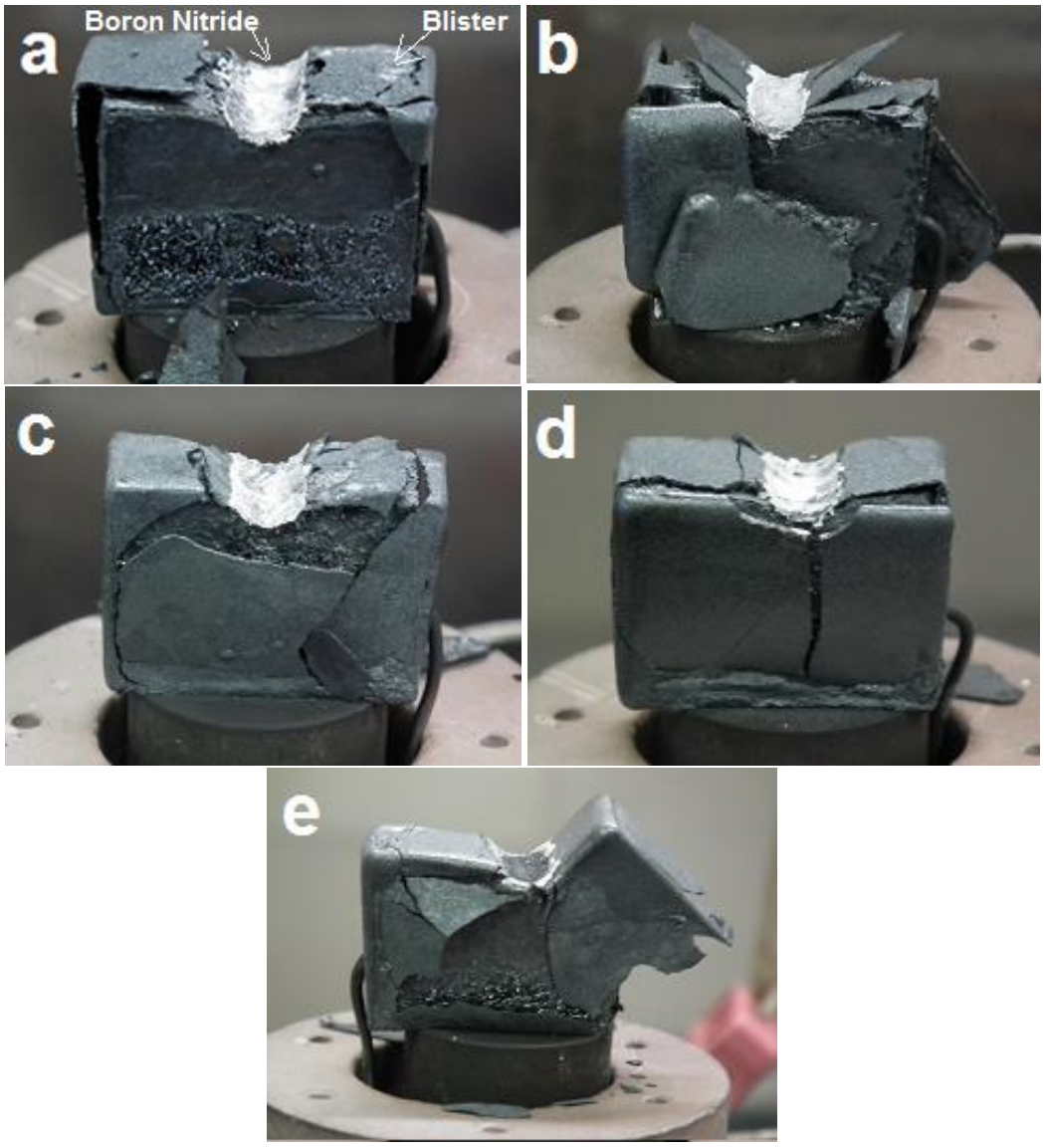

Figure 5.2.1.1.1 rail steel specimens after Hot compression tests deformed at a.850˚C b. 950˚C c. 1050 ˚C d.1150 ˚C e.1280 ˚C

Under these conditions, the bonding between the scale and substrate steel was weak, and the oxide scales were delaminated from the substrate at the early stage of deformation. It was interesting to note that during the deformation at 1280°C, the oxide scale buckled and lifted on the side of the arc of contact. This confirmed the ductile behaviour of the oxide scale under this condition. The other type of defects was oxide blistering, which was only observed in specimens deformed at 850°C and 1050°C.

5.2.1.2 Compression tests of DSP steel

Figures 5.2.1.2.1 display the DSP specimens oxidised at 1150˚C for 60 minutes and deformed at 850˚C, 950˚C, 1050˚C and 1150˚C. The maximum applied loads were recorded as 6.86 KN, 3.87 KN, 2.58 KN and 1.82 KN respectively. The produced oxide scales in all samples were thinner (~210 µm) and denser in comparison to the rail steel samples oxidised at a higher temperature. However, the bonding between the oxide scale and the substrate material was weak.

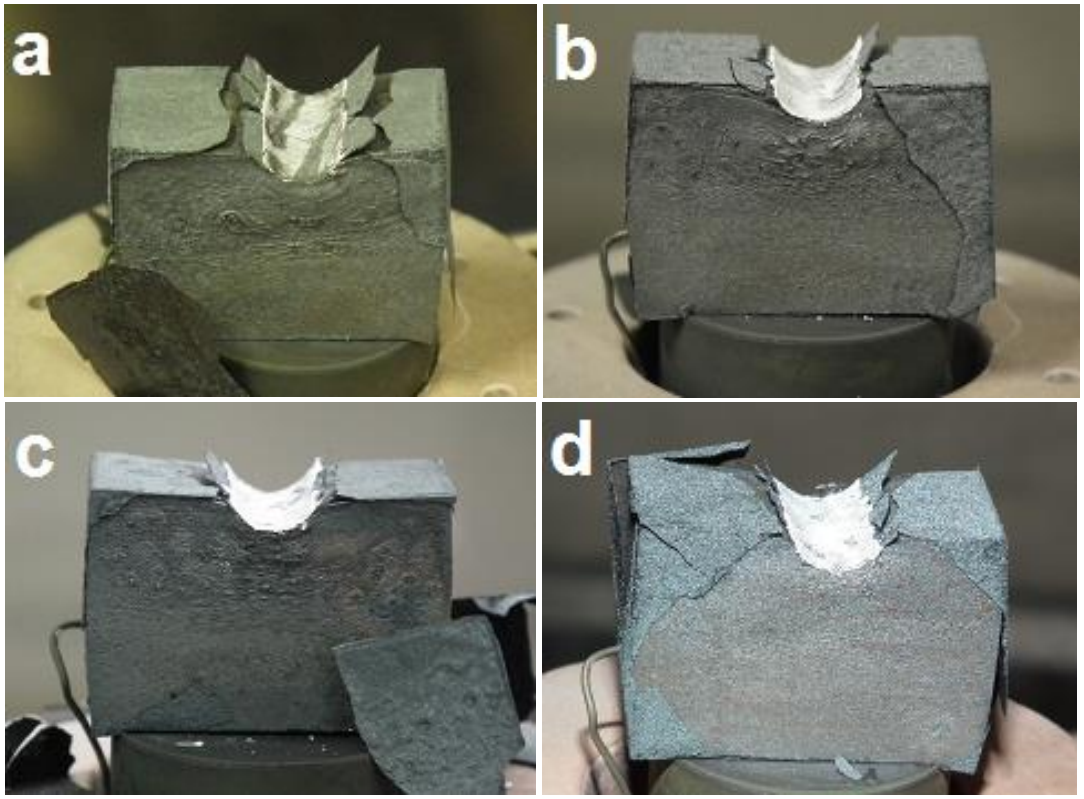

Figure 5.2.1.2.1 DSP steel specimens after Hot compression tests deformed at:
a.850˚C b. 950˚C c. 1050 ˚C d.1150 ˚C

On the top surface of all specimens, oxide scale fractured parallel to the compression tool in both sides of the arc zone. Furthermore, the residual oxide scales were lifted towards the compression tool at both sides of the arc zone. Although initial macro observations showed similar failure mode among all samples, later cross-sectional examinations revealed that the nature of defects and microstructure of crushed oxide scales were different for each test condition.

5.2.2 Cross section analysis

The general condition of the oxide scales, including morphology, microstructure and phase distribution were examined using optical microscopy and SEM.

5.2.2.1 Cross section observations of undeformed specimens

Figure 5.2.2.1.1.a illustrates the cross-section of the top surface of a non-deformed rail steel specimen, oxidised at 1280˚C for 60 minutes. The developed oxide scale was dense and homogenous. Two transverse cracks were apparent across the scale, which might develop during sample preparation. The oxide scale contained a thin layer of Hematite as the outermost layer, Magnetite in the mid-section and Wüstite with Magnetite precipitates at the lowermost segment.

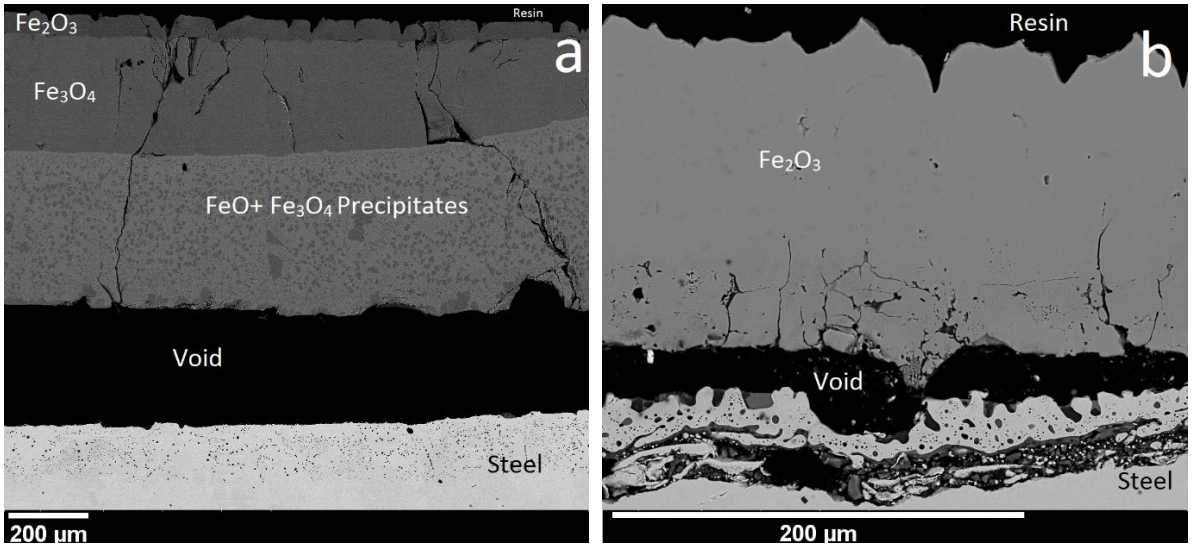

Figure 5.2.2.1.1 Non-deformed hot compression specimens oxidised for 60 minutes:
a. rail steel, at 1280˚C b. DSP steel, at 1150˚C

Figure 5.2.2.1.1.b demonstrates the cross-section of a non-deformed DSP steel specimen oxidised at 1150˚C for 60 minutes. The oxide scale mainly constructed of Hematite with a small quantity of Fayalite at the bottom section in forms of narrow lines. There were no signs of porosity, voids or porosities across the oxide scale. The oxide-metal interface was relatively rough, which was due to the development and growth of Fayalite at surface and subsurface of the interface.

5.2.2.2 Cross-section analysis of deformed rail grade

- **Deformation at 850˚C**

Figures 5.2.2.2.1.a demonstrates the backscattered image of the arc of contact area from a rail steel specimen deformed at 850˚C. As shown the highest amounts of defects, including voids and cracks, developed at the top section of the oxide scale. Few partial transverse cracks were visible on the bottom section of the oxide layer. Furthermore, a curved crack elongated parallel to the oxide-metal substrate. Figure 5.2.2.2.1.b shows the highlighted zone in the previous image. The contrast between different zones confirmed the presence of Hematite at the top section, Magnetite in the middle and Wüstite at the lower level of the oxide layer. Small amounts of Fayalite were present at the oxide-metal interface and below the metal surface. It is clear the most of the damage occurred within Magnetite and Hematite phases.

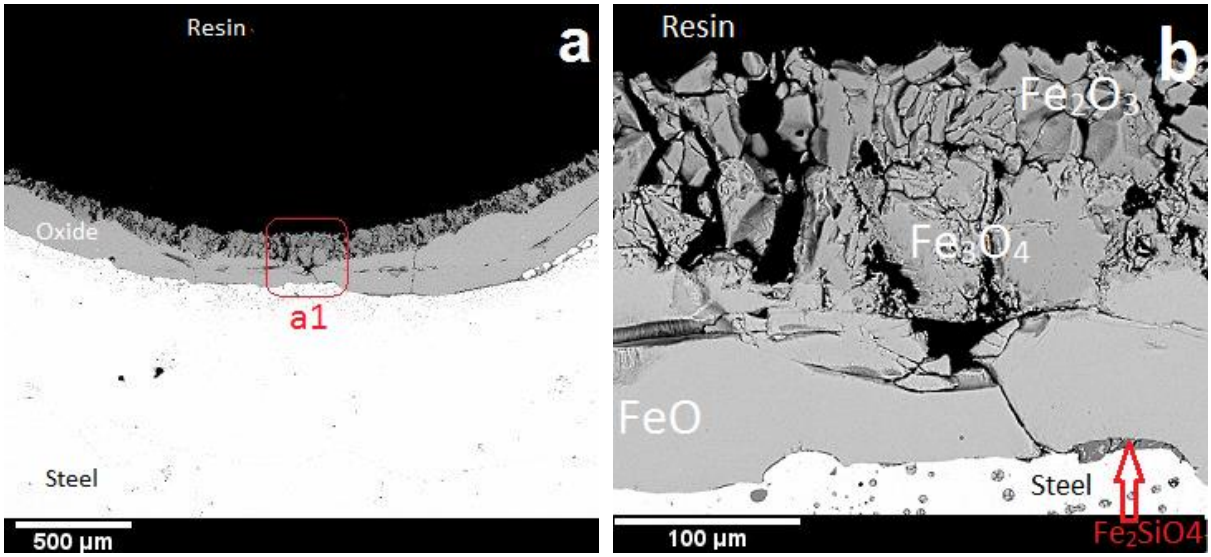

Figure 5.2.2.2.1 a. Oxide scale microstructure of rail steel deformed at 850˚C (Tox = 1280˚C, oxidation 60min) b. high magnification image of zone a1 in image a.

- **Deformation at 950˚C**

The optical image of the cross-section of a rail specimen deformed at 950˚C is shown in Figure 5.2.2.2.2.a. Through transverse cracks and partial transverse cracks developed across the arc of contact. Although defects such as cracks, pores and large voids were visible throughout the oxide scale, in contrast to deformation of material at a lower temperature the oxide scale did not crush into small particles at the top region. In a few locations around the oxide-metal interface, the substrate steel marginally penetrated the oxide scale. As shown in Figure 5.2.2.2.2.b, the oxide scale mainly comprised of Magnetite; however, at the outermost part of the oxide scale thin layer of Hematite was present. In addition, a small amount of Wüstite formed at the lower regions of the Magnetite phase. Fayalite was visible as a very thin dark layer between next to the oxide-metal interface, but it also diffused into the cracks and defects within the structure of the oxide scale.

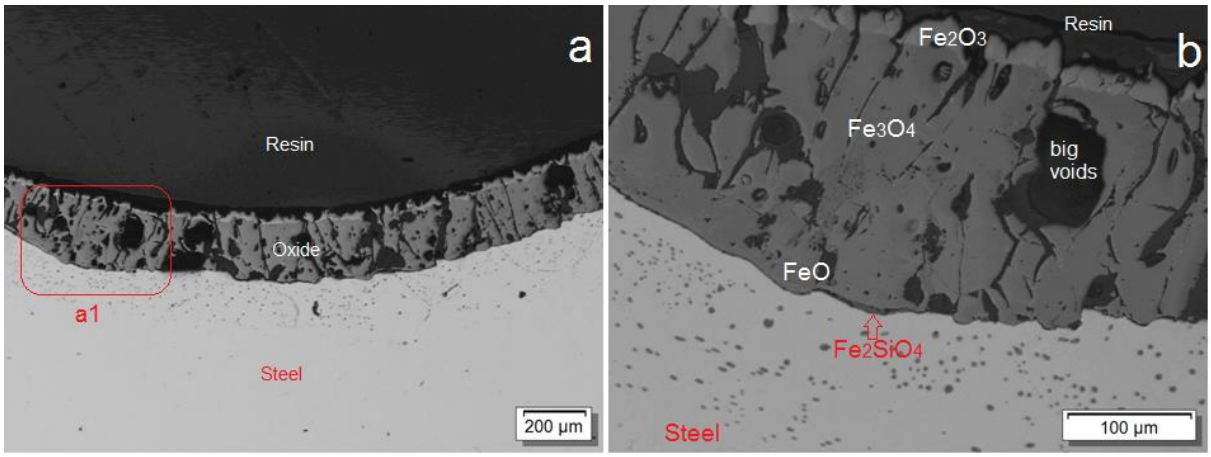

Figure 5.2.2.2.2 a. Optical images of oxide scale microstructure for a rail steel sample, deformed at 950˚C (Tox = 1280˚C, oxidation 60min) b. High magnification image of zone a1 in image a.

- **Deformation at 1050˚C**

The cross-section of deformed rail grade specimen at 1050˚C is shown in Figures 5.2.2.2.3.a and b. It is evident that even at 1050˚C, the areas containing Fe_2O_3 and Fe_3O_4 crushed under the compressive load confirming the brittleness of these phases at this temperature. Partial extrusions of metal substrate were visible across the scale (a1, a2, b1 and b2). At the side of the contact arc, the oxide scale detached from the substrate metal by developing through thickness crack, and it slightly lifted towards the compression tool. Figure 5.2.2.2.3.c is a

higher magnification image of zone a3. The EDX analysis confirmed the existence of Hematite, Magnetite and Wüstite within the oxide layer. As can be noted at the zone a3 the thickness of the Wüstite was insignificant, therefore developed cracks at the top of the scale, easily propagated through this phase. In contrast, wherever the thickness of FeO was considerably higher, the crack propagation significantly reduced or eliminated (see zone a4). The EDX analysis confirmed the presence of Fayalite, Wüstite and Manganese within the internal oxidation zone.

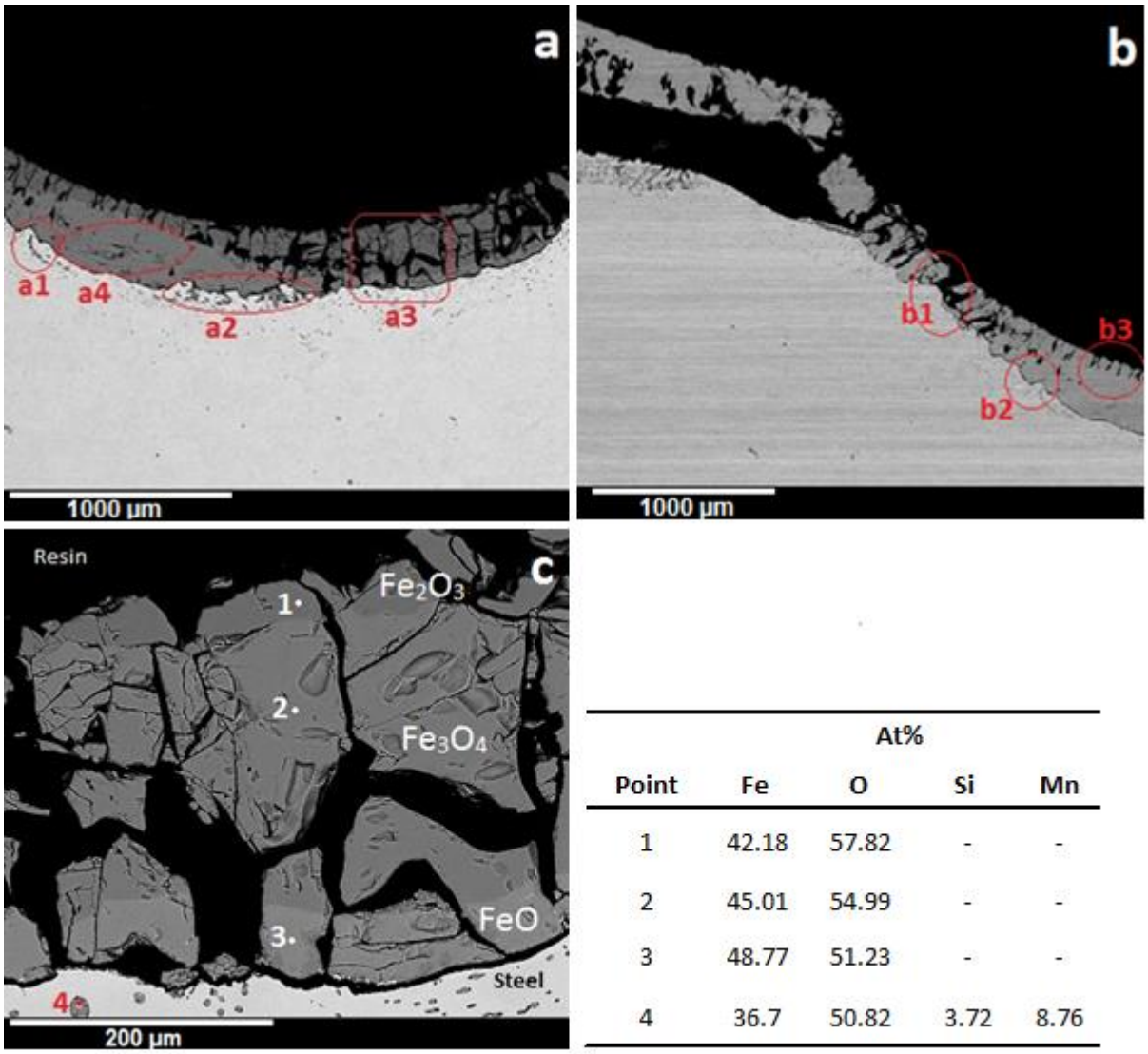

	At%			
Point	Fe	O	Si	Mn
1	42.18	57.82	-	-
2	45.01	54.99	-	-
3	48.77	51.23	-	-
4	36.7	50.82	3.72	8.76

Figure 5.2.2.2.3 a. Oxide scale microstructure of rail steel deformed at 1050˚C (Tox = 1280˚C, oxidation 60min) b. The side of the arc of the contact c. High magnification image of zone a3 in the image a, including the EDX point analysis.

- **Deformation at 1150˚C**

The microstructure of an oxidised rail steel specimen deformed at 1150˚C is given in Figure 5.2.2.2.4.a. The distributions of the iron oxide phases were more homogenous across the oxide scale in comparison to previous test conditions. Once again, Magnetite behaved in a brittle manner and many transverse cracks and large cavities developed throughout this phase. The number of defects within Wüstite were insignificant; only a few small pores and cracks along with a through thickness crack were visible.

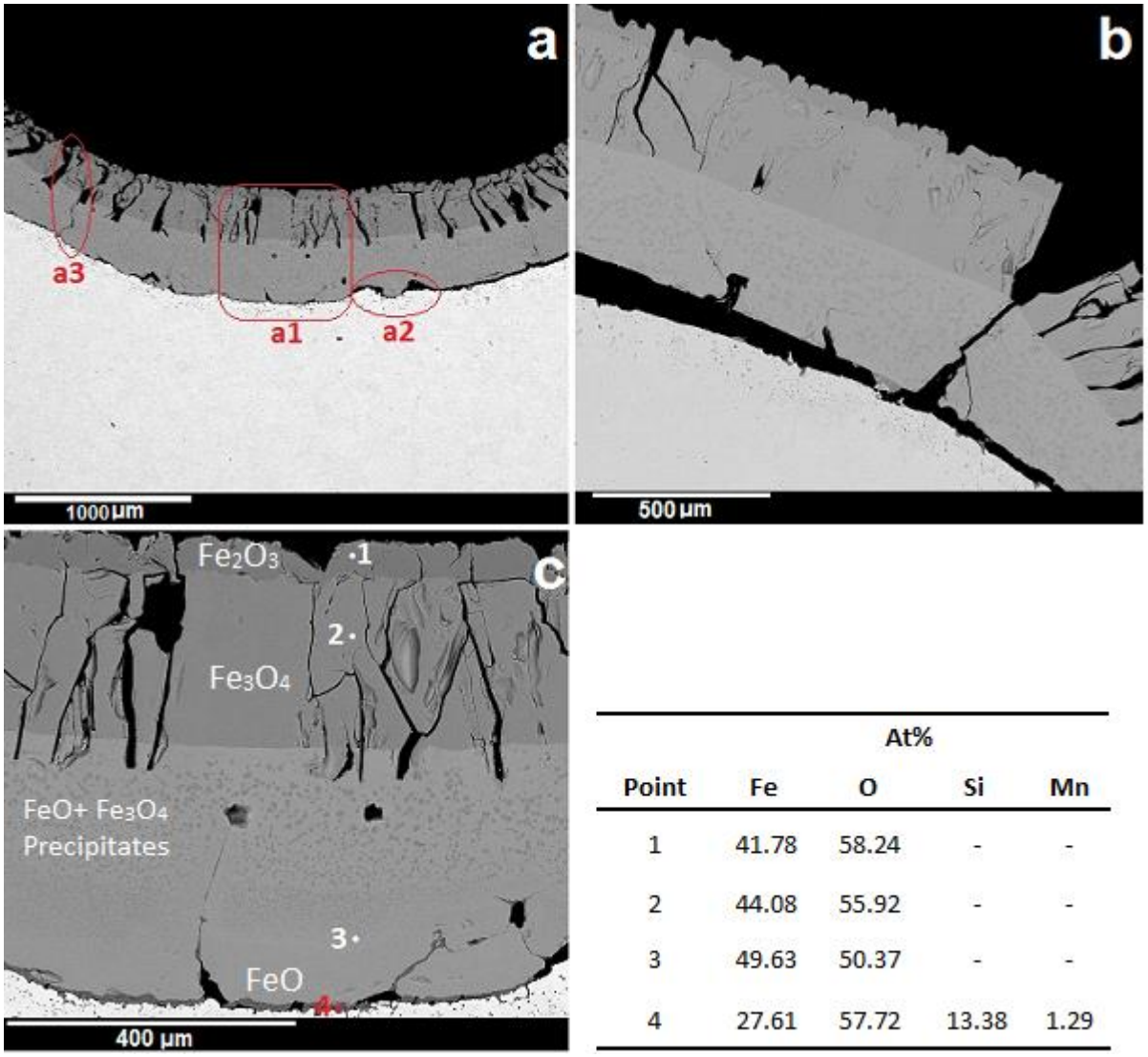

	At%			
Point	Fe	O	Si	Mn
1	41.78	58.24	-	-
2	44.08	55.92	-	-
3	49.63	50.37	-	-
4	27.61	57.72	13.38	1.29

Figure 5.2.2.2.4 a. Oxide scale microstructure of rail steel deformed at 1150˚C (Tox = 1280˚C, oxidation 60min) b. The side of the arc of the contact c. High magnification image of zone a1 in the image a, including the EDX point analysis.

In Figure 5.2.2.2.4.b, the oxide scale failed by development a through thickness crack right above the arc of contact. The EDX analysis confirmed the presence of all three iron oxide

constituents. A thin layer of Fayalite was detected at the oxide-metal interface, which partially entered to the Wüstite defects.

- **Deformation at 1280˚C**

Figure 5.2.2.2.5.a demonstrates the microstructure of a deformed rail steel specimen tested at 1280˚C. In this condition, the applied load formed relatively large cavities within Wüstite matrix where the Magnetite particles precipitated. The nature of Magnetite zone was more ductile in comparison to the results seen in a lower temperature, however as pointed in Figure 5.2.2.2.5.b in certain areas, the scale partially removed from the top of the oxide scale due to sticking effect.

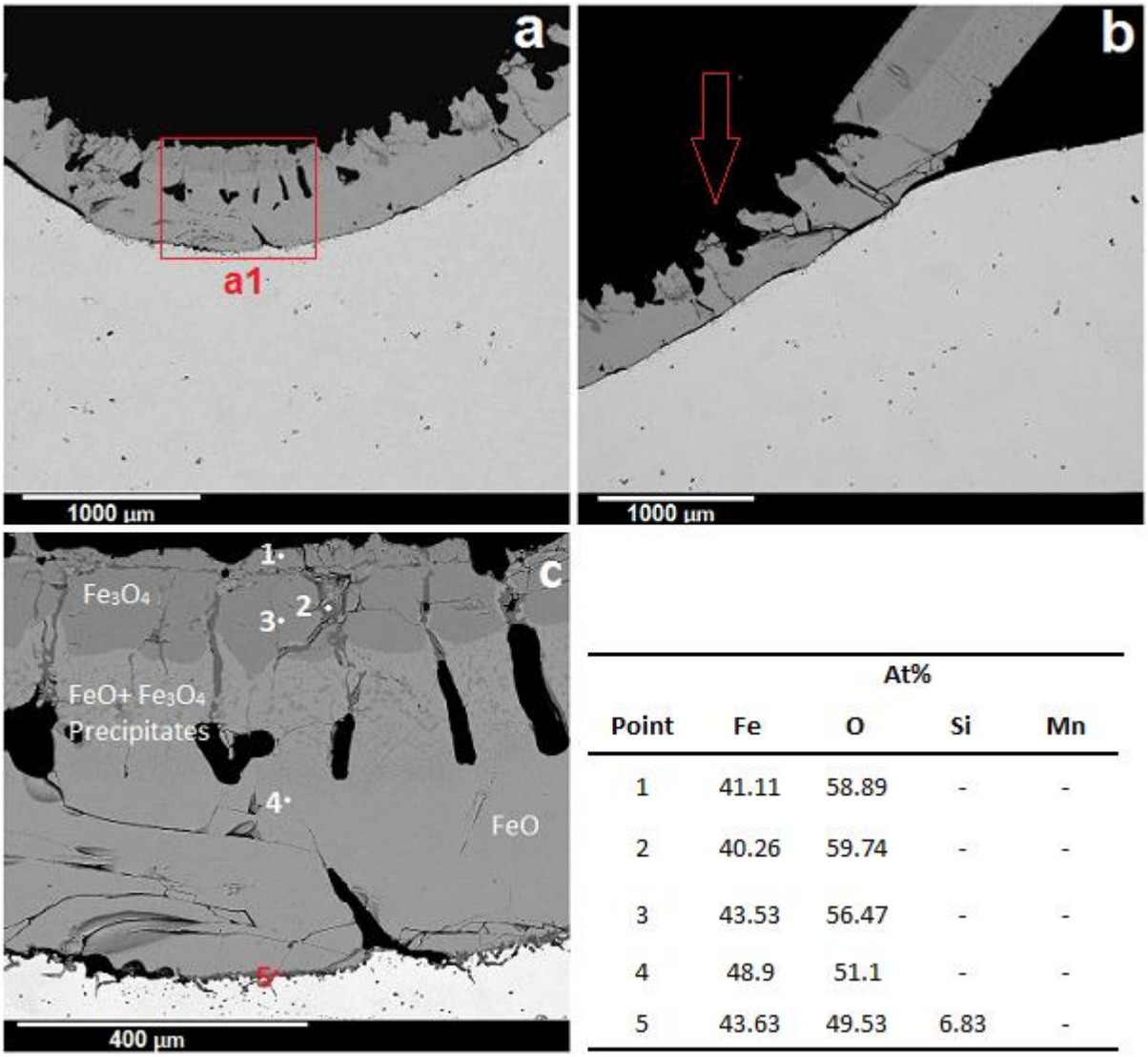

	At%			
Point	Fe	O	Si	Mn
1	41.11	58.89	-	-
2	40.26	59.74	-	-
3	43.53	56.47	-	-
4	48.9	51.1	-	-
5	43.63	49.53	6.83	-

Figure 5.2.2.2.5 a. Oxide scale microstructure of rail steel deformed at 1280˚C (Tox = 1280˚C, oxidation 60min) b. The side of the arc of the contact c. High magnification image of zone a1 in the image a, including the EDX point analysis.

The oxide scale plastically deformed in a ductile manner and as described in the macro observation section, the oxide scale detached from the shoulder of the sample and vastly lifted towards the compression tool. The EDX analysis revealed that Hematite was present within defects across the top section of the oxide scale (Fig. 5.2.2.2.5.c). A thin layer of Fayalite was detected at the oxide-metal interface, which penetrated fissures within the steel matrix.

5.2.2.3 Cross-section analysis of deformed DSP grade

- Deformation at 850˚C

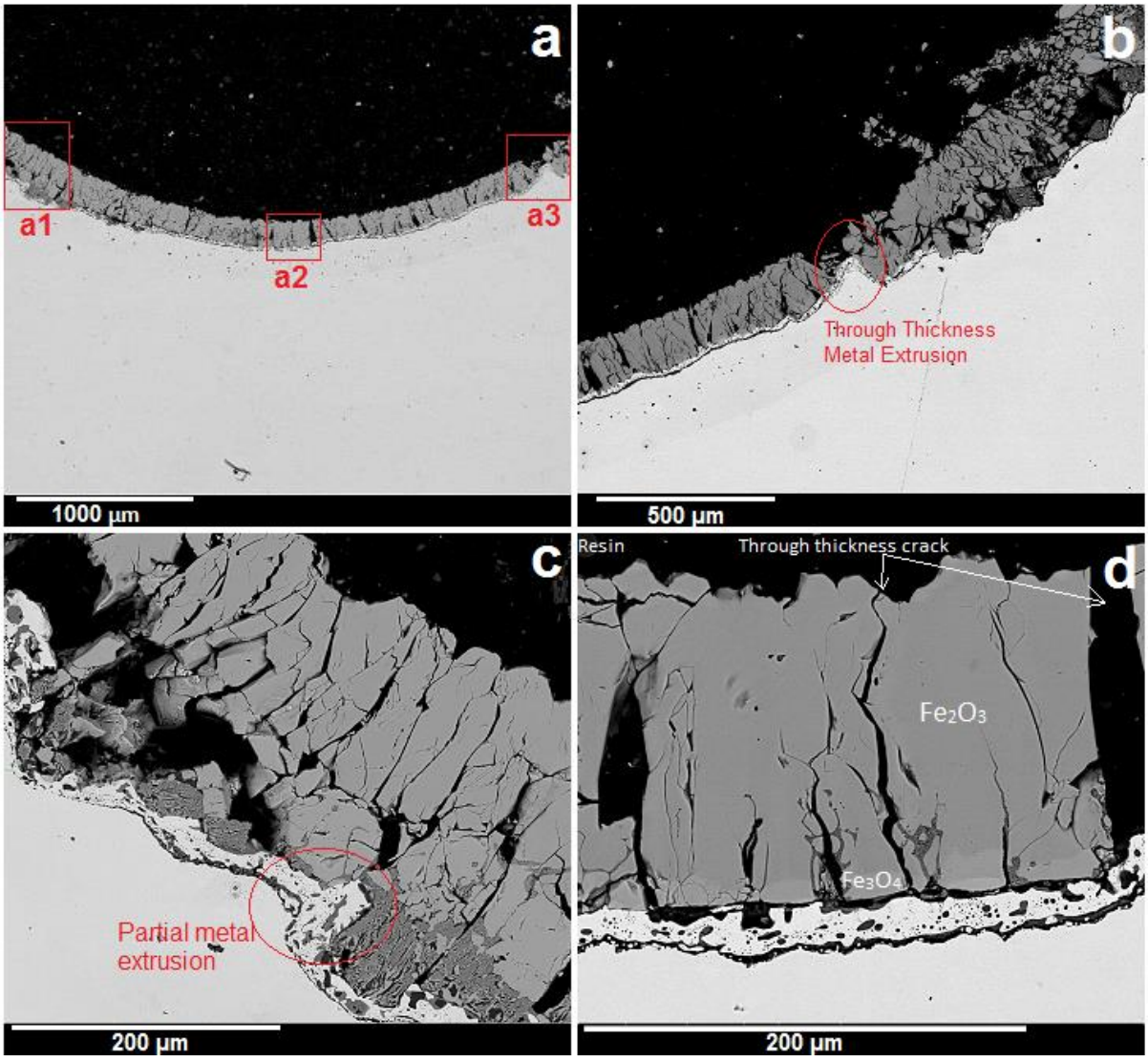

Figure 5.2.2.3.1 a. Oxide scale microstructure of DSP steel deformed at 850˚C (Tox = 1150˚C, oxidation 60min) b. The side of the arc of the contact c. High magnification image of zone a1 d. High magnification image of zone a3.

Figure 5.2.2.3.1.a shows the cross-section of a DSP steel sample deformed at 850˚C. Many through thickness transverse cracks were visible across the deformed oxide scale, which

confirmed the brittle failure of oxide scale under compressive load at this temperature. The scale mainly constructed of Fe_2O_3 but small amounts of Fe_3O_4 formed in the bottom of the oxide layer next to the oxide-metal interface (Figure 5.2.2.3.1.d). At the middle region of the arc, Fayalite phase was present as isolated dark particles within the steel matrix or as continues dark line below the interface. In contrast, in both sides of the deformation curve, Fayalite penetrated into micro-cracks and micro-cavities at the bottom of the oxide layer, as demonstrated in Figure 5.2.2.3.1.c. Through thickness and partial extrusion of metal into the oxide, the scale is shown in Figures 5.2.2.3.1 b and c, respectively.

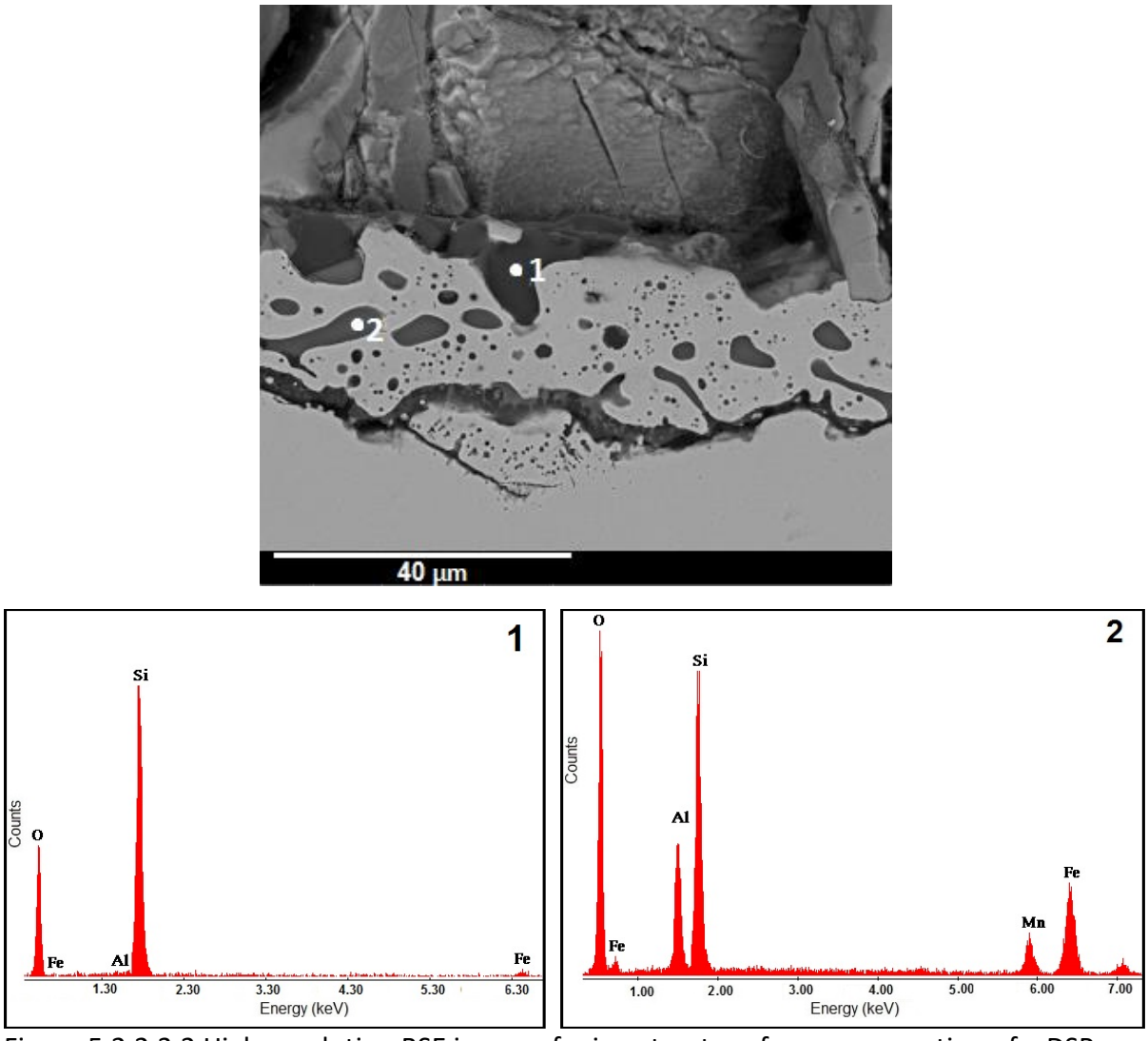

Figure 5.2.2.3.2 High-resolution BSE image of microstructure from cross section of a DSP steel sample deformed at 850˚C (Tox = 1150˚C, oxidation 60min) and EDX plots from the points 1 and point 2 marked on the image.

High-resolution BSE image of the oxide-metal interface and the associated EDX plots are shown in Figure 5.2.2.3.2. The analysis of the revealed that at the oxide-metal interface along

with Fe_2SiO_4 Silica phase (SiO_2) formed. At point 2, the EDX pattern indicated that Fayalite enriched with aluminium possibly in the form of formed of $FeAl_2O_4/Fe_2SiO_4$.

- Deformation at 950˚C

The cross-section of a curved deformation zone a DSP steel specimen at 950˚C is shown in Figure 5.2.2.3.3.a. Like failure of the oxide under the previous condition, through transverse cracks developed across the oxide scale. Partial metal extrusion was apparent in many different locations across the site.

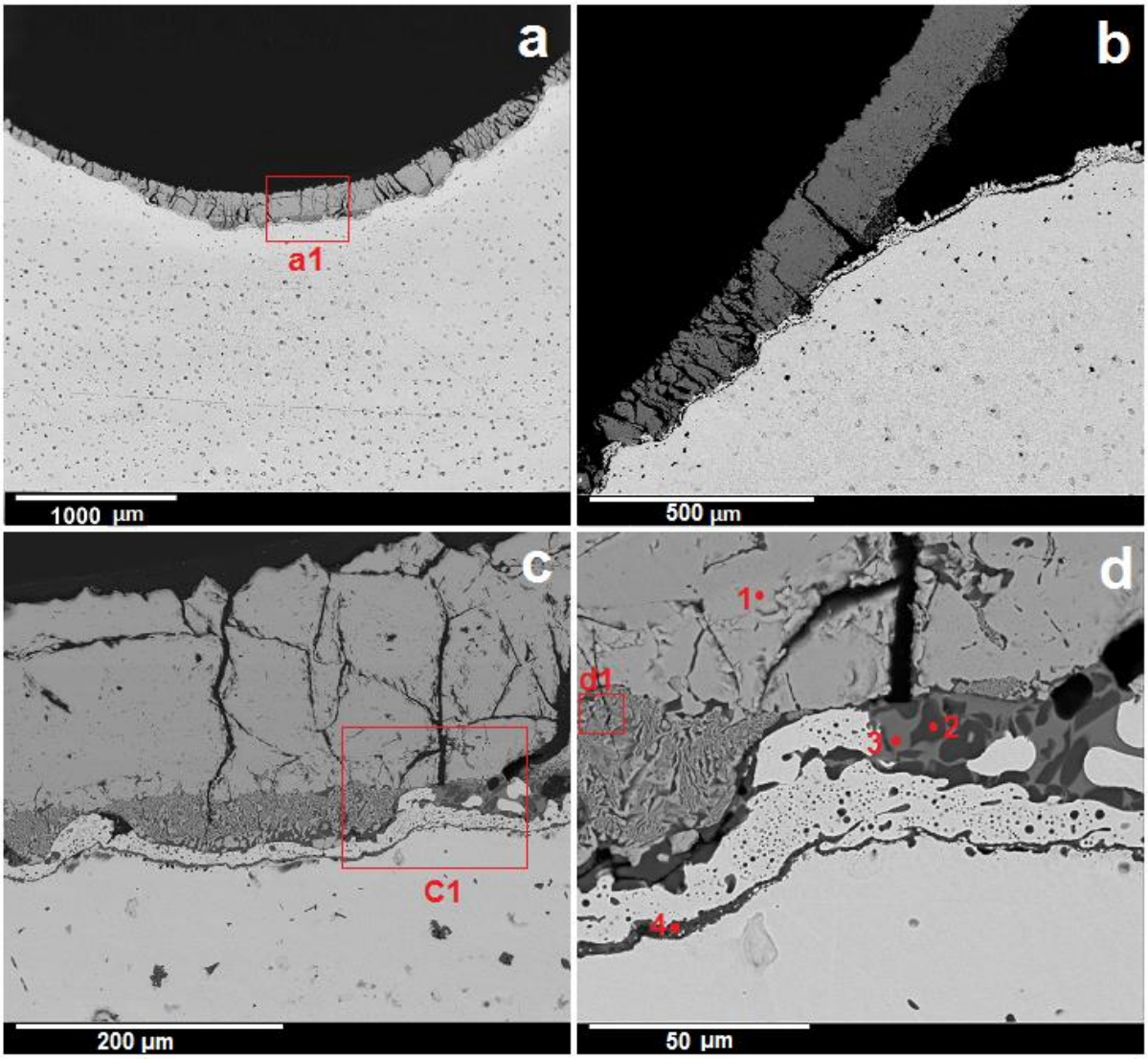

Figure 5.2.2.3.3 a. Oxide scale microstructure of DSP steel deformed at 950˚C (Tox = 1150˚C, oxidation 60min) b. The side of the arc of the contact c. High magnification image of zone a1 in image a. d. High magnification image of zone c1 in image c.

Figure 5.2.2.3.3.b shows the side of the deformation zone of the same sample. As can be seen the oxide was delaminated from the top surface and raised towards the compression tool,

which indicated the week bonding between the unreformed oxide scale and substrate metal. Figures 5.2.2.3.3 c and d clearly show that the cracks not only developed in transverse direction but also, they formed longitudinally.

The EDX plots from the points in image d are given in Figure 5.2.2.3.4. Once more, the main phase of the oxide scale was identified as Hematite, but there was no evidence of Magnetite. Also, Fayalite was present around the oxide-metal interface, which diffused into the micro-cavities under the compressive load. As can be seen in Figure 5.2.2.3.4.d minor quantity of Silica (SiO_2) was detected next to the oxide-metal interface; this can be seen as a dark phase (point 2) embedded in Fayalite matrix (Fig. 5.2.2.3.3.d).

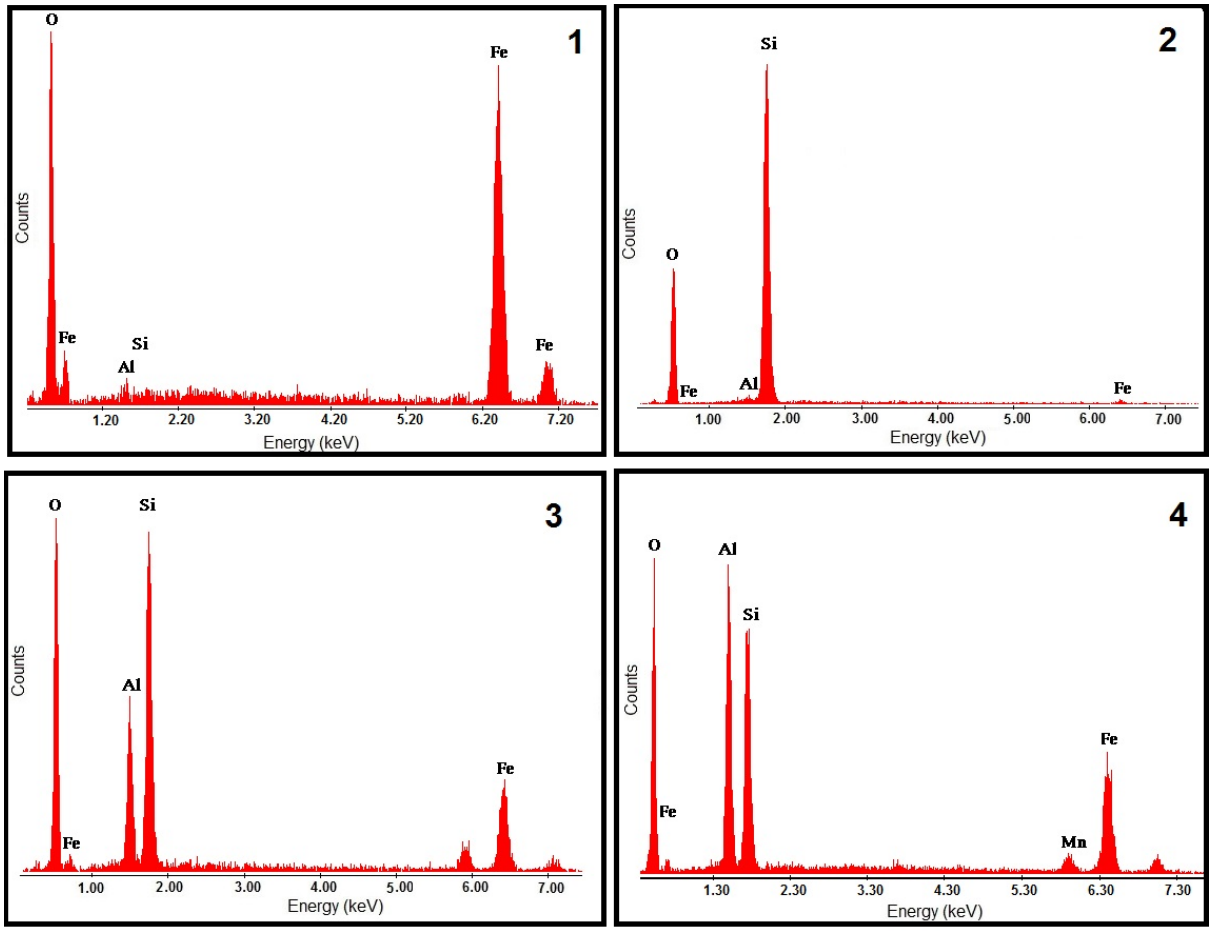

Figure 5.2.2.3.4 EDX plots from the points marked in Figure 5.2.2.3.3

High magnification of complex microstructure of bottom of the oxide layer marked as zone d1 in Figure 5.2.2.3.3.d is demonstrated in Figure 5.2.2.3.5. The EDX plot of the dark grey phase at point 1 confirmed that Silica, along with Fayalite penetrated the micro-cavities within

the lower section of Hematite. The EDX analysis at point 2 confirmed the presence of Fayalite within the complex zone.

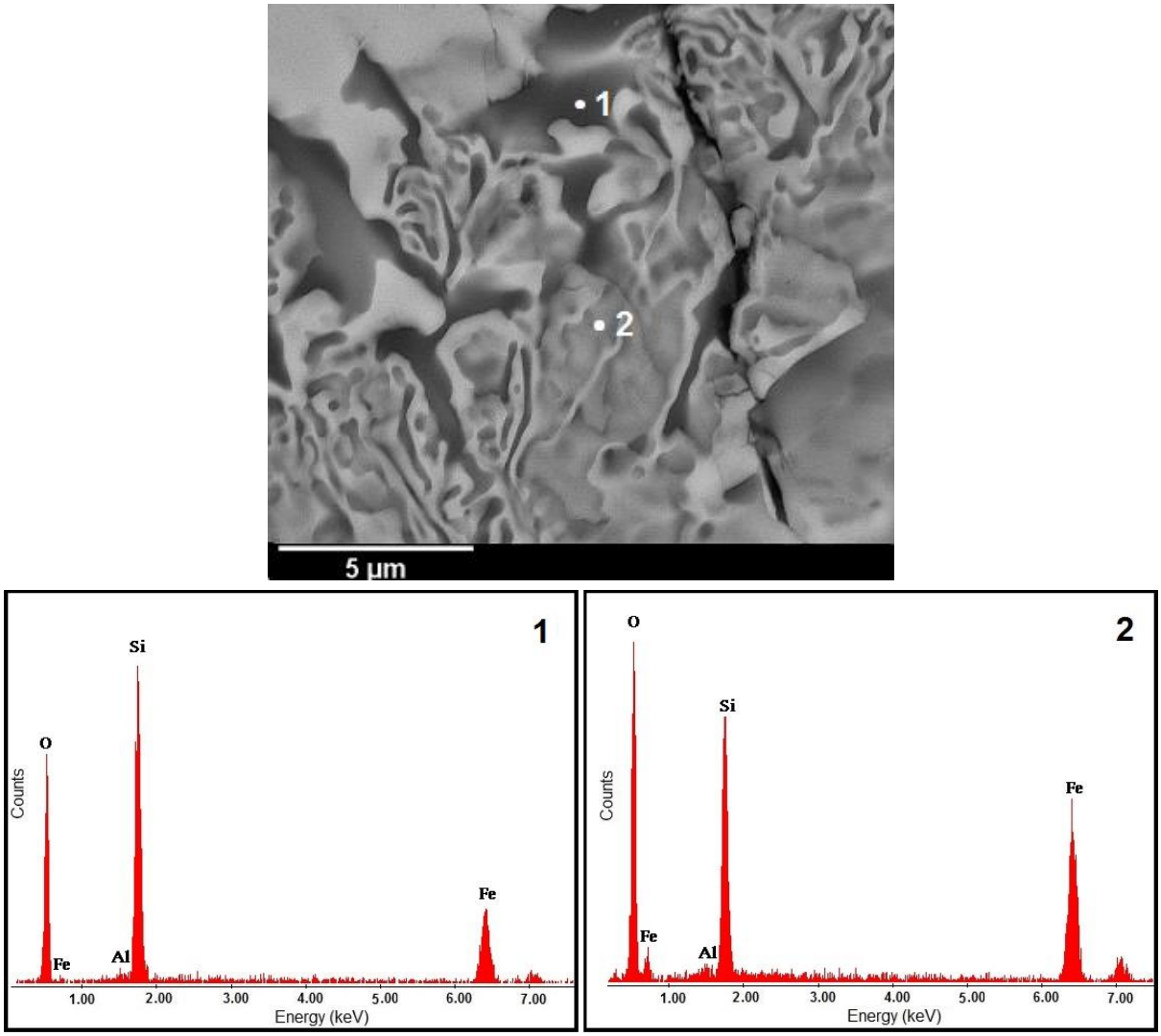

Figure 5.2.2.3.5 High-resolution BSE image of microstructure of a DSP steel sample cross-section deformed at 950˚C (Tox = 1150˚C, oxidation 60min) and EDX plots from the points 1 and point 2 marked on the image.

- Deformation at 1050˚C

Figure 5.2.2.3.6.a shows the microstructure of the cross-section of the deformation for a DSP steel specimen tested at 1050˚C. Like deformation of the material at lower temperature through transverse cracks formed across the oxide scale, however, the number of the cracks reduced significantly. Throughout the arched deformation area, partial metal extrusions into the oxide scale were apparent in many locations such as zones a1 and a2. The cross-section of the side of the deformed area is shown in Figure 5.2.2.3.6.b. As pointed in the image

through thickness extrusion of substrate metal was apparent at the top of the arc of the contact. The oxide scale on the shoulder of the sample detached from the interface and lifted towards the compression tool.

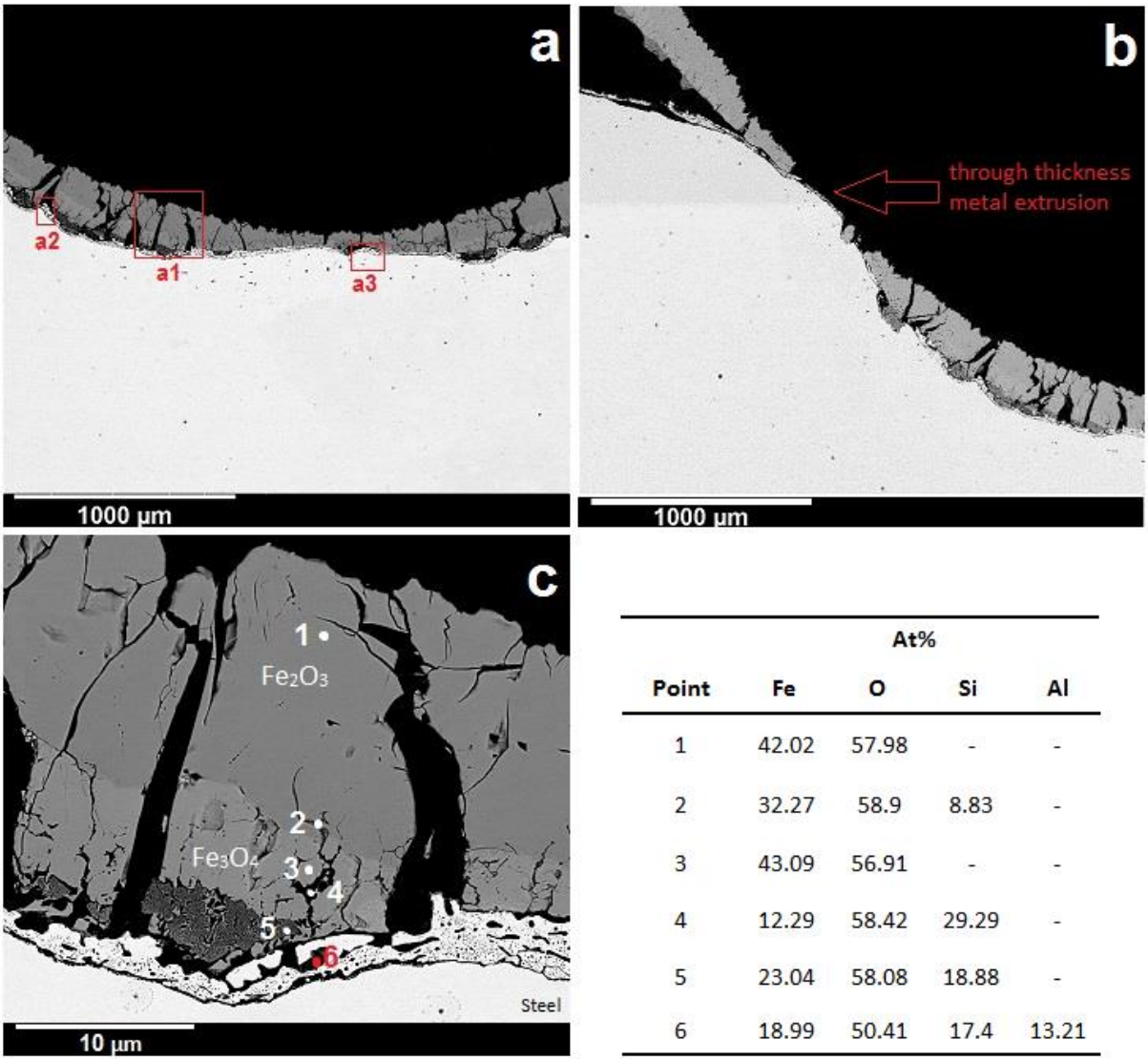

	At%			
Point	Fe	O	Si	Al
1	42.02	57.98	-	-
2	32.27	58.9	8.83	-
3	43.09	56.91	-	-
4	12.29	58.42	29.29	-
5	23.04	58.08	18.88	-
6	18.99	50.41	17.4	13.21

Figure 5.2.2.3.6 a. Oxide scale microstructure of DSP steel deformed at 1050˚C (Tox = 1150˚C, oxidation 60min) b. The side of the arc of the contact c. High magnification of zone a1 in the image a, including the EDX point analysis.

High-resolution BSE image of the zone a1 is given in Figure 5.2.2.3.6.c. The phase composition of the labelled locations was analysed via EDX. Hematite was the predominant phase, which developed at the outermost region of the oxide scale. A noticeable amount of Magnetite formed at lower section like testing the material at lower temperatures. Fayalite partially diffused into Hematite phase by passing through Magnetite layer. Furthermore, Silica and Fayalite penetrated to the lowermost section of the oxide scale and formed a complex

microstructure adjacent to the metallic substrate (point 5). At the oxide-metal interface, high concentration of Al was detected within the Fayalite phase, which indicated the presence of alumina in that region.

- Deformation at 1150˚C

The oxide scale morphology of the deformation zone of a DSP specimen after compression test at 1150 ˚C is shown in Figure 5.2.2.3.7.a. The roughness of the oxide-metal interface was much smoother than previous test conditions and only at point a2, a through thickness extrusion was observed. Like deformation at 1050˚C multiple through thickness cracks formed along the deformation radius however the number of the cracks reduced. At the side of the contact area, the number of defects was significantly less than the central deformation zone and thick undamaged piece of the oxide scale raised outside of the tool contact zone as shown in Figure 5.2.2.3.7.b. High magnification image of the bottom of the contact zone highlighted as zone a1 is shown in Figure 5.2.2.3.7.c. The damage on the top section of the oxide scale represented the sticking effect and removal of the oxide particles by the compression tool during deformation, which was not present at testing the material at lower temperatures. This phenomenon indicated that oxide scale was more ductile in this condition in comparison to the lower testing temperatures. The EDX analysis confirmed the presences of Hematite and Magnetite at top and mid regions, respectively. On below Fe_3O_4 a dense Fayalite layer was apparent, which contained small quantity. The examinations of the oxide scale at point 4, 5 and 6 revealed that by moving towards the oxide-metal interface, the concentrations of Si and Al increased and as a result, the shades of oxide scales darkened. Unlike microstructures of the deformed oxide scales at lower temperatures, no signs of complex penetrations of Fayalite or silica into the main body oxide were observed.

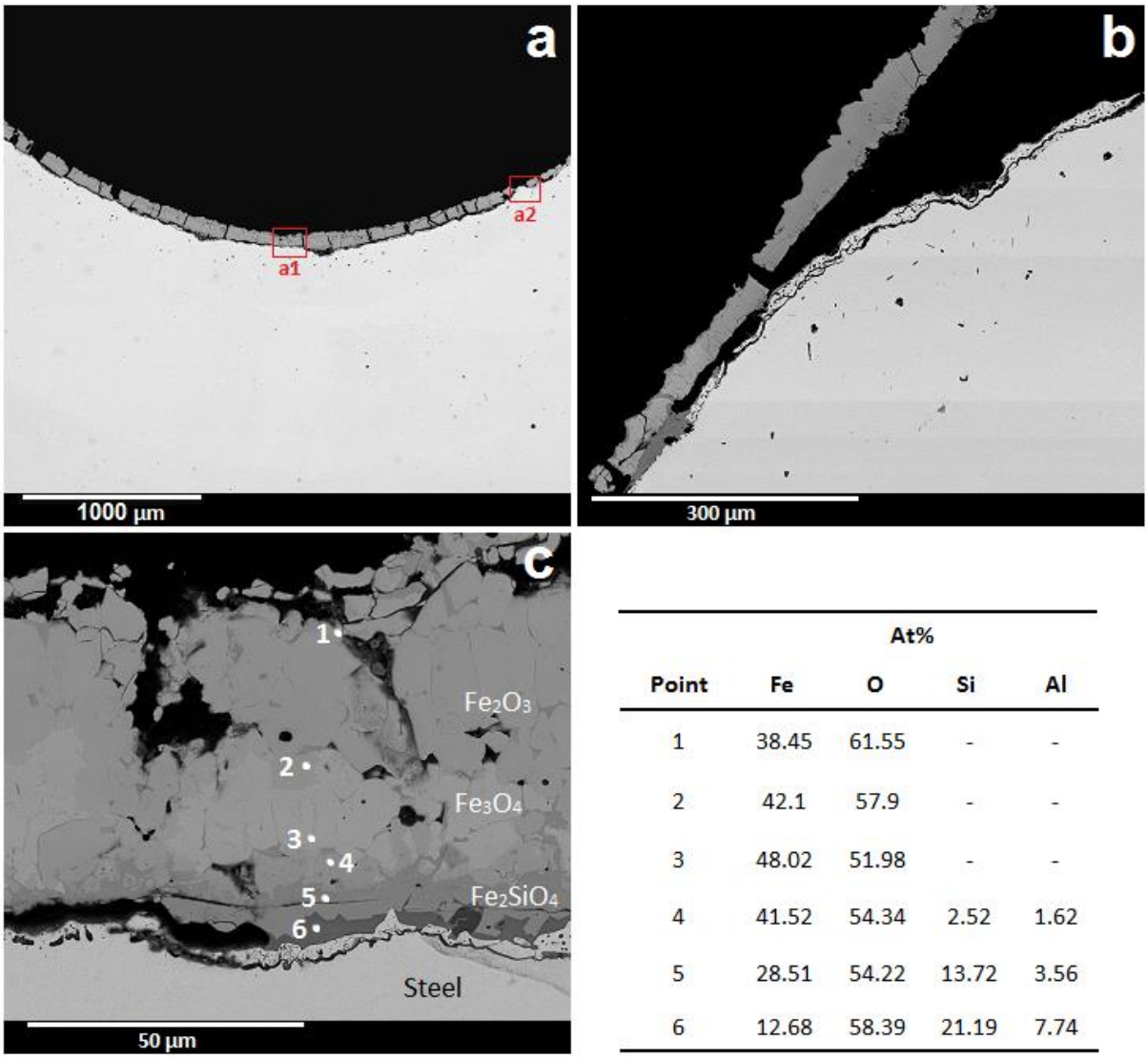

	At%			
Point	Fe	O	Si	Al
1	38.45	61.55	-	-
2	42.1	57.9	-	-
3	48.02	51.98	-	-
4	41.52	54.34	2.52	1.62
5	28.51	54.22	13.72	3.56
6	12.68	58.39	21.19	7.74

Figure 5.2.2.3.7 a. Oxide scale microstructure of DSP steel deformed at 1150˚C (Tox = 1150˚C, oxidation 60min) b. The side of the arc of contact c. High magnification of zone a1 in the image (a) including the EDX point analysis.

5.3 High temperature tensile tests

The behaviour of the oxide scales under uniaxial tensile load at elevated temperature is directly associated with deformation of the material prior to the roll entry in a hot rolling mill. The tests revealed the influence of the composition, microstructure, temperature and scale thickness on the oxide scale failure mode. The tests were carried out following the procedure detailed in Section 3.4. To reduce the thermomechanical bonding between the two segments of the test piece, the joint surfaces of each tensile sample segment was centrally bored to 5 mm depth, to create a tubular gauge with 2mm wall thickness. Furthermore, a thin layer of Boron Nitride was applied on the remaining joint surface (ring shape) using a fine brush. The surfaces of the gauge section were precisely levelled to produce a uniform continuous oxide scale on the surface of both parts.

Table 5.2 High temperatures tensile test parameters.

Test No	Steel Grade	Oxidation Time (min)	Oxidation Temp. (°C)	Deformation Temp. (°C)	Average Thickness (µm)	Ultimate Tensile Strength (MPa)	Residual Elongation (%)
1	rail	60	1150	750	213	8.16	0.12
2	rail	60	1150	850	206	11.60	0.18
3	rail	60	1150	1150	211	7.45	0.20
4	rail	60	1150	1200	215	5.61	0.16
5	DSP	60	1150	750	222	12.75	0.32
6	DSP	60	1150	850	238	5.83	0.12
7	DSP	60	1150	1150	235	7.91	0.56
8	DSP	180	1000	850	99	11.47	0.11

The specimens were oxidised at 1000°C or 1150°C for 60-180 minutes under dry airflow. The deformation was executed between 850°C to 1200°C with a velocity of 0.1mms^{-1}. The machine was under displacement control throughout the test. The high temperature tensile tests parameters are summarised in Table 5.2.

5.3.1 Macro observation of deformed specimens

Deformed test pieces were visually inspected at room temperature, and all were photographed using Fuji FinePix HS10 HS11 digital camera.

5.3.1.1 Macro assessments of deformed rail steel specimens

After the oxidation stage, a continuous oxide layer formed around the gauge length. The surface profile of the oxide scale varied between samples when the specimens stabilised at the required testing temperatures.

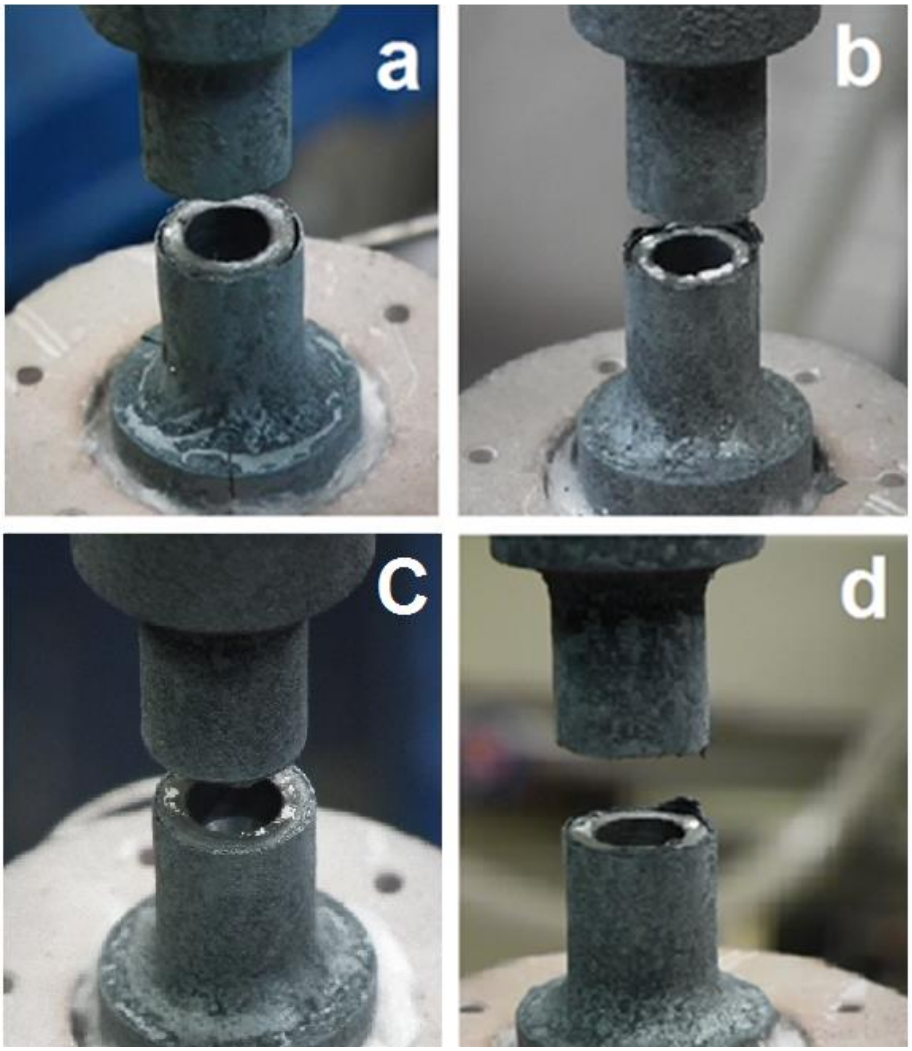

Figure 5.3.1.1 rail steel specimens oxidised at 1150°C for 60 minutes and deformed at: a) 750°C b) 850°C c) 1150°C d) 1200°C

Figures 5.3.1.1 a, b, c and d demonstrate the status of rail steel samples after deformation at 750˚C, 850˚C, 1150˚C and 1200˚C respectively. In all test conditions, the oxide scale failure

occurred by through-thickness cracking, which indicated the bonding between oxide scale and substrate metals was strong relative to oxide scale structural integrity. The failure was due to the initiation and propagation of transverse cracks perpendicular to the load direction. Although two cracks formed at the bottom of the gauge area in the sample tested at 750^{o}C, in all the other specimens, no longitudinal cracks were visible on the surface of the oxide layers around the gauge section. Oxide blistering was apparent across the gauge section of all specimens.

5.3.1.2 Macro assessments of deformed DSP steel specimens

Figure 5.3.2 shows the DSP tensile test pieces deformed under various conditions. Continuous oxide scales developed around the gauge section. Visual inspections confirmed that no surface defects such as longitudinal cracks and blisters were visible within gauge area after deformation stage. The oxide scale of the DSP grades under tensile stresses exhibited two different behaviours depending on the scale thickness. The specimens shown in Figures 5.3.1.2 a, b and c were oxidised at 1150˚C for 60 minutes, and the average thickness of the oxide layer for each sample measured as 222 µm, 238 µm and 235 µm respectively. As can be seen, regardless of the test temperature, the oxide scale failed by sliding along the oxide-metal interface that confirmed that the interface was weaker than the oxide scale structural integrity under these test conditions. At the end of deformation at 750˚C and 1150˚C, the oxide scales separated from the top part of the test piece at the edge of the curved area on top of the gauge. At 850˚C the oxide scale separation occurred at the within the top section of the gauge, slightly below the curved area. Figure 5.3.1.2.d displays a specimen oxidised at 1000˚C for 180 minutes and deformed at 850˚C. This test condition was selected to evaluate the effect of the oxide scale thickness on the failure mode. Under this test condition, the failures occurred by through-thickness fracture, which indicated that the bonding between the oxide scale and substrate metal was stronger than the oxide scale structure. Despite lower oxidation temperature, the surface profile of the oxide scale was much coarser than the oxide scale developed in previous conditions.

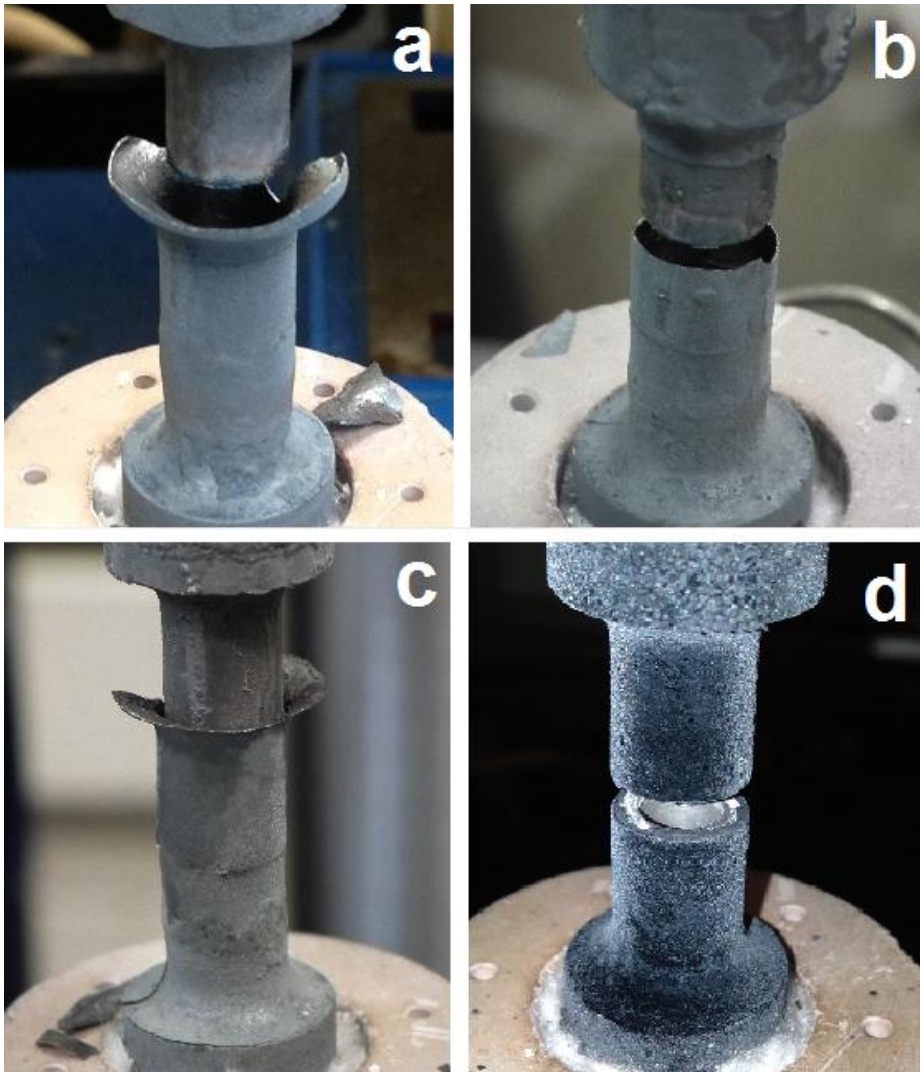

Figure 5.3.1.2 rail steel specimens oxidised at 1150°C for 60 min and deformed at:
a) 750°C b) 850°C c) 1150°C
d) Oxidised at 1000°C for 180 min and deformed at 850°C

5.3.2 Numerical results of high temperature tensile test

The load and displacement data were recorded during the tensile deformation with 200 reading/s sampling rate. The data acquisition and control signals were simultaneous. The data collected using National Instrument Compact-DAQ system via LabVIEW software. To increase the accuracy of the measurement of the load, a 3 KN external load cell was installed on the system. For elimination of undesirable factors including the gravitational force related to the weight of the sample's top segment and effect of thermomechanical bonding between the two parts of the sample, the tests were repeated under different atmosphere for each specific temperature. First, the specimen heated up and stabilised at the test temperature under

argon gas flow to eliminate the oxidation. Subsequently, the test was carried out, and the separation load was measured under an inert atmosphere. The atmosphere prevented the oxide development around the gauge section; therefore, the measured deformation load was only associated with the weight of the sample's top segment and thermomechanical bonding force between the joint surfaces. In the second step, the test repeated using an oxidised specimen under the same condition. Finally, the values measured in the test performed under inert gas were deducted from the values obtained from the oxidised specimen.

5.3.2.1 Numerical results of rail steel high temperature tensile test

Figure 5.3.2.1.1 presents loads versus displacement plots of all rail steel specimens tested at different temperatures. Each chart contained three curves. The curves plotted with red square icons represented the test results for the oxidised sample. The other ones plotted with green triangle icon displayed the test results for the sample without oxidation. Finally, the curves plotted by blue diamond icons illustrated the subtraction of the test results of the non-oxidised sample from values obtained from oxidised test piece. The lowest tensile load failure registered while testing the specimen at 1200˚C. As can be noticed, the highest load failure was not observed when the oxide scale tested at 750˚C, but it was achieved when material deformed at 850˚C. This occurrence can be explained by assessing the microstructure and composition of the oxide scale for each test condition, which will be reviewed in cross-sectional examination section.

The percentage of the engineering strain was calculated using equation 3-8 and the actuator displacement values, which represented the instantaneous gauge length (l). The engineering stress was calculated using the following Equation 94-1):

$$\sigma = {}^{F}/_{A_0} \qquad (5\text{-}1)$$

Where σ was engineering stress, F was instantaneous load and A_0 was the initial cross-sectional area of the oxide scale. A_0 was an estimated value, which was calculated based on the average thickness measurements of the oxide scale.

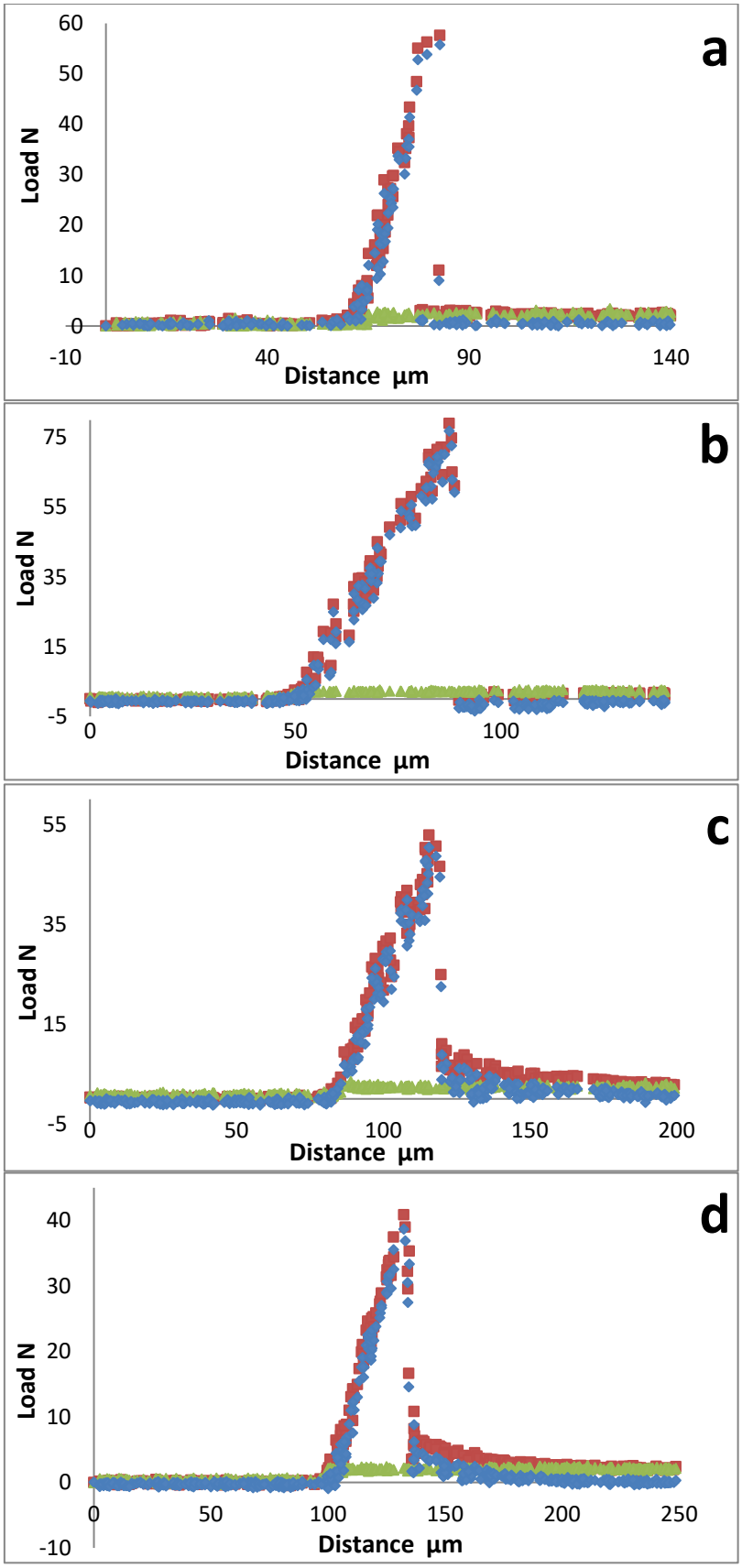

Figure 5.3.2.1.1 Registered tensile loads during testing of rail steel specimens at a.750˚C b. 850˚C c. 1150˚C d. 1200˚C (Tox = 1150˚C, oxidation 60min)

■ Testing with oxidation; ▲ Testing without oxidation; ◆ Subtraction of ▲ from ■

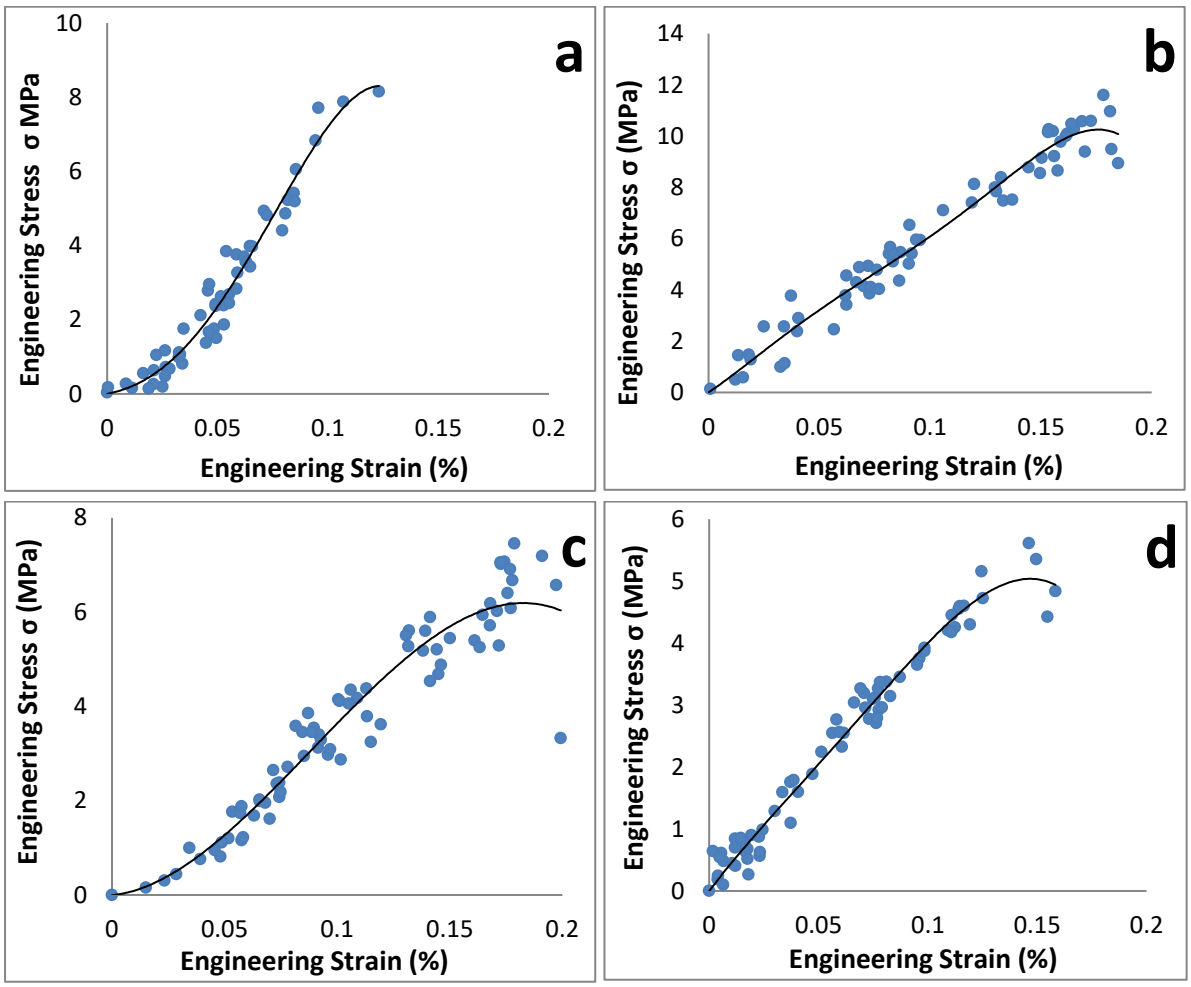

Figure 5.3.2.1.2 Stress-Strain Curves of rail steel specimens tested:
a.750˚C b. 850˚C c. 1150˚C d. 1200˚C

Stress-strain curves of all rail steel samples are given in Figure 5.3.2.1.2. As can be seen, the ultimate tensile strength (UTS) was directly related to the tensile load failure of each test. Comparably to Figure 5.3.3, the highest UTS value of the oxide scale was obtained when the material tested at 850˚C and likewise, the lowest UTS value was measured when specimen tested at 1200˚C.

5.3.2.2 Numerical results of DSP steel high temperature tensile test

The loads versus displacement plots of all DSP steel specimens tested at different conditions are shown in Figure 5.3.2.2.1. The curves plotted, in the same manner, explained earlier in the tensile testis of results rail steel.

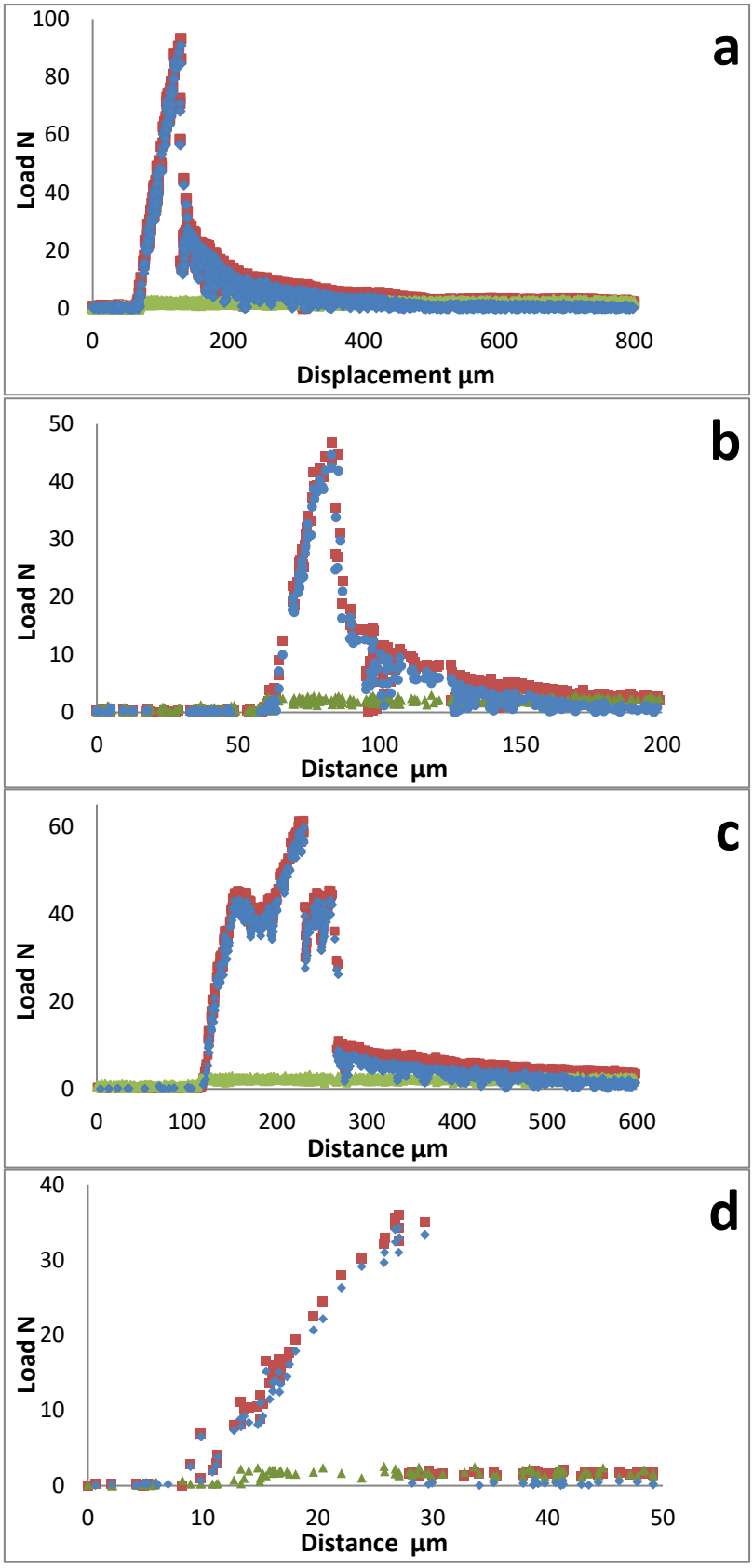

Figure 5.3.2.2.1 Registered tensile loads during testing of DSP steel specimens at:
a.750˚C b. 850˚C c. 1150˚C (Tox = 1150˚C, oxidation 60min)
d. 850˚C (Tox = 1000˚C, oxidation 180min)

■ Testing with oxidation; ▲ Testing without oxidation; ◆ Subtraction of ▲ from ■

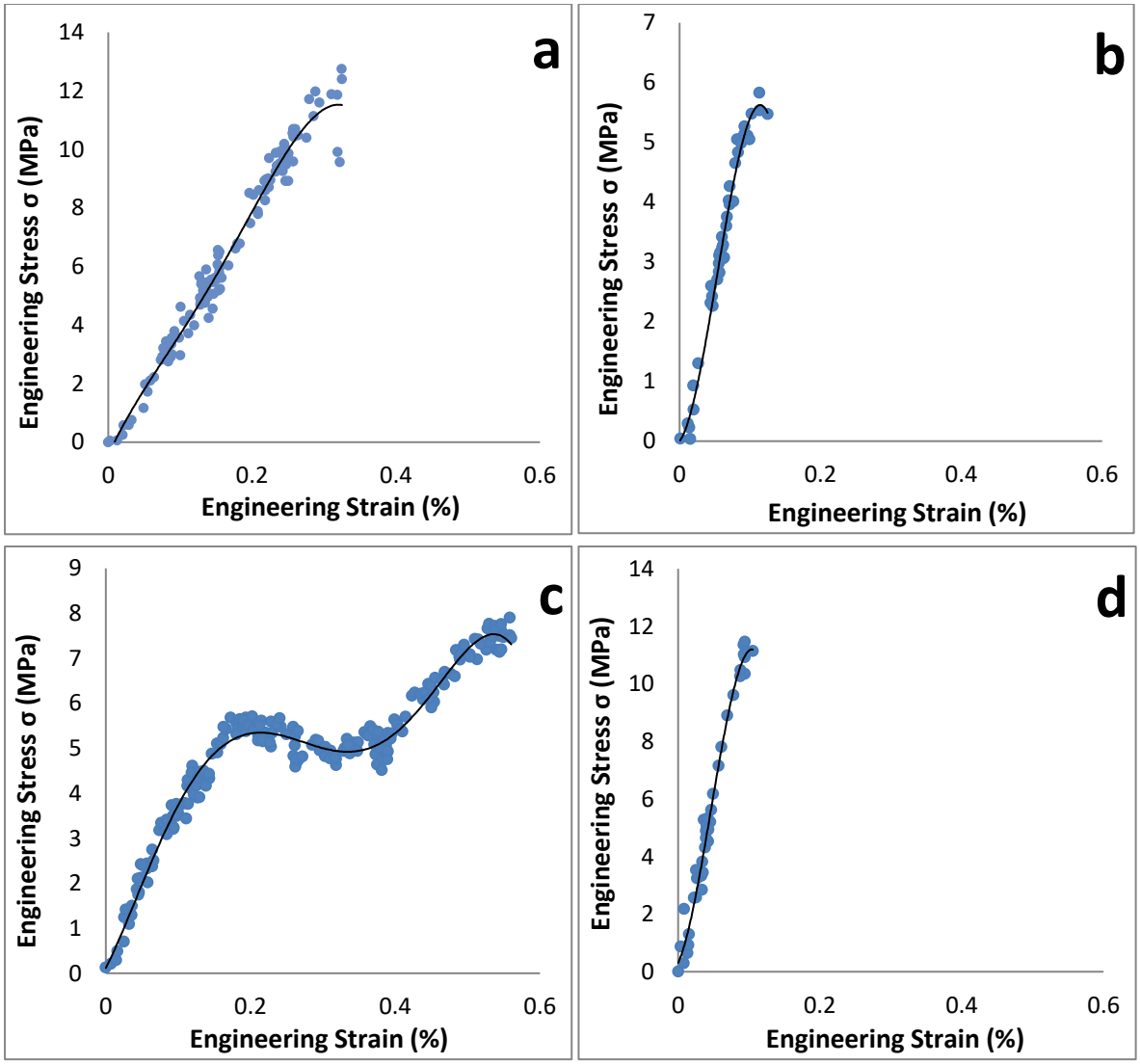

Figure 5.3.2.2.2 Stress-Strain Curves of DSP steel specimens tested (T_{Def}):
a.750˚C b. 850˚C c. 1150˚C (Tox = 1150˚C, oxidation 60min)
d. 850˚C (Tox = 1000˚C, oxidation 180min)

The Figure 5.3.2.2.1 a, b and c represented the results of the samples oxidised at 1150˚C for 60min and tested at 750˚C, 850˚C and 1150˚C respectively. As noted in the macro examination section, the oxide scales raft slid along the oxide-metal interface in all the above specimens. The highest failure load was registered while testing the material at 750˚C. The pattern of the tensile load curve was complex at 1150˚C, and two peaks were recorded during the deformation stage. The first peak of the curve was representing the highest tensile load just before initiation of the oxide scale sliding along the interface. The second peak was associated with the final failure and separation of the oxide scale on the top part of the gauge section. Figure 5.3.2.2.1.d gives the curve of tensile load against displacement for the sample oxidised at 1000˚C for 180 minutes and deformed at 850˚C. As reported earlier, the oxide

scale failed by through-thickness cracking at the joint section. For this test condition, the maximum-recorded failure load was 34 N, which was lower than the previous scenarios.
In the same manner, explained earlier for rail steel, the engineering stress and strain values were calculated using recorded load-displacement data. Figure 5.3.2.2.2 illustrates the engineering stress-strain curves of all DSP steel samples. Among samples oxidised at 1150˚C, the highest UTS value was achieved when the sample tested at 750˚C, whereas the lowest UTS value was attributed to the sample tested at 850˚C. The engineering stress-strain plot of the sample tested at 1150˚C followed its load-displacement curve pattern, exhibiting two distinctive peaks. The engineering stress-strain curve for the sample oxidised at 1000˚C for 180 minutes and tested at 850˚C is plotted in Figure 5.3.2.2.2.d. Although the maximum tensile load was lower than the same value measured for the sample oxidised at 1150°C for 60 minutes and deformed at 850°C, the calculated UTS was relatively higher due to smaller oxide scale cross section (A_0).

5.3.3 Cross section analysis

All samples were mounted using cold resin before sectioning to prevent the undesirable damage of the preparation process. The specimens then cut within the mid-region of the gauge section perpendicular to the load direction. The final preparation stage was completed by following the same method used for isothermal oxidation samples. The oxide scale microstructure and phase composition after deformation were evaluated by backscattered electron imaging and EDX analysis.

5.3.3.1 Cross-section analysis of rail steel specimens

All rail steel tensile samples oxidised at 1150˚C for 60minutes. After completion of the oxidation stage, the temperature was set to the required testing condition and specimens deformed under an inert atmosphere.

Figures 5.3.3.1.1 demonstrates a BSE image of a rail steel specimen gauge cross-section deformed at 750˚C. The main body of the oxide scale separated from the oxide-metal

interface with the development of vast separation space between the top section of the oxide layer and residual oxide scale at the interface. The detached oxide scale contained an extensive layer of Hematite on the outermost part and a lesser amount of Magnetite at the bottom section. The thin oxide layer next to the oxide-metal interface was identified as Wüstite. Within the Hematite and Magnetite regions, different defects including voids, pores and partial transverse cracks were observed.

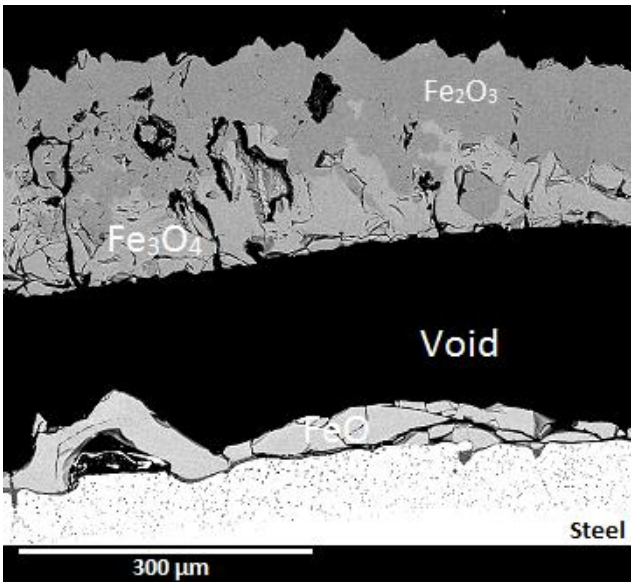

Figure 5.3.3.1.1 Oxide scale cross section of a rail steel specimen deformed at 750˚C (Tox = 1150˚C, oxidation 60min)

Higher magnification of the oxide-metal interface of Figure 5.3.7 is shown in Figure 5.3.3.1.2. The EDX analysis of zone 1 confirmed that the oxide scale only contained iron and oxygen. The EDX plots of point 2 revealed that at zone 2, the iron-rich layer only contained traces of silicon. In contrast, at point 3, the dark inner layer was rich in silicon.

The cross section of a rail sample deformed at 850˚C is shown in Figure 5.3.3.1.3. Comparable to the test at 750˚C, the main structure of the oxide scale detached from substrate metal, however, the extent of the separation gap reduced. The quantitative EDX analysis identified the top, middle and bottom sections of the oxide layer as Fe_2O_3, Fe_3O_4 and FeO, respectively. In comparison to the test performed at a lower temperature, the proportions of Wüstite and Magnetite increased, whereas the extent of the Hematite layer considerably reduced. This transformation could explain the higher UTS of the material at 850˚C as seen on the compression tests in comparison to Hematite or Magnetite, FeO is more ductile and resists the crack propagation. Furthermore, the microstructure of the oxide was more

heterogeneous in comparison to the previous test piece. The EDX analysis of zone 5 revealed that the dark oxide particles around the interface contained traces of Mn and Mo. No traces of Fayalite phase detected within the main body of the oxide scale.

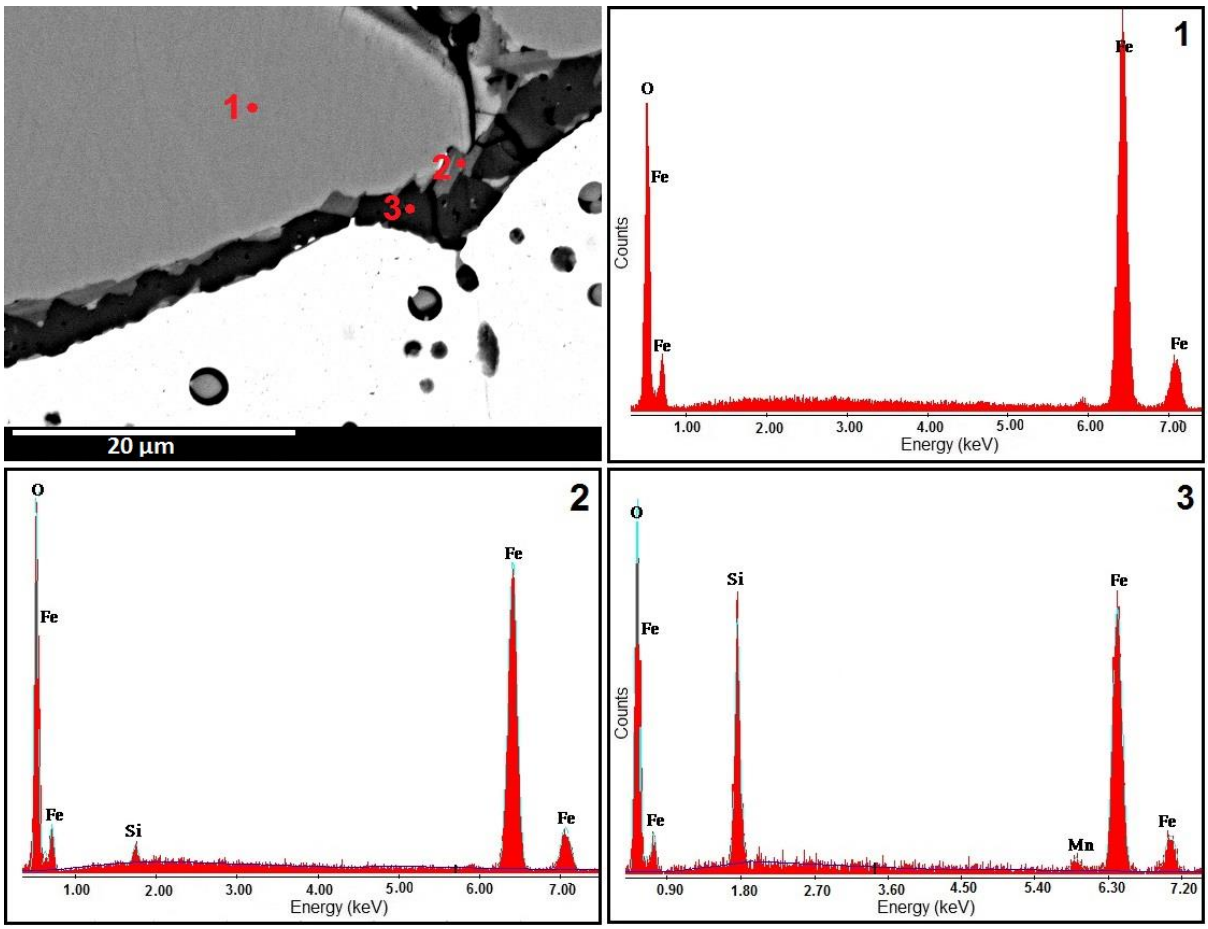

Figure 5.3.3.1.2 High magnification image the oxide-metal interface of Figure 5.3.3.1.1, including the EDX point analysis.

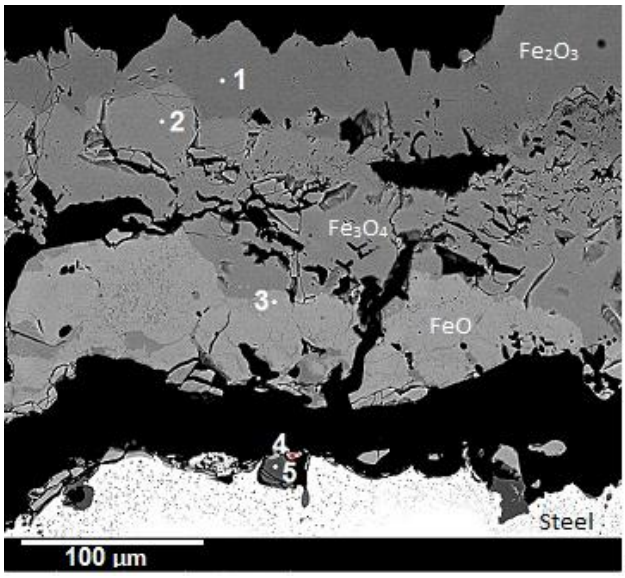

	AT%				
Point	Fe	O	Si	Mn	Mo
1	42.65	57.35	-	-	-
2	46.12	53.88	-	-	-
3	48.06	51.94	-	-	-
4	48.02	51.58	-	-	-
5	29.33	56.45	12.1	1.08	1.03

Figure 5.3.3.1.3 Oxide scale cross section of a rail steel specimen deformed at 850˚C (Tox = 1150˚C, oxidation 60min).

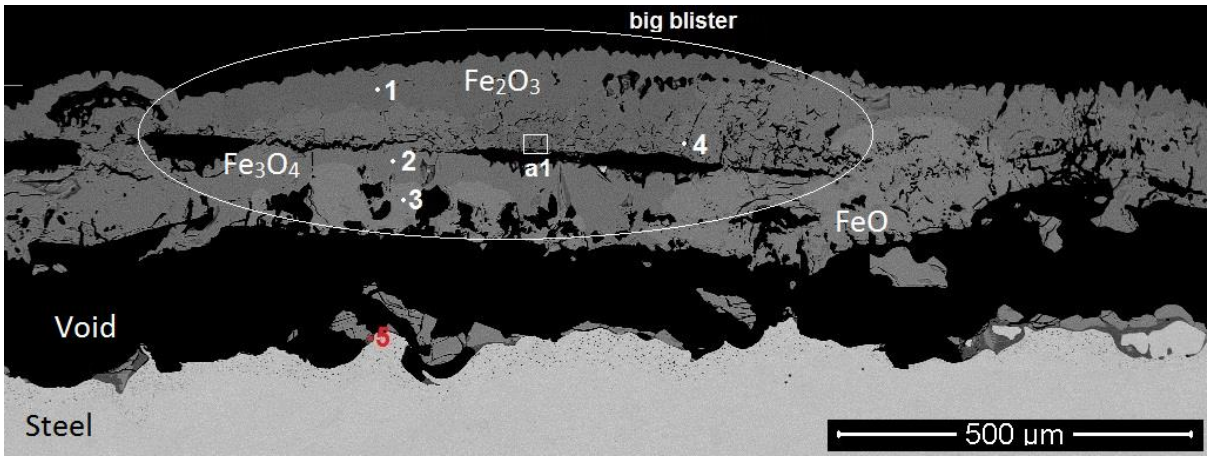

	At%				
Point	**Fe**	**O**	**Si**	**Mn**	**Mo**
1	41.15	58.85	-	-	-
2	43.94	56.06	-	-	-
3	49.32	50.68	-	-	-
4	31.46	47.82	20.72	-	-
5	34.02	51.04	12.77	1.16	1.01

Figure 5.3.3.1.4 Oxide scale cross-section of a rail steel specimen deformed at 1150˚C (Tox = 1150˚C, oxidation 60min) including the EDX point analysis.

The cross section of a rail specimen tested at 1150˚C is given in Figure 5.3.3.1.4. As observed in the previous tests, the oxide layer separated from substrate steel and only in random locations, small oxide particles adhered to the interface. As highlighted in the image, a big blister was apparent on the top section, and as a result, a linear defect developed within the middle of the oxide scale parallel to the oxide-metal interface. Also, many other defects, including voids pores, microcracks and small blister were visible throughout the oxide scale. The EDX point analysis confirmed the oxide contained Hematite, Magnetite and Wüstite. The analysis at location 4 confirmed that Fayalite was present at the top section of the oxide scale. This phenomenon can also be seen in Figure 5.3.3.1.5, which represents the zone a1 in higher magnification. The EDX plot confirmed that the dark phase was rich in silicon, but no other trace elements such as Mn or Mo were present in this region.

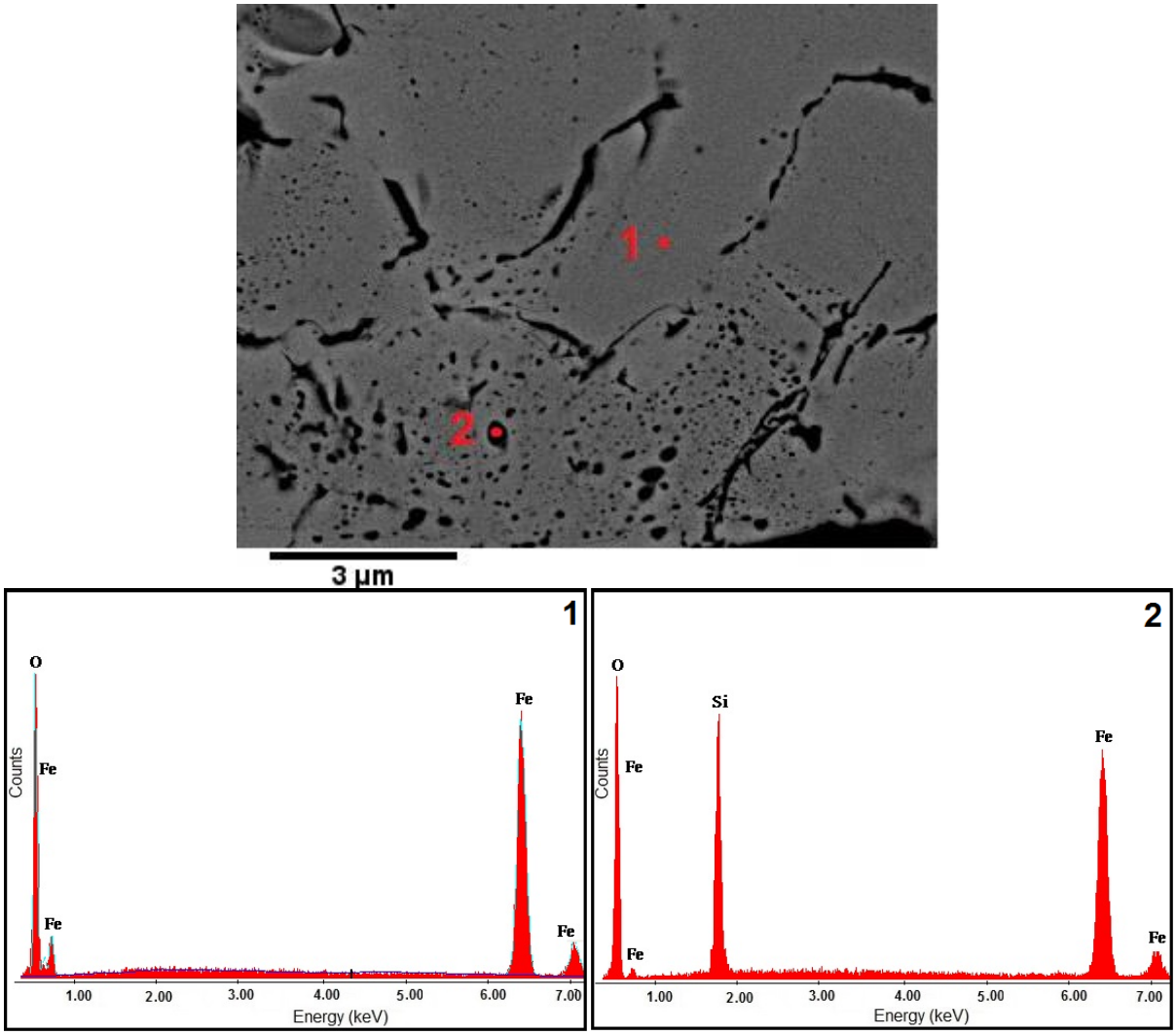

Figure 5.3.3.1.5 High magnification image of zone a1 in Figure5.3.10, including the EDX point analysis.

Figure 5.3.3.1.5 illustrates the cross-section of a rail specimen tested at 1200˚C. The structure of the oxide scale, including the development of defects, were similar to the sample tested at 1150˚C, including the development of a big blister at the top section of the oxide scale. The composition, phase distribution of the oxide also followed a similar pattern to the previous scenario by detection of Wüstite, Magnetite and Hematite in similar locations. The noticeable difference from the previous test was higher dispersion of Fayalite within the top layer of oxide scale. Figure 5.3.3.1.6 is a high magnification image of location a1 in Figure 5.3.3.1.5. The EDX analysis at point 2 confirmed that oxygen-rich outer layer contained traces of manganese. The EDX plots of point 1 and 3 confirmed the high concentration of silicon within the dark phase. A small trace of manganese was also detected at point 3.

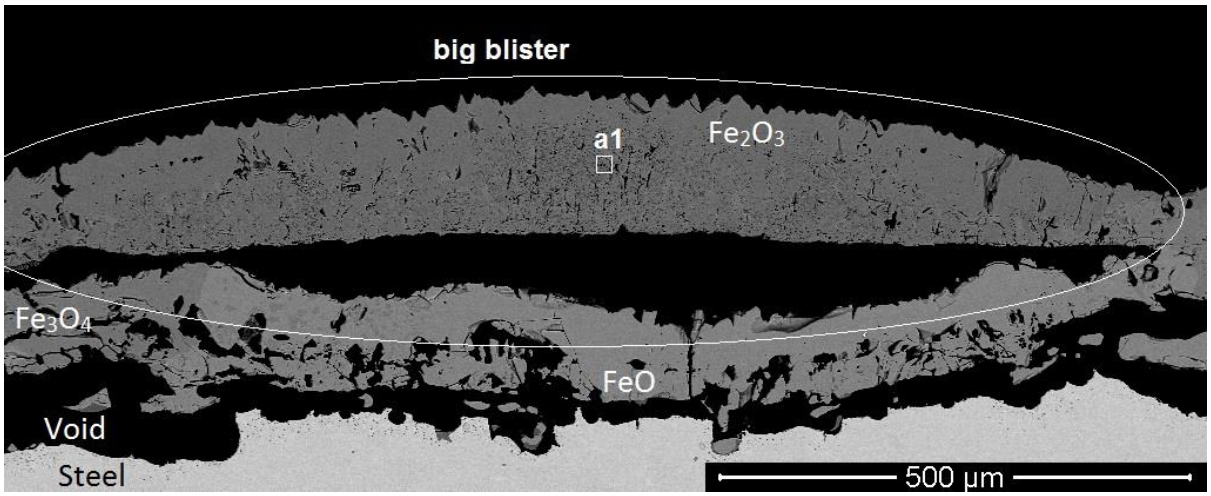

Figure 5.3.3.1.5 Oxide scale cross section of a rail steel specimen deformed at 1200˚C (Tox = 1150˚C, oxidation 60min)

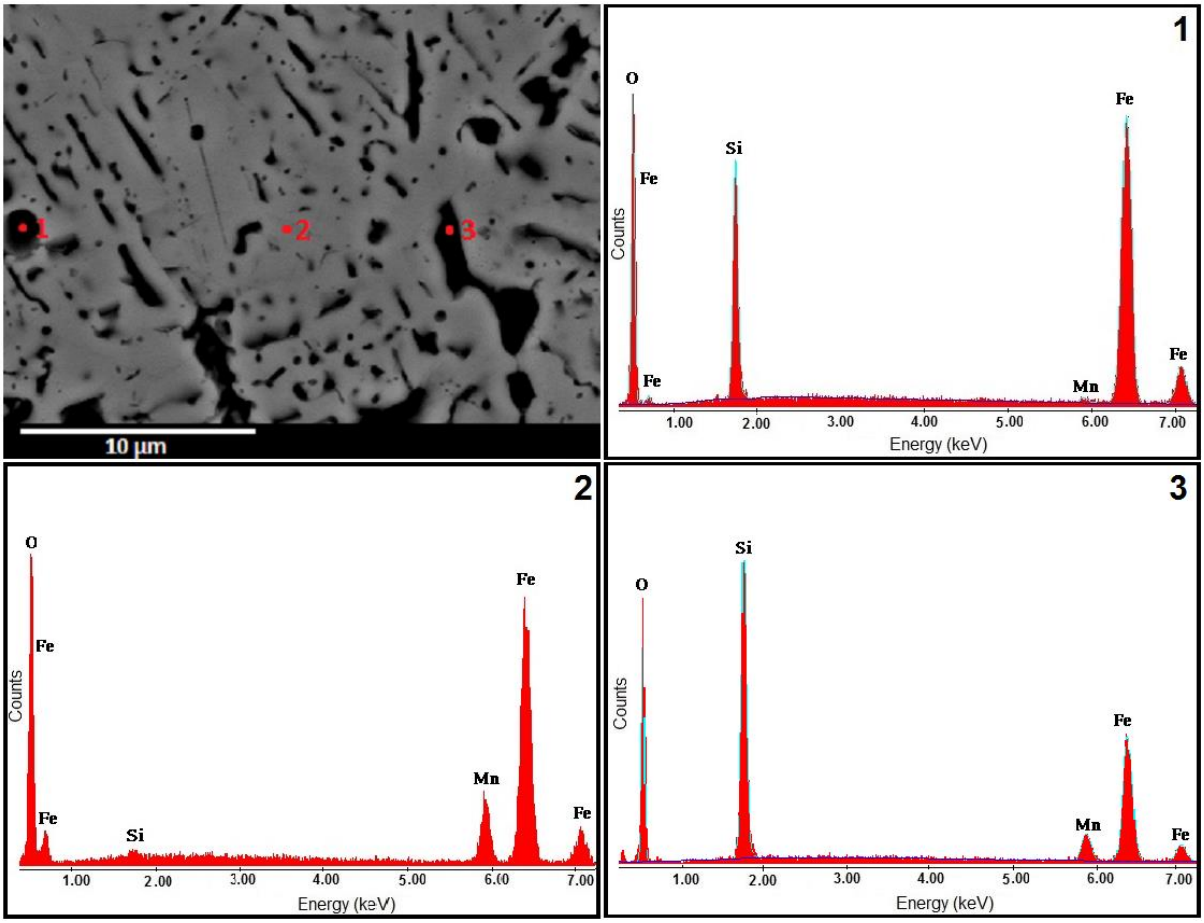

Figure 5.3.3.1.6 High-resolution image of zone a1 in Figure5.3.12, including the EDX point analysis.

5.3.3.2 Cross-section analysis of DSP steel specimens

Figure 5.3.3.2.1 demonstrates the cross-section of a DSP steel specimen, which was oxidised at 1150˚C and deformed at 750˚. In general, the outer oxide scale was dense with minimal defects such including a through thickness crack. The main body of the oxide layer separated from the interface by development a small gap. The EDX analysis at points 1 and 2 revealed that the concentration of oxygen increased towards the surface of the oxide scale. The EDX quantitative data at point 3 confirmed the presence of Fayalite in the lower section of the oxide layer. Under the tensile load, the Fe_2SiO_4 penetrated the cavities and created a complex microstructure, which previously observed during in compression tests of DSP specimen. At the oxide-metal interface (point 4) high concentration of silicon and traces of manganese and aluminium were detected. The analysis of point 5 revealed that the subsurface oxide particles were rich in aluminium and silicon. Moreover, a small quantity of Mn also detected within the subsurface oxide particles.

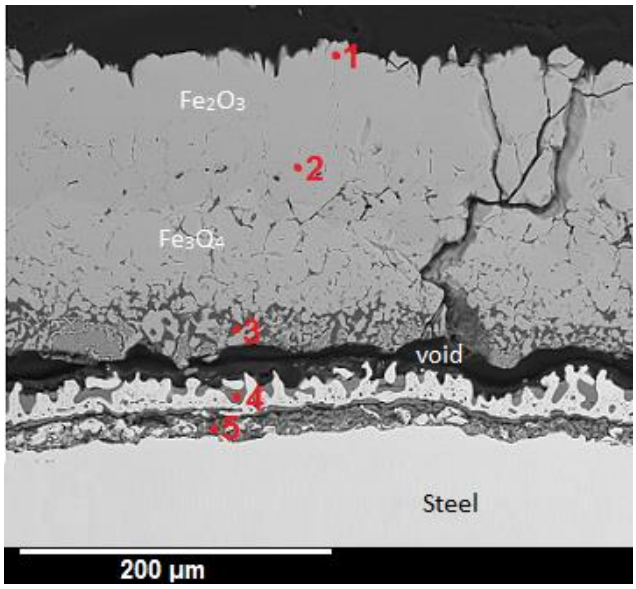

	AT%				
Point	**Fe**	**O**	**Si**	**Mn**	**Al**
1	44.4	55.6	-	-	-
2	47.28	52.72	-	-	-
3	1.62	61.95	36.4	-	-
4	7.91	61.12	23.7	1.07	2.48
5	26.03	49.24	15.5	0.91	8.36

Figure 5.3.3.2.1 Oxide scale cross section of a DSP steel specimen deformed at 750˚C (Tox = 1150˚C, oxidation 60min) including EDX point analysis

The cross section of tensile DSP specimen deformed at 850˚C is shown in Figure 5.3.3.2.2. The oxide scale was dense, and there were no signs of through-thickness cracks, voids or large cavities. However small partial fissures were apparent in the lower section of the oxide scale, which were packed with a dark phase (possibly Fayalite). The BSE image contrast indicated

the presence of Hematite and Magnetite at the top and bottom of the oxide layer, respectively. As can be seen, no complex penetration of Fayalite was apparent in this image, and this was possibly related to the vast separation space between the main oxide layer and the oxide-metal interface, which prevented Fayalite to be transported in mass scale under tension.

High magnification BSE image and EDX analysis of the oxide-metal interface of the above sample is demonstrated in Figure 5.3.3.2.3. The microstructure of the oxide-metal interface and internal oxidation zone was comparable to the specimen tested at 750˚C. The EDX assessment of point 1 revealed the oxide phase was rich in silicon and aluminium and only contained traces of manganese. The high concentration of silicon and oxygen at point 2 confirms the presence of silica. The EDX plot of internal oxidation zone (point 3) was similar to the EDX peaks detected in location 1.

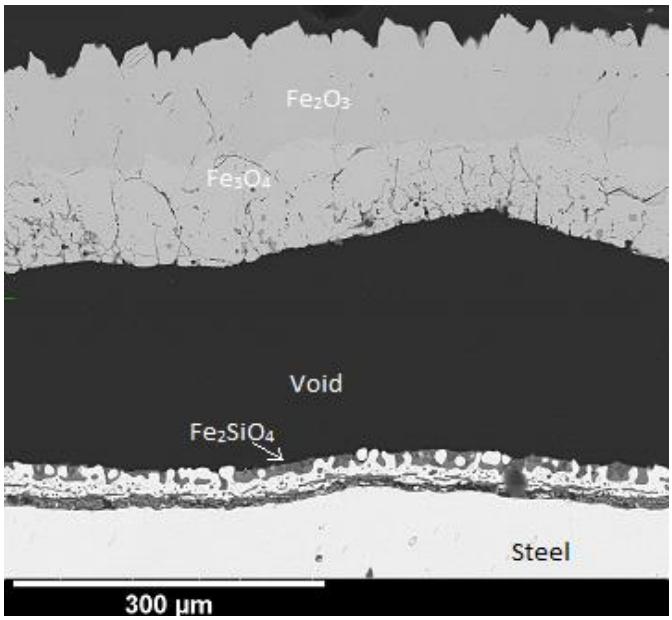

Figure 5.3.3.2.2 Oxide scale cross section of a DSP steel specimen deformed at 850˚C (Tox = 1150˚C, oxidation 60min)

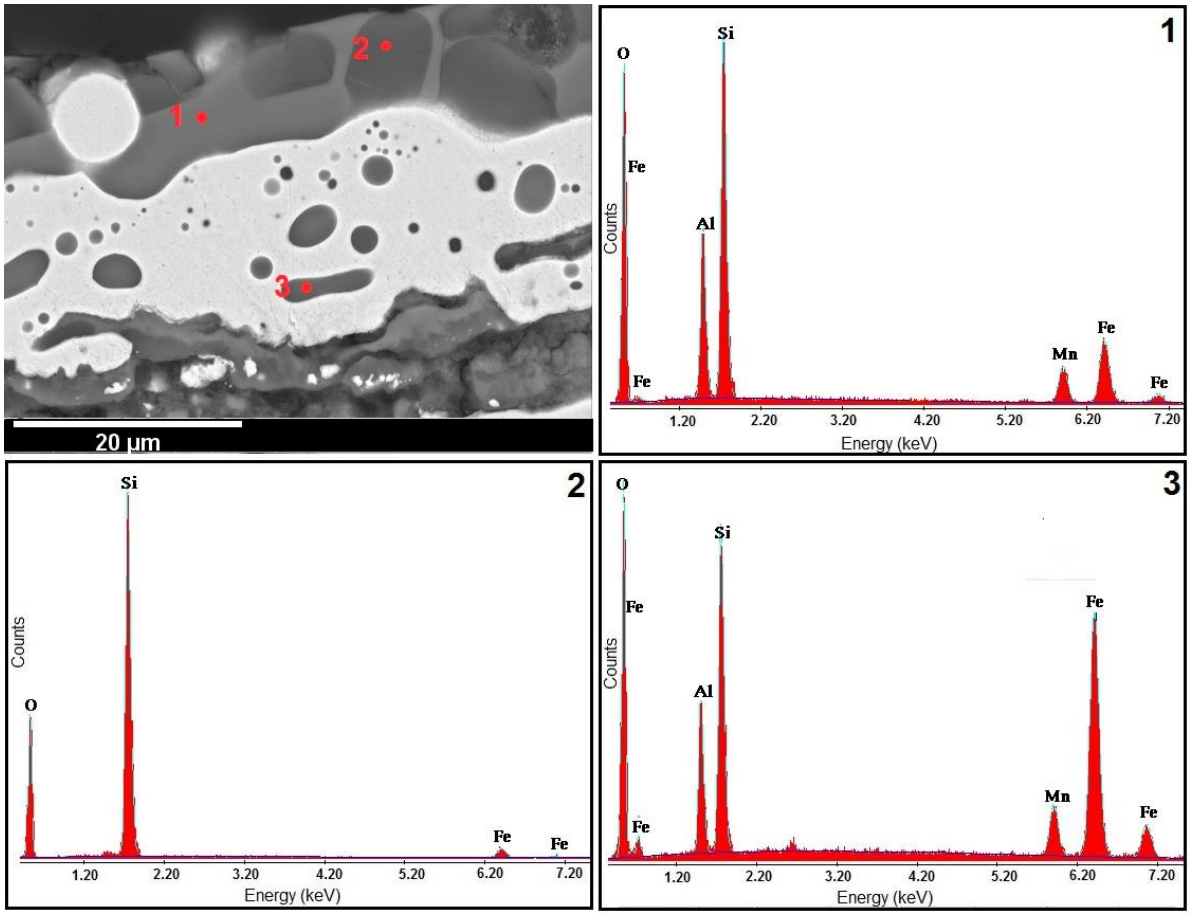

Figure 5.3.3.2.3 High magnification image the oxide-metal interface of Figure5.3.15, including the EDX point analysis.

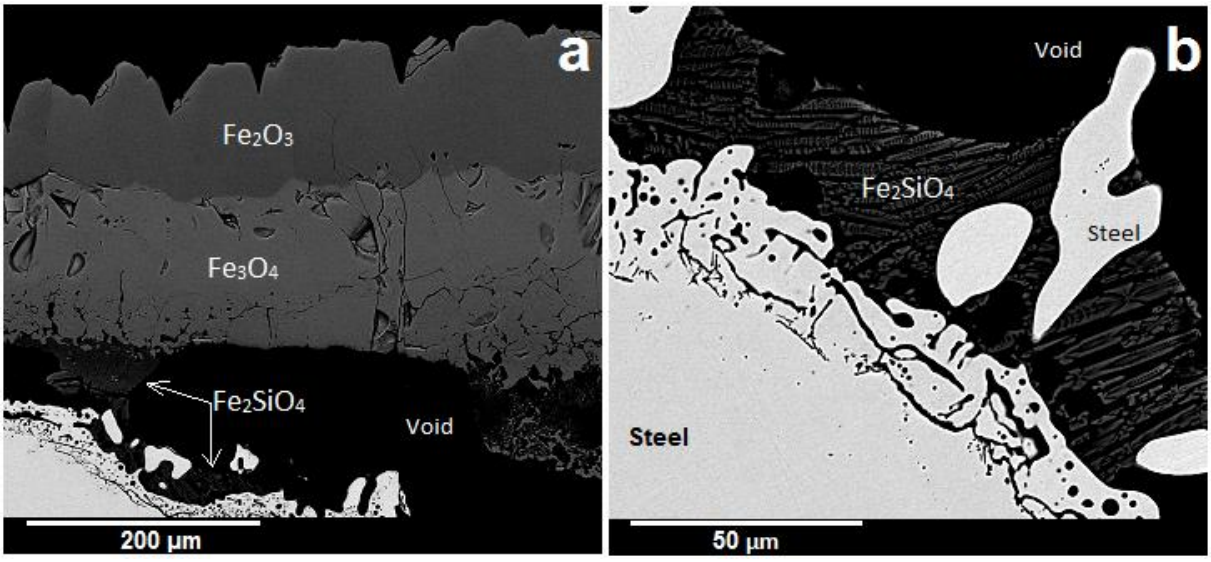

Figure 5.3.3.2.4 a. Oxide scale cross-section of a DSP steel specimen deformed at 1150˚C (Tox = 1150˚C, oxidation 60min) b. High magnification image the oxide-metal interface.

As can be seen in Figure 5.3.3.2.4.b, few individual steel particles were separated from the substrate parent metal and embedded within the Fayalite phase.

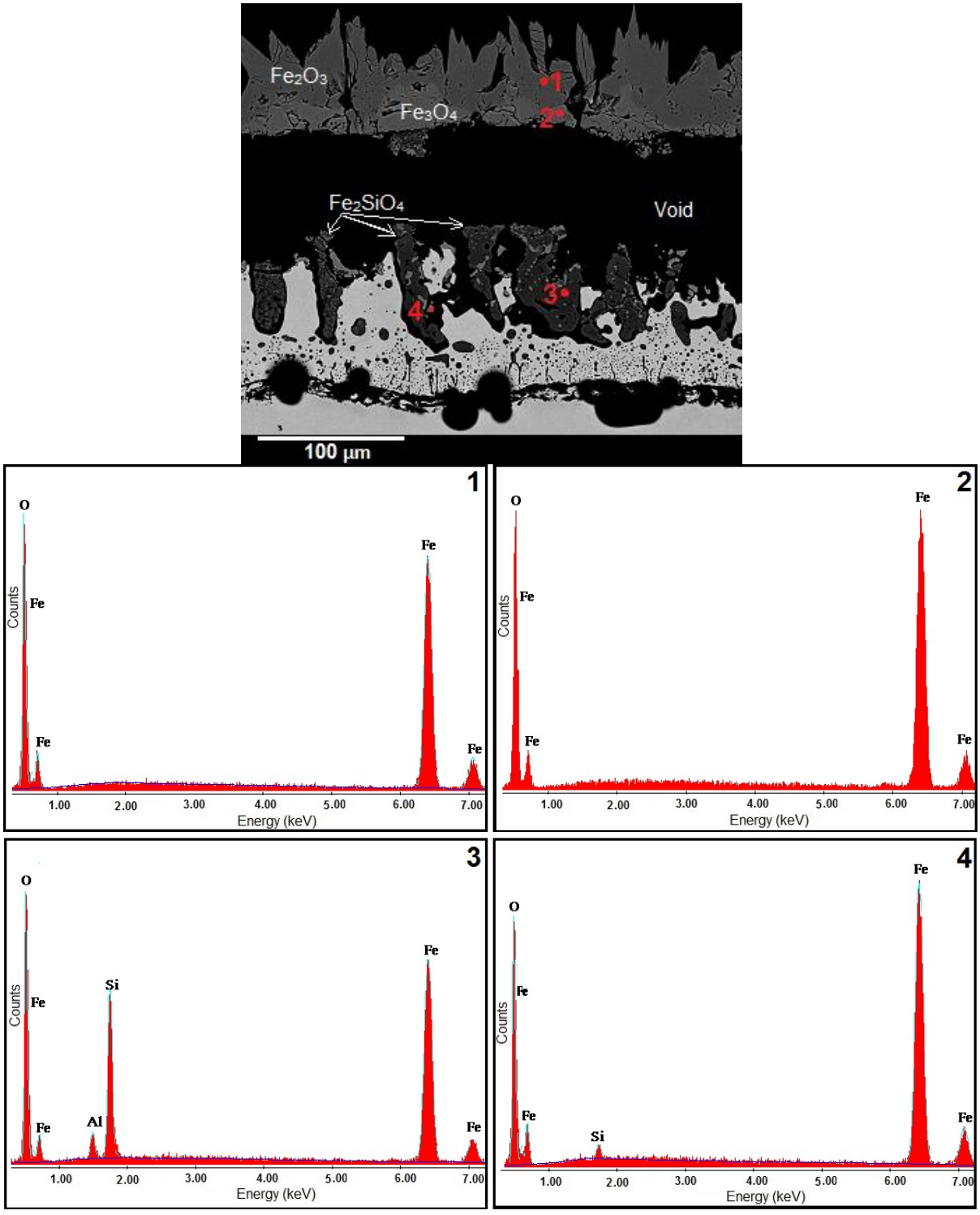

Figure 5.3.3.2.5 Oxide scale cross-section of a DSP steel specimen deformed at 850˚C (Tox = 1000˚C, oxidation 180min) including EDS point analysis.

The cross section of the DSP tensile sample that was oxidised at 1000˚C for 180 minutes and deformed at 850˚C is shown in Figure 5.3.3.2.5. The oxide scale was considerably thinner (avg. 99µm) in comparison to previous test conditions. As can be seen, the external surface of the

oxide layer was relatively rough — a wide separation space formed between the outer oxide layer and the oxide-metal interface. Backscattered electrons images revealed two distinctive zones of Hematite and Magnetite within oxide outer layer. The EDX analysis confirmed

§a higher concentration of iron on the lower section of the oxide layer that marked as zone 2. The analysis at zone 3, disclosed that the dark residual oxide particles contained a considerable amount of silicon, iron and oxygen along with traces of aluminium. The EDX plot of zone 4 was comparable to the peaks detected at zone 2 with additional traces of silicon.

Chapter 6

Discussion

6.1 Introduction

The results of the project experimentally obtained are discussed in this chapter, which contains two main sections:

- The results of isothermal tests are explicated to provide a better understanding of the effect of different oxidation parameters including time, temperature and environment on development and growth of oxide scale, phase distributions and the nature of the oxide scale defects before deformation.
- In the second part, the behaviour and failure mode of the oxide scale under compressive and tensile stresses at elevated temperature are discussed.

6.2 Isothermal oxidation

As previously stated, the focus of this research was on the developments and behaviour of the primary oxide scales; in various conditions. Therefore the research initiated by isothermal oxidation studies of the provided materials at a temperature range of 850°C to 1280°C. The literature concerning the oxidation of iron and steel was briefly reviewed in chapter 2.

6.2.1 Oxidation kinetics

The effect of oxidation parameters on the process kinetics was detailed in Chapter 2. The oxidation rates of all experiments were rapid due to the high temperature of the oxidation process. This rapid oxidation developed a thick multilayer oxide on the surface of the substrate of each specimen. The results of isothermal studies confirmed that the oxidation

kinetics of both steel grades were highly influenced by different parameters including time, temperature, oxidant atmosphere and parent metal composition. Although the oxidation kinetics for each steel grade were highly subjective to its composition, nevertheless it was noticed that the oxidation rates of two alloys were intensified as the oxidation temperature increased. This phenomenon can be explained by acknowledging Equation 2.15. As defined in Chapter 2, if under a constant partial pressure of oxygen, the oxidation process follows a single law (e.g. parabolic) then the activation energy remains constant, and the temperature directly governs the oxidation rate [1].

6.2.1.1 Oxidation kinetics of rail steel

Over the years, the isothermal oxidations of low to medium carbon steel have been extensively investigated. However, surprisingly, there are very limited data available for isothermal oxidation of high carbon steel at temperatures close to reheating temperatures of these alloys in the primary production line. Therefore, many of the experiments were performed at 1280˚C and 1150˚C. These temperatures were proposed based on the production mill reheating temperatures of rail steel and DSP steel respectively.

The isothermal oxidation of rail steel at 1280˚C and 1150˚C under an atmosphere containing 17% moisture revealed that after 10 minutes, the oxidation rate of the material obeyed parabolic law (Fig.4.2.1). In other words, the oxidation rate was time depended, and as the process progressed, the rate of the reaction reduced, which indicated that the process controlled by solid-state diffusion of the oxidising species. Regardless of the high carbon content of rail steel, the above observations were in good agreement with the works of Lee et al. [77]. They reported parabolic regimes for isothermal oxidations of medium carbon steel between 700˚C to 1200˚C where the atmosphere contained a high air/fuel ratio (112%). The equivalent air/fuel ratio of the mixed gases used in this research (for humid condition) was marginally higher than 112%. In contrast, Lee et al. [77] stated that as the air/fuel ratio reduced to 99%, the oxidation rate followed the linear law.

Furthermore, the work of Abuluwefa [74] confirmed that under an atmosphere containing N_2-O_2-CO_2-H_2O, the isothermal oxidations of medium and low carbon steels at 1200˚C were parabolic. The oxidation mode under the same atmosphere changed to a linear pattern when

the oxidation temperature reduced to 1000˚C. Abuluwefa concluded that the oxidation rates were governed by the total free oxygen atoms available within the oxidising atmosphere.
Wang et al. [75] also reported that the isothermal oxidation of medium and low carbon steels followed the parabolic law at 1100˚C and 1200˚C under a moist atmosphere.
For evaluation of the water vapour absence in the oxidant atmosphere, both steel grades were oxidised under a dry atmosphere. As shown in Figure 4.2.1 in comparison to the humid condition, the oxidation rate of the rail steel at 1280˚C under dry atmosphere was considerably lower. Nevertheless, like the humid condition, as the oxidation progressed, the scale development rate gradually decreased, and the process obeyed the parabolic law.
Abuluwefa [71] reported similar oxidation behaviour for low carbon steel. His research revealed that the isothermal oxidation of the low carbon steel longer than 10 minutes at 1250˚C under dry atmosphere obeyed the parabolic law.

6.2.1.2 Oxidation kinetics of DSP steel

As demonstrated in Figures 4.2.3 a and b, the isothermal oxidation of DSP steel at 1150˚C and 1280˚C under an atmosphere containing 17% water vapour followed the parabolic law. While the oxidation of this grade at both temperatures followed the parabolic growth rate but the oxidation at 1280˚C was significantly higher than 1150˚C. This matter was related to the higher Si content of the DSP grade and the development of a continuous Fayalite layer at the oxide-metal interface. As can be seen in SiO_2-FeO phase diagram (Figure 6.2.1) below 1183˚C, Fe_2SiO_4 is in solid state that retards the diffusion of iron ions towards the substrate metal and reduces the oxidation rate. In contrast, in temperatures greater than 1183˚C, Fayalite along with Wüstite appears in a liquid eutectic format, which stimulates the diffusion of iron ions and subsequently that increases the rapid growth of Wüstite. The observations of this research were in good agreement with the effect of temperature on the oxidation kinetics of silicon-containing steel reported by other researchers [76, 81, 82].
As described in Section 2.4.2, when a steel alloy containing 1.55% Si isothermally oxidised at 1100˚C under an atmosphere containing 15% water vapour, after 30 seconds, a passivation phenomenon decayed the oxidation rate [76]. The oxidation rate obeyed the parabolic law, once the oxidation process progressed beyond the passivation stage. Mouayd et al. [76]

testified isothermal oxidation of the above alloy at 1200˚C also followed a parabolic regime which was in good agreement with observations from the oxidation of the DPS steel at 1280°C.

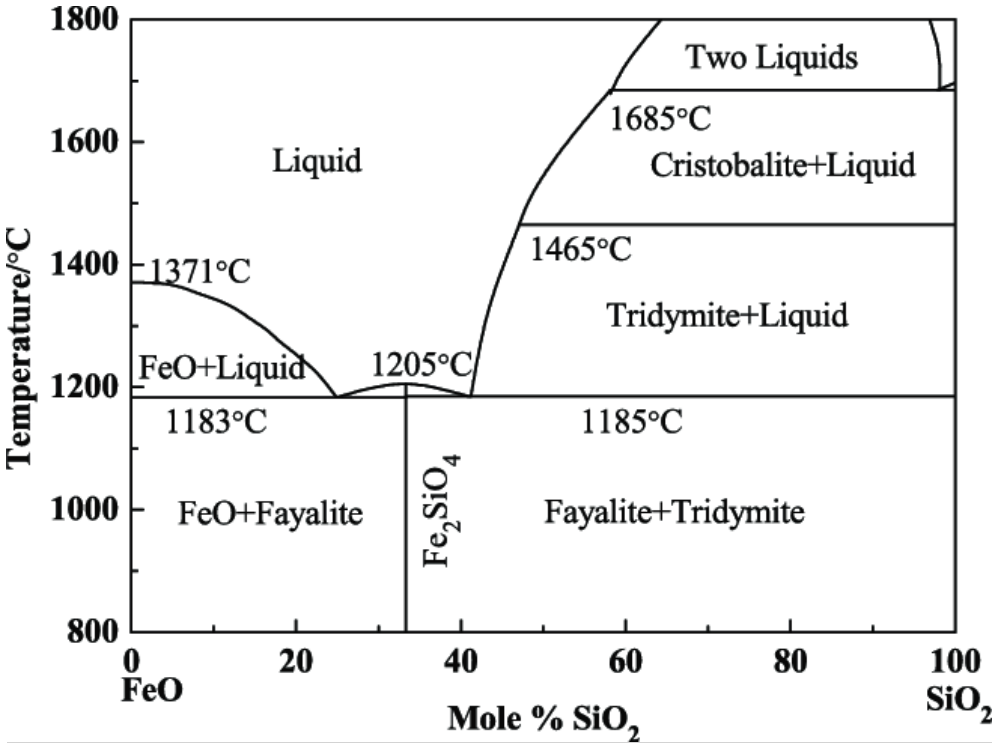

Figure 6.2.1 FeO-SiO2 binary system [103].

Furthermore, the works Suárez et al. [82] confirmed that the oxidation of steel alloys containing 2% and 3% silicon at 1150°C and 1200°C in the air atmosphere, also obeyed the parabolic law.

Figure 4.2.3.c shows that the oxidation of the DSP steel at 1150˚C under a dry atmosphere obeyed the logarithmic law. For the initial 20 minutes of the oxidation, the scale development rate was slightly higher than the oxidation of the material under a humid atmosphere. However, as the oxidation progressed, and the thickness of the oxide scale increased, the rate of the reaction rapidly dropped. The comparison of Figures 4.2.3 b and c revealed that after 60 minutes, the oxidation rate under dry condition was significantly less than that under the humid atmosphere.

The work of Martínez-Cázares et al. [79] demonstrated that in the oxidation of silicon-containing steel up to 20 minutes under a dry atmosphere; the oxidation rate obeyed the parabolic law for a temperature range of 950 - 1180˚C. The difference between the oxidation

mode reported by Martinez et al. and the results obtained from this research can be explained by appreciating the oxidation time. As described earlier, the oxidation kinetics of the DSP steel under dry atmosphere was calculated for a considerably longer oxidation period, and the study revealed that after 30 minutes the oxidation rate rapidly stagnated and followed the logarithmic law.

6.2.1.3 Mechanism of oxidation of iron in atmospheres containing H_2O and CO_2

The oxidation of iron and steel in an atmosphere containing mixed gases such as H_2O and CO_2 is more complex than oxidation of these materials in dry air. The atmosphere of an industrial combustion reheating furnace consists of mixed gases including O_2, N_2, H_2O, CO_2, H_2 and CO. The temperature of the furnace, the chemical composition of the parent material and the fuel and the air/fuel ratio govern the amount of the constituent gasses in the furnace atmosphere. As stated earlier, other researchers [71, 74, 77, 78, 86] confirmed that the composition of the oxidant atmosphere significantly influenced the oxidation kinetics of different types of steel, which was in line with the observations from this research.

Figure 6.2.2 demonstrates a schematic representation of a model proposed by Rahmel and Toboski [85] for high temperature oxidation of iron in atmosphere containing H_2O and CO_2, which was endorsed by Chang and Wie [5]. The model suggested that H_2O and CO_2 acted as oxidant gases by following the equations below:

$$Fe + H_2O \rightarrow (FeO, Fe_3O_4) + H_2 \quad (6.1)$$

$$Fe + CO_2 \rightarrow (FeO, Fe_3O_4) + CO \quad (6.2)$$

In contrast, H_2 and CO participated in reverse reactions as reducing agents:

$$(FeO, Fe_3O_4) + H_2 \rightarrow Fe^{2+} + H_2O + 2e^- \quad (6.3)$$

$$(FeO, Fe_3O_4) + CO \rightarrow Fe^{2+} + CO_2 + 2e^- \quad (6.4)$$

As described by Chang and Wie [5], the outward mobility of Fe ions from the substrate surface towards the reaction zones within the oxide scale frequently developed cavities and voids in regions near the oxide-metal interface.

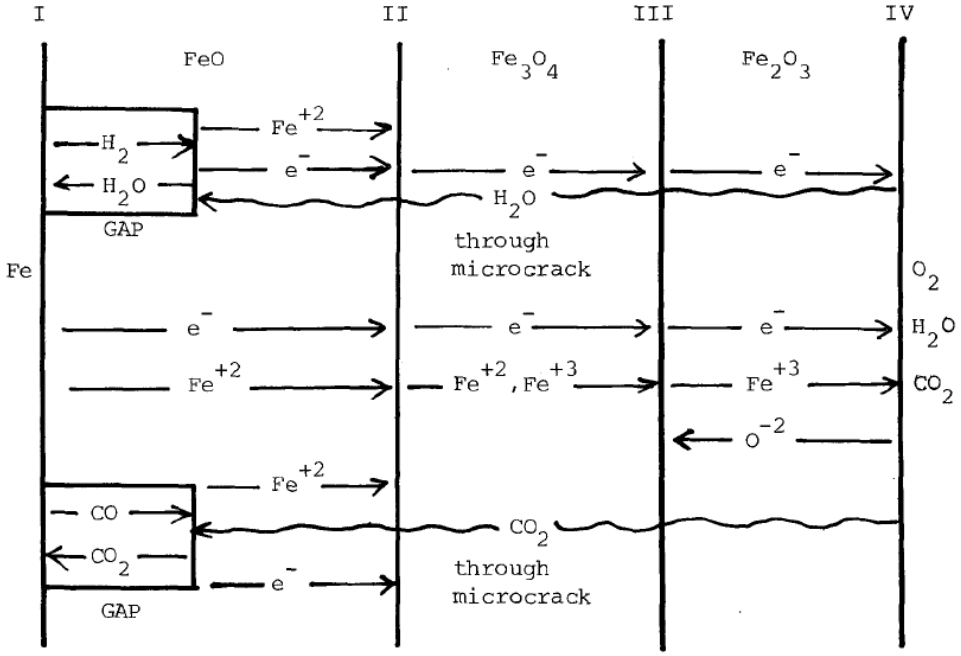

Figure 6.2.2 Schematic mechanism of oxidation of iron in atmospheres containing H_2O and CO_2 as suggested by Rahmel and Tobolski [85] after Chang and Wie [5].

In a dry atmosphere containing air or pure oxygen, the big voids evolution within the lower segments of the oxide scale delayed the movement of iron ions and subsequently reduced the oxidation rate. Conversely, if the oxidant environment contained sufficient amount of H_2O and CO_2, the rate of the reaction was sustained regardless of the cavities within oxide structure. It was claimed [5] that the diffusion of water and carbon dioxide through the gaps, maintained the oxygen transportation towards the oxide-metal interface. Eventually, H_2O and CO_2 disassociate at the oxide-metal interface. The substrate metal absorbed the released oxygen ions and new oxide scale formed as below:

$$H_2O \rightarrow H_2 + O_{absorbed} \quad (6.5)$$

$$CO_2 \rightarrow CO + O_{absorbed} \quad (6.6)$$

Furthermore, the released H_2 and Co diffuse into the scale inner surface and reduce the iron oxide as described in Equations (6.3) and (6.4). The above reactions continued as cyclic reactions.

Garza and Rainforth [32, 39] studied the effect of an atmosphere containing water vapour on the isothermal oxidation process of HS steel at 550°C and 610°C. The research revealed that the addition of steam to dry air increased the oxidation rate of high-speed steel. It was concluded that water vapour appeared as a second source of oxygen in addition to the oxygen molecules on dry air, which boosted the development of Magnetite phase and overall the oxidation rate.

The above observations were in good agreement with the research of Tuck et al. [38].

For a humid atmosphere, Laverde et al. [83] proposed an alternative oxidation reaction by considering the development of Hematite as a reaction between Magnetite and steam that expressed as:

$$2\ Fe_3O_4 + H_2O \rightarrow 3\ Fe_2O_3 + H2 \qquad (6.7)$$

Moreover, Kofstad [84] suggested that $HO^{\bullet}$ protons from water vapour in the oxidant atmosphere potentially dissolved into the oxide scale by the Equation (6.8):

$$^1/_2\ H_2O + O_2 \rightarrow HO^{\bullet} + e' + {}^1/_4\ O_2 \qquad (6.8)$$

If this reaction truly occurs, it promotes the progress of oxidation within the oxide scale by generating an additional oxygen source.

The results of the oxidation of the two steel grades in this study were in good agreement with all mechanisms described earlier.

6.2.1.4 Effect of alloying elements

As explained in Chapter 2, the oxidation kinetics of iron and steel at elevated temperature highly influenced by the chemical composition of the parent material. In general, most

alloying elements increase the oxidation resistance of iron by hindering the outward mobility of Fe cations. The results of isothermal oxidation experiments confirmed the importance of this phenomenon. Fig.4.2.6 demonstrates the isothermal oxidation rates of each steel grade at a temperature range of 850˚C to 1280˚C for 60 minutes under an atmosphere containing 17% water vapour. By comparing the oxidation rates of both alloys under a certain condition, it is clear the chemical composition of each grade immensely affected the oxidation rate of each alloy. Although due to the large variation in the chemical composition of the two steel grades used in this research, a direct comparison of the materials oxidation kinetics might not be a compelling approach, nevertheless, it provided valuable information.

Carbon

The addition of carbon alters the oxidation rate of ferrous alloys, and in general, it makes the oxidation rate more erratic [6]. Furthermore, it also extensively effects the phase composition and structure of the oxide scale, including the amount and nature of the oxide defects.

As demonstrated in Fig.6.2.3.a, Moore et al. [89] plotted the oxidation kinetic curve for a low carbon steel grade (0.028%C) at 1200˚C under an atmosphere containing 8.6% CO_2, 16.8% H_2O, 2.1% O_2 and 73.5% N. Likewise, the author plotted the oxidation kinetic curve for the rate of rail steel at 1280˚C under the humid condition in Figure 6.2.3.b. A comparison of the two curves revealed that even at 1200˚C, the oxidation rate of the low carbon steel was higher than that for the rail steel at 1280˚C.

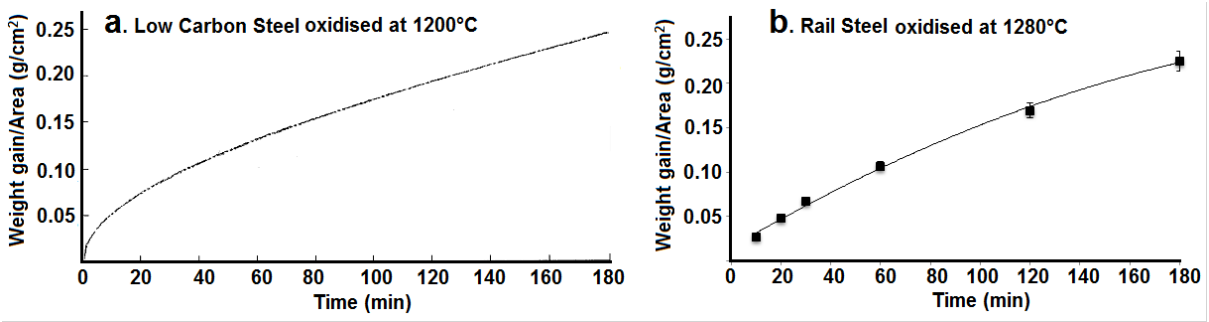

Figure 6.2.3 Oxidation kinetic curves for
a. low carbon steel at 1200°after Moore et al. [89] b. Rail steel at 1280°C.

The research of Wie et al. [90] confirmed that the oxidation rate of high carbon steel (0.82 C %) was lower than that for low carbon steel (0.06%) while the materials oxidised 700 to 900˚C under the air.

Likewise, Caplan et al. [7] demonstrated that the oxidation rates of high and medium carbon steel grades were lower than the oxidation rate of pure iron as a result of oxidation of Fe_3C and dissociation of carbon within the oxide-metal interface.

In high carbon steel grade such as rail steel used in this research, carbon could form CO or CO_2 by reacting with FeO at the oxide-metal interface [6, 115]. This phenomenon could introduce porosities and cavities within the oxide state and eventually generated a multilayer oxide scale. This hypothesis was in good agreement with observations made during oxidation of rail steel from this study.

Chang and Wie clarified when carbon limited the mobility of oxygen or iron ions throughout the oxide scale; it would reduce the oxidation process. In contrast, where the motion of the oxidant gases eased due to the development of transverse cracks, the oxidation rate would increase.

Likewise, García-Rincón [6] indicated that the pressure generated by carbon-monoxide and carbon-dioxide build-up within the oxide region could generate transverse cracks and boost the oxidation. On the other hand, if the integrity of the oxide scale maintained, because of the restricted movement of oxidant gases, the oxidation process would reduce. The above statements are in line with the outcomes of the isothermal oxidation studies of rail steel in this research.

Manganese

In this research, traces of manganese were only detected within the Fayalite phase at the oxide-metal interface of rail steel samples. As explained earlier in Chapter 2, manganese could replace the iron atoms in FeO, Fe_3O_4 and Fe_2O_3 lattices; hence, its role in the oxidation of ferrous alloys is insignificant. However, no evidence of (Fe, Mn)O, $(Fe, Mn)_3O_4$, and $(Fe, Mn)_2O_3$ phases was detected by EDX and XRD examinations of either of the steel grades in this study.

Mn might also precipitate in Si and Fe oxidation process to form iron-manganese-silicate within the oxide scale. In this research, the traces of Mn only detected within the Fayalite region at the oxide-metal interface of the rail steel samples that could be a piece of evidence for the above theory. The lack of manganese detection during the EDX analysis of the DSP samples might be related to the small quantity of this element within the parent metal original composition.

Silicon

As stated in the literature review, Si is one of the most important alloying elements in the production of electrical steel. The metallurgical characterises and properties of the final products is highly depended on its Si content and production and process parameters. Silicon is used as an alloying element in the production of electrical steel because it improves the permeability and resistivity and reduces the hysteresis loss and coercive force. Silicon also added to other steel grades because it can improve the ductility of the steel.

The effect of silicon on the oxidation rate of electrical steel was detailed in Chapter 2. The addition of silicon can potentially improve the high temperature oxidation resistance of ferrous alloys due to development of a protective layer of Silica or Fayalite at the oxide-metal interface. The composition of the protective layer significantly depends on the silicon percentage of the parent steel. The Si content 2.5-3% or higher leads to the development of SiO_2. In contrast, lower Si concertation in steel would enhance a reaction between Silica and Wüstite and subsequent development of Fayalite. Fayalite provides less protection against high temperature oxidation in comparison to Silica due to its lower melting temperature [5,6]. If during reheating the temperature reaches Fayalite-Wüstite eutectic point it can embed iron oxide particles within the Fayalite matrix and strongly bonded to the substrate after cooling, which can resist the water jet descaling process [31].

As observed in the DSP steel isothermal oxidation studies, below the eutectic temperature of Fe_2SiO_4-FeO (1177˚C), the addition of Si reduced the oxidation rate by preferential development of an enriched silicon layer at the oxide-metal interface. In contrast, at 1280˚C, the development of FeO-Fe_2SiO_4 eutectic phase promoted the mobility of iron ions across the oxide scale and enhanced the oxidation rate. The above results were in good agreement with the findings of Suárez et al. [80]. Their study demonstrated that once the oxidation temperature exceeded 1177˚C the oxidation rate of Si steel significantly increased which was due to development eutectic phases of Fe_2SiO_4-FeO and subsequent rapid oxidation because of liquid oxide attack. Furthermore, the study confirmed that the oxidation rate of Si steel below 1177˚C under a dry air atmosphere was considerably lower than the oxidation rate of low alloy steel.

Takeda and Onishi [81] also experienced similar results while studied the effect of Si content on the oxidation rate of low carbon steel. They witnessed that the oxidation rates of the

materials changed with Si content variations once samples were oxidised at 1100˚C and 1200˚C for 60 minutes. It was also observed that above 1100˚C the development of Wüstite was suppressed if the parent metal silicon percentage was adequate. Furthermore, the oxidation rate significantly increased when the oxidation temperature increased to 1200°C. The effect of Si concentration on the oxidation kinetics of silicon steel alloys has been summarised in Figure 6.2.4 [81]. The observations of Takeda and Takashi were in good agreement with isothermal oxidation results from this research.

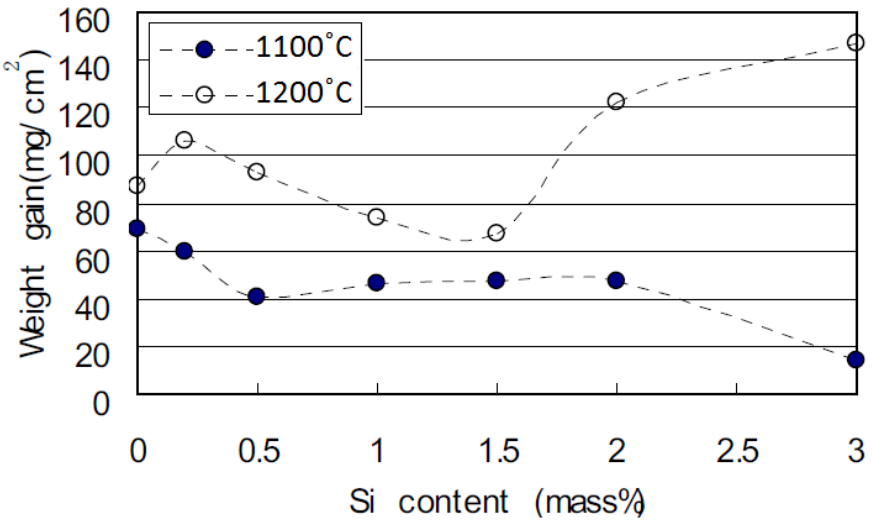

Figure 6.2.4 Effect of Si content on the oxidation rate of silicon steel [81].

Taniguchi et al. [72] observed a comparable scenario while examining the oxidation behaviour of low carbon steel alloys containing silicon up to 1.5 mass at 1103˚C and 1203˚C in a static laboratory air atmosphere. They witnessed, increasing the Si content of the parent materials led to the reduction of the oxide scales thickness at 1103˚C (Fig. 2.4.2.2.a) and the magnitude of the reduction had a direct relationship with the oxidation period. At 1203˚C the oxide development rate had a weak relation with the Si content of the parent material, although after 30 minutes they noticed a deviation in the oxidation rate of 0.5% Si steel.

Aluminium

As predicted in Ellingham diagram (Figure 2.2.1) aluminium is less noble than iron, and the addition of this element can form a protective oxide film at the oxide-metal interface and hinder the oxidation rate by reducing the outward diffusion of iron ions. Like silicon, the concentration of Al in parent steel and process temperature governs its effect on the oxidation kinetics [5].

The phase diagram proposed by Atlas and Sumida [130] revealed that $FeAl_2O_4$, FeO, Fe_3O_4, Fe_2O_3 and Al_2O_3 phases were all stable below 1250°C (Fig.2.4.2.4). It was clarified that because of cation deficiencies in Wüstite solid solution, the oxidation of materials containing iron, oxygen and aluminium could not be defined as a binary system of FeO-Al_2O_3.

Saegusa and Lee [91] demonstrated that when the steel alloy containing 1wt% Al, the developed Al-enriched layer at the oxide-metal interface was Al_2O_3, however when the reheating temperature exceeded 700°C the composition of the Al-enriched layer was $FeAl_2O_4$ spinel. Because the oxidation temperatures of the DSP specimens were well above 700°C in all isothermal experiments, therefore it can be concluded that the Al-enriched oxides scale most likely was $FeAl_2O_4$ phase.

6.2.2 Characterization of Oxides

The isothermal oxidation of both steel grades led to the development of multiphase oxide scales in all test conditions. The oxide scale microstructures and phase distributions were in agreement with the classic models of high-temperature oxidation of steel projected in the literature [1-3]. Characterisation of the oxide scales, including microstructural analysis and phase identifications, were completed using different analytical techniques including optical microscopy, XRD, backscattered electron imaging, EDX, and Laser Raman Spectroscopy. The experimental results were compared with literature including and published works of other researchers. The results confirmed that the type and extent of available phases vastly depended to the oxidation conditions including temperature, time, cooling rate and atmosphere along with parent metal composition. Based on the Fe-O equilibrium phase diagram (Fig.2.4.2.4), depending on the material and oxidation conditions, Wüstite, Magnetite and Hematite could be developed above 570˚C. However, Wüstite was not stable below 570˚C, hence depending on cooling rate this phase partially or completely transformed to Magnetite. Rapid cooling, such as quenching in cold water might eliminate this transformation. However, this process induced immense thermal shock stress, and due to the brittle nature of oxide scales, it might fail or damage. Therefore, all isothermal oxidised samples were cooled down to the room temperature under argon gas flow. Gleeson et al. [94] proposed a phase transformation diagram for the FeO scale layer, which was isothermally developed on a mild steel alloy at 900°C in air.

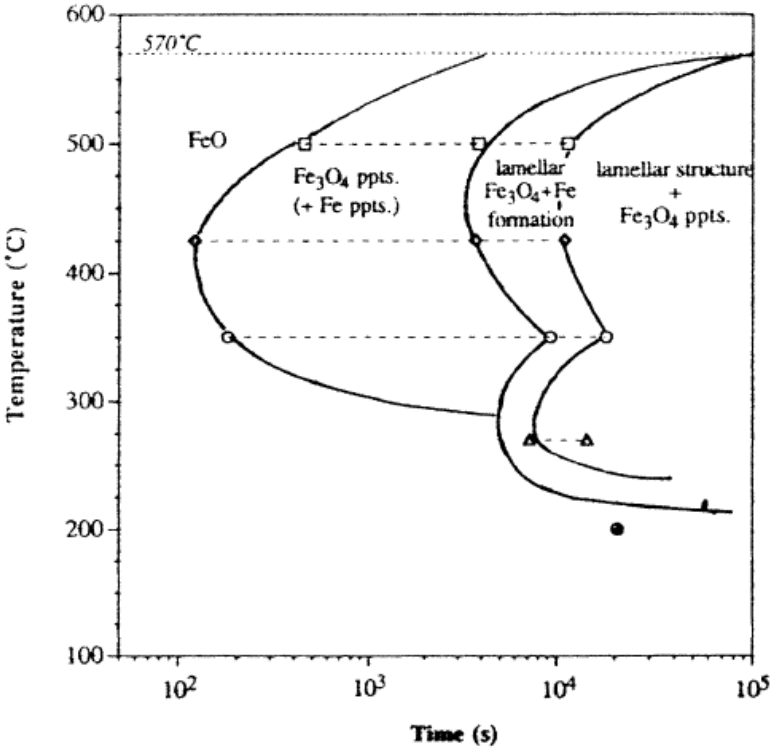

Figure 6.2.2.1 Phase transformation diagram for the FeO scale layer isothermally thermally grown on mild steel at 900°C in air proposed by Gleeson et al. [94].

As can be seen in Figure 3.3, the cooling stage in this research was quite rapid. By comparing the heating profile of the material and Figure 6.2.2.1, it was expected the transformation of Wüstite to be limited to minor precipitation of Magnetite within the FeO matrix.

X-ray diffraction analysis of the rail and DSP steels oxidised samples identified the composition of the oxide scales. The results were in good agreement with EDX microanalysis of the samples. The only difference between the XRD examination and the EDX analysis was the detection of small quantities of Hematite at the oxide-metal interface by XRD, which might be related to descaling and crushing process of the oxide scale. Residual of crushed oxide scales in the form of dust was apparent on the surface of the specimen during descaling, which possibly contained Hematite.

Cross-sectional analysis of rail specimen revealed that after 10 minutes of oxidation at 1280˚C under a humid atmosphere, a multiphase monolayer of oxide scale formed that included a very small separation gap between the substrate and oxide scale. However, as the oxidation progressed oxide sublayers were built up beneath the main outer scale by inward diffusion oxygen ions along with Co and H_2O gasses as described earlier in this chapter. As

demonstrated in Figure 4.4.1.1.3 up to 30 minutes, the extent of the separation gaps and voids rapidly increased, but in samples oxidised for longer, the growth of Wüstite reduced the development rate of the defects. The high concentration of such defects is a typical feature of high-temperature oxidation of steel alloys with high carbon content, which has been reported by other researchers [18, 33, 38, 74, 89]. The analysis confirmed that Wüstite was the predominant phase in all specimens.

Furthermore, a distinctive Magnetite layer was visible at the top region of the oxidised samples. The precipitation of Fe_3O_4 in the Wüstite matrix was limited to the outer layer. The pattern of the Magnetite precipitation was well fitted in the model proposed by Gleeson et al. [94]. Furthermore, very small quantities of Hematite only detected in samples oxidised for 30 minutes or longer.

As can be seen in Figure 4.4.1.1.9, after 10 minutes of oxidation of rail steel at 1150˚C in a humid atmosphere, multilayer oxide scales formed. Like oxidation at a higher temperature, a high concentration of defects such as gaps and cavities were apparent at the bottom of the scale. AS the oxidation progressed; the pores and cavities shifted into the Wüstite zones and became larger. These observations were in good agreement with works of Sheasby et al. [18] and Tulk et al. [38]. In the sample oxidised for 60 minutes, large elongated cavities were developed in the transverse direction within the outer oxide layer. The extent of the Magnetite precipitation zone was larger for longer oxidation period, which could be related to the slower cooling rate of the samples with thicker oxide scales. In all samples, Fayalite was only visible around the oxide-metal interface. Two layers multiphase oxide scale with a relatively large separation gap formed when the material oxidised at 1050˚C and 950˚C for 60 minutes under a humid atmosphere. At 850˚C, the structure of the oxide was quite dense, and the number of cavities at the oxide-metal interface was much smaller than previous scenarios. Fig.6.2.6.b shows the relation between the oxidation temperature and area faction of each iron oxide phase for the rail specimens oxidised between 850˚C-1280˚C under humid atmosphere for 60 minutes. The area fraction of the defects such as voids, porosity and separation gaps were excluded. As can be seen, Wüstite was the predominant phase in all temperatures with a maximum amount at 850˚C.

Additionally, the fair amount of Magnetite was detected in all specimens with a minimum quantity at 850˚C. The development of Hematite was very limited in all oxidation temperatures. Nevertheless, the highest quantity of this phase (2.3%) developed at 1050˚C.

Liu et al. [93] studied the relation of the temperature on the development rate of FeO, Fe_3O_4 and Fe_2O_3, for the oxidation of low carbon steel under an atmosphere containing 80%N_2–15%CO_2–5%O_2. Their research showed that Wüstite had the highest thickness fraction in all conditions. Despite the difference in the carbon content of Rail steel and low carbon steel used by Liu et al., the results of the two studies were comparable to an extent. As can be seen, in both images, above 1050˚C, the curves followed horizontal lines meaning the proportion of each phase remained almost the same. In Figure 6.2.2.2.a the lines only represented the thickness of each phase but in Figure 6.2.2.2.b, the image analysis included the area fraction of Fe_3O_4 precipitates.

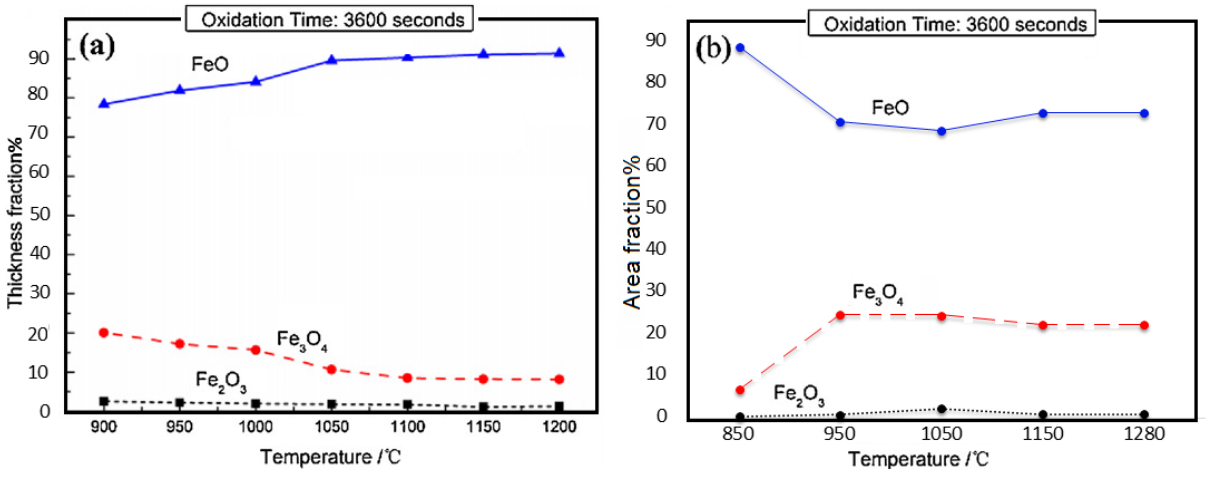

Figure 6.2.2.2 Effects of temperature on the development rate of FeO, Fe_3O_4 and Fe_2O_3: a. Thickness fraction of each phase for low alloy steel after Liu et al. [93] and b. Area fraction of each phase for Rail steel oxidised under humid condition.

The cross-sectional analysis of the Rail steel specimen oxidised at 1280˚C for 10 minutes confirmed the presence of a single layer oxide scale that contained Magnetite and Wüstite. In comparison to oxidation of this grade under a humid atmosphere, the width of the Wüstite noticeably reduced. In contrast, the Magnetite phase and the precipitation zone extensively widened; in fact, the Fe_3O_4 precipitates were even visible near the oxide-metal interface. Furthermore, small quantities of Fayalite only developed at the oxide-metal interface, and there was no sign of penetration of this phase into the oxide scale. After 180 minutes of oxidation under a dry atmosphere, the oxide scale constructed of only two distinctive layers. The outer layer contained Wüstite, Magnetite and a small amount of Hematite. The inner layer was mainly constructed of Wüstite; however, narrow lines of Fayalite also visible in this

segment. Under the dry condition, the oxide scales completely detached from the substrate metal. Similar observations were made by Tuck et al. [38] for the oxidation of low carbon steel at 950˚C under dry environment and by Sheasby et al. [18] for the oxidation of medium carbon steel at 1200˚C under moist free atmosphere. Sheasby and associates [18] claimed that because of this phenomenon, after 15 minutes of oxidation, the scales were over-oxidised while limited or no further oxidation of the metal occurred. They reported that a small amount of manganese and silicon did not reduce the oxidation of carbon steel. Furthermore, when Mn oxidised with Fe simultaneously, it eventually dissolved within the FeO phase without influencing the iron ions diffusivity.

The cross-sectional analysis of the DSP samples oxidised at 1280˚C under humid atmosphere confirmed that the rapid oxidation of all samples seen in isothermal oxidation studies was due to extensive development of Wüstite -Fayalite eutectic phase at the oxide-metal interface. The microstructures of all specimens were dense and free of porosity and cavities. However there were few cracks visible across the scales in samples oxidised for 60 and 120 minutes, these cracks may be developed by shear stresses induced during rapid cooling. The scale mainly constructed of Wüstite; however, a narrow zone of Magnetite was apparent as the outermost layer in all specimens. Furthermore, within the Wüstite matrix, small precipitation of Magnetite was observed. Fayalite penetration in Wüstite was visible in all samples. Zhou et al. [96] also witnessed this phenomenon in the oxidation of high silicon steel alloys under a binary gas mixture of oxygen (4%) and nitrogen. They believed that the penetration of liquid Fayalite-Wüstite was due to compressive stresses generated by the development of oxide scale. They clarified that Pilling–Bedworth ratio (PBR) was the ratio of the oxide volume to the consumed metal volume. Because the volume of the oxide scale was higher than the consumed Fe or Si, therefore, the PBR ratio of the Fe and Si oxide scales were greater than 1, and as a result, compressive stresses were developed within the oxide structure. At the oxide-metal interface, the presence of non-oxidised iron particles within the Fayalite layer was another indication for the development of liquid Wüstite -Fayalite phase. This observation was in good agreement with the report of Martinez et al. [79]. The observations made in this research were comparable to microstructures observed by other researchers for the oxidation of high Si steel above FeO-Fe_2SiO_4 eutectic temperature [80, 95, 96].

In the oxidation of DSP steel at 1150˚C under a humid atmosphere, very different microstructures were observed. Thick continues layer of Fayalite along with a small quantity of Wüstite, which was highly adherent to the substrate metal. As diffusivity of iron ions through solid Fayalite was extremely lower than liquid FeO-Fe_2SiO_4; therefore, the oxidation was much lower than1280˚C. In all specimens, the outer oxide layer detached from the oxide sublayer. Up to 30 minutes of oxidation, the outer oxide layer containing Magnetite and Hematite was developed with no signs of large porosity or cavities. However, large elongated cavities were formed within the outer oxide layer when the oxidation time extended. The population and extent of these defects had a direct relationship with the development of Wüstite within the outer oxide layer because of these defects concentrated within the Wüstite where Magnetite precipitation occurred (Figure 4.4.2.1.5).

In contrast, during the oxidation of DSP steel at 1150˚C under the dry atmosphere, there were no indications of these defects as oxide only contained Magnetite and Hematite (Figure 4.4.2.2.1). However, as demonstrated in Figure 4.4.1.1.13, similar defects were observed in the rail steel sample oxidised at 1150˚ for 60 minutes under a humid atmosphere. This observation confirmed the development of large elongated cavities highly influenced by the oxidation temperature and the composition of the oxidant atmosphere. Once again, the development of large elongated voids along with small pores and cavities were only visible if Wüstite phase was present. This occurrence could explain the lack of porosity defects within Fayalite layer at the oxide-metal interface of DSP specimen oxidised for 10 minutes under a humid atmosphere (Fig.4.4.2.1.5.a). As mentioned in Chapter 2, The high-density of defects within Wüstite phase was due to the higher mobility of defects in FeO because of its NaCl crystal structure in comparison to α-Fe2O3 with a rhombohedral structure. The porosity development initiated, once Wüstite sufficiently formed around Fayalite layer at the oxide-metal interface. As the development of Wüstite increased the extent and population of the pores augmented. Figures 6.2.2.3 a and b demonstrate the interface of DSP and rail steel samples, respectively. Both samples were oxidised at 1150°C for 60 minutes under a humid atmosphere. As can be seen, in rail steel due to lack of a continuous layer of Fayalite, a large amount of Wüstite formed next to the interface; as a result, the number and size of the cavities increased.

Development of oxide precipitates within the substrate metal could be defined as internal oxidation. This phenomenon may occur where inward diffusion of oxygen is higher than the

migration of active elements toward the surface. The oxygen dissolves into the metal substrate at the oxide-metal interface and subsequently reacts with metal atoms below the surface. Internal oxidation zones were apparent in both samples. However the depth of this zone was more extensive in rail steel Once more, this was due to lack of a protective layer of Fayalite in the rail grade which eased the outward diffusion of iron ions and inward diffusion of oxygen ions [2].

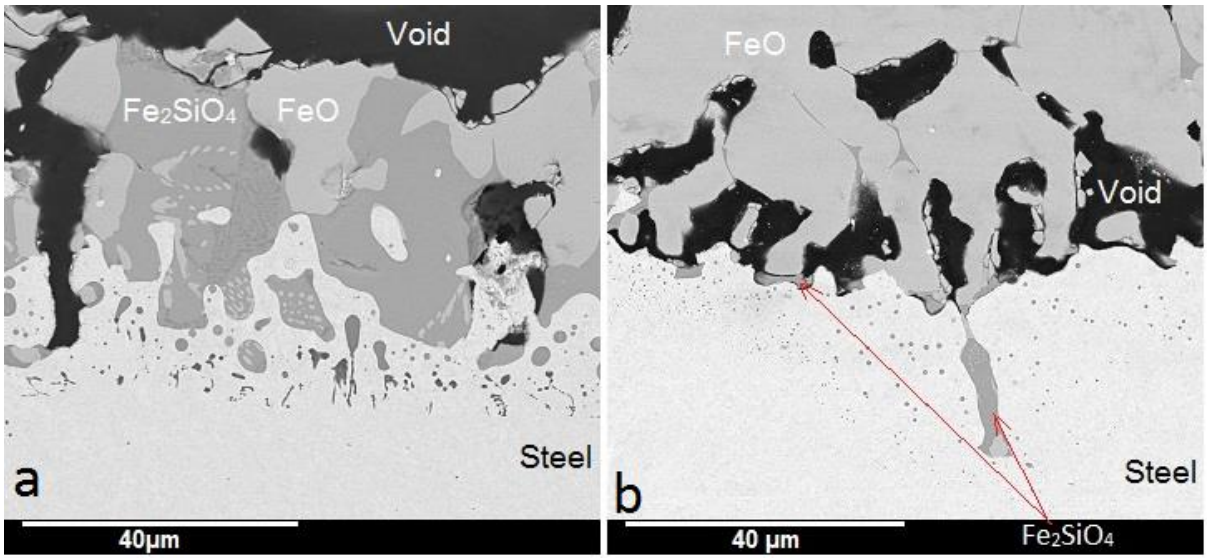

Figure 6.2.2.3 BSE imaging of the oxide-metal interface of the samples oxidised at 1150°C for 60min under humid atmosphere: a. DSP steel b. Rail steel.

The isothermal oxidation of the DSP steel at 1050˚C and 950˚C for 60 minutes under humid condition led to the development of multi-layer oxide scales containing Wüstite, Magnetite and Hematite along with Fayalite. In Figures 4.4.2.1.13 and 4.4.2.1.15, the development of a transition layer with a fine and complex microstructure containing Wüstite and Fayalite was one of the oxide scales characteristics. Song et al. [95] observed a similar transition zone in the oxidation of low carbon steel with 0.94% Si at 1000˚C in the air. In this research, a similar transition layer was detected during the oxidation of DSP steel at 850˚C. However, the microstructure of this zone was considerably finer than the samples oxidised at higher temperatures. Furthermore, whiskers of Hematite grew on the oxide surface (Figure 4.4.2.1.18). The development of Hematite whiskers reported in high-temperature oxidation of iron and steel by other researchers [27, 32, 39, 97]. Yuana et al. [97] investigated the mechanism of Hematite whiskers growth during the thermal oxidation of iron. They confirmed that the Fe_2O_3 whiskers could develop in four-layered ($Fe/FeO/Fe_3O_4/Fe_2O_3$) or the

three-layered ($Fe/Fe_3O_4/Fe_2O_3$) oxide scales. They suggested that the relaxation of the compressive stresses generated by solid-state transformation at the Fe_3O_4/Fe_2O_3 interface was the driving force for spontaneous development of Hematite whiskers. Figure 6.2.2.4.a demonstrates the schematic mass transportation and the diffusion mechanism of Fe ions for development of Hematite whiskers proposed by Yuana et al. [97]. As can be seen, the diffusion of Fe ions from Magnetite-Hematite interface towards the outer surface of the oxide scale via grain boundaries under compressive stresses was required to persist the growth of the whiskers. Furthermore, it was observed that the Fe_2O_3 whiskers formed on top of the Hematite grains rather than the grain boundaries.

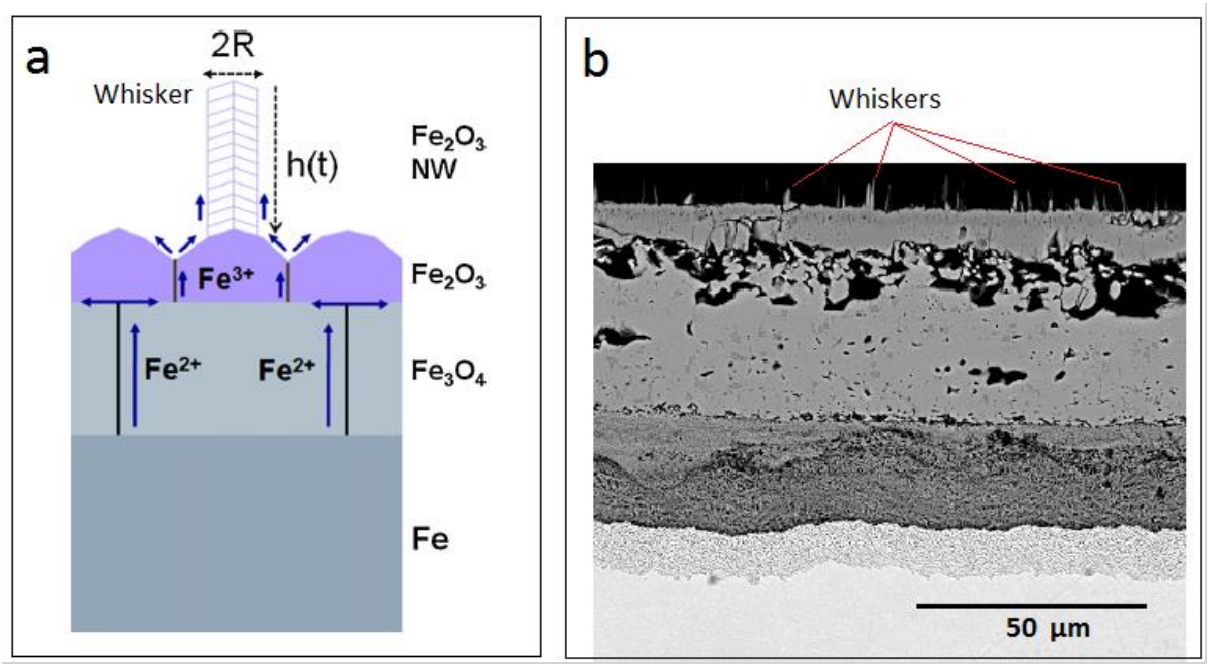

Figure 6.2.2.4 a. Schematic model of the mass transportation mechanism by diffusion of Fe ions for development of Hematite whiskers proposed by Yuana et al. [97].
b. Whiskers developed on a DSP sample oxidised at 850°C for 60 minutes under an atmosphere containing 17% moisture.

The microstructure of the oxide sale under dry atmosphere was completely different from the oxide scales developed under humid condition. As shown in Figure 4.4.32, the outer oxide scale was made of a single dense layer. Up to 60 minutes, the outer scale contained Hematite and Magnetite, however after 180 minutes almost the entire layer transformed to Fe_2O_3. In contrast to oxidation in humid condition, Wüstite was apparent in any of the DSP samples oxidised under a dry atmosphere. As demonstrated in Figure 6.2.2.5, this was likely due to the development of a thin layer of SiO_2+ Fe_2SiO_4 beneath the oxide-metal interface, which was enriched with Aluminium (possibly in the form of $FeAl_2O_4$). This observation was in good

agreement with the work of Li et al. [78] during oxidation of high silicon steel at 800 ˚C under dry and humid CO_2 atmospheres. In terms of oxidation of steel, Fayalite spinel phase is less protective than SiO_2 [5]. According to Chang and Wei [5], the development of continues layer of SiO_2 is subject to Si concentration of the parent metal and the composition of the oxidant atmosphere.

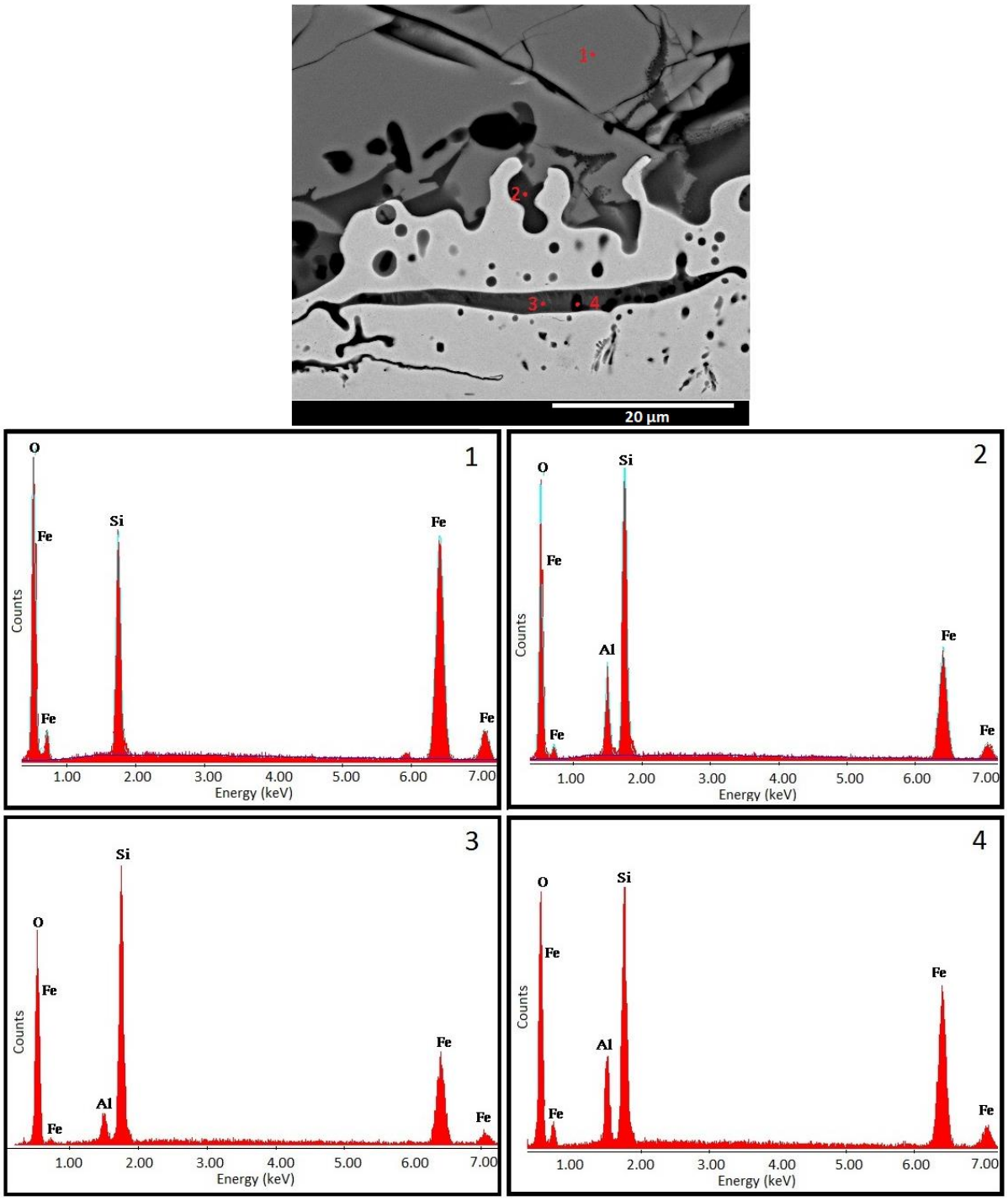

Figure 6.2.2.5 BSE image and EDX chemical composition analysis of the oxide-metal interface of a DSP specimen oxidised for 60 minutes at 1150°C in a dry atmosphere.

6.3 High-temperature mechanical testing of the Oxide Scale

The high-temperature mechanical testing of the oxidised samples aimed to evaluate the scale failure modes under compressive, tensile and shear stresses. The variations of the deformation temperature helped to understand the effect of temperature on morphology, phase distribution, defects evolution and plasticity of the oxide scales under high-temperature deformation condition.

.

6.3.1 High-temperature compression tests

It is extremely difficult to mimic the deformation process in an industrial rolling mill because the process conditions are complex due to process parameters variation, including temperature, atmosphere, and the irregularity of the strain rate.

Nevertheless, the tailored compression test in this study provided valuable information for understanding the nature of the oxide scale under hot working conditions. The distinguished aspect of the test was designing a compression tool with a curved tip, which allowed the study of the behaviour of the primary oxide scale under compressive forces along with shear stresses. The hot compression experiments confirmed that the test temperature significantly influenced the failure mode of the oxide scale of both steel grades and depending on the test condition, ductile or brittle behaviour were observed across the oxide scale.

6.3.1.1 Evaluation of undeformed samples

The microstructure of the oxide scale of undeformed rail steel specimen oxidised in the test rig chamber at 1280°C under dry gas flow was in line with the pattern of the scales developed in isothermal oxidation studies. The dense multilayer scale was constructed of three types of iron oxide with an average thickness of 723 µm. The area fraction ratios of Fe_2O_3: Fe_3O_4: FeO were quantified as 7: 49: 44, respectively. In the calculation, the area fraction of pro-eutectoid Magnetite precipitates was added to the total amount of this phase. There was no sign of residual oxide particles, including Wüstite and Fayalite at the oxide-metal interface. However, small quantities of these phases were apparent across the internal oxidation zone as isolated particles within the steel matrix.

The microstructure of undeformed DSP steel oxide scale sample that oxidised at 1150°C under dry gas flow was similar to the oxide scale developed in isothermal studies of DSP steel apart from the absence of Magnetite in the undeformed compression test sample. The dense monolayer scale was mostly constructed of Hematite. The area fraction of Fe_2O_3 / Fe_2SiO_4 was calculated as 95 / 5, respectively.

Although for both steel grades, the thick oxide scales were almost intact during the macro examination, after sectioning the specimen, it was established that the scales almost entirely detached from the substrate steel. This kind of oxide scale behaviour was previously observed during isothermal oxidation of rail steel and DSP steel under a dry atmosphere. The delamination of the thick primary oxide scale was related to the generation of stresses during the oxidation and cooling stages.

Initially, the stresses were generated, particularly at the oxide-metal interface, as a result of oxide scale development and growth on the substrate metal. As described in Chapter 2, this phenomenon could be defined by the Pilling-Bedworth ratio ($P.B_{ratio}$). The $P.B_{ratio}$ for Fe-FeO Fe-Fe_3O_4 and Fe-Fe_2O_3 were reported as 1.78, 1.90 and 2.14 respectively thus oxidation of iron above 700°C generated compression stresses [6], [10], [11], [12], [13].

Furthermore, due to differences between the coefficient of thermal expansions of the oxide constituents and the substrate steel, stresses were generated between the oxide and substrate metal which hypothetically developed defects within the scale or even led to final delamination of the scale. It was assumed that cooling from oxidation temperature led to compressive strains in the oxide and, thus, to spalling. Similarly, externally induced compressive oxide strains under isothermal conditions can lead to the same processes.

Different theories proposed for defects development mechanism and subsequent delamination of the oxide scale during the cooling stage. Figure 6.3.1 demonstrated the two different failure modes were proposed for oxide failure by Schütze [7]. It was assumed in failure mode I, the bonding of the oxide-metal interface was strong, and it was not weakened by pores and voids developments and segregation of alloying elements. The failure of the oxide scale started with crack formation under the influence of shear stress, followed by a crack development and propagation along the oxide-metal interface (Figure 6.3.1.a). As this model was based on a strain-energy criterion, the spallation arose when the induced strain energy within the oxide, equalled or exceeded the energy required for decohesion along the oxide-metal interface. In the failure mode II, decohesion of the oxide layer from substrate

metal along with buckling of scale led to the development of through-thickness cracks and extended the decohesion region (Figure 6.3.1.b).

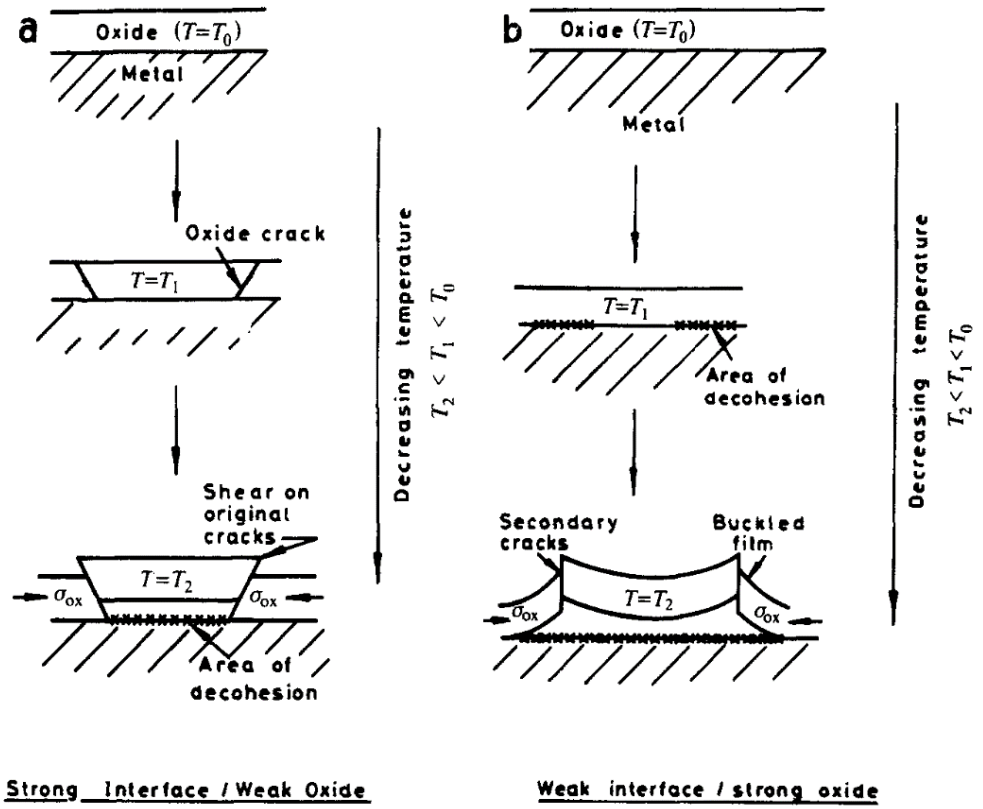

Figure 6.3.1 Schematic representation of the steps in the oxide failure mechanism (a) Mode I: strong interface, weak oxide, through-scale shear cracking precedes interfacial decohesion; (b) Mode II: weak interface, strong oxide, decohesion, and buckling precede through-scale cracking, after Schütze [7].

This could be related to the difference between coefficients of expansion of the oxide scale and the steel substrate. Because contraction of the substrate steel was greater than the oxide scale, tensile and shear stresses were generated between the oxide and substrate metal which potentially lead to final delamination of the scale while the thick primary oxide resisted retaining its shape and integrity.

6.3.1.2 Evaluation of deformed rail steel specimens

As stated in Section 5.2, all rail steel specimens were oxidised at 1280° and then deformed at various temperatures. The cooling the samples to the test temperature, deformation, and

cooling to ambient temperature were all performed under argon gas flow. The cross-sectional examination of all deformed samples confirmed the presence of a Fe_2O_3, Fe_3O_4 and FeO in all specimens, however, depending on the deformation temperature, the percentage of each oxide constituent slightly varied between the specimens.

In deformation of the oxide scale at 850°C, the area fraction ratios of FeO: Fe_3O_4: Fe_2O_3 were calculated as 22: 8: 70, respectively. The cross-sectional analysis revealed that Hematite layer was crushed to small fragments under the compressive load that confirmed the brittle nature and low plasticity of this phase. Moreover, Fe_3O_4 layer was fragmented into several pieces within the mid-region of the oxide scale; however, the size of the fragments was larger than the Hematite segments. In contrast, the dense plastically deformed Wüstite layer, which contained a limited number of defects confirmed the higher ductility of FeO at this temperature in comparison to the other two phases.

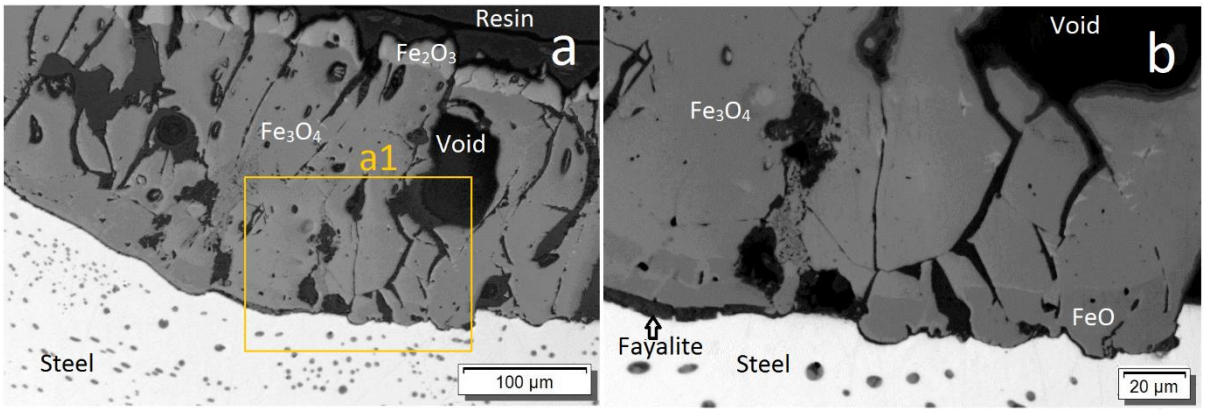

Figure 6.3.2 a. Optical images of oxide scale microstructure for a rail steel sample, deformed at 950˚C (Tox = 1280˚C, oxidation 60min) b. Higher magnification of zone a1 in Figure 6.3.2 a.

The sample deformed at 950°C also contained all three types of iron oxide along with small quantities of Fayalite at the oxide-metal interface. The Wüstite: Magnetite: Hematite area fraction ratios established as 22: 8: 70, respectively. Several relatively large voids were apparent within the oxide scale. Like deformation at a lower temperature, most of the damage occurred within the thin outermost layer of Hematite confirming the brittleness of this phase at 950°C. On the other hand, although the cracks were developed within the Magnetite layer, fragmentation did not occur across this phase. However, the higher density of porosity was apparent within Magnetite region.

As demonstrated in Figure 6.3.2.b, the amount of Wüstite significantly reduced, nevertheless this phase deformed in a ductile manner. The increase of the Magnetite and Hematite segments and reduction of Wüstite region were in good agreement with the works of Schweighofer and Tyas [64].

The morphology of the oxide scale observed in rail steel sample deformed at 1050°C was more complex than the previous test conditions. As can be seen in Figure 6.3.3 in the right-hand side of the sample, Wüstite was the predominant phase. Consequently, more ductility was observed after deformation. Contrary on the left-hand side of the BSE image, Magnetite was the main oxide constituent, and a small amount of Hematite and Wüstite were apparent at the top and bottom of the oxide scale respectively. This inconsistency could also be observed within the internal oxidation zone, on the right section large elongated FeO particles were present below the oxide-metal interface, however on the other side only fine dispersed particles of FeO-Fe_2SiO_4 were visible.

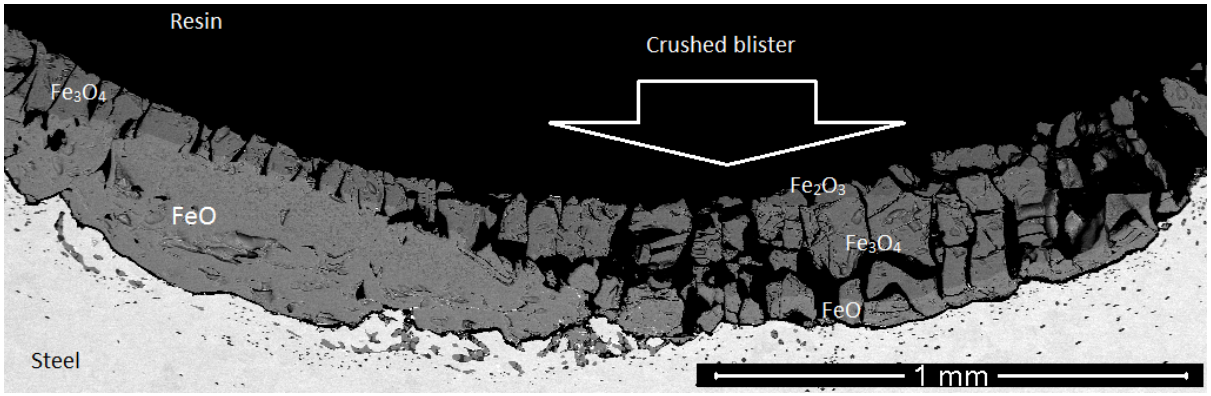

Figure 6.3.3 Oxide scale microstructure of rail steel deformed at 1050˚C (Tox = 1280˚C, oxidation 60min).

The structural inconsistency was related to the development of blisters on one side of the sample during oxidation stage, as demonstrated in Figure 6.3.4. The subsequent crush of the blisters under compressive load, triggered the through-thickness destruction of the oxide scale, as highlighted in Figure 6.3.3. Trull [4] observed similar features during hot plane strain compression test of mild steel. Comparable features also witnessed by García-Rincón [6] while rolling mild steel samples at elevated temperatures. The white boron nitride coating was deposited on the oxide scale surface by the tip of the tool during the deformation, which lasted 3 seconds. The other distinctive feature was the partial extrusion of the substrate metal

into the lower section of the oxide scale due to higher plasticity of the rail steel at this temperature. Although the distribution of the iron oxide phases was heterogeneous across the arc of the contact, the overall area fractions of FeO: Fe_3O_4: Fe_2O_3 were measured as 55: 40: 5 via image analysis.

Figure 6.3.4 rail steel specimen after Hot compression tests deformed at 1050˚C (Tox = 1280˚C, oxidation 60min).

In the sample deformed at 1150˚C, the oxide scale structure was more homogenous in comparison to previous test conditions. This homogeneity included the proportions and distributions of iron oxide phases along with the population of the defects. The observation was in line with the visual assessment of the sample during and after the test. The surface of the oxidised test piece was smooth, and there were no signs of blistering across the oxide scale (Figure 5.2.7.a). The area fractions of FeO: Fe_3O_4: Fe_2O_3 were quantified as 50: 39: 11. The amount of porosity and cracks within the Wüstite region reduced in comparison to previous tests due to higher ductility of this phase at elevated temperature. Partial extrusion of metal into Wüstite phase was visible in few locations. Once more, a high density of cracks was apparent within the Hematite and Magnetite layers. The total oxide scale failure by through-thickness cracking and delamination was observed around the top of the arc of contact.

Furthermore, as demonstrated in Figure 6.3.5, the columnar Magnetite grains were inclined under the loads imposed by the side of the compression tool. The deformation of the grains in this manner induced shear stresses within the scale, which could jeopardise the oxide scale

integrity. Trull [4] reported a comparable oxide scale structure containing inclined columnar grains after a plane strain compression test on a mild steel specimen at 1070˚C. It was suggested that the subsequent development of shear stresses was a potential mechanism for delamination under compressive load. Other researchers [107] also acknowledged a similar effect of phase boundaries sliding on duplex stainless steel.

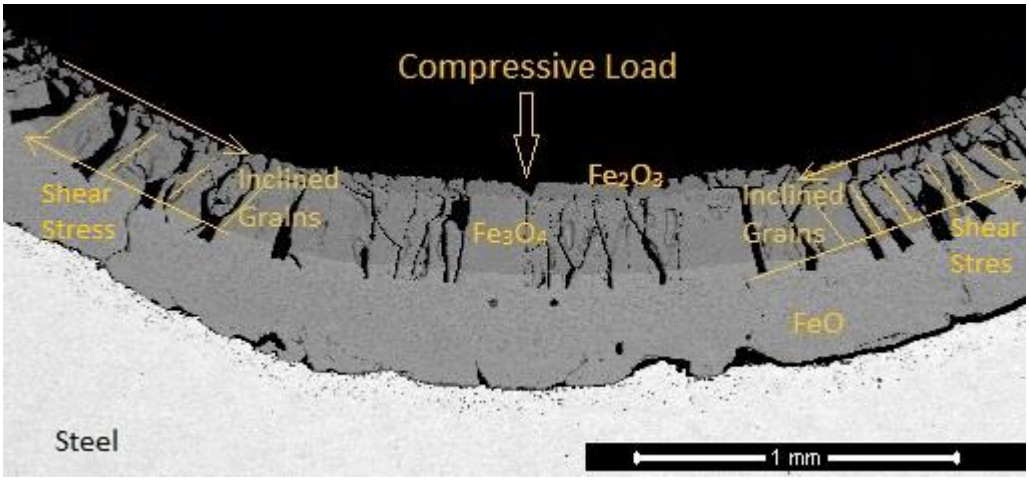

Figure 6.3.5 Oxide scale microstructure of rail steel deformed at 1150˚C (Tox = 1280˚C, oxidation 60min).

As witnessed during the visual inspection of the test piece (Figure 5.2.1 e), the deformation of the oxide scale was entirely ductile when the rail steel sample tested at 1280˚C. Regardless of applying boron nitride coating on the tip of the tool, the outermost layer of Hematite was completely removed after deformation due to high ductility and stickiness of this phase. A major part of the Magnetite layer was also snatched by the compression tool. However, Wüstite completely persisted around the arc of the contact. As can be seen in Figure 5.2.8, the irregular shapes of the residual oxide scale indicated that the Fe_3O_4 layer was severely torn apart when the tool was uplifted at the end of deformation. The detection of the sticking phenomenon at high temperature was in good agreement with the observations made by other authors [4], [108]. However, Trull [4] indicated that the sticking effect occurred when the thickness of the oxide was about 50 µm and no such effect was observed on the deformation of the oxide scale with 100- 250 µm thickness. This was not in contradiction to the observations made in this research, because Trull used a temperature range of 870°C-1070°C, correspondingly no sticking effect was detected below 1150°C in current work. Several large elongated voids were visible within the FeO-Fe_3O_4 precipitation zone, which was

formed as a result of inclined columnar grains by the mechanism explained earlier. Due to partial removal of the oxide scale, the proportions of the iron oxide phases measured by analysing the undamaged section of the oxide scale, which was located next to the arc of the contact. The area fractions of FeO: Fe_3O_4: Fe_2O_3 were measured as 46: 50: 4. The details of compression tests analyses of rail steel samples are summarised in Table 6.3.1

Table 6.3.1 High-temperature compression test conditions and analysis of rail steel specimens oxidised at 1280°C for 60 minutes.

Deformation Temp (°C)	FeO Failure Mode	Fe_3O_4 Failure Mode	Fe_2O_3 Failure Mode	FeO: Fe_3O_4: Fe_2O_3 Area Fraction Ratio
850	Ductile	Brittle	Brittle	22: 8: 70
950	Ductile	Brittle	Brittle	3: 81: 16
1050	Ductile	Brittle	Brittle	55: 40: 5
1150	Ductile	Brittle	Brittle	50: 39: 11
1280	Ductile	Ductile	Ductile	46: 50: 4

6.3.1.3 Evaluation of deformed DSP steel specimens

As detailed in Table 5.1, the isothermal oxidation stage of the compression tests of all DSP steel specimens was performed under a dry air flow at 1150°C. Subsequently, the samples were deformed in a temperature range of 850°C - 1150°C and cooled down to ambient temperature under Argon atmosphere. The cross-sectional assessment via BSE imaging and EDX confirmed that the microstructure and failure of the oxide scales of the DSP steel were methodically different in comparison to rail steel. In all DSP specimens the oxide scale mainly constructed of Hematite and Magnetite alongside small quantities of Fayalite. Similar to the previous tests, the proportion of each phase was relatively depended on the deformation temperature.

As demonstrated in Figure 5.2.9, the Hematite was the predominant phase; the image analysis confirmed that Fe_2O_3: Fe_3O_4 ratio was approximately 87:13. As established earlier at 850°C, both phases were brittle; therefore, as expected, the oxide scale failed in a brittle manner. Many through thickness cracks, particles and cavities were developed under the compressive load. The size of the oxide fragments was much smaller in regions distant from the centre of the sample (Figure 5.2.9). This phenomenon could be explained by appreciating the nature of the stresses applied across the arc of the contact. The intensity of the shear

load (from the curved surface of the tool) multiplied by moving away from the sample centre line and because of the brittle nature of the oxide constituents at this temperature, the defects density increased or in other words the size of the fragments reduced. The other oxide present phase was Fayalite, which was mostly concentrated at the oxide-metal interface. However, due to the high applied load and higher plasticity of Fe_2SiO_4, it was squeezed into the micro-cavities at the lower region of the oxide layer. Fayalite was also visible below the steel surface in the form of a thin continues layer.

Furthermore, small particles of SiO_2 along with slight amount aluminium enriched oxide (possibly Fe_2SiO_4+$FeAl_2O_4$) detected within the Fayalite matrix. Other researchers reported the development of this compound during the oxidation of high Si steel [78], [109]. SiO_2 particles were also spotted during the tensile testing of DSP steel sample at 850°C, which would be discussed later. Partial and complete through thickness extrusions of metal into oxide scale were apparent within the arc of the contact.

At the temperature 950˚C, phase distribution was comparable to the previous test of DSP steel sample. The Fe_2O_3: Fe_3O_4 ratio was estimated as 89:11 in the top of the arc of the contact, however in mid-region of the deformation zone, the main body of the oxide was solely constructed of Hematite. Once again, the penetration of Fayalite into micro-cavities of the oxide scale was detected. The expanded penetration depth of Fayalite confirmed higher ductility of this phase at a higher temperature. The EDX analysis confirmed the presence of SiO_2 isles within the Fayalite matrix around the interface.

Moreover, a thin layer of Fayalite covered the substrate beneath the oxide-metal interface. Like deformation at a lower temperature, the Fayalite phase was enriched with aluminium creating a similar compound at the oxide-metal interface (possibly $FeAl_2O_4$-Fe_2SiO_4). Although Hematite was not categorically ductile at this temperature, nevertheless the number of through-thickness cracks across the oxide scale reduced due to an increase in the deformation temperature. On the top regions of the contact curve, oxide scale was crushed to various small fragments under the shear load. Like deformation at 850°C partial metal extrusion was visible in multiple locations. However, no evidence of through-thickness extrusion was detected across the arc of the contact. Several failure mechanisms were identified across the oxide scale at 950°C. As Fe_2O_3 was brittle at this temperature, various cracks were formed within the oxide scale in different directions. Like deformation at a lower temperature,

through thickness cracks were observed across the arc of the contact due to a compressive load.

On the other hand, horizontal and angled cracks were shaped under shear stresses. Furthermore, near the top of the arc, small Hematite particles were formed as a result of the oxide scale crushing under shear load. Although the failure modes were similar to previous test condition, the density of the defects comparatively reduced due to an increase in the test temperature and subsequent slight upsurge in dislocations movement across the oxide scale structure.

The oxide phases detected in the specimen deformed at 1050˚C were similar to the samples deformed at lower temperatures. However, the extent of Magnetite considerably increased in comparison to the previous test conditions. The Fe_2O_3: Fe_3O_4 ratio was evaluated as 71:29. As anticipated, Fayalite pentation into the micro-cavities within the lower section of Magnetite, formed a complex structure. Around the oxide-metal interface, the typical thin layer of Fe_2SiO_4 was observed. Like previous tests, this zone contained a limited quantity of aluminium. Due to higher deformation temperature, the characteristics of the defects changed. Accordingly, the number of through-thickness cracks considerably reduced; in contrast, the width of the crack significantly increased. Although Hematite was still brittle at 1050°C, its failure pattern was an indication of a slight improvement in the plasticity of this phase. Furthermore, a small number of partial metal extrusions into the scale were apparent across the arc of the contact. On the other hand, only one through thickness extrusion was observed, which was located at the arc of the contact top section.

When DPS steel specimen tested at 1150°C, the number oxide scale transverse cracks significantly reduced. The oxide scale was mainly constructed of Hematite along with small quantities of Magnetite and Fayalite. Although the tip of the compression tool coated with boron nitride suspension, due high adhesiveness of Hematite at the test temperature, a large portion of the oxide scale was removed by the tool after deformation. The shape of the failed oxide scale surface verified that Hematite failed in a ductile manner, as demonstrated in Figure 5.12.c. It was noticed the application of boron nitride as a coating agent, immensely reduced this destructive phenomenon. The sticking effect is one of the main causes of the oxide failure in a hot rolling mill which can deteriorate the surface quality of the finished products. The compression tests revealed that the sticking effect highly depended on the temperature at the point of contact, or in other words to the oxide constituent plasticity. As

stated earlier Trull [4] experienced the sticking effect and partial removal of oxide scale during plane strain compression test of mild steel at temperatures as low as 870°C. It was claimed that the oxide pick up by the tool was highly influenced by the thickness of the oxide scale. The complex penetration of Fayalite into the lower section of Magnetite was not apparent at this testing temperature, which could be associated with multiple grounds. First of all, due to the high temperature of the test, the parent steel was much softer, or in other words, the compressive stresses within the system significantly reduced. Furthermore, although at 1150°C Magnetite was still brittle, the extent of micro defects within this phase was very limited, which was possibly due to a slight improvement in the plasticity of Fe_3O_4. The composition of the oxide constituents around the oxide-metal interface was similar to the previous test samples, which included Fayalite and aluminium enriched oxide (possibly in the form of Fe_2SiO_4+$FeAl_2O_4$). The details of compression tests analyses of DSP steel samples are summarised in Table 6.3.2.

Table 6.3.2 High-temperature compression test conditions and analysis of DSP steel specimens oxidised at 1150°C for 60 minutes.

Deformation Temp (°C)	Fe_3O_4 Failure Mode	Fe_2O_3 Failure Mode	Fe_3O_4: Fe_2O_3 Area Fraction Ratio
850	Brittle	Brittle	13:87
950	Brittle	Brittle	11:89
1050	Brittle	Brittle	29:71
1150	Brittle/Ductile	Brittle	-

6.3.1.4 General inferences of the high temperature compression test

The hot compression experiments confirmed that the test temperature and parent metal composition significantly influenced the failure mode of the oxide scale. In general term, the plasticity of the oxide scale was improved as deformation temperature increased. However, the behaviour of the multi-phase oxide scale was complex. It was established that the behaviour each oxide constituent was ductile, brittle or a mix of both modes based on the test condition and parent metal chemical composition. The diverse plastic and elastic behaviours of the oxide scale were previously reported by other researchers [12, 16, 22, 24, 28, 29, 31, 34, 80] through various test methods. As demonstrated in Figure 6.3, the ductile

to brittle failure mode transition temperatures reported by other authors were not entirely consistent. This scenario was similar to the variations in oxide scale behaviours of two different steel grades in this work. The overall failure mode of the oxide sale was directly associated with the proportion of each oxide constituent. In other words, a multi-phase oxide scale must be considered as a composite state, which the failure of the system is highly depended on each component. This was the main reason for the relatively higher ductility of rail steel oxide scales in comparison to the DSP grade samples.

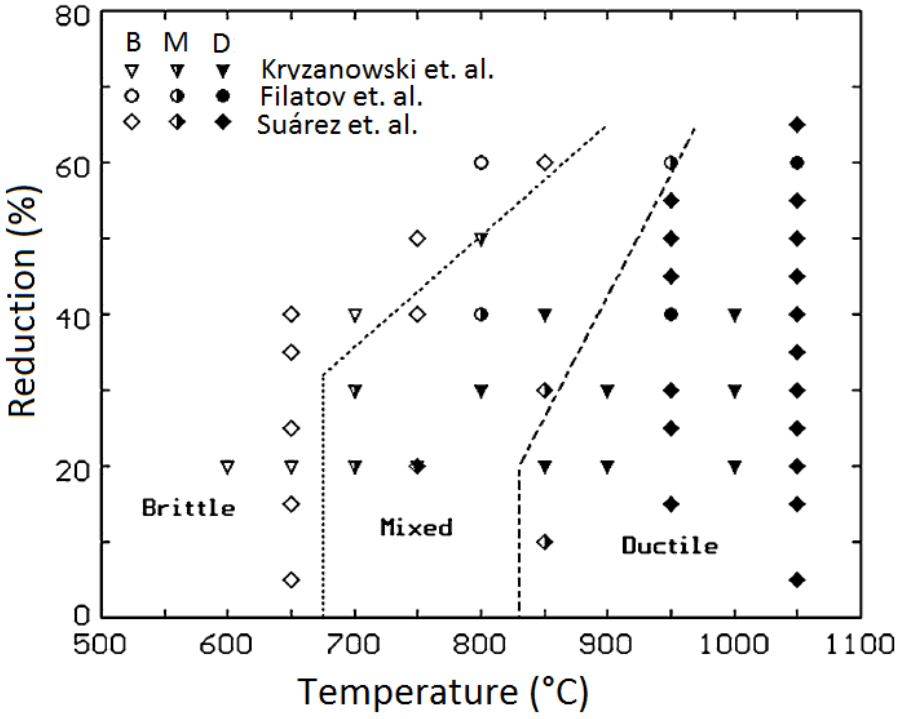

Figure 6.3.6 Behaviour of the scale during deformation; reported by different authors; [16, 22, 24, 28, 110] after Suárez [28].

Furthermore, the thermomechanical behaviour of the oxide scale was highly influenced by the type and shape of the defects, including blisters, voids, and pores. As explained earlier, the blister could change the local proportions of the oxide phases. This was possibly due to a delay in the migration of metal ions throughout the large spaces. Because even at 1150°C Hematite was brittle, it could explain why the number of cracks augmented when the amount of this phase increased within the oxide layer. As observed in cross-sectional examinations, Wüstite had the highest plasticity among the all three iron oxide constituents. A thick FeO layer could exhibit desirably, as it did not only act as a protective layer but also could reduce

the friction stresses between the workpiece and the tool during the high temperature deformation of steel.

Deformation of the oxide at higher temperature confirmed the ductile behaviour of the oxide scale, as explained in Section 5.2. The strength of the oxide-metal interface was decreased by increasing the temperature; conversely, the plasticity of the oxide scale was increased. The results were comparable to the findings of Trull et al. [5]. Partial and through-thickness metal extrusion was observed in compression at higher temperatures, which were similar to rolling experiments done by Garcia et al. [6].

6.3.2 High-temperature tensile tests

The behaviour and failure modes of the oxide scale at elevated temperature are complex and yet no single theory can predict the behaviour of oxide scale under different conditions.
The distinctive high temperature tensile test in this work was designed to provide a better understanding of oxide scale macro/microstructural transformation, defects evolution and failure mechanisms of oxide scales under tensile loads. The study included the effects of temperature and parent metal compositions on the failure modes of the oxide scale. Moreover, the obtained numerical data through the experimental work was used to calculate mechanical properties of the oxide scale, including the ultimate tensile strength at various temperatures. This innovative test method could be used to improve the descaling of the oxide scale by integrating the experimental data into computerised modelling of the process.

6.3.2.1 Evaluation of the high temperature tensile test system

The oxidation conditions of the tensile tests were chosen to be similar to the isothermal oxidation of the alloys under dry atmosphere during the isothermal studies of both grades. Introduction of water vapour was not feasible due to complex test assembly and condensation of the water vapour within the connection pipes before injection of the gases into the oxidation chamber.
In the early stage of the project, the author followed the path of Krzyzanowski et al. [14, 31], which included a similar test rig assembly and a comparable specimen design. In this method, a 1.5 mm diameter ceramic pin was installed within the axisymmetrical pin-hole in the specimen gauge section to prevent the cross-sectional movement of the top and bottom parts of the sample (Figure 6.3.7 a). Unfortunately, the early high temperature tensile tests were unsuccessful due to three different reasons. Generally, the test results were vastly influenced by the errors associated with the insertion of the ceramic pin. As a result, the final failure load was significantly high, as demonstrated in Figure 6.3.7.b. This matter will be discussed in Section 6.3.2.4. Furthermore, the vibrations of the test rig's hydraulic arm hypothetically generated micro defects within the oxide structure that might affect the integrity of the oxide scales before the final stage of the test. This issue is a common problem of such a test system, and it was previously reported by Trull et al. while using a similar hydraulic test rig [4].

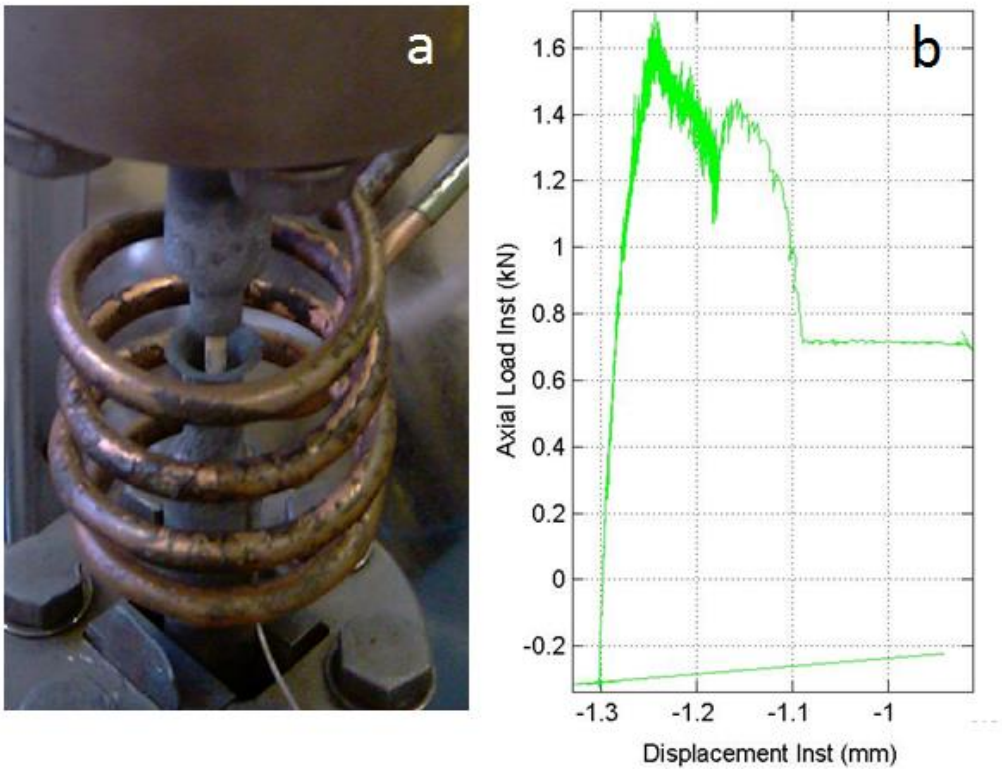

Figure 6.3.7 a. High-temperature tensile test of a pinned DSP steel specimen, oxidised at 1150°C for 60minutes and deformed at 1100°C. b. The raw test data were demonstrating tensile load against the displacement of the sample a.

Also, the resolution of the 100KN load cell installed on the test rig was not high enough to measure the small load failure of the oxide scale. Therefore, as described in Section 3.4, the tensile test rig and the specimen assembly were modified to resolve the above issues. Although the new test design was still comparable to the works of Krzyzanowski and Beynon [34], the errors associated with the original test setup were eliminated by the pragmatic changes made on the test assembly.

The drawing and schematic representation of the hot tensile test specimen is demonstrated in Figure 6.3.8. The axisymmetrical hole was created at the centre of the test pieces significantly reduced the thermomechanical bonding of the two parts of the test piece at the joint section. Moreover, the application of a thin layer of Boron Nitride between the top and bottom parts helped to eliminate the bonding of the two parts of the test sample at elevated temperatures.

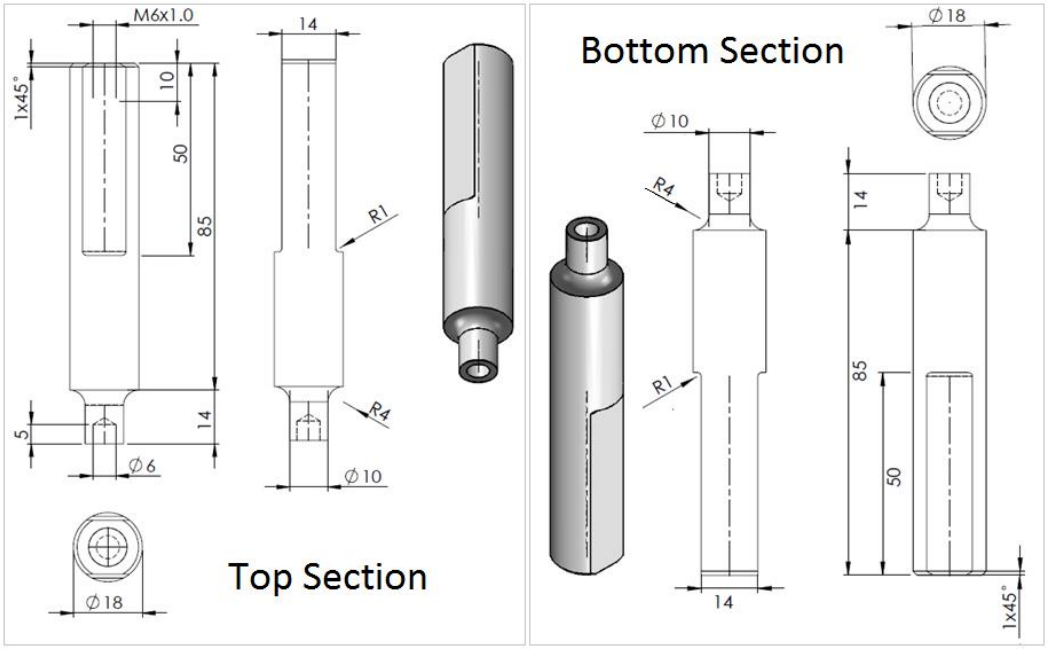

Figure 6.3.8 Drawing and schematic demonstration of the top and bottom sections of the hot tensile test specimen.

As demonstrated in Figure 6.3.9, the pulling shaft and the base of the steel frame were disengaged up to the last stage of the test, which was the application of the tensile load on the oxidised sample.

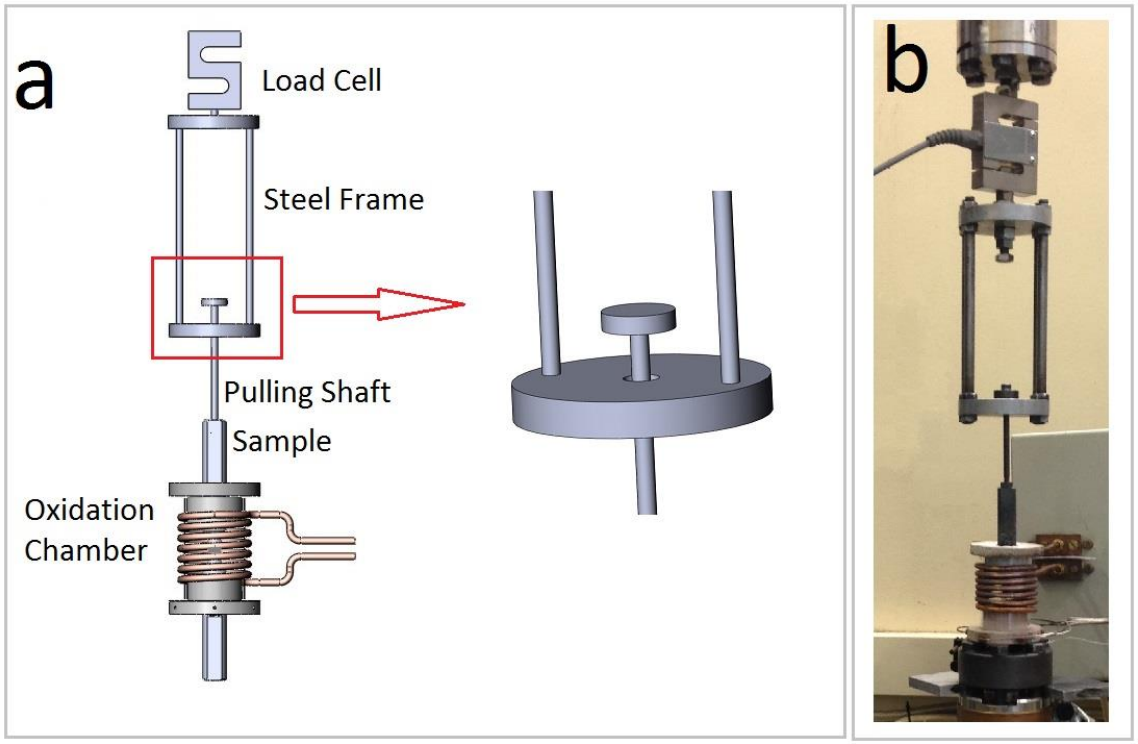

Figure 6.3.9 a: Schematic representation of hot tensile test assembly and the separation point of the pulling shaft and the steel frame b: actual demonstration of the test assembly.

The free movement of the long pulling shaft not only omitted the stresses generated by micro-vibrations of the hydraulic system but also vastly reduced the thermal expansion stresses of the system during reheating, cooling and stabilisation stages. For improving the load measurement, a 3KN load cell in conjunction with a highly sensitive data logger was added to the test assembly. The experimental data confirmed the employed load cell was adequately sensitive to measure the critical load failure of the primary oxide scale at elevated temperatures.

6.3.2.2 Macro assessments of deformed specimens

The high temperature tensile test conditions and scale failure modes are summarised in Table 6.3.3. As established in isothermal oxidation studies, the nature of the oxide scales was highly influenced by the alloy composition and oxidation conditions. Visual assessments of the oxidised samples confirmed that the development of the oxide scale of each steel grade was similar to the observations made during isothermal studies of these materials under a dry atmosphere.

Table 6.3.3 High-temperature tensile test conditions and the state of the oxide scale after deformation for two steel grades.

Steel grade	Oxidation Time (min)	Oxidation Temp. (°C)	Deformation Temp. (°C)	Scale state after deformation
Rail	60	1150	750	Through-thickness failure in the middle
Rail	60	1150	850	Through-thickness failure in the middle
Rail	60	1150	1150	Through-thickness failure in the middle
Rail	60	1150	1200	Through-thickness failure in the middle
DSP	60	1150	750	Sliding along the oxide-metal interface and final detachment at the top of the gauge
DSP	60	1150	850	Sliding along the oxide-metal interface and One through-thickness crack in the middle of the top section
DSP	60	1150	1150	Sliding along the oxide-metal interface and final detachment at the top of the gauge
DSP	180	1000	850	Through-thickness failure in the middle

Overall, the surface of the rail steel oxide scales was considerably rougher than the surface of the oxide scales of the DSP grade. This was due to the development of blisters during oxidation of all the rail steel specimens and the absence of such defects in all the oxidised DSP steel samples. This observation was in line with the principles of the oxide blistering detailed in the literature [9, 33, 35, 70]. In all test conditions, no visual defects were apparent before the tensile stage, including the development of macrocracks and oxide scale spallation.

As described in Chapter 5, two different failure modes were observed during the hot tensile tests of the oxide scale depending on the alloy composition and the test conditions as previously reported by Krzyzanowski et al. [14, 31, 34]. In the first mode, the failure occurred by through-thickness cracking in the middle at edges of the sample joining plane. The failure was due to the initiation and propagation of transverse cracks perpendicular to the applied load. This event revealed that the cohesion of the oxide scale and substrate metal was stronger than the structural integrity of the oxide layer. Based on the literature [14, 31, 34], typically, this type of failure could be observed at lower deformation temperatures. Figures 5.3.1 a, b, c, and d demonstrate the failure mode of the rail steel samples after deformation at 750˚C, 850˚C, 1150˚C and 1200˚C respectively. As can be seen, the failures of all specimens followed the above pattern despite testing the material at different temperatures. However, for DSP steel, this type of failure was only observed when the specimen oxidised at 1000°C for 180 minutes and deformed at 850°C (Figure 5.3.2 d). The lack of delamination and spallation of the oxide scale in all samples revealed that the plastic stress relaxation was similar to the model suggested by Robertson and Manning [51].

The second mode of the oxide failure was sliding the scale raft along the oxide-metal interface due to weaker bonding force between the oxide layer and substrate metal in comparison to oxide scale structural integrity which was previously described by Krzyzanowski and Beynon [14, 31, 34]. In all the DSP samples oxidised at 1150°C for 60 minutes and deformed at or above 750°C, the failure mode was slipping of the oxide scale along the metal-oxide interface. This type of failure was only apparent in hot tensile testing of the DSP steel samples while oxidised at and tested at or above (Figure 5.3.2 a, b and c). The sample oxidised at 1000°C for 60 minutes and deformed at 850°C was the only DSP grade specimen failed by through-thickness cracking at the joint section.

These observations proved that the failure mode of the oxide scale not only depended on the test temperature but also it was extremely influenced by the base metal composition. The

importance of the chemical contents of the steel was also recognised by Krzyzanowski et al. [31]. They experimentally and numerically established that small variation in the number of alloying elements including Si and Mn could change the failure mode of the oxide scale developed on mild steel containing 0.02-0.07% Ni and 0.08-0.14% Cu [31]. Furthermore, the presence of a small percentage of alloying elements with high tendency to form oxides such as Si, Ce, Hf, and Y could promote the development an adherent oxide layer that was more resistance to applied stresses [31]. Other researchers also reported similar scenarios for steel grades containing the small amount of Si [6, 72].

Nevertheless, the results of this research revealed that although during the oxidation of high silicon steel a strong Fayalite layer was formed at the oxide-metal interface, the main body of the oxide scale was weakly bonded to the Fayalite phase adjacent to the interface or even detached from this layer when oxidation occurred under a dry atmosphere. Different theories were proposed for the role of alloying elements on the behaviour of the oxide scale including the promotion of the scale plasticity, alteration of the oxidation rate, oxide protrusions into the substrate metal and enhancement of the oxide adherence [100, 101]. The results of this work were in good agreement with the above principles. Based on another theory [102], the active elements reduced the number of active sites, including dislocations, which encouraged the diffusion at the oxide-metal interface and subsequently altered the oxidation rate and oxide scale adhesion.

6.3.2.3 Cross section analysis

6.3.2.3.1 Oxide scale phase distribution

As demonstrated in Section 5.3, the oxide scale microstructure and phase composition of deformed specimens were evaluated by backscattered electron imaging and EDX analysis. In general term, the microstructure of the oxide scale of all the rail steel tensile specimens followed the classic multi-layer oxide pattern suggested by Gittins [60]. However, the tensile stresses not only influenced the extent and nature of the defects within the oxide scales but also altered the structure, proportions, and distributions of the oxide constituents. In all specimens, the detached oxide scale contained all three types of iron oxide; however, the amount of each phase was strongly governed by the test condition. A small quantity of

Wüstite was only visible at the oxide-metal interface when the sample deformed at 750˚C; nevertheless, the amount of this phase amplified by increasing the test temperature. In samples tested at 750˚C and 850˚C Fayalite, particles were only detected at the interface and within the internal oxidation zone. In contrast in samples deformed at 1150˚C and 1200˚C Fayalite was not only observed at the oxide-metal interface and internal oxidation zone but also it was apparent as fine round and needle shape particles dispersed across the oxide top layer. In samples tested at 750˚C and 850˚C Fayalite, particles were only detected at the interface and within the internal oxidation zone.

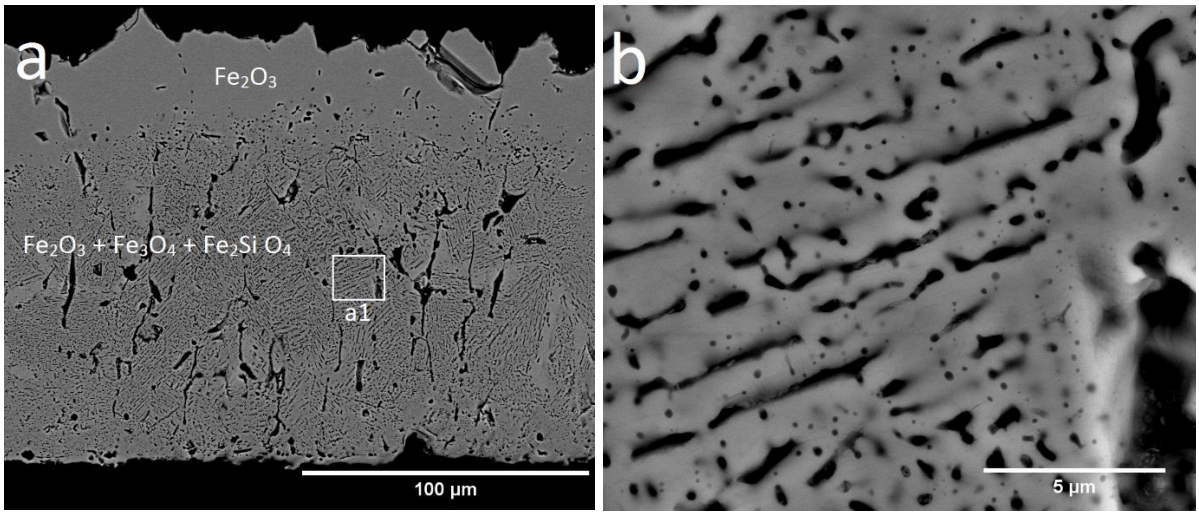

Figure 6.3.10 a. Oxide scale cross-section of a rail steel specimen deformed at 1200˚C (Tox = 1150˚C, oxidation 60min) b. High-resolution BS image of zone a1.

In contrast in samples deformed at 1150˚C and 1200˚C Fayalite was not only observed at the oxide-metal interface and internal oxidation zone but also it was apparent as fine round and needle shape particles dispersed across the top oxide layer as demonstrated in Figure 6.3.10. The migration of Fayalite to the upper section of the oxide scale can be explained first by appreciating the melting temperature of Fe_2SiO_4 as demonstrated in FeO-SiO_2 phase diagram in Figure 6.2.1. As can be seen, the melting temperature of the Fayalite was 1205°C, but this phase could coexist in a eutectic form along with FeO above 1183°C. This occurrence eased the diffusion of Fayalite through oxide scale defects, including voids and cracks.

Moreover, as explained in the literature view Section 2.6, if the Pilling-Bedworth ratio (Equation 2.18) was greater than 1, the compressive stresses were generated during oxidation and oxide scale growth at the oxide-metal interface. As the P.B ratio of FeO-iron was reported to be 1.78 [6], [10], [11], [12], [13], thus oxidation of the rail steel above 750°C would generate

compressive stresses which might stimulate the diffusion of Fayalite into the oxide scale defects. Nevertheless, this type of Fayalite structure was not observed during isothermal studies of rail steel even at a higher temperature, i.e., 1280°C.

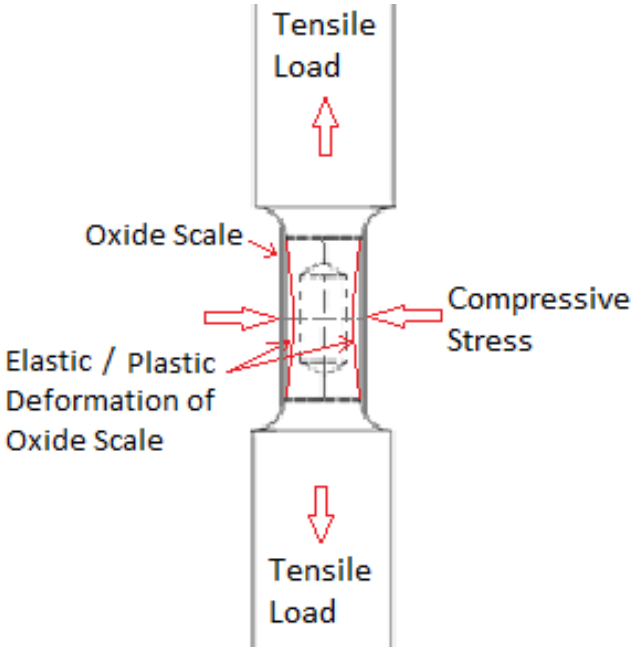

Figure 6.3.11 Schematic demonstration of generated stresses during the hot tensile test.

There was another important factor associated with the development of such microstructure. The main driving force behind the diffusion of liquid Fayalite was the applied tensile load during the final step of the test. As schematically demonstrated in Figure 6.3.11, due to the applied tensile load, the oxide scale was elastically and eventually plastically deformed (necking). Although the deformation exaggerated in the drawing and the real deformation was minor, but it was enough to generate compressive stresses within the oxide scale towards the substrate metal. It is important to recognise that the top and bottom parts of the specimen were sectioned in the middle; therefore, no tensile load was applied on the substrate steel. Therefore, unlike the stress generation scenario within the oxide scale, there were no compressive stresses generated within the substrate metal by slight necking. As a result, in the horizontal direction, the oxide-metal interface was almost static during the tensile stage. Furthermore, shear stresses were generated at the oxide-metal interface due to the movement of the substrate metal in the direction of the tensile load (vertical). Consequently, the liquid Fayalite was pushed into the oxide scales defects.

In contrast to the rail steel samples, the microstructure of the DSP tensile samples followed the duplex oxide scale structure suggested by Metcalfe [65], which contained Hematite and Magnetite along with Fayalite. This was in line with observations made during isothermal oxidation of DSP steel under a dry atmosphere. Once again, the proportion of each phase highly depended on the test conditions. In all DSP tensile samples, the main body of the oxide scale was constructed of Fe_2O_3 and Fe_3O_4 with small quantities of Fe_2SiO_4 embedded within the defects in Magnetite layer. The diffusion of Fayalite into the main body defects followed the same principles described earlier; however, the microstructure of the Fayalite observed in rail steel sample tested at 1200°C, was different to any microstructure of the DSP steel specimens. This was because, during testing all DSP samples, the oxidation and deformation temperatures never reached the FeO-Fe_2SiO_4 eutectic temperature. Another distinctive feature was the detection of SiO_2 particles via BSE imaging and EDX analysis. This phase was only detected in the DSP sample oxidised for 60 minutes at 1150°C and deformed at 850°C. The BSE image revealed that the small bodies of SiO_2 embedded within the Fayalite phase at the oxide-metal interface. Based on FeO-SiO_2 phase diagram, this mixture could be developed when the local saturation of SiO_2 exceeded 32% mole fraction limit. The observations were in good agreement with the hot compression test of DSP steel experiments when the environments kept the same.

Table 6.3.4 Phase and defect area fractions of the oxide scale after high temperature tensile test for two steel grades.

Steel Grade	**Oxidation Time (min)**	**Oxidation Temp. (°C)**	**Test Temp. (°C)**	**Average Thickness (µm)**	**FeO Area %**	**Fe_3O_4 Area %**	**Fe_2O_3 Area %**	**Fe_2SiO_4 Area %**
Rail	60	1150	750	213	2.28	46.03	50.81	0.88
Rail	60	1150	850	206	9.65	41.61	47.95	0.79
Rail	60	1150	1150	211	19.34	40.36	38.82	1.48
Rail	60	1150	1200	215	24.16	18.38	52.81	4.65
DSP	60	1150	750	222	0	36.39	46.40	17.3
DSP	60	1150	850	238	0	33.59	58.09	8.32
DSP	60	1150	1150	235	0	47.14	32.97	19.89
DSP	180	1000	850	99	0	30.52	43.48	26.00

The amount of each phase for both steel grades was determined using image processing method as described in isothermal studies in Chapter 3, and the results were summarised in

table 6.3.4. As can be seen, regardless of the deformation temperature, the average thickness the oxide scales of all rail steel samples were comparable. The average thickness of oxide scales for DSP steel grade was slightly higher than the rail grade when oxidised at 1150°C. The thinnest oxide scale was observed in the DSP steel specimen oxidised at 1000°C for 180 minutes.

6.3.2.3.2 Evaluation of the defects and failure of the oxide scale

The cross-sectional assessment confirmed the presence of various defects, including pores, voids, blisters, and cracks across the oxide scale in all the tensile samples. Regardless of the test conditions, the main body of the oxide scale of all rail steel samples delaminated from the oxide-metal interface and accordingly a large separation cavity was formed between the thick upper oxide layer and the residual oxide scale at the interface.

Although all the rail steel samples were oxidised at 1150°C for 60 minutes, depending on the deformation temperature, the extent and characteristics of the defects were considerably diverse. It was evident that the number and size of the defects extended as the deformation temperature increased. The density and size of the porosity were significantly larger within the Wüstite and Magnetite zones. The development of porosity followed the model proposed by Basabe and Szpunar [9]. The pores were formed at the grain boundaries because of Wüstite grains growth on the metal surface. Moreover, the porosity was formed within the oxide layer through the on-going oxide growth and the subsequent rise of the compressive stresses. Further oxidation enhanced the merge of the small pores within Wüstite and Magnetite layers, which eventually formed larger defects.

The actual fractured surface of a rail specimen oxidised at 1150°C for 60 minutes and deformed at 1150°C is demonstrated in Figure 6.3.12. As expected from the multiphase structure of the oxide scale, a composite failure was apparent on the fractured surface. Two typical fracture modes of Hematite below 1200°C were observed across the top section of the oxide scale. The first failure mode was brittle intergranular fracture within the Fe_2O_3 outermost layer. As marked the other type of the failure was brittle cleavage fracture that occurred within the lower section of the Fe_2O_3 phase. In contrast, a ductile failure mode was observed within Wüstite phase at the lower part of the oxide scale. The failure modes terminology used above is detailed in reference [105].

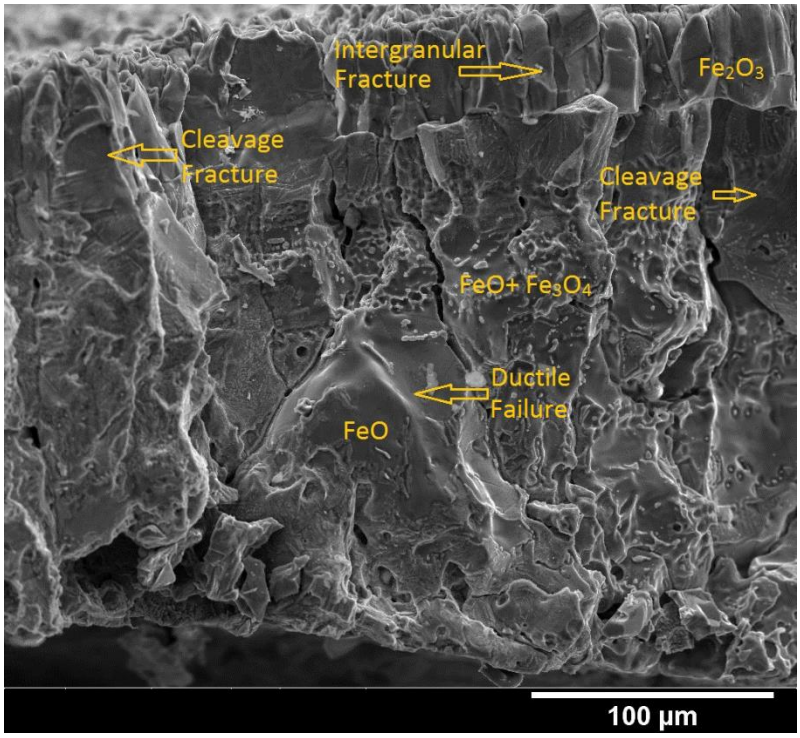

Figure 6.3.12 Scanning electron image of the fractured surface of the rail steel sample after the tensile test at 1150°C (Tox 1150°C).

Hidaka et al. observed similar failure modes for Hematite, Magnetite, and Wüstite while fully oxidised samples deformed at elevated temperatures under tension [17]. The experimental studies confirmed that Magnetite could be plastically deformed when the deformation temperature exceeded 800°C. Correspondingly, Wüstite could behave in the same manner when tested under tension above 700°C. The plastic deformation occurred as a result of dislocation glide, which was accompanied by work hardening. The occurrence of this phenomenon was much easier in cubic type crystals such as Wüstite with NaCl structure and Magnetite with cubic inverse spinel structure in comparison to Hematite with rhombohedral structure. The other factor that played an important role in dislocation mobility was the lattice parameter of the crystal. By considering Peierls–Nabarro stress proportionality, the dislocation mobility had an inverse relation with the lattice constant of the crystal. Since Wüstite had a smaller lattice constant (a =4.3 Å) than Magnetite (a=8.4 Å) and Hematite (a=b=5.0 Å, c=13.7 Å), therefore the plasticity of FeO was higher than the plasticity of the other two iron-oxide constituents [17]. The oxide transforms into steady-state deformation at higher temperatures. The mechanism for this type of plasticity is defined as dislocation climb or diffusion creep (Nabarro–Hering creep). As stated by Hidaka [17], the plasticity

regime of Wüstite above 1000°C and Magnetite above 1200°C followed the dislocation climb model, which can be considered as a ductile failure. This was in good agreement with composite failures of the oxide phases observed in this research.

As described earlier in all rail steel samples, the oxide blisters were observed within the outermost layer of the oxide scale, i.e. Hematite region.

Partial transverse cracks were detected in all rail specimens. Crack development was related to three different root causes. Initially, the cracks were possibly formed due to the existence of compressive stresses. The other root cause was the application of the tensile load during the deformation stage, which triggered the final failure of the oxide scale.

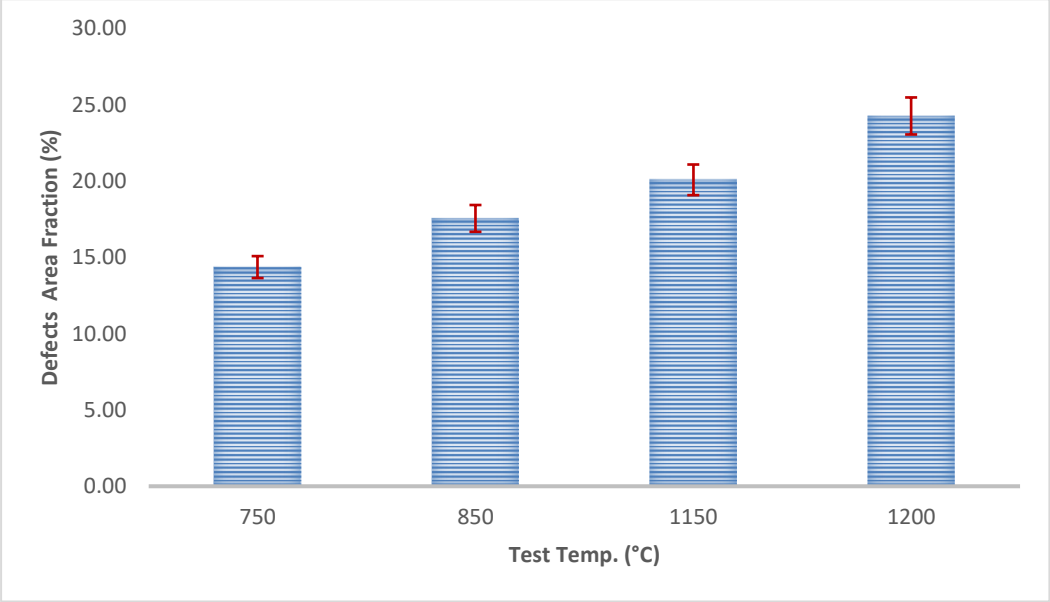

Figure 6.3.13 Relationship of the defects area fractions (excluding the separation gap) and the tensile test temperatures of rail steel samples oxidised at 1150°C for 60 minutes.

And finally, the thermal shock stresses generated during the cooling stage contributed towards the propagations of existing cracks or hypothetically introduced new defects across the oxide scale. The structure, size, and proportion of the defects not only subjected to material composition and the oxidation temperature but also it was highly influenced by the deformation temperature as demonstrated in Figure 6.3.13.

Like the high temperature tensile tests of the rail steel, the main body of the oxide scale of all the DSP steel samples detached from the residual oxide scale at the interface irrespective of the test condition. In contrast to the rail steel, the thick oxide outer layer of all DSP specimen oxidised at 1150°C was denser with a much smaller proportion of porosity. As demonstrated

in cross-sectional BSE images of the rail steel samples, most of the defects distributed across Wüstite and Magnetite regions phase. As no evidence of FeO was detected during the assessments of the DSP oxide scales. Therefore the percentage of porosity considerably reduced.

`

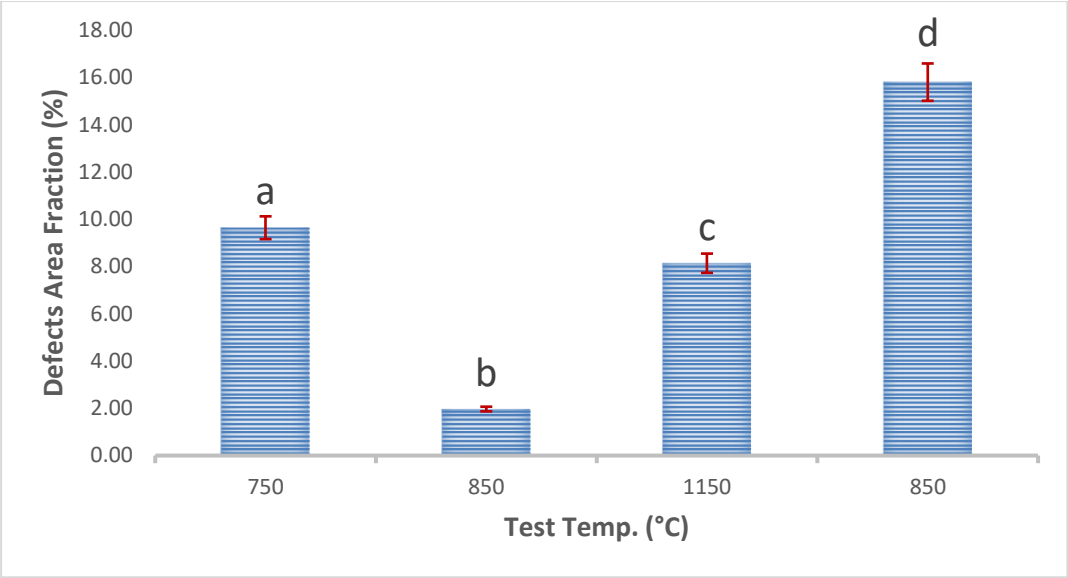

Figure 6.3.14 Relationship of the defects area fractions (excluding the separation gap) and the tensile test temperatures of DSP steel. Samples a, b and c: oxidised at 1150°C for 60 minutes. Sample d: oxidised at 1000°C for 180 minutes

As demonstrated in Figure 6.3.14, the defects area fraction of the DSP sample oxidised at 1000°C for 180 minutes was noticeably higher than the other three specimens. This was due to two different reasons:

1. At 1000°C relatively large cavities were formed within the Fe_2O_3 due to irregular grain growth of He5matite at the outermost layer.
2. In the sample oxidised at 1000°C, the oxide scale was much thinner than the other samples; this could relatively exaggerate the size of the cavities.

Correspondingly García-Rincón [6] reported the adverse effect of the oxide scale thickness on the oxide porosity fraction.

6.3.2.4 Evaluation of the tensile test numerical results

As described in Section 5.3.2, to eliminate the undesirable test elements including the gravitational force associated with the weight of sample's top part and the thermomechanical bonding at the sample's joint section, the hot tensile tests were performed under oxidant a

protective atmosphere at any required temperature. The final results of the tensile tests were the subtraction of the results obtained from non-oxidised samples from the values acquired from oxidised specimens. The results of the tensile test for both steel grade are summarised in Table 6.3.5. As can be seen, the ultimate tensile load failure of the oxide scale for rail steel at 850°C was measured as 77N. As described earlier, the original design of high temperature tensile tests in this research was based on the method suggested by Krzyzanowski and Beynon [31]. Because the UTS value was not reported on the referenced paper, it was only possible to compare the ultimate tensile failure loads of this work and the reported values by Krzyzanowski and Beynon.

Table 6.3.5 High temperatures tensile test results.

Steel Grade	Oxidation Time (min)	Oxidation Temp. (°C)	Deformation Temp. (°C)	Average Thickness (µm)	Ultimate Failure Load (N)	Ultimate Tensile Strength (MPa)	Residual Elongation (%)
Rail	60	1150	750	213	56	8.16	0.12
Rail	60	1150	850	206	77	11.60	0.18
Rail	60	1150	1150	211	50	7.45	0.20
Rail	60	1150	1200	215	39	5.61	0.16
DSP	60	1150	750	222	91	12.75	0.32
DSP	60	1150	850	238	45	5.83	0.12
DSP	60	1150	1150	235	60	7.91	0.56
DSP	180	1000	850	99	34	11.47	0.11

Figure 6.3.15 demonstrated the load versus displacement curves for through thickness crack failure mode of the oxide scales under tension for a mild steel specimen which was oxidised at 830°C for 6000s. The ultimate tensile failure load (subtracted) from the curves was estimated as 1400N. This value was abnormally higher than the measured ultimate tensile failure load (subtracted) of 77N for the rail steel specimen, which was tested at 850°C.

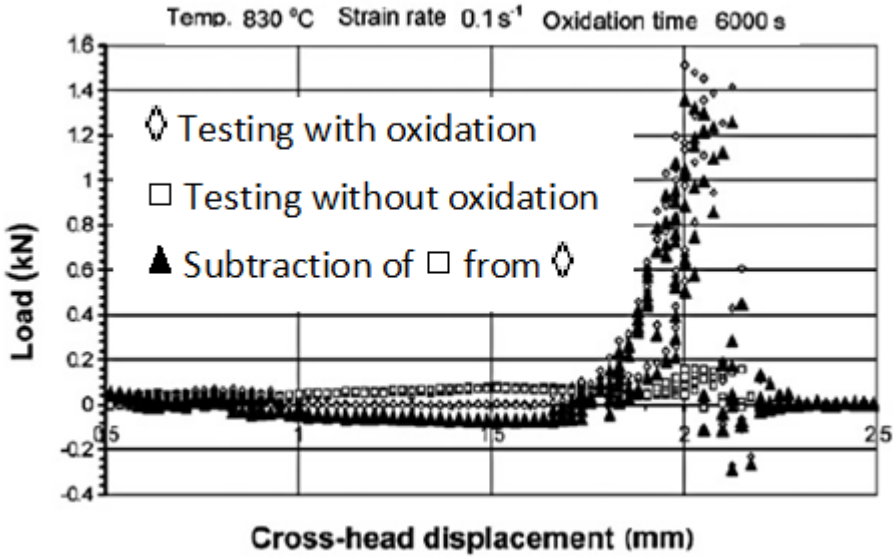

Figure 6.3.15 Load versus displacement curve plotted for the through-thickness failure of oxide scales under the tension of mild steel [31].

The comparison of the ultimate tensile loads for sliding failure mode disclosed a similar scenario. Figure 6.3.16 demonstrated the load versus displacement curves for sliding mode of the oxide scales under tension for a mild steel specimen which was oxidised at 1150°C for 800s. The ultimate tensile failure load (subtracted) was estimated as 690N from Figure 6.3.16. On the other hand, the same value for the failure of DSP steel sample deformed at 1150°C was measured as 60N. Again, the value measure by Krzyzanowski and Beynon was remarkably higher. It was appreciated that the chemical compositions of the two steel grades and the test conditions used in this study were different from the material and test conditions used in the research referred above. However, the author strongly believes that considerable errors were associated with the experimental results obtained by Krzyzanowski and Beynon. As explained in the literature review Chapter, a ceramic pin was included in their inventive test assembly to eliminate the transverse movements of the specimen's top and bottom parts. They performed the test under two different atmospheres. Initially, the separation load was measured under an inert environment, i.e., the sample was not oxidised. Then they repeated the measurement after oxidising the sample. And finally, the final value was calculated by subtracting the measured value of non-oxidised sample from the same value measured for the oxidised sample.

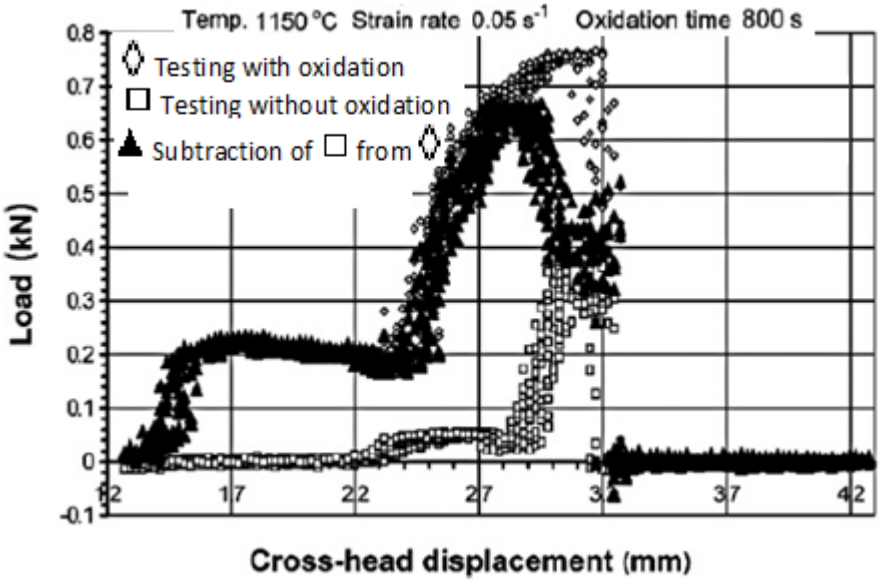

Figure 6.3.16 Load versus displacement curve plotted for sliding failure mode of oxide scales under the tension of mild steel [31].

Their measured load of failure was affected by the oxidation of the pin-hole inner wall while testing was carried out under oxidant atmosphere. The development of oxide film between the ceramic pin and the wall of the pin-hole could generate a large resistance force in the form of friction during the deformation stage. Moreover, they applied a small load to prevent the movement of the sample. As a result, the two sections of the test piece could thermomechanically bonded and generate a false reading. As can be seen in Figure 6.3.16, the separation load for the non-oxidised sample was over 400N. A similar error was observed by the author using a similar test setup in the early stage of the experiment. However, after the modification of the test assembly, the same value measured was about 2.4N or 239gr force. This was almost equal to the total weight of the top section of the tensile specimen and the connected pooling shaft. It should be noted that the geometry of the sample used was much larger than the sample used by Krzyzanowski and Beynon, so in theory, the value measured by them under protective atmosphere should be smaller.

As explained in Chapter 2, Hidaka succeeded to measure the tensile load failures of Wüstite, Magnetite and as Hematite experimentally by producing a sample constructed of a sole phase sample in any single test [17]. In his research, all pure iron specimens fully oxidised, i.e., no metal substrate remained on the test piece. For producing a suitable sample that only constructed of a single phase, complex oxidation regimes were adopted. The experimental data were used to produce the ultimate tensile strength of each phase at elevated

temperatures. The calculated tensile strengths of α-Fe_2O_3, γ -Fe_3O_4 and FeO for a strain rate of 2.0 × 10^{-4} s^{-1} for a temperature range of 600°C-1200°C are demonstrated in Figure 6.3.17.

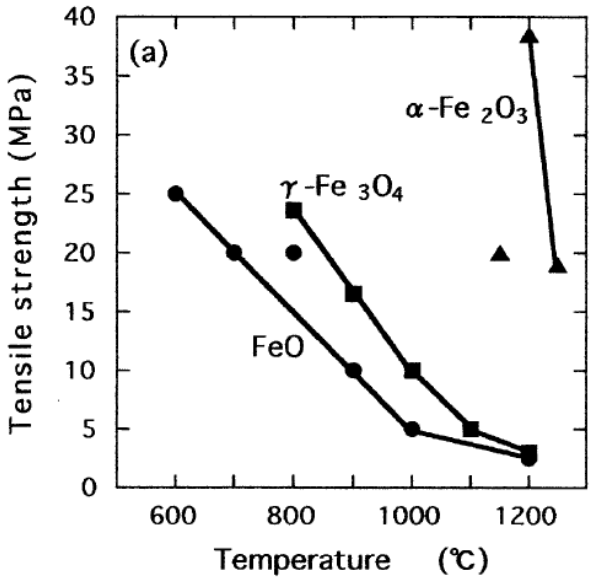

Figure 6.3.17 Apparent tensile strength (a) and elongation (b) of the α-Fe_2O_3, γ -Fe_3O_4 and FeO specimens for a strain rate of 2.0 × 10^{-4} s^{-1} after Hidaka et al. (2002).

As can be seen, the highest tensile strength (which was below 40 MPa) attained when Fe_2O_3 tested at 1200°C. Even at lower temperatures, the tensile load failure of FeO and Fe_3O_4 were considerably lower than the equivalent value reported for Hematite. Although the design of Hidaka's tensile test [17] was fundamentally different compared to the method used in this research, the reported test results were comparable to the UTS results calculated in this study. It has to be noticed that the UTS value calculated in this work was a consequential value, and it was highly depended on the percentage and crystal structure of each oxide constituent, as explained earlier.

Chapter 7

Conclusions and suggestions for further work

7.1 Conclusions

7.1.1 Isothermal oxidation studies

The research initially focused on the isothermal oxidation progress and oxide scale behaviour of the two steel grades proposed by Tata Steel Europe; Rail B9S34 (high carbon steel) and DSP B9S23 UT23 (high silicon steel) under controlled atmosphere. The analysis lead to following conclusions:

1. Overall, the results of isothermal studies confirmed that the oxidation kinetics of both steel grades were highly influenced by different parameters, including time, temperature and the compositions of the parent metal and the atmospheric conditions.
2. Although the oxidation rate of rail steel at 1280˚C was higher in comparison to oxidation at 1150˚C, the oxidation rates of this alloy obeyed the parabolic law at both temperatures under a humid atmosphere. This phenomenon confirmed that the oxidation rate was time-dependent, and the process controlled by solid-state diffusion of the oxidising species and the oxide scale growth retarded the mobility of iron and oxygen ions throughout the oxide scale.
3. The isothermal oxidation of rail steel at 1280˚C under dry atmosphere also followed the parabolic law. However, the comparison of the oxidation rates for humid and dry atmospheres confirmed that the addition of water vapour considerably accelerated the oxidation rate. Although the addition of water vapour reduced the partial pressure of oxygen, the H_2O appeared as an additional oxygen ions source and consequently augmented the reaction rate.

4. The cross-sectional analysis of the rail steel specimens revealed that the multiphase oxide scales were developed in all test conditions. The oxide scale microstructures and phase distributions followed the classic models of carbon steel oxidation at elevated temperatures that projected in the literature [1-3]. The study revealed that in high temperature oxidation of rail steel under humid and dry atmosphere, the oxide scale contained all three iron oxide constituents including FeO, Fe_3O_4 and Fe_2O_3 along with minor quantities of Fayalite. The phase analysis of the samples oxidised in a temperature range of 850˚C to 1280˚C confirmed that Wüstite was the predominant phase, and the development of Hematite was considerably small. This discrepancy was due to the higher mobility of defects in FeO with a NaCl crystal structure in comparison to α-Fe_2O_3 with a rhombohedral structure.
5. The proportion of defects including porosities, cracks and separation cavities gradually reduced ad the oxidation progressed. This was due to the growth of the oxide phases, particularly Wüstite into cavities and porosities in longer oxidation periods. Furthermore, extending the oxidation period, enhanced the oxide/metal adherence while the external and internal oxidations simultaneously occurred around the oxide-metal interface. Contrary, in isothermal oxidation of the rail steel under a dry atmosphere at 1280˚C, the oxide scale completely detached from substrate metal.
6. The study confirmed that the isothermal oxidation of DSP steel at 1150˚C and 1280˚C under a humid atmosphere obeyed the parabolic law. In contrast, the oxidation rate of this alloy at 1150˚C under dry atmosphere followed the logarithmic law. This was associated with the development of a subsurface layer of SiO_2 and Fe_2SiO_4 near the oxide-metal interface. Furthermore, it was confirmed that the oxidation rate of this grade could rapidly increase above the Wüstite-Fayalite eutectic temperature (11803°C) due to the higher mobility of iron irons through the liquid phase.
7. Oxidation of the DSP steel at 1280˚C, oxide scale was constructed of Wüstite and Magnetite along with Fayalite. FeO was the predominant phase throughout the oxidation process, and there was no sign of Hematite. The oxidation of DSP steel at 1150˚C was more complex. In the early stage of the oxidation, Hematite was the predominant phase, however as the oxidation progressed the proportion of Wüstite rapidly increased and the fraction of Hematite significantly reduced. Oxidation of DSP steel at 850˚C-1150˚C for 60 minutes under humid atmosphere confirmed that Wüstite was the predominant phase in

all temperatures. The highest amount of Magnetite was observed in the oxidation of the material between 950˚ to 1050˚C. The proportion of Fayalite was almost constant at all temperatures. In the oxidation of DSP steel under a dry atmosphere at 1150˚, the main body of the oxide scale was delaminated. However, the residual oxide particles remained at the oxide-metal interface.

8. Increasing the time of the oxidation increased the oxide layer thickness as well as the defects formation such as porosities and cracks within the oxide structure. Nevertheless, the oxidation rate decreased by oxide growth.
9. Laser Raman spectroscopy studies confirmed that it was an effective method for phase analysis of the oxide scale. Therefore, this technique could potentially be used as a routine method for the identification of various oxide phases.

7.1.2 Compression test

The oxide scale behaviour and mechanical failure modes of the oxide scale of rail steel and DPS steel were studied via a tailored compression test method. The design of the test allowed simultaneous evaluation of the oxide scale under shear and compressive stresses. The main conclusions based on the macro and micro analysis of the test pieces are as follow:

1. Macro observations of the oxidised rail steel specimen revealed that the oxide scale failure type and the extent of the damage were subject to the deformation temperature. The bucking and lift of the oxide scale towards the compression tool at 1280˚C confirmed the high plasticity of the oxide scale at such temperature. In contrast, at lower defamation temperatures, the development of transverse cracks at the top of the arc and the shape of the oxide layer indicated that the oxide scale was failed in a brittle-ductile manner.
2. The isothermal oxidation of the rail steel led to the development of a dense and homogenous oxide scale that contained Fe_2O_3, Fe_3O_4, and FeO. Although the proportion of iron oxide phases for each test after oxidation stage were all consistent but depending on each test deformation temperature, the amount of each phase changed.
3. The cross-sectional assessments of the rail steel specimens confirmed that at 1280°C, all phases were ductile. Above 1150°C, several transverse cavities were developed within the Magnetite region. During the deformation stage, the size of the cavities was reduced as

Magnetite columnar grains were inclined under shear stresses imposed by the compression tool. The destruction of Hematite at 1150°C confirmed the brittle nature of this phase at this temperature. Magnetite failure patterns confirmed the brittleness of this phase in test temperatures below 1150°C. In contrast, Wüstite deformed in a complete ductile manner in the test temperature range of 850°C to 1280°C.

4. The failure mode could be entirely transformed beneath the oxide blisters, which were only present in specimens deformed at 850°C and 1050°C. The oxide scale was crushed into smaller particles where the blisters destructed under compressive load.
5. In comparison to rail steel compression tests, fewer variations were apparent in the macro assessment of the deformed DSP steel specimens. However, many microscale differences were revealed during the cross-sectional analysis for each test condition. Furthermore, it was noticed the bonding between the main body of the oxide scale and the Silica-Fayalite layer at the oxide-metal interface was relatively weak.
6. The cross-sectional analysis of the DSP samples confirmed that the oxide scale only contained Hematite and Magnetite along with Silica and Fayalite in all test temperatures.
7. The appearance of numerous cracks across the Fe_2O_3 and Fe_3O_4 regions revealed the brittle nature of the two iron oxide constituents at 850°C. The reduction of the number of transverse cracks in DSP samples deformed at higher temperatures confirmed the higher plasticity of Hematite and Magnetite.
8. In general, the oxide scale of DSP steel was more brittle than rail grade under the same test condition. This was due to lack of presence of Wüstite phase in DSP specimens.
9. The compression test studies revealed that overall failure mode of the oxide sale was directly associated with the proportion of each oxide constituent. The multi-phase oxide scale must be considered as a composite state, which the failure of the system is highly depended on each component.
10. The study proved the importance of the chemical composition of the parent metal in development and failure mode of the oxide scale during hot deformation. This important element must be certainly considered in the design of any descaling process in an industrial mill.
11. At higher deformation temperatures, partial and through-thickness metal extrusions were observed through the cracked oxide scales under compressive load which could similarly occur in an industrial rolling mill.

7.1.3 Tensile test

The test methodology was based on the original method developed by Krzyzanowski and Beynon [34] to measure tensile failure load at elevated temperature. The test design was modified to eliminate the experimental errors associated with the original test method. The test facilitated the study of the two distinguished failure modes of the oxide scale under tension reported by the above researchers. The major conclusions of the hot tensile tests could be summarised as follow:

1. The oxide scales failed in two different manners during the hot tensile testing. All rail steel samples were failed by through-thickness cracks initiation within the oxide structure and final failure of the oxide scale in the transverse direction. All the DSP steel specimens oxidised for 60 minutes at 1150˚C, the scales failed by sliding along the oxide-metal interface. The only through thickness failure mode was observed in sample oxidised for 180 minutes at 1000˚c and deformed at 850˚C. According to Krzyzanowski and Beynon [31], the failure mode of the oxide scale at lower temperatures was through thickness failure, and by increasing the deformation temperature, it would transform to failure by sliding along the oxide-metal interface. The current study confirmed that the failure mode of the oxide sale was not only depended on the test temperature but also it was highly influenced by the chemical composition of the parent material.
2. The ultimate tensile failure load of the rail steel oxide scale at 850°C was measured as 77N (through thickness failure), which was significantly lower the value estimated by Krzyzanowski and Beynon [31] for low alloy steel at the same temperature. Despite the compositional difference between the rail steel and the alloy used by the above researchers, the reported results seemed to be abnormally high. Likewise, based on the above reference, the ultimate tensile failure load for sliding failure type was considerably higher than the measured ultimate tensile load of 60N of a DSP steel sample deformed at 1150°C. The high reported values by Krzyzanowski and Beynon [31] were believed to be related to the errors associated with the test set up and in particular with the insertion of a ceramic pin in the middle of the samples.

3. Oxide blistering was observed during the oxidation stage of rail steel specimens, but no such defects were apparent during oxidation of the DSP samples. This observation was in line with the hypothesis that suggested for oxide blistering in high temperature oxidation of steel, the parent steel need to contain sufficient amount of carbon.
4. The assessment of a rail specimen oxidised at 1150°C for 60 minutes and deformed at 1150°C via SEM revealed that the failure of the scale was a composite failure. The outermost layer failed Hematite due to brittle intergranular fractures. Furthermore, brittle cleavage fractures were apparent within Magnetite layer just beneath the Fe_2O_3 layer. In contrast, a ductile failure mode was observed within Wüstite phase at the lower part of the oxide scale. These observations confirmed that the scale failure in an industrial steel rolling mill is a complex failure which potentially includes both brittle and ductile failure modes.

7.2 Suggestions for further work

1. The current study focused on the isothermal oxidation of two entirely different steel grades. One of the alloys was high carbon steel for railway production and the other one high silicon steel sheet for electrical applications. It is proposed a similar study to be carried out using different type of steel alloys including a low alloy steel grade to allow the assessment of alloying elements effects on oxidation kinetics and oxide scale microstructure.

2. Correspondingly the effect of the alloying elements on mechanical properties and failure modes of the oxide scale can be better understood if the oxide scale of a low alloy steel grade assessed by compression and tensile testing methods designed in this research.

3. In future studies, it is sensible to expand the oxidation temperature range to lower temperatures, i.e. 650°C to evaluate the oxidation behaviour of the steel alloys at a lower temperature. The study should also include similar a thermomechanical assessment of the oxide scale at a lower temperature.

4. In this research, the number of tensile tests performed in different oxidation temperatures was limited. The above study can be expanded by using different isothermal oxidation temperatures to examine the effect of the oxidation temperature and microstructure of the materials on the failure mode.

5. As demonstrated in the isothermal studies, the addition of moisture into the oxidant environment completely transformed the oxidisation kinetics and microstructure of the oxide scale. Hence it is recommended in future studies the atmosphere of the tensile and compression experiments to be modified by adding water vapour. This would allow the oxidation atmosphere to be much more like an industrial reheating furnace.

References:

1. Kofstad P. (1966): “High-temperature oxidation of metals”. John Wiley & Sons, Inc.
2. Birks N., Meier G. H. (1983): “Introduction to high temperature oxidation of metals”. First Edition. E. Arnold. London.
3. Khanna A. S. (2002): “Introduction to high temperature oxidation and corrosion”. First Edition. ASM International.
4. Trull M. (2002): “Modeling of oxide failure in hot metal forming operations.” PhD Thesis. Department of Engineering Materials, the University of Sheffield, UK.
5. Chang Y.N., Wei F.I. (1989): “Review High temperature oxidation of low alloy steels”, Journal of Materials Science, 24, (1), 14–22.
6. García-Rincón O. (2006): “Oxide scale failure during multi-stage deformation in the hot rolling of mild steel.” PhD Thesis. Department of Engineering Materials, the University of Sheffield, UK.
7. Schütze M. (1995): "Mechanical Properties of Oxide Scales", Oxidation of Metals, 44(1/2), 29-61.
8. Jones D. A. (1996): “Principles and prevention of corrosion”. Second Edition. Prentice-Hall, USA, p. 419.
9. Basabe, V. V. and Szpunar, J. A. (2004): "Growth rate and phase composition of oxide scale during hot rolling of low carbon steel." ISIJ International 44 (9), 1554-59.
10. Cottrell, A. H. (1975): “An introduction to metallurgy”. Second Edition. Edward Arnold; distributed by Crane Russak. New York, p. 548.
11. Sherwood W., Shatynski S. R. (1984): "The effect of temperature on oxide scale adherence during descaling operations." Surface Technology 21 (1), 39-51.
12. Nagl M. M., Evans W. T. (1993): "The Mechanical Failure of Oxide Scales under Tensile or Compressive Load." Journal of Materials Science 28 (23), 6247-6260.
13. Lorman V., Lahoche L., Rochal S. B., Roelandt J. M. and Vallino, N. (1999): "Duplex structure formation and adherence properties of oxide scale on a metal." Surface and Coatings Technology 111 (1), 22-28.
14. Krzyzanowski M., Beynon J.H., Farrugia D.C.J (2010): “Oxide Scale Behaviour in High Temperature Metal Processing.” Wiley-VCH Verlag GmbH & Co. KGaA

15. Yu Y., Lenard J.G. (2002): “Estimating the resistance to deformation of the layer of scale during hot rolling of carbon steel strips.” Journal of Materials Processing Technology, 121, 60-68.
16. Krzyzanowski M., Beynon J.H. (1999): “The tensile failure of mild steel oxides under hot rolling conditions.” Steel Research, 70 (1), 22-27.
17. Hidaka Y., Anraku T., Otsuka N. (2003): “Deformation of iron oxide upon Tensile Tests at 600-1250°C.” Oxidation of Metals, 59 (1/2), 97-113.
18. Sheasby J., Boggs W. E., Turkdogun E. T. (1984): “Scale growth on steels at 1200°C: rationale of rate and morphology.” Metal Science, 18, 127-136.
19. Davis M.H., Simnad M.T., Birchenall C.E. (1951): “On the mechanism and kinetics of the scaling of iron.” Transactions of the ASME, 191, 889-896.
20. Li Y.H., Sellars C.M. (1996): Modelling deformation behaviour of oxide scales and their effects on interfacial heat transfer and friction during steel rolling.” In Proceedings of Second Int. Cnf. Modeling Metal Rolling Processes (eds J.H. Beynon, P. Ingham, H. Teichert, K. Waterson), Institute of Materials and Mining London, 192-206.
21. Munther P.A., Lenard J.G. (1999): “The effect of scaling on interfacial friction in hot rolling of steels.” Journal of Materials Processing Technology, 88, 105-113.
22. Krzyzanowski M., Sellars C.C., Beynon J.H. (2002): “Characterisation of oxide scales in thermomechanical processing of steel,” in Proceedings of Int. Conf. Thermomechanical Processing: Mechanics, Microstructure & Control, 23-26 June 2002 (eds E.J. Palmiere, M. Mahfouf, C. Pinna), University of Sheffield, Sheffield UK, 94-102.
23. Boelen R., Thomson P.F., Brownrigg A. (2002): “Controlled oxidation rolling,” in Proceedings of Int. Conf. Thermomechanical processing: Mechanics, Microstructure & Control, 23-26 June 2002 (eds E.J. Palmiere, M. Mahfouf, C. Pinna), University Sheffield, Sheffield UK, 103-108.
24. Filatov D., Pawelski O., Rasp E. (2004): “Hot rolling experiments on deformation behaviour of oxide scale.” Steel Research International, 75, 20-25.
25. Schutze M. (1988): "Stresses and Decohesion of Oxide Scales", Materials Science and Technology, 4, 407-14.

26. Saunders S.R.J., Nicholls. J.R. (1996): “Oxidation, hot corrosion and protection of metallic materials,” in Physical Metallurgy, Fourth, Revised and Enhanced Edition (eds Cahn R.W. and Hassen P.), Elsevier Science BV, Amsterdam, 1291-1362.
27. Gaballah, I., Raghy, S., Gleitzer, C. (1978): “Oxidation kinetics of fayalite and growth of hematite whiskers”, Journal of Materials Science, 13 (9), 1971-1976.
28. Suárez L., Houbart Y., Vanden Eynde X., Colas R. (2008): “Development of experimental device to study high temperature oxidation.” Oxidation of Metals, 70, 1-13.
29. Grenier C., Bouchard P.O., Montmitonnet P., Picard, M. (2008): “Behaviour of oxide scales in hot steel strip rolling.” International Journal of Materials Forming, 1 (Suppl. 1), 1227-1230.
30. Le H.R., Sutcliffe M.P.F., Wang P., Burstein G.T. (2005): “Surface generation and boundary lubrication in bulk forming of aluminium alloy.” Wear, 258, 1567-1576.
31. Krzyzanowski M., Beynon J. H. (2000): “Effect of oxide scale failure in hot steel rolling on subsequent hydraulic descaling: numerical simulation.” Proceeding 3rd Int. Conf. on Hydraulic Descaling, September 14-15, 2000, IOM Communications Ltd., London, 77-86.
32. Garza-Montes-de-Oca N. F. (2009): “Oxidation and wear behaviour of a work roll grade high speed steel.” PhD Thesis. Department of Engineering Materials, the University of Sheffield, Sheffield.
33. Chen R. Y., Yeun W. Y. D. (2003): “Review of the high-temperature oxidation of iron and carbon steels in air or oxygen.” Oxidation of Metals, 59, 433-468.
34. Krzyzanowski M., Beynon J. H. (2002): “Measurement of oxide properties for numerical evaluation of their failure under hot rolling conditions”, Materials of Processing Technology, 125-126, 398-404.
35. Matsuno F. (1980): “Blistering and hydraulic removal of scale films of rimmed steel at high temperature”, Transaction ISIJ, 20, pp. 413-421.
36. Kofstad P. (1972): Nonstoichiometry, Diffusion, and Electrical Conductivity in Binary Metal Oxide. Wiley-Interscience. P.382.
37. Sherwood W., Shatynski S. R., in Louthan M. R., Jr., McNitt R. P., Sisson Jr R. D., (eds.), (1981): “Environmental Degradation of Engineering Materials in Aggressive Environments”, Vol. 1, Virginia Polytechnic Institute, Blacksburg, VA, 1981, p. 383.

38. Tuck C.W, Odgers M., Sachs K. (1969): “The oxidation of iron at 950˚C in oxygen/water vapour mixtures”. Corrosion Science, Vol. 9. 271-285.
39. Garza-Montes-de-Oca. N. F., Colas. R, Rainforth W.M. (2011): “High Temperature Oxidation of a Work Roll Grade High Speed Steel”, Oxidation of Metals, Vol. 76 (5-6), 451-468.
40. Jansson L. and Vannerberg, N. (1971): “The Effect of the Oxygen Pressure and the Growth of Whiskers on the Oxidation of Pure Fe”, Oxidation of metals Vol. 3 (5), 453-461.
41. Caplan D., Cohen M., Comen M. (1970): “Effect of oxygen pressure and experimental method on the high temperature oxidation of pure Fe”, Corrosion Science Vol.10,1-8.
42. Picqué B., Montmitonnet P. O., Picard M. (2005): “Mechanical behaviour of iron oxide scale: Experimental and numerical study”, Wear, Vol. 260, 231-242.
43. Utsunomiya H., Hara K., Matsumoto R., Azushima A. (2014): “Formation mechanism of surface scale defects in hot rolling process”, CIRP Annals - Manufacturing Technology, Vol. 63 (1), 261-264.
44. Levin E. M., Robbins C. R., Mcmurdie H. F. (1964): Phase diagrams for ceramists, Columbus, Ohio: American Ceramic Society.
45. Wriedt H. A., Massalski T .B. 1990, “Binary Alloy Phase Diagrams”, ASM International, Materials Park, OH, 1739–1744.
46. Yu X., Jianga Z., Zhao J., Wei D., Zhoub J., Zhou C., Huang Q. (2013): “Tribological properties of magnetite precipitate from oxide scale in hot-rolled microalloyed steel”, Wear Vol. 302, 1286–1294.
47. Yang Y., Yang C., Lin S., C. Chen, Tsai W. (2008): “Effects of Si and its content on the scale formation on hot-rolled steel strips”, Materials Chemistry and Physics, Vol. 112, 566–571.
48. Genève D., Rouxel D., Pigeat P., Confente M. (2010): “Descaling ability of low alloy steel wires depending on composition and rolling process”, Corrosion Science, Vol. 52, pp. 1155–1166.
49. Chandra-Ambhorn C., Klubvihok N. (2015): “Quantification of adherence of thermal oxide scale on low carbon steel using tensile test”, Oxidation of Metal, Online first.
50. Evans H.E. (1988): "Spallation of Oxide from Stainless Steel AGR Nuclear Fuel Cladding: Mechanisms and Consequences", Materials Science and Technology, 4, p. 415-20.

51. Robertson J., Manning M.I. (1990): "Limits to Adherence of Oxide Scales", Materials Science and Technology, 6, p. 81-91.
52. Budi Aulia T. (2000): "Strain Localization and Fracture Energy of High-Strength Concrete under Uniaxial Compression", Leipzig Annual Civil Engineering Report, (5), p. 221-40.
53. Meyer J. (1997): "Deformation Capacity of the Concrete Compression Zone Stress-Strain Curves for Nonlinear Calculation", Leipzig Annual Civil Engineering Report, (2), p. 87-102.
54. Coleman J., Spacone, E. (2001): "Localization Issues in Force-Based Frame Elements", Journal of Structural Engineering, 127, p. 1257-65.
55. Lemaitre J. (1996), “A Course on Damage Mechanics”. 2nd ed. Berlin: Springer-Verlag. 227.
56. Tvergaard V. (1990): "Material Failure by Void Growth to Coalescence", Advances in Applied Mechanics, 27, p. 83-151.
57. Pardoen T., Hutchinson J.W. (2000): "An Extended Model for Void Growth and Coalescence", Journal of the Mechanics and Physics of Solids, 48, p. 2467-512.
58. Feenstra P.H., De Borst R. (1995): "A Composite Plasticity Model for Concrete", International Journal of Solids and Structures, 33(5), p. 707-30.
59. De Borst R. (2002): "Fracture in Quasi-brittle Materials: a Review of Continuum Damage-based Approaches", Engineering Fracture Mechanics, 69, p. 95-112.
60. Gittins, A. (1975): "Fracture in Hot Working of Steel", The Journal of the Australian Institute of Metals, 20(4), p. 184-200.
61. Bernard J., Coquelle O. (1946): "Nouvelle recherches sur l'oxydation du fer aux temperatures elevees par la methode micrographique", Compte Rendus, 222, p. 796.
62. Garber S., Sturgeon G.M. (1961): "Scale on Wire Rod and its Removal by Mechanical Means", Wire Industry, (March/June), p. 257-9; 295; 369-76.
63. Sheppard T., Steen W.M. (1970): "Hydraulic descaling of steel, a preliminary experimental study", Journal of the Iron and Steel Institute, p. 797-805.
64. Schweighofer A., Tyas S. (2000): “VAI's Solutions on Hydraulic Descaling”. Proceedings 3rd International Conference on Hydraulic Descaling. London, 65-74.

65. Metcalfe E. (1989): “Oxide Characterisation for Life Prediction”, in Proc. Seminar on ‘surface stability: oxidation-corrosion-erosion-wear’, No. 6, (ed. T. N. Rhys-Jones), London, The Institute of Metals, p. 145.
66. Wrazej W.J. (1953): "Observation on Scaling of Iron", Transactions of the American Institute of Mining and Metallurgical Engineers, 197, p. 265-6.
67. Merz M.D. (1979): "The Oxidation Resistance of Fine-Grained Sputter- Deposited 304 Stainless Steel", Metallurgical Transactions A, 10A, p. 71-7.
68. Schmitz-Niederau M., Schutze M. (1999): "Cracking and Healing of Oxide Scales on Ti-Al Alloys at 900oC", Oxidation of Metals, 52(3/4), p. 241-76.
69. Banovic S.W., DuPont J.N., Marder, A.R. (2000): "Growth of Nodular Corrosion Products on Fe-Al Alloys in Various High-Temperature Gaseous Environments", Oxidation of Metals, 54(3-4), p. 339-69.
70. Chen R. Y., Yuen W. Y. D. (2002): "Oxidation of low-carbon low-silicon mild steel at 450°- 900°C under conditions relevant to hot strip processing." Oxidation of Metals 57 (1-2), 53-79.
71. Abuluwefa H.T., Guthrie R.I.L., Ajersch F. (1997): "Oxidation of Low Carbon Steel in Multicomponent Gases: Part I. Reaction Mechanisms during Isothermal Oxidation", Metallurgical and Materials Transactions. 28A, 1633-1641.
72. Taniguchi S., Yamamoto K., Megumi D., Shibata T. (2001): “Characteristics of scale: substrate interface area of Si-containing low-carbon steels at high temperatures”, Materials Science and Engineering, 308, 250–257.
73. Goldstein J.I., Newbury D.E., Echlin P., Joy D.C., Fiori C., Lifshin E. (1981): “Scanning Electron Microscopy and X-Ray Microanalysis”, Plenum Press. 673.
74. Abuluwefa H.T. (2012): “Kinetics of High Temperature Oxidation of High Carbon Steels in Multi-component Gases Approximating Industrial Steel Reheat Furnace Atmospheres”, Proceeding of the International Multiconference of Engineers and Computer Scientists 2012 Vol II, IMECS, March 14-16, 2012, Hong Kong.
75. Wang N., Dong J., Huang W., Li, B., Chen M. (2014): “Growth rate, microstructure and phase composition of oxide scales for three typical steels in simulated continuous casting process”, Journal of Iron and Steel Research, International, 1065-1072.

76. Mouayd A.A., Koltsov A., Sutter E., Tribollet, B. (2014): “Effect of silicon content in steel and oxidation temperature on scale growth and morphology”, Materials Chemistry and Physics, 143, 996-1004.
77. Lee V., Gleeson B., Young D. (2005): "Scaling of Carbon Steel in Simulated Reheat Furnace Atmospheres", Oxidation of Metals, 63 (1-2):
78. Li H., Zhang J., Young D. (2012): “Oxidation of Fe–Si, Fe–Al and Fe–Si–Al alloys in CO2–H2O gas at 800˚C”, Corrosion Science, 54, 127-138.
79. Martínez-Cázares, G.M., Mercado-Solís, R.D., Colás, R., Garza-Montes-de-Oca. N.F. (2013): “High temperature oxidation of silicon and copper–silicon containing steels”, Ironmaking & Steelmaking, 40:3, 221-230.
80. Suárez L., Schneider J., Houbart Y. (2008): “Effect of Si on High-Temperature Oxidation of Steel during Hot Rolling”, Defect and Diffusion Forum, Vols. 273-276, 655-660.
81. Takeda M., Onishi T. (2006): “Oxidation behaviour and scale properties on the Si-containing steels”, Materials Science Forum, Vols. 522-523, 477-488.
82. Suárez L., Rodríguez-Calvillo P., Houbart Y., Colas R. (2010): “Oxidation of ultra-low carbon and silicon bearing steels”, Corrosion Science, 52, 2044–2049.
83. Laverde D., Gomez-Acebo T., Castro F. (2004): “Continuous and cyclic oxidation of T91 ferritic steel under steam”, Corrosion Science, 46, 613–631.
84. Kofstad P. (1995): “Defects and Transport Properties of Metal Oxides”, Oxidation of Metals, 44, 1/2.
85. Rahmel A., Tobolski J. (1965): “Einfluss von wasserdampf und kohlendioxyd auf die oxydation von eisen in sauerstoff bei hohen temperaturen”, Corrosion Science, 5, 333.
86. Abuluwefa H.T., Guthrie R.I.L., Ajersch F. (1996): " The Effect of Oxygen Concentration on the Oxidation of Low-Carbon Steel in the Temperature Range 1000 to 1250˚C”, Oxidation of Metals, 46, (5/6), 423-440.
87. Caplan D., Sproule G.I., Hussey R.J., Graham M.J. (1979): “Oxidation of Fe-C Alloys at 700˚C”, Oxidation of Metals, 13, 256-272.
88. Malik A. U., Whittle D. P. (1981): “Oxidation of Fe-C Alloys in the Temperature Range 600-850˚C”, Oxidation of Metals, 16, 339-353.
89. Moore N., Oldroyd P., Lewis P., Westacott M. (1990): “An investigation of the formation, constitution and properties of scale formed in the reheating furnace and

during the hot rolling process", technical steel research of British Steel strip products, Welsh Technology Centre, (1997), ISBN 92-828-1682-6.

90. Wei F. I., Cheng K. H., Wu J. Y. (1981): "The Study Of Scaling Mechanism Of CSC Rod & Bar", China Steel Corporation Report PJ-70-003.
91. Saegusa F., Lee L. (1966): "Oxidation of iron-aluminium alloys in the range 500 - 1000˚C", Corrosion, 22, 168-177.
92. Huang Z.Z., Zhu R.Z. (1982), Proc. JIMIS-3 "High Temperature Corrosion of Metals and Alloys", Mt. Fuji, Published by Japan Institute of Metals, (1983), 24, p.231.
93. Liu S., Di T., Wu H., Wang L. (2013): "Oxide Scale Characterization of Micro-Alloyed Steel at High Temperature", Journal of Materials Processing Technology, 7, 1068-1075.
94. Gleeson B., Hadavi S.M.M., Young D. J. (2000): "Isothermal transformation behaviour of thermally-grown Wüstite", Materials at High Temperatures. 17, 311–319.
95. Song E. J., Suh D. W., Bhadeshia H. K. D. H. (2012): "Oxidation of silicon containing steel", Ironmaking and Steelmaking, 39, 8, 599-604.
96. Zhou M., Xu G., Hu H., Yuan .Q, Tian J. (2017):" The Morphologies of Different Types of Fe2SiO4–FeO in Si-Containing Steel", Metals, 7, 1- 8.
97. Yuana L., Wang Y., Cai R., Jiang Q., Wang J., Li B., Sharma A., Zhou G. (2012): "The origin of hematite nanowire growth during the thermal oxidation of iron", Materials Science and Engineering B 177, 327– 336.
98. Singh Raman R. K., Gleeson B., and Young D. J. (1998): "Laser Raman spectroscopy: a technique for rapid characterisation of oxide scale layers", Materials Science and Technology, Vol. 14, 373-376.
99. Takeda M., Onishi T., Nakakubo S. and Fujimoto S. (2009): "Physical properties of iron-oxide scales on Si-containing steels at high temperature", Materials Transactions, Vol. 50, No. 9, 2242 to 2246.
100. Whittle D. P., Stringer J. (1980): "Improvements in high temperature oxidation resistance by additions of reactive elements or oxide dispersions", Philosophical Transactions of the Royal Society of London, 295.
101. Strawbridge A., Hou P. Y. (1994): "The role of reactive elements in oxide scale adhesion", Materials at High Temperatures, 12:2-3, 177-181.

102. Pieraggi B, Rapp R. (1994): Interfacial scaling reactions and the reactive element effect, Materials at High Temperatures, 12:2-3, 229-235.
103. Pelton A. D., Blander M. (1986): “Thermodynamic analysis of ordered liquid solutions by a modified quasichemical approach—Application to silicate slags”, Metallurgical Transactions B, Volume 17, Issue 4, 805-815.
104. Bassett W. A., Ming L. (1972): “Disproportionation of Fe_2SiO_4 to $2FeO+SiO_2$ at pressures up to 250kbar and temperatures up to 3000°C”, Phys. Earth Planet. Interiors 6, 154-160.
105. Ashby M. F., Gandhi C, Taplin D. M. R. (1979): “Fracture-mechanism maps and their construction for f.c.c. metals and alloys”, Acta Materialia, Vol. 27, 699-729.
106. Thouless M.D. (1990): "Crack spacing in brittle films on elastic substrates", Journal of American Ceramic Society, 73(7), 2144-6.
107. Pinna C., Beynon, J.H., Sellars C.M., and Bornert M. (2000): “Experimental Investigation and Micromechanical Modelling of Hot Deformation of Duplex Stainless Steels”, Annual Conference of Metallurgists, Thermomechanical Processing of Steel, Ottawa, Canada.
108. Krzyzanowski M., Trull, M., Beynon J. H. (2005): Proc. 11th Int. Symposium on Plasticity and Its Current Applications: PLASTICITY ‘05, Ed. By A. S. Khan and A. R. Khoei, Neat Press, Fulton, Maryland, USA, 106.
109. Zhang J., Li H., Kong C., Young D. J. (2013): “Oxidation and carburisation of Fe–6Al/Fe–6Al–3Si in dry and wet CO_2 gases”, Corrosion Science, 74, 256–264.
110. Krzyzanowski M., Beynon, J.H., Sellars C.M. (2000): “Analysis of secondary oxide scale failure at entry into the roll gap”, Metallurgical and Materials Transactions, 31B, 1483-1490.
111. Coudurier L., Hopkins, D.W., Wilkomirsky I. (2013): “Fundamentals of Metallurgical Processes: International Series on Materials Science and Technology”, Vol. 27, Pergamon international library of science, technology, engineering, and social studies, Edition 2, Elsevier.
112. Ashby M. F., Shercliff H., Cebon D. (2009): Materials: engineering, science, processing and design, Elsevier.
113. Ahmed A., Sturges J. (2014): Materials science in construction: an introduction, Routledge.

114. Fletcher D. I. (1999): “The influence of lubrication on the fatigue of pearlitic rail steel”, PhD Thesis, Department of Mechanical Engineering, University of Sheffield, UK.
115. Carroll R. I. (2006):“Surface metallurgy and rolling contact fatigue of rail”, PhD Thesis, Department of Engineering Materials, University of Sheffield, UK.
116. Kavishe F. P. L. and Baker, T. J. (1986): “Effect of prior austenite grain size and pearlite interlamellar spacing on strength and fracture toughness of a eutectoid rail steel”, Materials Science and Technology, 2 (8), 816-822.
117. Price K., Goode B., Power D. (2016): “Grain-oriented electrical steels for power and distribution transformers”, Ironmaking & Steelmaking, 43 (9), 636-641.
118. Rodriguez-Calvillo P., Houbaertc Y., Petrovc R., Kestensc L., Colásd R. (2012): “High temperature deformation of silicon steel”, Mater. Chem. Phys., 136 (2–3), 710–719.
119. Cornelissen M. C. M., Kromhout J. A., Kamperman A. A., Kick M., Mensonides F. (2006): “High productivity and technological developments at Corus DSP thin slab caster”, Ironmaking & Steelmaking, 33(5), 362-366.
120. Petrovič D. S. (2010): “Non-oriented electrical steel sheets”, Materials and technology, 44 (6), 317-325.
121. Bemmer V. L. (2013): "The Properties of Electrical Steels and Their Coatings", PhD Thesis, Department of Chemistry, Cardiff University, UK.
122. Massalski T. B. (1991): Binary Alloy Phase Diagrams, ASM, Materials Park, Ohio, pp. 1772.
123. Schulte M., Steentjes S., Leuning N., Bleck W., Hameyer K. (2019): “ Effect of manganese in high silicon alloyed non-oriented electrical steel sheets”, Journal of Magnetism and Magnetic Materials, 477, 372-381.
124. Ghosh P., Chromik R. R., Knight A. M., Wakade S. G. (2014): “Effect of metallurgical factors on the bulk magnetic properties of non-oriented electrical steels”, Journal of Magnetism and Magnetic Materials, 356, 42–51.
125. Nakayama T., Honjou N. (2000): “Effect of aluminum and nitrogen on the magnetic properties of non-oriented semi-processed electrical steel sheet”. Journal of Magnetism and Magnetic Materials, 213, 87-94.
126. Collocott S.J. (2001): “Magnetic Materials: Domestic Applications”, Encyclopedia of Materials: Science and Technology, 4804-4812.

127. Jackson P. R. S., Wallwork G. R. (1983): “The oxidation of binary iron-manganese alloys”, Oxidation of Metals, 20, 1-17.
128. Mao W., Sloof W. G. (2017): “Relation between oxygen activity gradient in the internal oxidation zone of Mn alloyed steel and the composition of oxide precipitates”, Scripta Materialia, 135, 29–32.
129. Aghaei Lashgari V. (2014): “Internal and external oxidation of manganese in advanced high strength steels”, PhD Thesis, Delft University of Technology.
130. Atlas L. M., SUMIDA W. K. (1958): “Solidus, subsolidus, and subdissociation phase equilibria in the system Fe-Al-O”, Journal of the American Ceramic Society, 41, 5, 150-160.
131. Guan Sh. (1993): “external and internal oxidation properties of ternary Fe-Fi-Al, and Ni-Si-Al alloys, PhD Thesis, McMaster University.
132. Muan A. (1957): “Phase equilibria at liquidus temperatures in the system Iron Oxide-Al_2O_3-SiO, in Air Atmosphere”, Journal of the American Ceramic Society, 40, 4, 121-133.